

Study of Dense Core Property and Core Mass Function with Simulation and Observation Data to Reveal the Core Growth with Observations

by

Hideaki Takemura

Submitted in Partial Fulfillment of the Requirements for the Degree of
Doctor of Philosophy

Supervised by

Assoc Prof. Fumitaka Nakamura

Assis Prof. Tomoya Hirota

Assis Prof. Akimasa Kataoka

Department of Astronomical Science, School of Physical Sciences
The Graduate University for Advanced Studies, SOKENDAI



January 2023

Acknowledgments

I would like to thank the following people, without whom I would not have been able to complete this research, and without whom I would not have had productive days during my entire five-year Ph.D. program in SOKENDAI at NAOJ.

First and foremost, I would like to express my sincere gratitude to my main supervisor, Prof. Fumitaka Nakamura. He shared the physics and history of star formation study from basic. In addition, he gave me plenty of ideas for the analysis and constructive feedback on the results and discussion. He also gave me opportunities to conduct collaborative research with many astronomers around the world, and I constructed this thesis based on the results of it.

I also highly appreciate the kind support of my associate supervisors: Prof. Tomoya Hirota and Prof. Akimasa Kataoka. They gave me feedback on my study and research plan from the different views of the main supervisor. Besides, when I started the Ph.D. program at NAOJ, I was in the same office as Prof. Akimasa Kataoka. He told me about the atmosphere of NAOJ and the attitude of being a

graduate student.

I am grateful to Prof. Yoshito Shimajiri, Dr. Patricio Sanhueza, Prof. Shun Ishii, Prof. Ryohei Kawabe, Prof. Takashi Tsukagoshi, Prof. Kazuhito Dobashi, and Prof. Tomomi Shimoikura, who taught me basics of radio observation, star formation, and data analysis mainly in the first few years of the Ph.D. program. They also had a discussion on my analysis, and it improved the published papers and my understanding of star formation.

In addition, I would like to express my gratitude to my collaborators in the analysis of observational data, who are Prof. Hector G. Arce, Dr. Nicola Schneider, Dr. Volker Ossenkopf-Okada, Dr. Shuo Kong, Prof. Paolo Padoan, Prof. Ralf Klessen, Prof. Paul Goldsmith, Prof. Blakesley Burkhart, Dr. Alvaro Sanchez-Monge, Prof. Dariusz Lis, Prof. John Carpenter, Dr. Jens Kauffmann, Dr. Thushara Pillai, Prof. Adam Ginsberg, Dr. Rowan Smith, Prof. John Bally, Dr. Steve Mairs, Dr. Jaime Pineda, Prof. Peter Schilke, Dr. Hope Chen, Prof. Andrea Isella, Prof. Rachel Friesen, Prof. Alyssa Goodman, Prof. Doyal Harper, and the above people for the observation and simulation data, scientific discussion, and constructive feedback. I would also like to extend my thanks to Dr. Benjamin Wu for giving me numerical simulation data. If it were not for the collaboration with them, this thesis and published papers would not have been completed.

I greatly thank the referees of this Ph.D. thesis: Prof. Hideko Nomura, Dr. Doris Arzoumanian, Prof. Satoko Takahashi, Prof. Toshikazu Onishi, and Prof. Koji Sugitani. They gave me valuable suggestions and feedback on the draft of this thesis and the presentation for the Ph.D. defense.

I would like to mention that my student life was supported by the secretary's office of the Division of Science and the Graduate Student Affairs Unit of NAOJ. I am thankful for Ms. Shioko Izumi, Ms. Megumi Noguchi, Ms. Manami Watanabe, Ms. Mihiro Fujimori, Ms. Mizuho Inoue, Ms. Yumiko Omura, Ms. Kaya Kitabayashi, and Ms. Yukie Mastuda. Thanks to their help, I could concentrate on my research during this Ph.D. program.

I had wonderful days outside of my study as well. I want to thank all students who spent time with me at NAOJ, especially Mr. Shinichi Kinoshita, Ms. Kaho Morii, Mr. Kosuke Ishihara, Mr. Yuta Yano, and Mr. Yuto Komichi, who had a regular seminar with my main supervisor.

Finally, but most importantly, I deeply thank my family, who always understand and encourage me. Their kindness is essential to begin the Ph.D. program and finish this Ph.D. thesis.

I received enormous support from the Division of Science, National Astronomical Observatory of Japan, The Graduate University for Advanced Studies, SOKENDAI, and JSPS KAKENHI Grant Number of 22J13587. Data analysis was carried out on the Multi-wavelength Data Analysis System operated by the Astronomy Data Center (ADC), NAOJ.

Abstract

Star formation takes place in the gravitationally unstable dense cores of molecular clouds. The stellar evolution process and the impact on the cloud environment of stars greatly depend on the stellar mass. The dense core mass, the birthplace of a star, is one of the targets being actively researched. The relationship between mass distributions of dense cores (Core Mass Function, CMF) and stars (Initial Mass Function, IMF) has been expected to imprint the statistical information of evolution from dense cores to stars. Today, IMF is thought to be a universal feature based on observations that can resolve individual stars. The nearby low-mass star-forming regions' observations reported that CMFs resembled slopes at the high-mass ends to IMF and larger turnover massed than IMF. A core-collapse star formation scenario is proposed based on the one-to-one correspondence between CMF and IMF. In this model, the final stellar mass is determined by the parental core mass with the mass ratio of the star and dense core (Star Formation Efficiency, SFE), which is a constant independent of mass and less than unity. The numerical

simulations of the evolution of prestellar cores confirmed that SFE is less than one since protostellar outflow blows off a part of the material in the parental core. However, the recent ALMA continuum observations reported top-heavy CMFs in the high-mass star-forming regions. The interpretation of the result is under discussion.

On the other hand, because dense cores are deeply embedded in the molecular cloud, the core growth with mass accretion from the surrounding material is also studied observationally, theoretically, and analytically. As an observational study, we reported that CMF resembles IMF in the Orion Nebula Cluster (ONC) region from a dense core survey. This result suggests that external mass supply is expected when considering the protostellar feedback. In addition, we found that protostellar cores tend to have larger masses than starless cores, which also supports the possibility of core growth with mass accretion. The cloud-scale numerical simulation showed that CMF resembles IMF even if mass accretion is taken into account. However, the Bondi accretion rate is much lower than the calculated mass accretion rate. The analytical study which constructed CMF with the fragmentations of filaments predicted that the power-law slope of CMF is not affected by mass accretion along the filaments.

We suppose we can explore the core growth with mass accretion by comparing the CMFs in various star-forming regions in different stages of star formation. Using CMFs instead of individual core masses enables such statistical studies. Before furthering such observations, we suggest the following two tasks should be addressed. One is investigating whether we can obtain true CMF from observations.

The other is establishing a fiducial core catalog that can be compared with other star-forming regions. In this thesis, we conduct the above two studies. We think this study is also helpful in ongoing CMF studies such as ALMA-IMF.

First, we construct CMFs with the three-dimensional numerical simulation data in the position-position-position (PPP) space of collisions of two molecular clouds. Using the data, we created the column density data in position-position (PP) and position-position-velocity (PPV) spaces that assume the continuum and molecular line observations and derived CMFs. We treated PPP CMF as a true CMF and compared it with PP and PPV CMFs. Then, We found that the slope of PP CMF becomes shallower by overlapping multiple cores in the line of sight direction. Also, the column density of the cloud along the line of sight makes the core mass larger and PP CMF's slope steeper. In the case of the PPV CMF, the slope is steeper than the true CMF due to the line broadening that causes the underestimation of core mass. Based on the above results, we conclude that compensation for the effects should be done to derive a true CMF from observations.

Second, we performed an unbiased and wide-field dense cores survey in Orion A using the CARMA+NRO45-m combined $C^{18}O$ ($J=1-0$) data. Orion A is the nearest giant molecular cloud and has been observed with various wavelengths so far. In addition, the map spatial resolution is comparable to the ALMA data of star-forming regions at a few kpc. Thus, we judge the core catalog with this data in Orion A as suitable for the fiducial core catalog. In addition to providing the core catalog, we explored the core physical properties of this region. The observed CMF has a turnover at $\sim 0.1 M_{\odot}$, which is similar to IMF, supporting

the possibility of core growth. By dividing the map into subregions based on the declination, we found that massive cores locally distribute around the cloud center, OMC-1/2/3 area. In addition, the CMF in the region has a significantly shallower slope than CMFs in the other subregions. This implies that cores in the high-column density region accumulate material more effectively. Interestingly, more than half of starless cores are classified as gravitationally unbound cores. The estimated core lifetime from the number ratio of bound starless cores and Class II objects is consistent with previous studies for other star-forming regions. Next, we calculated an expected mass accretion rate required to double the core mass in the core lifetime. The mass accretion is higher than the Bondi mass accretion rate by orders of 2. The mass accretion from filaments is supposed to achieve such a high-mass accretion rate.

Contents

Acknowledgments	ii
Abstract	v
List of Tables	xvi
List of Figures	xxiii
1 Introduction	1
1.1 Molecular Cloud and Dense Core	1
1.2 Standard Star formation Scenario	3
1.3 Initial Mass Function (IMF) and Core Mass Function (CMF)	8
1.3.1 Initial Mass Function	8
1.3.2 Core Mass Function	13
1.3.3 The Relationship Between IMF and CMF	21
1.3.4 The effects of SFE, multiplicity, and fragmentation	27
1.4 Core Identification Method: Dendrogram	32
1.5 Dense Core Survey in Orion A with NRO45-m data	36

1.6	Comparison of IMF and CMF in the Orion Nebula Cluster (ONC) Region	38
1.7	Growth of Core Mass and CMF	45
1.7.1	Observational Study	48
1.7.2	Numerical Simulation	50
1.7.3	Analytical Study	55
1.8	Binning of CMF	55
1.9	Summary of This Chapter	58
1.10	Purpose and Structure of This Thesis	61
2	Dense Core Survey with Numerical Simulation Data	64
2.1	Numerical Simulation Data	66
2.2	Preparation of Data Set: PP data and PPV data	67
2.3	Core Identification	69
2.4	Dense Core Survey and Construction of CMFs - PPP data -	72
2.4.1	Overlap Effect	75
2.5	Dense Core Survey and Construction of CMFs - PP data -	83
2.5.1	CMFs with Simulated Radio Flux and Constant Temperature	91
2.5.2	CMFs with Various Distances from the Peak of Column Density	95
2.6	Dense Core Survey and Construction of CMFs - PPV data -	99
2.7	Summary of This Chapter	108
3	Dense Core Survey with Observational Data	111

3.1	Observational Data	112
3.1.1	CARMA+NRO45-m Combined C18O ($J=1-0$) Data	112
3.1.2	<i>Herschel</i> H ₂ Column Density Data	115
3.1.3	YSO Catalog	115
3.2	Dense Core Survey in Orion A	117
3.2.1	Core Identification	117
3.2.2	Calculation of the Core Physical Properties	118
3.3	Analysis of the Core Physical Properties	123
3.3.1	Histograms of the Core Physical Properties	123
3.3.2	Correlations Among the Core Physical Properties	139
3.3.3	Core Physical Quantities Along the Declination Axis	151
3.4	CMFs in Orion A	156
3.4.1	CMFs in Entire Cloud	158
3.4.2	CMFs in Subregions in Orion A	159
3.5	Core Growth with Mass Accretion from Surrounding Material	163
3.6	Summary of This Chapter	167
4	Conclusions and Future Prospects	169
4.1	Observation of True CMFs	169
4.2	Filaments and Their Hubs	170
4.3	Gravitationally Unbound Cores	171
	Bibliography	173

A	Appendix of Chapter 2	189
A.1	Analysis of PP Data	189
A.1.1	Dense Core Survey and Construction of CMFs with PP data in yz and zx planes	189
A.2	Analysis of PPV Data	196
A.2.1	Dense Core Survey and Construction of CMFs with PPV Data in yzv and zxy Spaces	196
B	Appendix of Chapter 3	200
B.1	Virial Analysis	200
B.2	Two-Sample KS Test of Core Properties in Subregions of Orion A	202
B.3	CMF with Variable Sized Bin	204
B.4	CMFs with Column Density Threshold	209

List of Tables

1.1	The Summary of the Properties of Molecular Clouds in Bodenheimer (2011)	2
1.2	The summary of the resultant mass functions in Swift and Jonathan P. Williams (2008)	32
2.1	The Input Parameters of Dendrogram for PPP data	71
2.2	The Input Parameters of Dendrogram for PP data	71
2.3	The Input Parameters of Dendrogram for PPV data	72
2.4	The Results of Dense Core Survey with PPP Data	74
2.5	The Results of Dense Core Survey with PPP Data	74
2.6	The CMF Properties with PPP Data	75
2.7	The CMF Properties of Variably Sized Bins with PPP Data	78
2.8	The CMF Properties with PPP Data and $R_{z,2nd}$ Values	79
2.9	The Results of Dense Core Survey with PP Data (xy Plane)	83
2.10	The Summary of Core Properties Identified with PP Data (xy Plane)	85
2.11	The CMF Properties with PP Data in xy Plane	88
2.12	The CMF Properties of Variably Sized Bins with PP Data in xy Plane	90

2.13	The CMF Properties with PP Data with Uniform Temperature in xy Plane	93
2.14	The CMF Properties for Cores in Various Distances from Column Density Peak without Subtraction	96
2.15	The CMF Properties for Cores in Various Distances from Column Density Peak with Subtraction	96
2.16	The Results of Dense Core Survey with PPV Data (xyv Space)	99
2.17	The Summary of Core Properties Identified with PPV Data (xyv space) Using Fiducial Parameter	101
2.18	The CMF Properties with PPV Data in xyv Space	101
2.19	The CMF Properties of Variably Sized Bins with PPV Data in xyv Space	103
3.1	The summary of identified cores in Orion A and its subregions	119
3.2	The summary core physical properties in Orion A	123
3.3	The Results of Two-Sample KS Test of Core Properties in Orion A	127
3.4	The Summary Core Properties in OMC-1/2/3 Area	129
3.5	The Summary Core Properties in OMC-4/5 Area	136
3.6	The Summary Core Properties in L1641N/V380 Ori Area	137
3.7	The Summary Core Properties in L1641C Area	138
3.8	The Summary of CMF Properties in Orion A and its Subregions	158
A.1	The Results of Dense Core Survey with PP Data (yz Plane)	189
A.2	The Results of Dense Core Survey with PP Data (zx Plane)	190

A.3	The Summary of Core Properties Identified with PP Data (yz plane) Using Fiducial Parameter	190
A.4	The Summary of Core Properties Identified with PP Data (zx Plane) Using Fiducial Parameter	190
A.5	The CMF Properties with PP Pata in yz Plane	195
A.6	The CMF Properties with PP Data in zx Plane	195
A.7	The Results of Dense Core Survey with PPV Data (yzv Space)	196
A.8	The Results of Dense Core Survey with PPV Data ($z xv$ Space)	196
A.9	The CMF Properties with PPV Data in yzv Space	199
A.10	The CMF Properties with PPV Data in $z xv$ Space	199
B.1	The Summary of Number of Starless Cores with $\alpha \leq 1$	200
B.2	The Summary of CMF Parameters in Orion A and Subregions in Figure B.2	202
B.3	The Results of KS Test of Core Properties in OMC-1/2/3 Area	204
B.4	The Results of KS Test of Core Properties in OMC-4/5 Area	205
B.5	The Results of KS Test of Core Properties in L1641N Area	206
B.6	The Results of KS Test of Core Properties in L1641C Area	207
B.7	The Results of KS Test of Core Diameter Among Four Subregions	207
B.8	The Results of KS Test of Core Aspect Ratio Among Four Subregions	208
B.9	The Results of KS Test of Core Velocity Width Among Four Sub- regions	208
B.10	The Results of KS test of Core Mass Among Four Subregions	208

B.11 The Results of KS Test of Core Density Among Four Subregions .	208
B.12 The Results of KS Test of Virial Ratio Among Four Subregions . .	209
B.13 The Summary of CMF Properties in Subregions of Orion A with Variable Sized Bin	211
B.14 The Summary of CMF Parameters in Orion A with Column Density Thresholds	211

List of Figures

1.1	The timescale of free-fall t_{ff} , magnetic flux loss t_B and ohmic dissipation t_{od} calculated by Nakano, Nishi, and Umebayashi (2002).	6
1.2	The snapshot of each time in the simulation from prestellar core to protostellar core with outflow done by Machida and Matsumoto (2012).	9
1.3	The mass ratios of the disk, protostellar core, and outflowing material and initial prestellar core calculated by Machida and Matsumoto (2012).	10
1.4	The IMF, original mass function in the paper, constructed in Salpeter (1955).	11
1.5	The IMFs of star clusters NGC2024, Chameleon I, IC 348 and Taurus derived in Dib (2014).	14
1.6	The same figures as Figure 1.5 for ρ Ophiucus, ONC, NGC 2264 and NGC6611 derived in Dib (2014).	15
1.7	The "alpha-plot" shown in Bastian, Covey, and Meyer (2010).	16
1.8	The CMF for 60 small scale structures constructed by Motte, Andre, and Neri (1998).	17

1.9	The distributions of starless cores in Aquila and in the main subfield identified with the column density map from Herschel SPIRE/PACS observation (Könyves, Ph. André, Men'shchikov, Schneider, et al. 2010).	19
1.10	The CMFs in Aquila and the main subfield identified with the column density map from Herschel SPIRE/PACS observation (Könyves, Ph. André, Men'shchikov, Schneider, et al. 2010).	20
1.11	The diagram of the resultant IMF expected from each star formation condition and initial CMF (Offner et al. 2014).	24
1.12	The image of 1.3 mm dust continuum emission of the W43-MM1 cloud, observed by the ALMA (Motte, Nony, et al. 2018).	25
1.13	The observed CMFs in (a) differential form and (b) cumulative form of the W43-MM1 cloud derived in Motte, Nony, et al. (2018).	26
1.14	The CMF and the resultant stellar mass functions with the one-to-one model, multiplicity models in Swift and Jonathan P. Williams (2008)	29
1.15	The CMF and resultant stellar mass functions of fragmentation models in Swift and Jonathan P. Williams (2008).	30
1.16	The resultant stellar mass functions with the composite model in Swift and Jonathan P. Williams (2008).	31
1.17	The schematic diagram of use-defined parameters in Dendrogram algorithm: min_value, min_delta, and min_npix.	34

1.18 The schematic diagram of Dendrogram's hierarchy for a one-dimensional data.	35
1.19 The schematic diagram of Dendrogram's hierarchy for a two-dimensional data.	36
1.20 The relation between the mass ratio $M_{\text{core}}/M_{\text{projection}}$ and mean core column density in Takemura, Nakamura, Ishii, et al. (2021).	39
1.21 The observed CMF for all identified cores and the completeness corrected CMF in Takemura, Nakamura, Ishii, et al. (2021).	40
1.22 The distributions identified cores and stars in the ONC region in Takemura, Nakamura, Kong, et al. (2021).	42
1.23 The CMF for starless cores and bound starless cores and IMF in Takemura, Nakamura, Kong, et al. (2021).	43
1.24 The schematic diagram of a current standard star formation scenario.	46
1.25 The schematic diagram of a new star formation model which considers the mass accretion and core growth with it.	47
1.26 The mass histograms of protostellar cores and starless cores of the Dragon IRDC from Kong, Arce, Shirley, et al. (2021).	49
1.27 The histograms of stellar mass and progenitor core mass from Pelkonen et al. (2021).	52
1.28 The fraction of the final stages of mass of each massive ($> 5M_{\odot}$) progenitor cores from Pelkonen et al. (2021).	53
1.29 The time evolution of mass accretion rate calculated in Pelkonen et al. (2021).	54

1.30	The time evolution of CMF when the filament power spectrum is -1.5 derived in S.-i. Inutsuka (2001).	56
1.31	The histograms of $(\gamma + 2.35)/\sigma$ values with mass functions with uniform sized logarithmic bins of mass method and variably sized logarithmic bins of mass method in Maíz Apellániz and Úbeda (2005).	59
2.1	The distributions of identified cores with PPP data.	73
2.2	The PPP CMFs for all parameter cases.	76
2.3	The same as Figure 2.2 but CMF with variably sized bins.	77
2.4	The normalized density profiles with the core peak density at core peaks along z axis for six selected cores.	80
2.5	The relationships between R_z and core mass and $R_{z,2nd}$ and core mass.	81
2.6	The CMFs for various $R_{z,2nd}$ values.	82
2.7	The identified cores with xy PP data are potted onto the column density map in xy plane.	84
2.8	The PP CMFs for all parameter cases in xy plane.	87
2.9	The same as Figure 2.8 but CMF with variably sized bins.	89
2.10	The PP CMFs for all parameter cases with uniform temperature in xy plane.	94
2.11	The distribution of identified cores with PP data in xy plane and concentric circles centers at the peak of column density.	97

2.12	The CMFs for cores in various distances from the column density peak.	98
2.13	The PPV CMFs for all parameter cases in xyv space.	100
2.14	The same as Figure 2.13 but CMF with variably sized bins.	102
2.15	The normalized histograms of PPP masses and PPV masses.	104
2.16	The mass–velocity width in FWHM relation for PPV cores with case 2 parameter set.	105
2.17	The schematic figure of PPP slope and PPV slope that have power-law indices of α_{PPP} and α_{PPV}	106
2.18	The relationship between column density ratio of trunk and leaf from Takemura, Nakamura, Ishii, et al. (2021).	109
3.1	The distributions of identified starless cores and protostellar cores C18O ($J=1-0$) data in Orion A.	114
3.2	The distributions of Class-0/I objects and Class-II objects in VISION catalog in Orion A.	116
3.3	The bound starless cores (red) and unbound cores (blue) are plotted on the integrated intensity map of the C18O ($J=1-0$) line. The details are the same as Figure 3.1.	122
3.4	The histograms of core diameter, an aspect ratio, a velocity width in FWHM, a core mass, a core number density, and the virial ratio of starless cores and protostellar cores in Orion A.	125

3.5	The histograms of core physical properties of bound starless cores and unbound starless cores.	126
3.6	The histograms of core size in four subregions.	130
3.7	The same figure as Figure 3.6 but for aspect ratio.	131
3.8	The same figure as Figure 3.6 but for velocity width in FWHM.	132
3.9	The same figure as Figure 3.6 but for core mass.	133
3.10	The same figure as Figure 3.6 but a core number density.	134
3.11	The same figure as Figure 3.6 but for virial ratio.	135
3.12	The correlations between core physical properties in Orion A	140
3.13	The velocity width – diameter relations of four subregions.	142
3.14	The diameter – mass relations of four subregions.	143
3.15	The FWHM – mass relations of four subregions.	144
3.16	The virial ratio – mass relations of four subregions.	145
3.17	The core free-fall time – mass relation in Orion A.	147
3.18	The core free-fall time – mass relation in four subregions in Orion A.	148
3.19	The core lifetime as a function of a minimum core density in four subregions.	149
3.20	Same figure as Figure 3.19 but for Orion A.	150
3.21	The declination – core central velocity relation in the four subregions in Orion A.	152
3.22	The declination – core velocity FWHM relation in the four subregions in Orion A.	153

3.23	The declination – core mass relation in the four subregions in Orion A.	154
3.24	The declination – core density relation in the four subregions in Orion A.	155
3.25	The observed CMFs in Orion A and IMF in the ONC region.	160
3.26	The CMFs of subregions in Orion A.	162
3.27	The CMF of bound starless cores in Orion A and predicted CMF with Bondi accretion.	166
A.1	The distribution of identified cores with yz PP data.	191
A.2	The distribution of identified cores with zx PP data.	192
A.3	The PP CMFs for all parameter cases in yz plane.	193
A.4	The PP CMFs for all parameter cases in zx plane.	194
A.5	The PPV CMFs for all parameter cases in yzv space.	197
A.6	The PPV CMFs for all parameter cases in zrv space.	198
B.1	The same as Figure 3.19 but $\alpha_{\text{vir}} < 1$ is a condition of a bound core.	201
B.2	The same as Figure 3.26 but $\alpha_{\text{vir}} < 1$ is a condition of a bound core.	203
B.3	The CMFs of subregions in Orion A with variable sized bin.	210
B.4	The cumulative PDF of mean column density at a core position.	212
B.5	The CMF in Orion A with column density thresholds.	213
B.6	The fraction of subregions of cores compose each CMF with col- umn density threshold.	214

1. Introduction

1.1 Molecular Cloud and Dense Core

The interstellar medium (ISM), which consists of gas and dust, fills the space between stars in the galaxy. It is typically composed of 70% hydrogen, 28% of helium, and 2% of heavy elements such as oxygen, carbon, and nitrogen ([Spitzer and Army 1978](#)). The ISM can be classified into four groups by their phases of the main element, hydrogen ([Mathis 1990](#)): the hot ionized medium (HIM), HII regions, neutral medium, and molecular clouds. HIM is a very diffuse hot gas. Energetic events such as stellar winds and supernovae may create and influence HIM. The HII region is the region with ionized/partially-ionized gas created around high-mass stars and is the main component of the galactic disk. The neutral medium is often classified into two categories: warm neutral medium (WNM) and cold neutral medium (CNM). WNM and CNM are considered to be roughly in pressure equilibrium.

Molecular clouds are composed mainly of hydrogen molecules and more massive molecules because of the very low temperature (~ 10 K) and relatively

high density ($\geq 10^2$ - 10^3 cm^{-3}). The typical properties of molecular clouds and their internal structures are summarized by [Bodenheimer \(2011\)](#) as shown in Table 1.1 (see also [Goldsmith \(1987\)](#)). The typical radius, density, mass, linewidth, and temperature of the giant molecular cloud (GMC) are 20 pc, 100 cm^{-3} , $10^5 M_{\odot}$, 7 km s^{-1} and 15 K, respectively. The mean lifetime of molecular clouds is ~ 10 Myr. The molecular clouds contain dense and compact structures. We call such structures "dense cores." The dense cores are sometimes associated with near-infrared point sources, which are likely to be protostars. Thus, the dense cores are thought to be the birthplace of stars. The typical radius, density, mass, linewidth, and temperature are estimated to be 0.08 pc, 10^5 cm^{-3} , $10^1 M_{\odot}$, 0.3 km s^{-1} and 10 K, respectively. We note that these values are not the definitions of the structures.

Table 1.1: The Summary of the Properties of Molecular Clouds in [Bodenheimer \(2011\)](#)

Property	Giant molecular cloud	Molecular cloud	Molecular clump	Dense core
Mean radius (pc)	20	5	2	0.08
Density $n(\text{H}_2)$ (cm^{-3})	100	300	10^3	10^5
Mass (M_{\odot})	10^5	10^4	10^3	10^1
Linewidth (km s^{-1})	7	4	2	0.3
Temperature (K)	15	10	10	10

Although the most abundant element of molecular clouds is hydrogen, most hydrogen molecules in the clouds do not emit strong emissions because they are in their lowest-excited state of rotational transition because of the low temperatures of ~ 10 K. The energy difference between the lowest-excited and ground states is

about $\Delta E \sim 500$ K. Their lowest rotational transition emission is observed in the infrared wavelength. Thus, molecular clouds are often observed by dust particles. Molecular clouds include 1% of dust particles by mass (Bohlin, Savage, and Drake 1978). The dust particles cause the extinction of background starlight in infrared and optical wavelengths. In addition, they also emit thermal emission, which is observed as a continuum emission from radio to infrared wavelengths. Another essential way to observe molecular clouds is spectral line observations from various molecules such as carbon monoxide, CO. CO is the second most abundant after hydrogen molecules in molecular clouds. The isotopologues of $^{12}\text{C}^{16}\text{O}$ such as $^{13}\text{C}^{16}\text{O}$ and $^{12}\text{C}^{18}\text{O}$ are also often observed. Other molecules such as CS, NH_3 , N_2H^+ , N_2D^+ , HCN and H^{13}CO^+ are also used to observe dense cores since they have higher critical densities for excitation. If the fractional abundance of the observed molecule relative to H_2 is estimated from other measurements, the masses contained in the regions that emit the observed spectral line can be derived.

1.2 Standard Star formation Scenario

Previous observations suggest that stars are born in dense cores. The evolution processes of dense cores are likely to depend on the balance of the self-gravity and kinematic energy due to the turbulence and thermal motion, and magnetic energy. The thermal energy is minimal compared to the other energies on the cloud scale. Therefore, molecular clouds are not supported by thermal pressure. Molecular clouds are thought to be supported by turbulence and magnetic field against global

gravitational contraction. However, the dense cores should be gravitationally unstable to form stars from dense cores. It is still unclear when and how it happens, but once gravity becomes dominant over the other forces, the formation of stars begins.

Since the dense cores are thought to be self-gravitating objects, the timescale of star formation is determined by the free-fall time, which is calculated as

$$t_{\text{ff}} = \sqrt{\frac{3\pi}{32G\rho}} = 4 \times 10^5 \left(\frac{10^4 \text{ cm}^{-3}}{n} \right)^{1/2} \text{ yr} \quad (1.1)$$

where G , ρ and $n = n(H) + n(H_2)$ are gravitational constant, density and the number density of hydrogen, respectively.

In the classical star formation scenario, the dense cores are considered to be mainly supported by magnetic fields, i.e., the Lorentz force. If this is the case, the timescale of star formation is determined by the timescale of magnetic leakage, which initiates the gravitational contraction. There is a critical magnetic strength that determines the timescale of star formation. The critical magnetic field strength for cloud support is calculated as

$$\begin{aligned} B_{\text{cr}} &\approx 4 \left(\frac{\pi k T \rho}{\mu m_{\text{H}}} \right)^{1/2} \\ &\approx 6.4 \times 10^{-5} \left(\frac{T}{10 \text{ K}} \cdot \frac{n_{\text{H}}}{10^5 \text{ cm}^{-3}} \cdot \frac{2.37}{\mu} \right)^{1/2} G \end{aligned} \quad (1.2)$$

where k , μ and m_{H} are Boltzmann constant, mean molecular weight and mass of atomic hydrogen. A cloud with a magnetic field weaker than B_{cr} is called

magnetically supercritical, and it can dynamically collapse in order of a free-fall time. On the other hand, a cloud with a magnetic field stronger than B_{cr} is called magnetically subcritical, and the magnetic field completely supports it. The magnetically subcritical cloud can contract when the magnetic flux escapes from the cloud by some magnetic diffusion. In Figure 1.1, we compare the free-fall time with a couple of timescales determined by magnetic diffusion as a function of the cloud density. The magnetic flux loss time is basically more prolonged than the free-fall time. So then, if the dense cores are supported by a strong magnetic field enough to overcome the self-gravity, the timescale of star formation becomes longer.

It is noted that the cooling time of molecular gas is much shorter than the other timescales: It is $\sim 10^4$ yr for clouds whose density is 10^2 cm^{-2} and $\sim 10^3$ yr for cores whose density is 10^4 cm^{-2} . Thus, the temperatures of clouds and cores stay nearly isothermal.

As mentioned before, once gravity dominates the dense core, the gas falls into the central denser part, where a protostar grows. In the course of protostellar evolution, molecular outflows and jets are launched. Machida and Matsumoto (2012) conducted three-dimensional resistive magneto-hydrodynamic (MHD) simulations of the collapse of magnetized, rotating prestellar cores as shown in Figure 1.2. The authors calculated from the prestellar cores to the end of the main accretion phase. The results show that the circumstellar disk drives the outflow during the star formation phase. They also revealed that a large fraction of core mass is blown out by the outflow, as shown in Figure 1.3. Then, the gas-to-star fraction

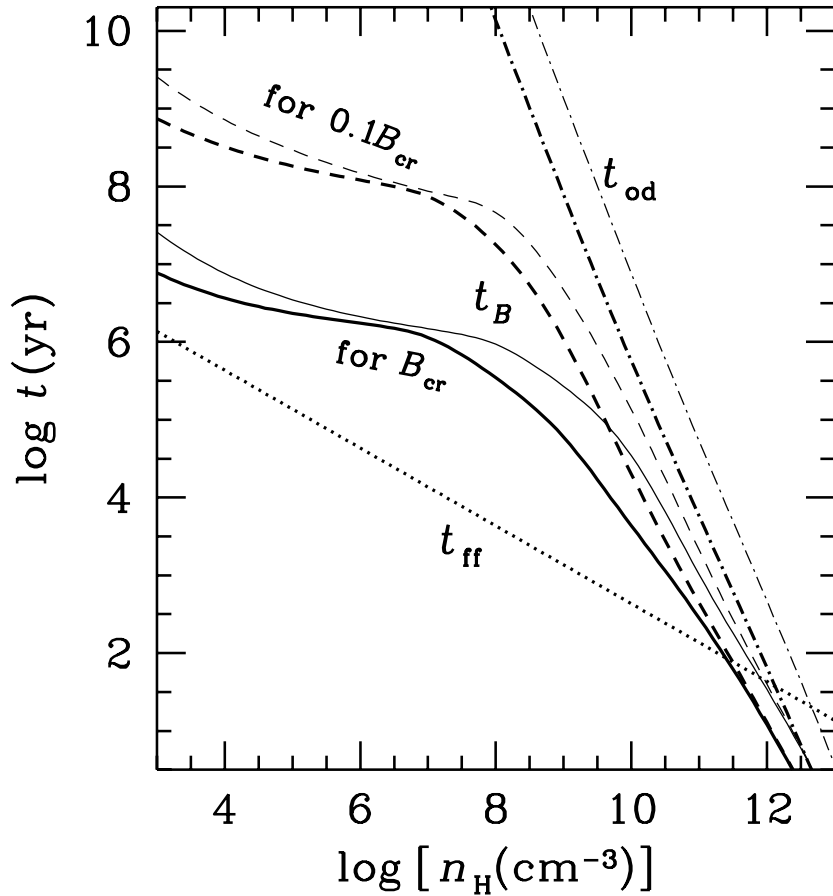


Figure 1.1: The timescale of free-fall t_{ff} (dotted line), magnetic flux loss t_B (solid and dashed lines) and ohmic dissipation t_{od} (dot-dashed) calculated by Nakano, Nishi, and Umebayashi (2002). The critical magnetic field B_{cr} is given in Equation 1.2. The two cases of ionization rate by cosmic rays of $\zeta_0 = 1 \times 10^{-17}$ (thick line) and $\zeta_0 = 1 \times 10^{-16}$ (thin line) are shown. The authors have assumed that 20% of C and O and 2% of metallic elements are in the gas phase, and the rest is in grains.

or star formation efficiency suppressed to $\geq 50\%$ (see also Nakano, Hasegawa, and Norman 1995; Matzner and C. F. McKee 2000; Machida, S. Inutsuka, and Matsumoto 2009; Price, Tricco, and M. R. Bate 2012).

Most of the star formation scenarios previously discussed have assumed that the final stellar masses are determined during the stage of core formation. This scenario is sometimes referred to as the core accretion scenario or core collapse scenario. However, recently, some authors proposed that the accretion of ambient gas outside the core may largely determine the final stellar mass (e.g., Ian A. Bonnell, Vine, and Matthew R. Bate 2004; I. A. Bonnell et al. 2011). This scenario is sometimes called the competitive accretion scenario. The numerical simulation by Ian A. Bonnell, Vine, and Matthew R. Bate (2004) showed that the final stellar mass does not depend on the initial core mass. The cores grow with the Bondi-Hoyle accretion from the surrounding cloud. In addition, modifying the competitive accretion scenario, a clump-fed model for high-mass star formation is proposed (e.g., P. Wang et al. 2010; J. C. Tan et al. 2014). P. Wang et al. (2010) showed that a large part of the mass of a high-mass star came not from the core itself but the clump or outside of the core with their numerical simulation. Then, J. C. Tan et al. (2014) presented the average mass accretion rate of clump-fed model $\langle \dot{m}_{*d} \rangle$ as Equation 1.3.

$$\langle \dot{m}_{*d} \rangle = 1.46 \times 10^{-4} \left(\frac{\epsilon_{\text{ff}}}{0.1} \right) \left(\frac{m_{*f}}{50 M_{\odot}} \right) \left(\frac{\epsilon_{\text{cl}}}{0.5} \right)^{-1} \times \Sigma_{\text{cl}}^{3/4} \left(\frac{M_{\text{cl}}}{1000 M_{\odot}} \right)^{-1/4} [M_{\odot} \text{ year}^{-1}] \quad (1.3)$$

where ϵ_{ff} , m_{*f} , ϵ_{cl} , Σ_{cl} , and M_{cl} are SFE per free-fall time, final stellar mass, final SFE of the parental clump, clump column density, and clump mass, respectively.

It is a matter of debate which essential to determine the final stellar masses: parental cores or accretion of ambient gas.

1.3 Initial Mass Function (IMF) and Core Mass Function (CMF)

1.3.1 Initial Mass Function

Salpeter (1955) investigated the distribution of stellar masses when the stars are born for the first time, as shown in Figure 1.4. The function is called initial mass function (hereafter, IMF) today. The author calculated the average stellar mass as a function of the absolute visual magnitude for nearby main-sequence stars. Then, the author derived the best-fit power-law function between $\log(M/M_{\odot}) = -0.4$ and $+1.0$ as

$$\frac{dN}{d\log M} \propto M^{-\Gamma} \quad (1.4)$$

or

$$\frac{dN}{dM} \propto M^{-\Gamma-1} = M^{-\alpha} \quad (1.5)$$

and found that the power-law index was $\Gamma = 1.35$ ($\alpha = 2.35$). This IMF is called "Salpeter-IMF" today.

So far, many observations of star clusters have been conducted to derive the

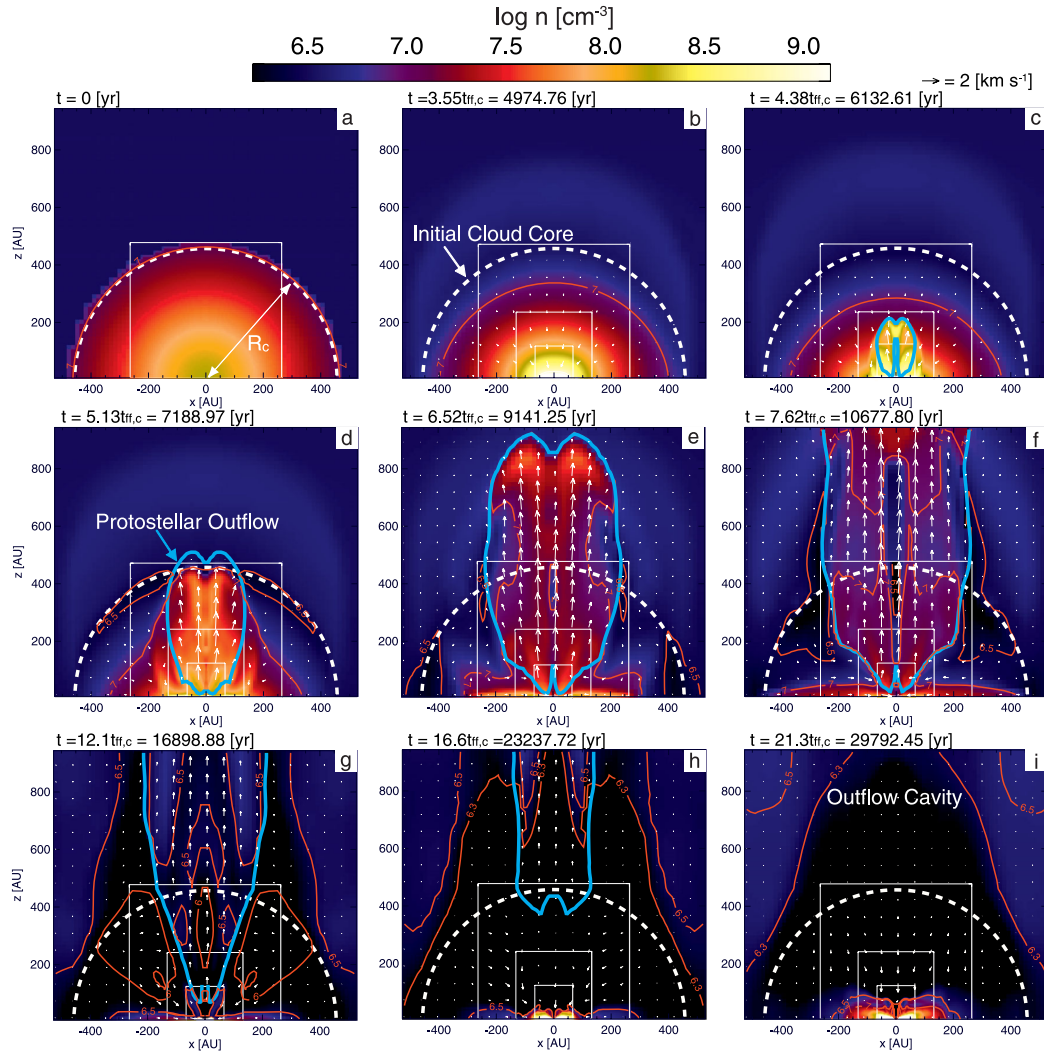


Figure 1.2: The snapshot of each time in the simulation from prestellar core to protostellar core with outflow done by Machida and Matsumoto (2012). The colored background images and white arrows are the density and velocity distributions. The initial core is shown as the white dashed lines. The blue lines represent the boundaries with supersonic velocity from the center to the outward. The white square in each panel is the boundary of the subgrid.

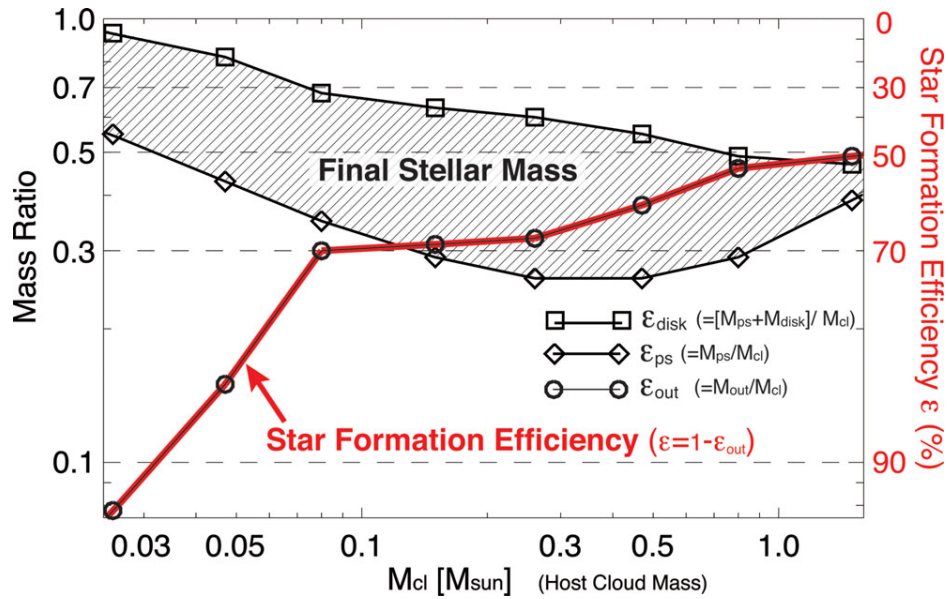


Figure 1.3: The mass ratios of the protostar plus circumstellar disk to the initial core (ϵ_{disk} ; square), the protostar to the initial core (ϵ_{ps} ; diamond) and the outflowing mass to the initial core (ϵ_{out} ; circle) calculated by Machida and Matsumoto (2012). The star formation efficiency is calculated as $\epsilon = 1 - \epsilon_{\text{out}}$.

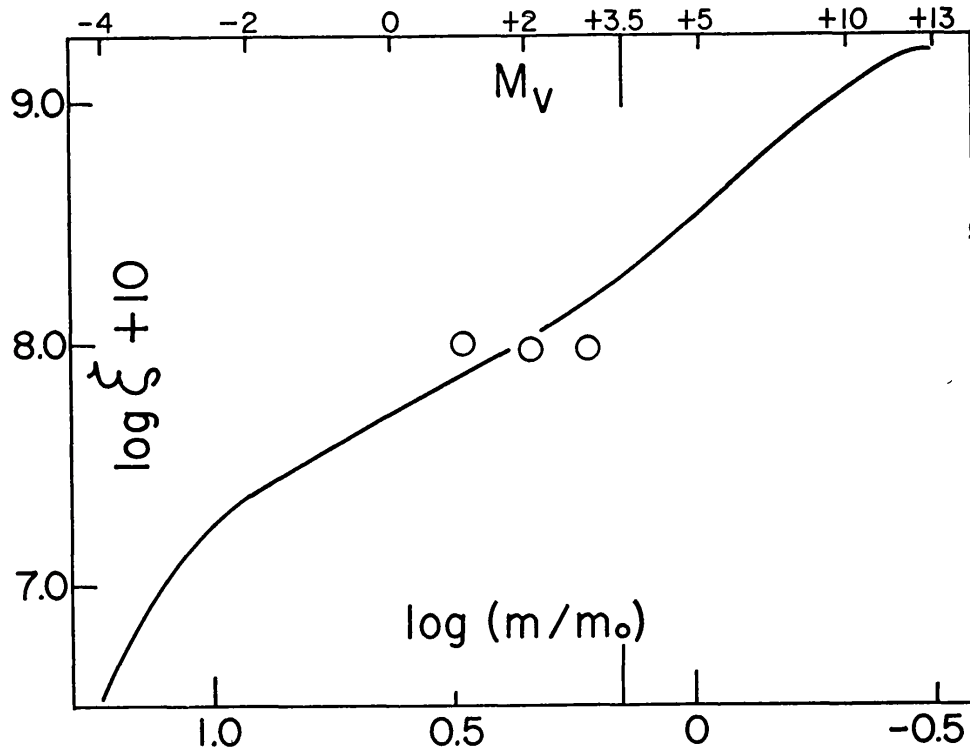


Figure 1.4: The IMF, original mass function in the paper, constructed in [Salpeter \(1955\)](#). $\xi(m)$ represents the "original mass function" defined by $dN = \xi(m)d(\log m)dt/T_0$. Here, $dN/d\log M = dN/dM \times M \times \log 10$. Then, N , T_0 , M_v , m , and m_{\odot} are the number of stars, age of the galaxy, absolute visual magnitude, stellar mass, and solar mass, respectively. The three circles are the data that are not on the solid line.

IMFs, as shown in Figure 1.5 and 1.6 and revealed the peaks at low-mass parts (hereafter referred to as the turnovers): (e.g., Comeron, G. H. Rieke, and M. J. Rieke 1996; Haisch, E. A. Lada, and C. J. Lada 2000; Levine et al. 2006) for NGC 2024, (e.g., E. E. Mamajek, Lawson, and Feigelson 2000; Song, Zuckerman, and M. S. Bessell 2004; Luhman, Peterson, and Megeath 2004; Lyo et al. 2006; Luhman 2007; Mužić et al. 2011) for Chameleon I, (e.g., E. A. Lada and C. J. Lada 1995; Najita, Tiede, and Carr 2000; A. A. Muench et al. 2003; Luhman, Stauffer, et al. 2003; Preibisch, Stanke, and Zinnecker 2003; Burgess et al. 2009) for IC 348, (e.g., Luhman 2000; C. Briceño et al. 2002; Luhman, César Briceño, et al. 2003; Luhman 2004; Scelsi, Maggio, et al. 2007; Scelsi, Sacco, et al. 2008; Luhman, E. E. Mamajek, et al. 2009) for Taurus, (e.g., G. H. Rieke, Ashok, and Boyle 1989; D. M. Williams et al. 1995; Luhman and G. H. Rieke 1999; Erickson et al. 2011; Alves de Oliveira et al. 2012) for ρ Ophiuchi, (e.g., L. A. Hillenbrand 1997; Palla and Stahler 1999; L. A. Hillenbrand and Carpenter 2000; Slesnick, L. A. Hillenbrand, and Carpenter 2004; Da Rio, Robberto, Soderblom, et al. 2010; Andersen et al. 2011; Da Rio, Robberto, L. A. Hillenbrand, et al. 2012) for the Orion nebula cluster (ONC), (e.g., Flaccomio et al. 1999; Park et al. 2000; Sung, M. S. Bessell, et al. 2008; Sung and M. S. Bessell 2010) for NGC 2264, (e.g., Walker 1961; Sagar and Joshi 1979; Bonatto, Santos, and Bica 2006; Oliveira, Jeffries, and van Loon 2009) for NGC 6611 and (e.g., A. A. Muench, E. A. Lada, and C. J. Lada 2000; A. A. Muench, E. A. Lada, C. J. Lada, and Alves 2002) for the Trapezium Cluster. For nearby stars, (e.g., Miller and J. M. Scalo 1979; Rana 1987) derived MFs and found the steeper the slope at the high-mass ends

than Salpeter-IMF of $\Gamma \sim 1.7$. (J. Scalo 1998; Kroupa 2002; Bastian, Covey, and Meyer 2010) summarized the power-law index as a function of the stellar mass of each IMF as a "alpha-plot" (Figure 1.7) and resolved that most of the IMFs have Salpeter-like slopes at the high-mass ends.

There are three IMF models which reproduce the turnover at the low-mass part, and Salpeter-like slope at the high-mass ends a multicomponent power-law function (Kroupa 2001; Kroupa 2002), combination of a lognormal distribution below $1 M_{\odot}$ and the Salpeter-like slope above $1 M_{\odot}$ (G. Chabrier 2003; Gilles Chabrier 2005) and a tapered power-law function (De Marchi, Paresce, and Portegies Zwart 2010; Parravano, C. F. McKee, and Hollenbach 2011). The universality of the IMFs has not been solved, and it is one of the most essential questions in modern Astronomy.

1.3.2 Core Mass Function

Stars are formed in dense cores of molecular clouds. In the classical standard star formation scenario, a star is created in the dense core. Therefore, it is crucial to understand how dense cores form from parental molecular clouds. Since the evolution processes of stars are mainly determined by their masses at birth, it is essential to reveal what determines the mass distribution of dense cores in molecular clouds. One of the candidates of origin of the IMFs is the core mass functions (hereafter, CMFs).

Motte, Andre, and Neri (1998) conducted mosaic observations of 1.3 mm continuum toward $\sim 1 \text{ pc}^2$ of ρ Ophiuchi whose distance is $\sim 160 \text{ pc}$ with the IRAM 30-m telescope and the MPIfR bolometer array. The authors identified

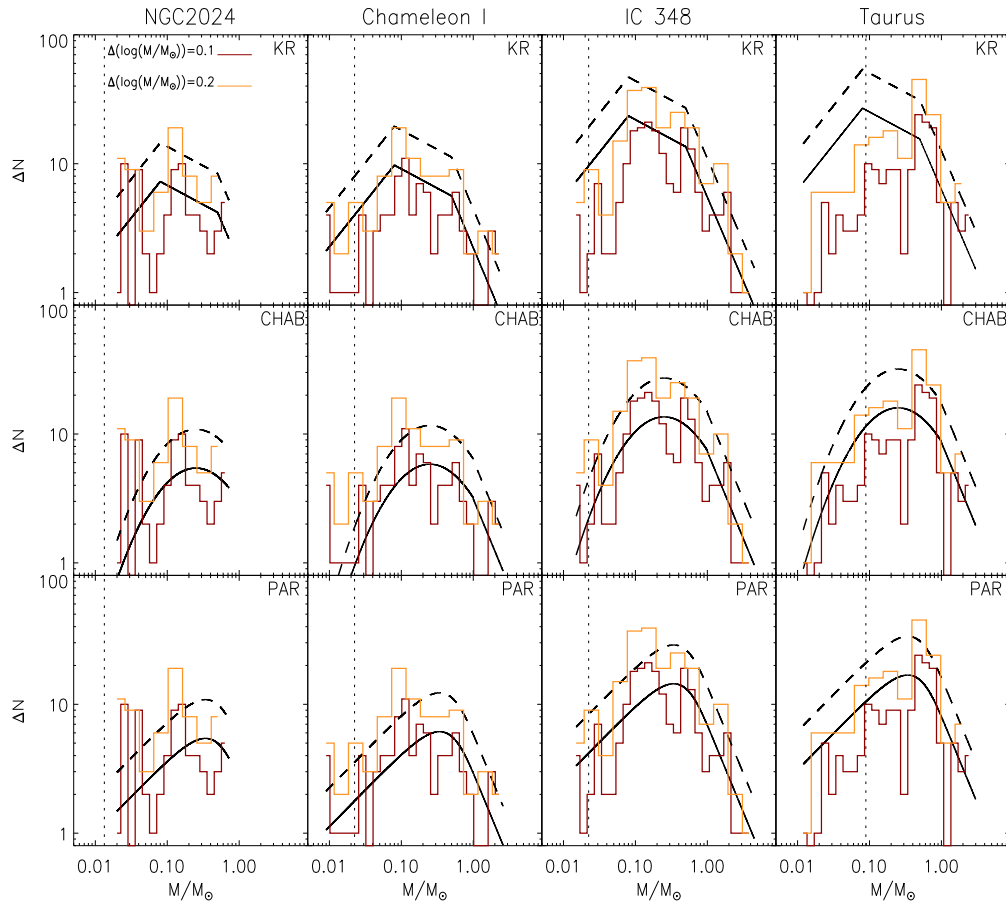


Figure 1.5: The IMFs of star clusters NGC2024, Chameleon I, IC 348 and Taurus derived in Dib (2014). The red and orange lines show the IMFs with bin sizes of $\log(M/M_{\odot}) = 0.1$ and $\log(M/M_{\odot}) = 0.2$. The dashed and solid lines are the MFs of Kroupa (2001) (top panels), Gilles Chabrier (2005) (middle panels) and Parravano, C. F. McKee, and Hollenbach (2011) (bottom panels), respectively. All functions are normalized to the total mass in each cluster.

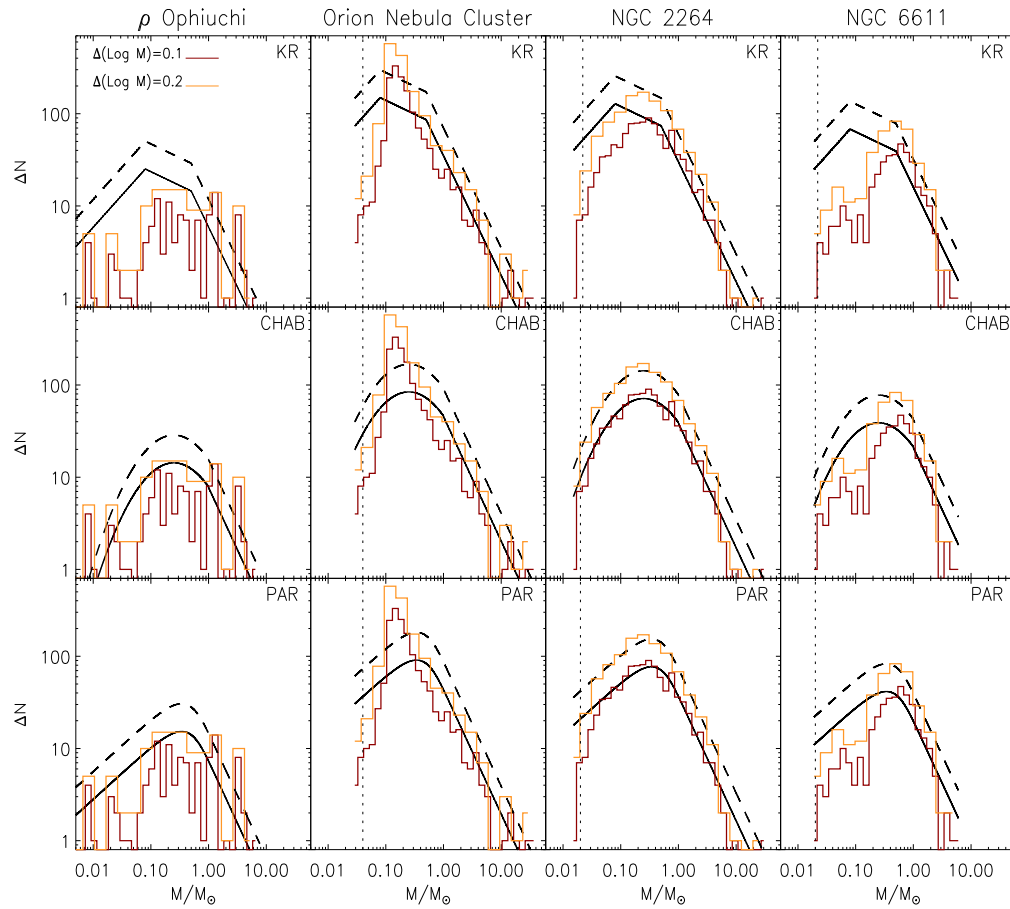


Figure 1.6: The same figures as Figure 1.5 for ρ Ophiucus, ONC, NGC 2264 and NGC6611 derived in Dib (2014).

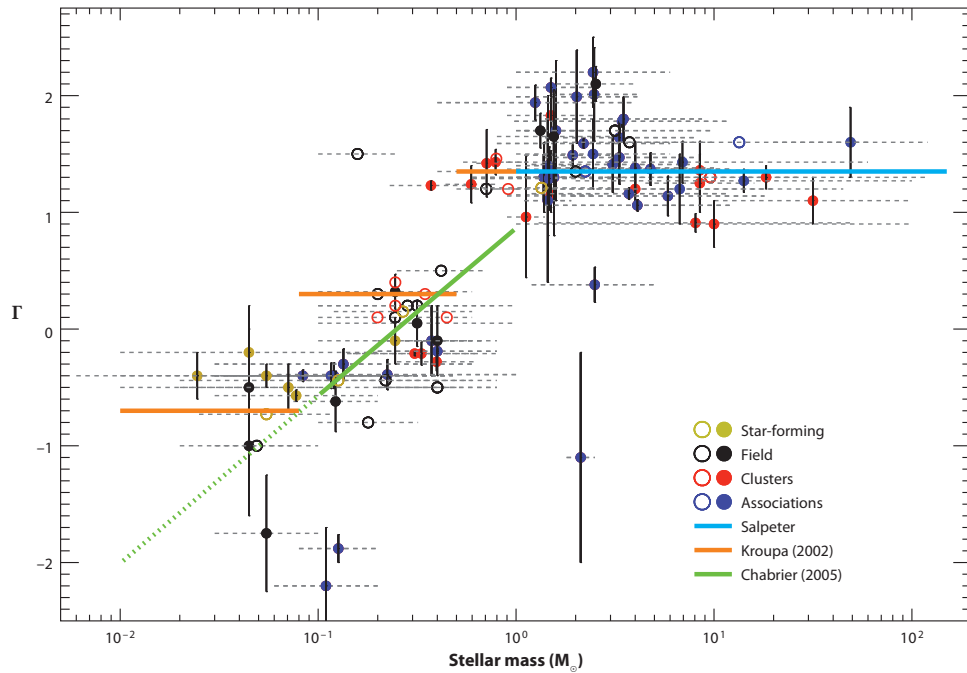


Figure 1.7: The "alpha-plot" shown in [Bastian, Covey, and Meyer \(2010\)](#). The power-law index of IMF is derived as a function of stellar masses. The filled circles show the data provided with errors on the Γ , and open circles show the data provided without errors on the Γ . The colored solid lines show the IMF models of [G. Chabrier \(2003\)](#), [Kroupa \(2002\)](#) and Salpeter-IMF above $1 M_{\odot}$ ([Salpeter 1955](#)).

small-scale structures called clumps in the paper whose sizes are smaller than $15'' - 30''$ corresponding to 2400 au to 5000 au. Then, the authors derived the mass spectrum for them. They revealed that the CMF has a Salpeter-like slope at the high-mass end with an index of the best-fit power-law functions above $\sim 0.5 M_{\odot}$ of $\alpha = -2.5$. The similarity between the CMF and IMF may indicate that the cores identified are likely to be the progenitors of stars, and the mass of the cores determines the final mass of stars formed.

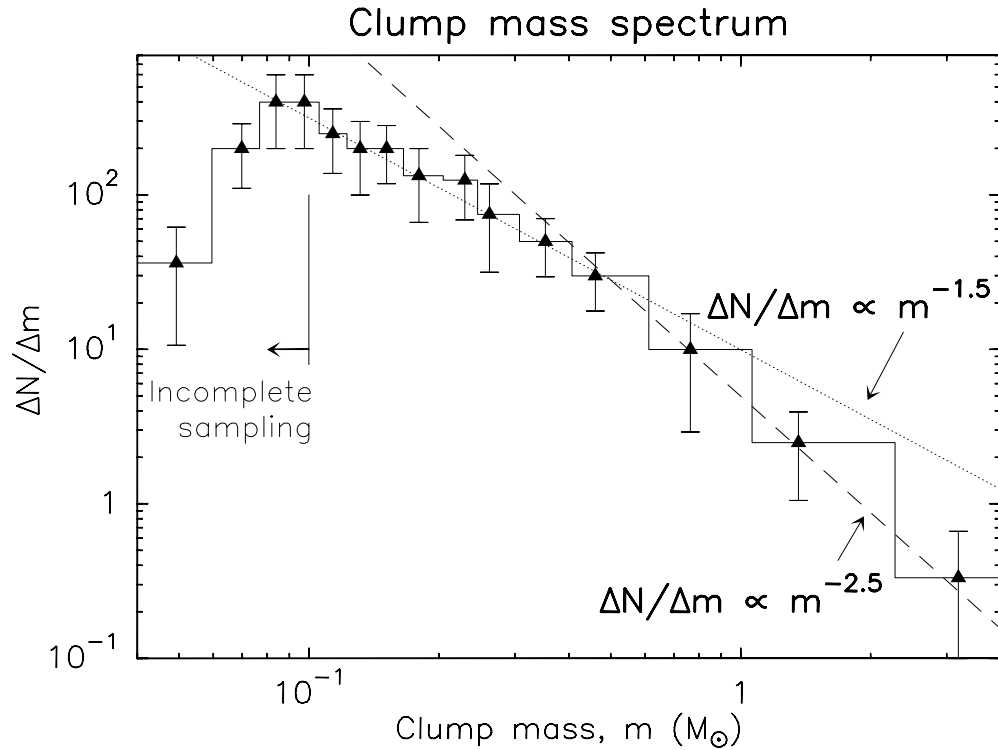


Figure 1.8: The CMF for 60 small scale structures constructed by [Motte, Andre, and Neri \(1998\)](#). The dotted and dashed lines show the best-fit functions whose indexes are -1.5 below $0.5 M_{\odot}$ and -2.5 above $0.5 M_{\odot}$, respectively. The error bars show the statistical uncertainty of \sqrt{N} .

Könyves, Ph. André, Men'shchikov, Schneider, et al. (2010) also identified dense cores in the Aquila rift cloud complex at ~ 400 pc (see Bontemps, Ph. André, et al. 2010) from the Herschel data with SPIRE and PACS shown in 1.9. The authors defined sources identified by *getsources* algorithm (Men'shchikov et al. 2010) with enough signal-to-noise ratio of greater than 7.5 in at least two bands of SPIRE: $250\mu\text{m}$ (the map resolution is $\sim 18'' \sim 4700$ au), $350\mu\text{m}$ ($\sim 25'' \sim 6500$ au) and $500\mu\text{m}$ ($\sim 36'' \sim 9400$ au) as cores. They also identified young stellar objects (YSOs) with *Spitzer* $24\mu\text{m}$ data and PACS $70\mu\text{m}$ data. Then, they derived CMFs for 452 starless cores and 314 candidate prestellar cores, which are gravitationally bound starless cores (see di Francesco et al. 2007; Ph. André, Men'shchikov, et al. 2010) as shown in Figure 1.9. Figure 1.10 shows the CMFs, and they have turnovers at $\sim 0.6 M_{\odot}$ for starless cores and $\sim 0.9 M_{\odot}$ for prestellar cores. The slopes are $\Gamma = -1.5 \pm 0.2$ for starless cores and $\Gamma = -1.45 \pm 0.2$ for prestellar cores. Besides these cases, many observations of CMFs have reported similar shape CMFs (e.g., Testi and Sargent 1998; Johnstone, Wilson, et al. 2000; Johnstone, Fich, et al. 2001; Motte, P. André, et al. 2001; Beuther and Schilke 2004; Stanke et al. 2006; Alves, Lombardi, and C. J. Lada 2007; Nutter and Ward-Thompson 2007; Ph. André, Belloche, et al. 2007).

Ikeda, Sunada, and Kitamura (2007) and Ikeda and Kitamura (2009) discussed the confusions among cores. They conducted observations toward Orion A with the H^{13}CO^+ ($J=1-0$) and C^{18}O ($J=1-0$) emissions and mentioned that the turnover of the CMF is an artifact of the confusion, and the power-law shape continues to the low-mass part determined by their resolution limit. Here the confusion

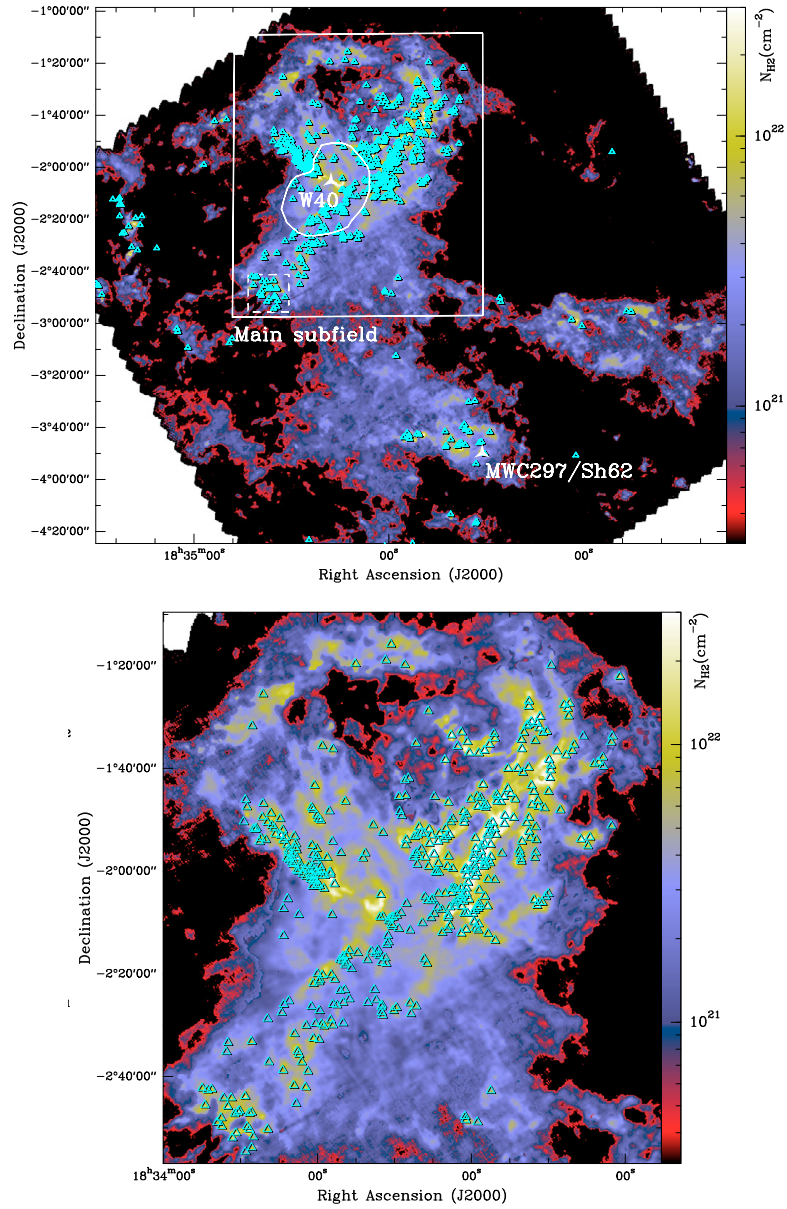


Figure 1.9: The identified 541 starless cores in Aquila (top panel) and 452 starless cores in the main subfield (bottom panel) are plotted as cyan triangles onto the column density map from Herschel SPIRE/PACS observation (Könyves, Ph. André, Men'shchikov, Schneider, et al. 2010).

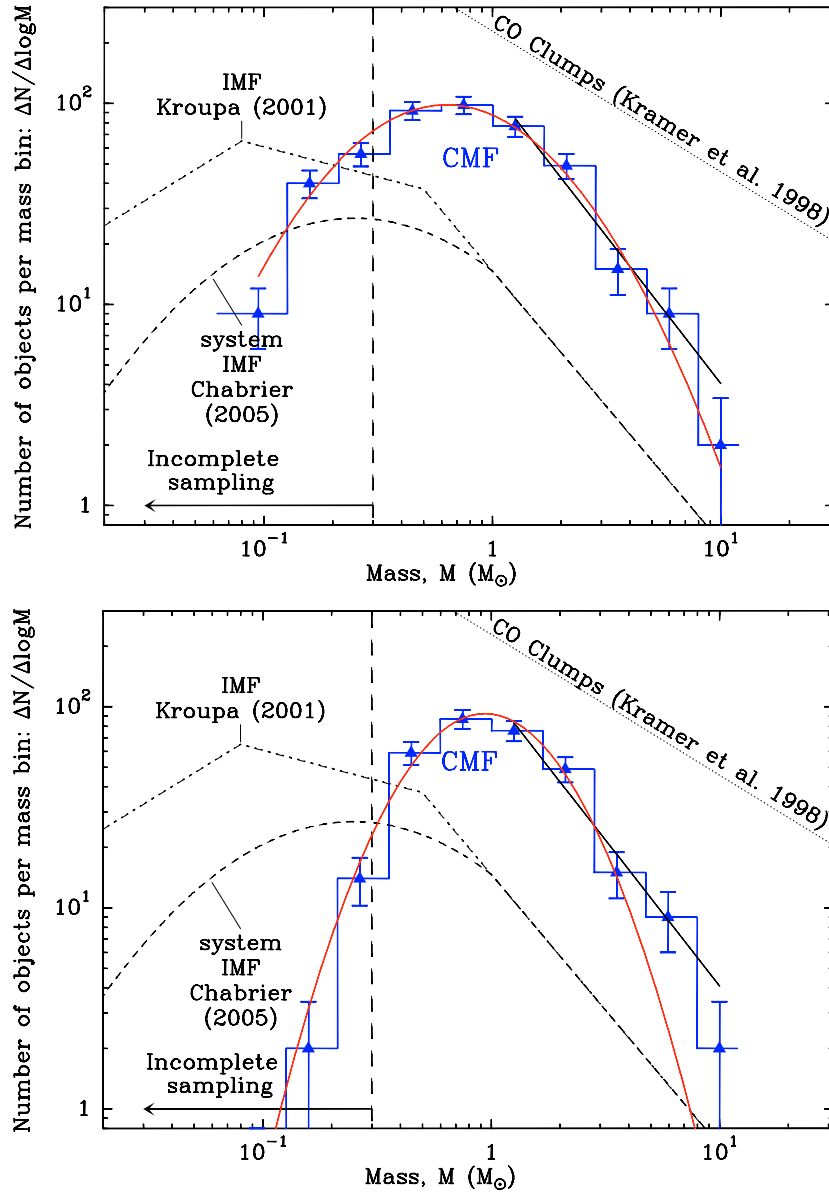


Figure 1.10: The CMFs for 452 starless cores (top panel) and 314 prestellar cores (bottom panel) in the Aquila main subfield with Herschel SPIRE/PACS data (Könyves, Ph. André, Men'shchikov, Schneider, et al. 2010). The CMFs have turnovers at $\sim 0.6 M_{\odot}$ for starless cores and $\sim 0.9 M_{\odot}$ for prestellar cores. The slopes are $\Gamma = -1.5 \pm 0.2$ for starless cores and $\Gamma = -1.45 \pm 0.2$ for prestellar cores. The error bars represent the statistical uncertainty of \sqrt{N} . The dotted line shows the clump mass function whose index is $\Gamma = 1.6$ (Kramer et al. 1998). The dashed curve and dash-dotted line are the IMF of Gilles Chabrier (2005) and Kroupa (2002).

effects mean the situation that the separations among plural cores are so slight compared to the map resolution that we cannot identify each core. Whether the CMFs have turnovers are still unclear. The observed angular resolutions will likely affect the previously obtained CMFs significantly. Thus the observations with the much higher spatial resolution are necessary to constrain the actual turnovers of the CMFs. The properties of CMFs still need to be clarified.

For larger scale in the molecular clouds, the mass functions for clumps which are the larger lower-density structures than cores and include cores, are derived by (Kramer et al. 1998) with CO observations of the seven molecular clouds L1457, MCLD 126.6 + 24.5, NGC 1499 SW, Orion B South, S140, M17 SW, and NGC 7538. The authors identified clumps with the GAUSSCLUMPS algorithm (J. Stutzki and Guesten 1990), and the mass range of identified clumps are $0 \leq \log(M/M_{\odot}) \leq 3$. The indexes of the power-law functions of the clump MFs are $-1.9 \leq \Gamma \leq -1.4$ between $\log(M/M_{\odot}) = 0$ and $\log(M/M_{\odot}) = 7$. The results suggest that the ratio of the massive clumps in all clumps is larger than that of massive cores in all cores in molecular clouds. The slope of the mass functions of clumps is shallower than those of CMFs and IMF.

1.3.3 The Relationship Between IMF and CMF

Previous studies revealed that two parameters characterize both IMFs and CMFs: the turnover masses and the slope at the high-mass ends. In general, both the observed IMFs and CMFs have similar slopes to that of the Salpeter-IMF as shown in Figure 1.10. If we assume the following two things, IMFs are inferred from

observed CMFs: (1) the star formation efficiencies in individual cores are constant, and (2) only one star is formed in a single core in the future. Also, the similar slopes of IMFs and CMFs imply that the timescale of star formation is independent of the core and stellar masses. This model is called a core-collapse model of star formation, and the final stellar mass is already determined at the stage of a prestellar core.

(Offner et al. 2014) discuss the emerging IMF from CMF and star-forming conditions for some cases as shown in Figure 1.11.

- (i) IMF has a larger turnover mass than CMF and the same slope as CMF when small dense cores do not form stars.
- (ii) IMF has a larger turnover mass and a steeper slope than CMF when high-mass stars are formed more rapidly than low-mass stars: Low-mass stars are still accumulating masses via mass accretion.
- (iii) IMF has a larger turnover mass and a steeper slope than CMF when star formation efficiency varies among core masses: Star formation efficiency of low-mass cores is larger than high-mass cores.
- (iv) IMF has a smaller turnover mass and a steeper slope than CMF when cores fragment based on the jeans masses of their initial clouds before stars are formed.
- (v) IMF has a similar turnover mass to CMF and a steeper slope than CMF when low-mass stars are formed more rapidly than high-mass stars: High-mass stars are still embedded in cores.

Therefore, as in the above cases, the relationship between CMF and IMF is expected

to imprint some information about star formation and its evolutionary processes.

The recent observations with Atacama Large Millimeter/ submillimeter Array (ALMA) by (Motte, Nony, et al. 2018) found the shallower CMF than Salpeter-IMF. The authors conducted a 1.3 mm observation toward W43-MM1, a massive cloud ($\sim 2 \times 10^4 M_{\odot}$) cloud located at ~ 5.5 kpc with a high spatial resolution of ~ 2400 au. They identified cores with *getsources* algorithm and derived CMFs as shown in Figure 1.12 and 1.13. The range of core masses is $\sim 1 - \sim 100 M_{\odot}$. The CMFs have a turnover at $\sim 2 M_{\odot}$ and the slope of $\Gamma = 0.90 \pm 0.06$. The authors discussed the two possible origins of the shallow slope of the CMF when star formation is self-similar. (i) The W43-MM1 cloud does not cover the entire region, which provides the complete IMF. In this case, to derive the complete CMF, the W43-MM1 cloud should be combined with the region with high low-mass cores to a high-mass cores ratio. Since the field IMF and IMFs in active star-forming regions are similar, this scenario is hard to adopt. (ii) The high-mass cores exist longer than low-mass cores and/or the star formation in the W43-MM1 cloud is protracted, and then massive cores are formed faster than low-mass cores. The former case is against the current lifetime derivations (e.g., Motte, Bontemps, and Louvet 2018). The latter case is also different from the current understanding of the period of star formation: the period of low-mass stars should be about ten times longer than that of high-mass cores. Then this scenario is difficult to justify as well. The authors argued that their results imply that the process of representing IMF from CMF is not statistically self-similar.

In addition to these results, the top-heavy CMFs are reported by ALMA con-

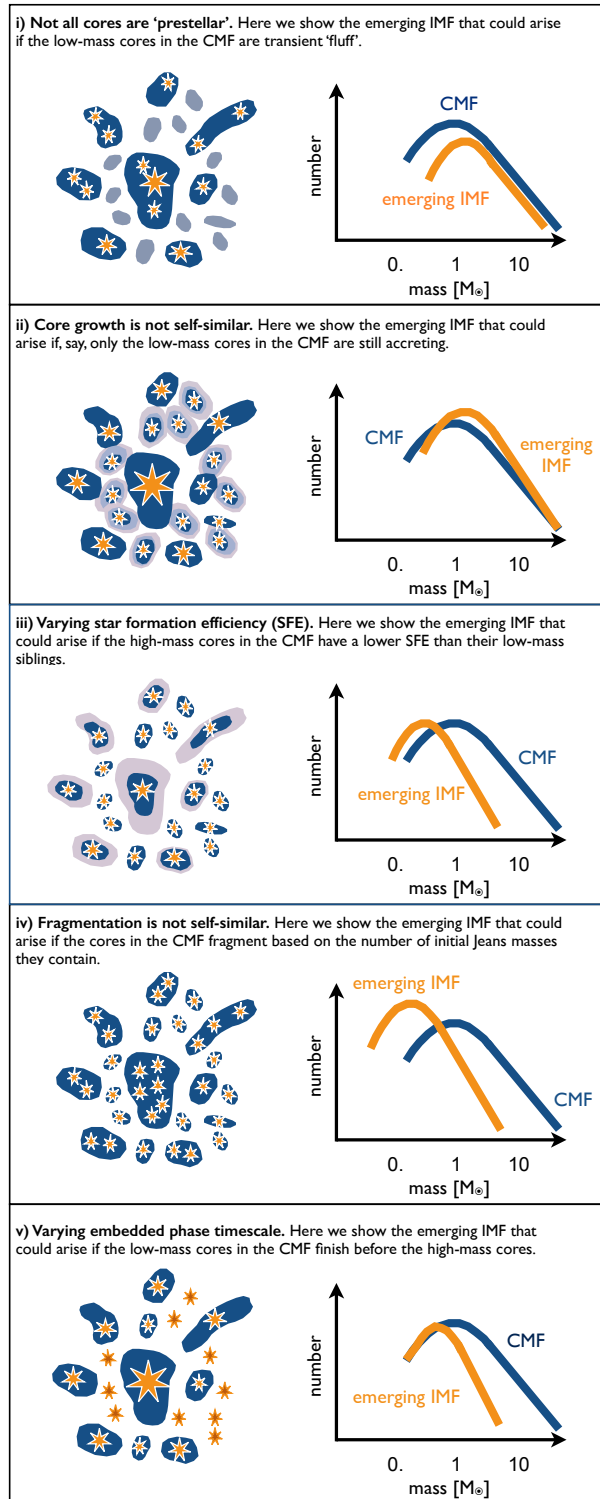


Figure 1.11: The diagram of the resultant IMF expected from each star formation condition and initial CMF (Offner et al. 2014).

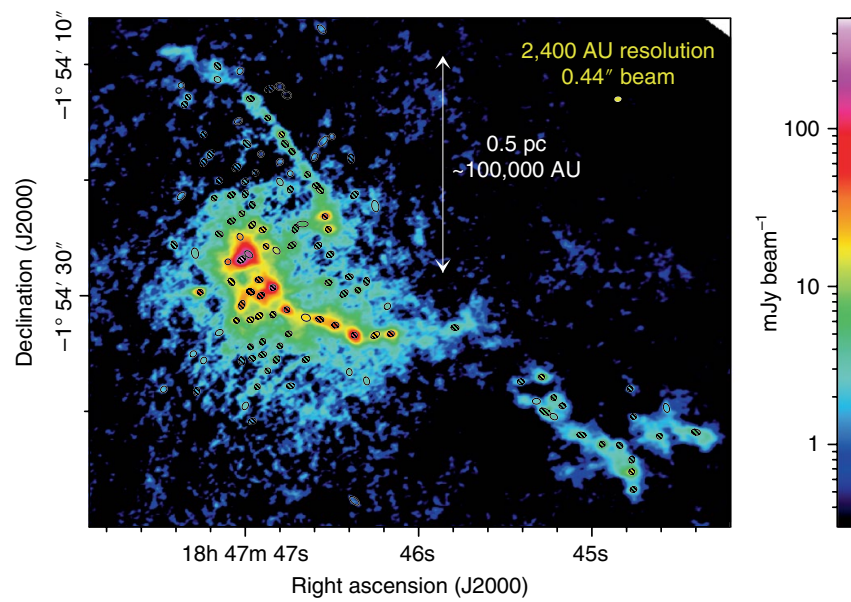


Figure 1.12: The image of 1.3 mm dust continuum emission of the W43-MM1 cloud, observed by the ALMA (Motte, Nony, et al. 2018). The filled yellow ellipse shows the map resolution of the observations. The identified cores are shown as ellipses.

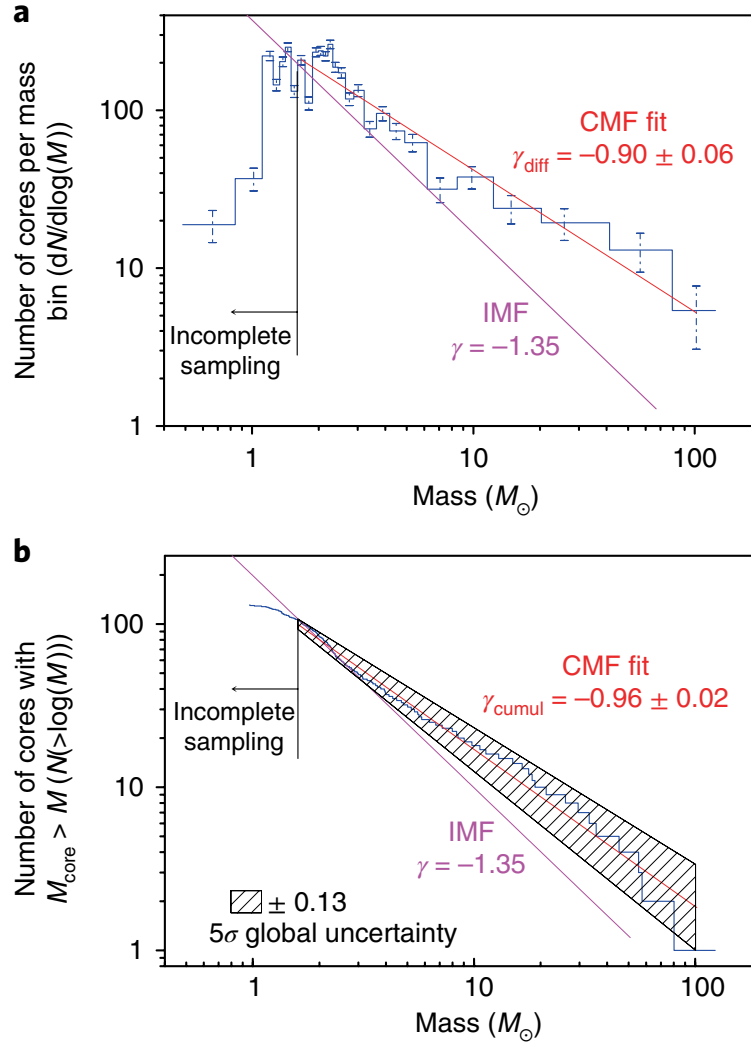


Figure 1.13: The observed CMFs in (a) differential form and (b) cumulative form of the W43-MM1 cloud derived in [Motte, Nony, et al. \(2018\)](#). The CMF in differential form has a turnover at $\sim 2 M_{\odot}$ and the slope of $\Gamma = 0.90 \pm 0.06$, which is shallower than the Salpeter-like slope.

tinuum observations toward distant high-mass star-forming regions (Zhang et al. 2015; Sánchez-Monge et al. 2017; Cheng et al. 2018; Liu et al. 2018; Kong 2019; Sanhueza et al. 2019; Sadaghiani et al. 2020). Therefore, unbiased dense core surveys with high enough spatial resolution in various regions are needed to derive CMFs and revealing the properties. Besides, revising the relation between CMFs and IMFs of the same region is necessary to investigate the evolution process from dense cores to stars.

1.3.4 The effects of SFE, multiplicity, and fragmentation

As we showed in Section 1.3.3, the observed one-to-one correspondence between CMF and IMF is interpreted that all cores form single stars with constant SFE. However, it is known that not all stars form as single stars, and the multiplicity increases with the stellar mass (e.g., Duchêne and Kraus 2013). On the contrary, most high-mass stars are formed in multiple systems. The multiple system formation probably impacts the mapping from CMF to IMF. Besides, there is a possibility that SFE is not uniform among cores, and this also influences the mapping. Swift and Jonathan P. Williams (2008) constructed IMF from CMF considering the inconstant SFE, multiplicity, and fragmentation of a core. The conditions to derive IMF from CMF are as follows. In parentheses after the condition names are the labels of models used by authors in the paper.

[One-to-one (REF)] This is predicted from a core-collapse model of star formation, and all cores form single stars with a constant SFE of 0.3. The mapping is self-similar.

[Variable star formation efficiency (SFEVAR)] The SFE of each core is a randomly chosen value between 0 and 1 as $\text{SFE} \in [0, 1]$.

[Multiplicity 1 (MULT1)] A single, binary, triple, or quadruple system is allowed. The probability that each system is created is 57%, 37%, 4%, and 1%, respectively. The mass ratio is randomly assigned, and the ratio of total stellar mass and parental core mass is fixed at 0.3.

[Multiplicity 2 (MULT2)] Only the binary system is considered, but the mass dependency of the probability for binarity is taken into account. The probability increases linearly from 10% at $M_{\text{core}} \leq 0.03 M_{\odot}$ to 100% at $M_{\text{core}} \geq 100 M_{\odot}$. The mass ratio of two stars is also randomly chosen. The mean binarity is $\sim 30\%$.

[Fragmentation 1 (FRAGPDF)] A core fragments into smaller cores repeatedly, and the mass is derived from the initial PDF of core mass. This case supposes the turbulent fragmentation of cores. Then, the fragmentation finishes when the original core contains no mass.

[Fragmentation 2 (RAGUNI)] A core also fragments into smaller cores repeatedly. However, the mass of the fragment is randomly selected from between zero and the original core mass with a uniform probability.

[Composite (COMP)] The composite model of SFEVAR, MULT1 and FRAGPDF. The initial CMFs of all models are the same and obtained by [Padoan and Nordlund \(2002\)](#), and they created cores through turbulent fragmentation, which is consistent with observations.

Figure 1.14 shows the initial CMF and the expected stellar mass functions

with the one-to-one model, multiplicity 1 model, and multiplicity 2 model. The stellar mass functions with multiplicity models have similar turnover masses and power-law indices at the high-mass end to REF stellar mass function. Then, except for the low- and high-mass ends, the effect of multiple system formation on the properties of stellar mass function is negligible. We note that the influence of multiple system formation highly depends on its property, such as multiplicity frequency and mass ratio, and the different mapping is possible under specific conditions (Holman et al. 2013).

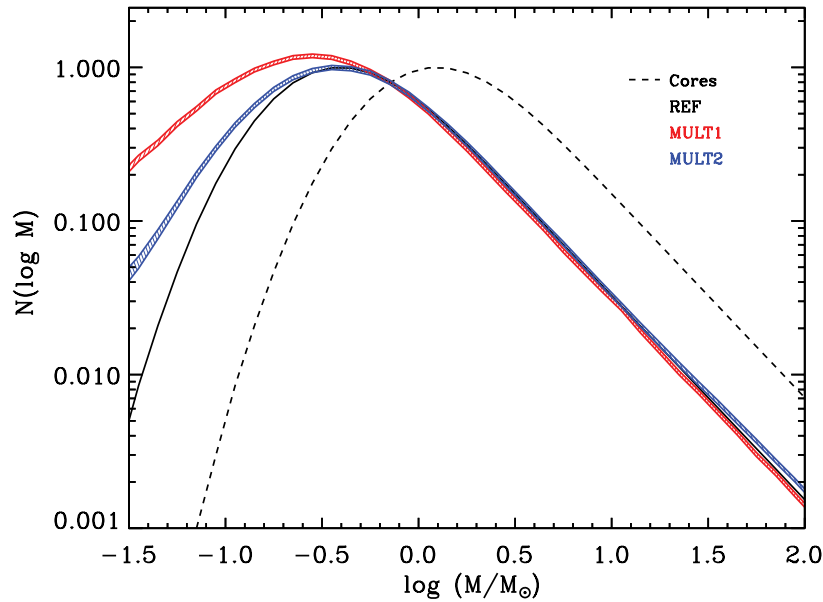


Figure 1.14: The CMF (dashed line) and the resultant stellar mass functions with the one-to-one model (REF; solid black line), multiplicity models (MULT1 and MULT2) in [Swift and Jonathan P. Williams \(2008\)](#). The mass distributions of multiplicity models are shown in red (MULT1) and blue (MULT2) curves.

Next, the resultant stellar mass functions with fragmentation models are shown in [Figure 1.15](#). The FRAGPDF mass function is narrower than the REF mass

function, but the turnovers are similar. On the other hand, The slope of the FRAGUNI mass function resembles the REF mass function. Although the turnover mass becomes smaller than the REF mass function due to random fragmentation, such fragmentation does not affect the slope.

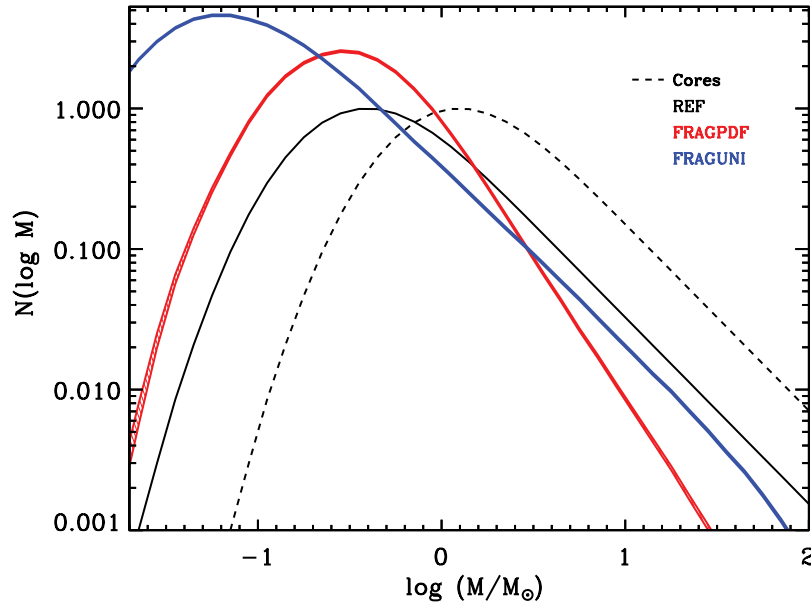


Figure 1.15: The resultant stellar mass functions of fragmentation models in [Swift and Jonathan P. Williams \(2008\)](#). FRAGPDF and FRAGUNI mass functions are in red and blue curves, respectively.

In addition to REF, MULT1, FRAGPDF, and FRAGUNI mass functions, the resultant stellar mass functions with the composite model are presented in [Figure 1.16](#). In addition, the properties of resultant mass functions with all models are summarised in [Table 1.2](#). The power-law index α_S , dispersion of a lognormal initial CMF σ_S , and the peak of the distribution μ_S are shown in the table. As mentioned above, the FRAGPDF model narrows the mass distribution and broadens with

variable star formation efficiency and multiple system formation. So then, even if each physical process causes the difference in mass distribution, the combination cancels the difference between each other.

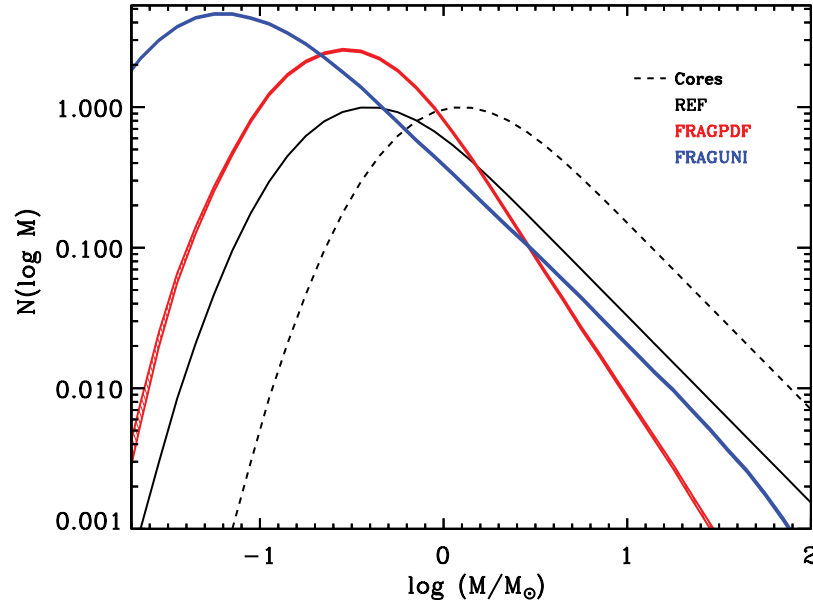


Figure 1.16: The resultant stellar mass functions with the composite model (green curve). The REF, MULT1, FRAGPDF, and FRAGUNI mass functions are also shown in black, red, purple, and blue curves. In the REF mass function, the error bars represent the measurement errors of \sqrt{N} . (Figure 3 of [Swift and Jonathan P. Williams \(2008\)](#)).

The authors conclude that the effects of varying star formation efficiency, stellar multiplicity, and global core fragmentation on the mapping from CMF to stellar mass function are minor. They also claimed that the observational accuracy at this moment is not enough to detect the effects and distinguish the star formation model, but observations over a wide range, including low- and high-mass ends, have the potential to investigate the models.

Table 1.2: The summary of the resultant mass functions in [Swift and Jonathan P. Williams \(2008\)](#)

Model	x_S	σ_S (dex)	μ_S (M_\odot)
Control Model			
REF	1.3	0.37	0.39
Variable SFE Model			
SFEVAR	1.3	0.48	0.63
Multiplicity Models			
MULT1	1.3	0.46	0.29
MULT2	1.3	0.40	0.42
Fragmentation Models			
FRAGPDF	2.0	0.34	0.30
FRAGUNI	1.3	0.51	0.23
Composite Model			
COMP	2.0	0.53	0.34

1.4 Core Identification Method: Dendrogram

In order to identify dense cores in the observational data, several automatic methods have been established so far, and we will introduce three well-known algorithms of them in this section.

First, [J. Stutzki and Guesten \(1990\)](#) proposed the Gaussclump method, which aims to detect clumps rather than cores, assuming that the source is composed of many triaxial gaussian clumps. The disadvantage of this method is that one clump is not always detected as one structure even if the clump seemingly does not have multiple peaks. Second, the Clumpfind algorithm is developed by [J. P. Williams, de Geus, and Blitz \(1994\)](#) after the Gaussclump method. This algorithm searches peaks of input data and boundaries among them with a user-defined input parameter. It traces structures by drawing contours from the peak of the data, and

the input parameter is used as the lowest level and step of a contour. When another peak appears, the algorithm decides the boundary between them. Then, all pixels are assigned to any cores if only the flux above the input parameter, which may make cores larger and more massive. This point is improved by [Padoan, Nordlund, et al. \(2007\)](#); they only assign pixels to a core within the density isosurface, which defines the core. The third method is the Dendrogram algorithm ([Brunt and Heyer 2002](#)). This algorithm identifies hierarchical structures of input data with three user-defined input parameters. The structures have named a trunk, a branch, and a leaf. The lowest hierarchy is a trunk, the highest is a leaf, and the rest are branches. We describe a detailed procedure of structure identification with this method later in this section. When the Dendrogram algorithm is used to detect dense cores of a molecular cloud, Dendrogram's leaves are usually treated as a dense core. [Pineda, Erik W. Rosolowsky, and Goodman \(2009\)](#) compared the Clumpfind method and Dendrogram method in the study of the mass function. The two algorithms represent the method that does not and does take into account the hierarchy of the cloud. Therefore, the authors conclude that a preferred way to study the molecular cloud structures is a method that considers the cloud's hierarchical structures, such as a Dendrogram. That is, we utilized Dendrogram in our previous dense core survey ([Takemura, Nakamura, Kong, et al. 2021](#); [Takemura, Nakamura, Ishii, et al. 2021](#), see Sections 1.5 and 1.6) and this thesis.

In the rest of this section, we show the core identification with Dendrogram. This algorithm searches the hierarchy with three input parameters: `min_value`, `min_delta`, and `min_npix`. Figure 1.17 shows a schematic diagram of a one-

dimensional case, and the process is as follows.

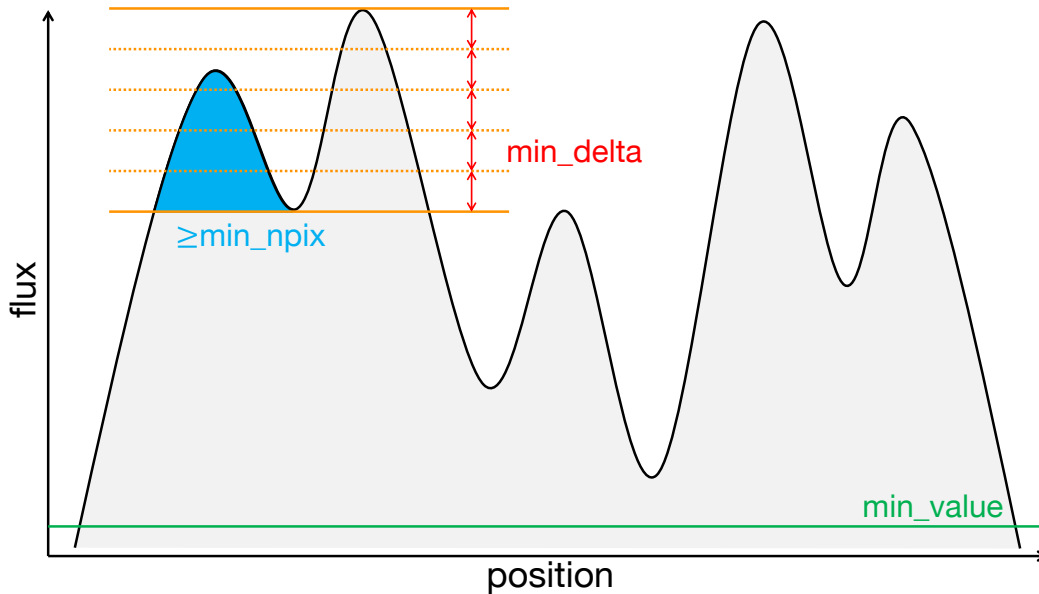


Figure 1.17: The schematic diagram of use-defined parameters in Dendrogram algorithm: min_value , min_delta , and min_npix . The vertical and horizontal axes are flux and position.

1. Find a peak of the input data.
2. Look for the next peak with a step defined with min_delta , and the two peaks are classified with leaves (leaf1 and leaf2 in Figure 1.17). Here, each leaf needs to include more pixels than min_npix , and the number of pixels is calculated as an area for two-dimensional data and a volume for three-dimensional data. Then, two leaves are combined as a branch (branch1 in Figure 1.17).
3. Combine the pair of two leaves, one leaf, one branch, and two branches as a new branch.

4. Repeat the above processes until the algorithm searches the structure down to the lowest value defined with `min_value`.
 5. Compound the bottom two branches or one leaf and one branch as a trunk.
- Then, we obtain hierarchical structures as Figure 1.18. The hierarchy looks like Figure 1.19 for two-dimensional data.

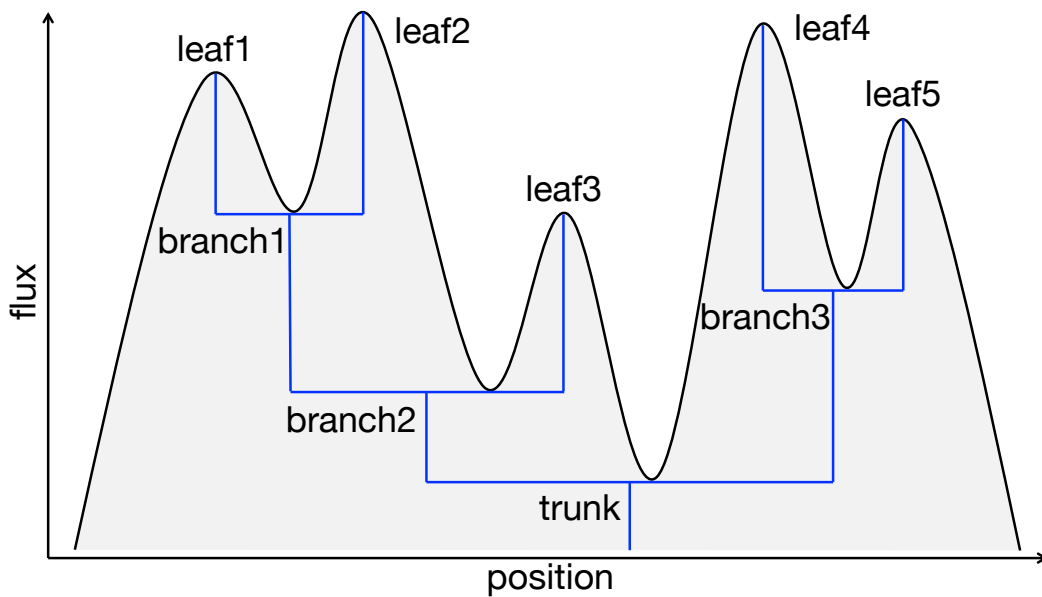


Figure 1.18: The schematic diagram of Dendrogram's hierarchy for a one-dimensional data.

The output of this algorithm includes a position, a projected area, a position angle, major and minor axes, and a total flux for two-dimensional data. If the input data is position-position-velocity (PPV) three-dimensional data, a velocity width is also calculated.

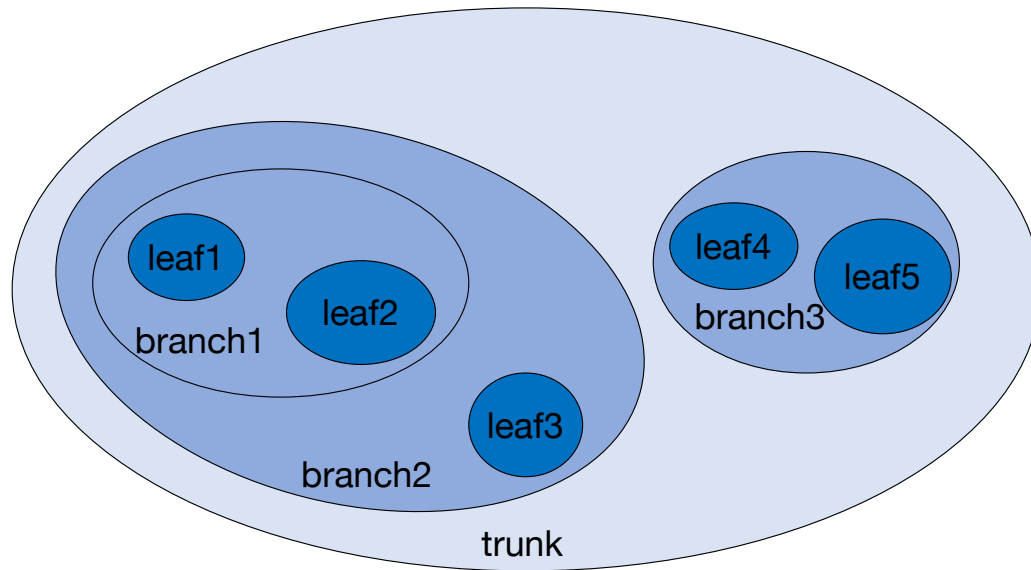


Figure 1.19: The schematic diagram of Dendrogram's hierarchy for a two-dimensional data.

1.5 Dense Core Survey in Orion A with NRO45-m data

We conducted a dense core survey in Orion A with the $C^{18}O$ ($J=1-0$) emission observed with Nobeyama Radio Observatory (NRO) 45-m Telescope in [Takemura, Nakamura, Ishii, et al. \(2021\)](#). Orion A is the nearest and well-studied Giant Molecular Cloud (GMC) (e.g., [Bally et al. 1987](#); [Genzel and Juergen Stutzki 1989](#); [L. A. Hillenbrand 1997](#); [Ikeda, Sunada, and Kitamura 2007](#); [Ikeda and Kitamura 2009](#); [Shimajiri, Kawabe, et al. 2011](#); [Nakamura, Miura, et al. 2012](#); [Tatematsu et al. 2016](#); [Hacar et al. 2017](#); [Kirk et al. 2017](#); [Nakamura, Ishii, et al. 2019](#)) prior to our dense core survey. Based on the very-long-baseline interferometry (VLBI)

observations, the source distance is derived as 414 pc (Menten et al. 2007). This map has an effective angular resolution of $\sim 26''.4$ (FWHM) corresponds to ~ 0.05 pc at the source distance and velocity resolution of $\sim 0.1 \text{ km s}^{-1}$ (See Nakamura, Ishii, et al. (2019) for more details).

We identified 746 cores with the Dendrogram algorithm and classified 709 cores of them as starless cores using Herschel Orion Protostar Survey (HOPS) catalog (Furlan et al. 2016). Since dense cores are thought to be deeply embedded into the molecular cloud, a core mass is calculated with Dendrogram's hierarchy and *Herschel-Planck* H_2 column density map (Lombardi et al. 2014; Stutz and Kainulainen 2015) which have an angular resolution of $36''$ as Equation 1.6 (Equation (2) in the paper).

$$M_{\text{core}}^k = \mu m_{\text{H}} \times \sum_i (N_{\text{H}_2, i} \times F_i^k) \quad (1.6)$$

where F_i^k is the total intensity ratio of k th leaf I_i^k and trunk T_i at i th pixel described as $F_i^k = I_i^k / T_i$. Using this method, we subtracted the column density in front of and behind the core along the line of sight and estimated core mass. The core mass and mass calculated with total column density are compared as a function of the mean column densities at core positions in Figure 1.20 (Figure 8 in the paper). The later mass is named as $M_{\text{projection}}$ in the figure. The ratios of two masses $M_{\text{core}} / M_{\text{projection}}$ for most cores are smaller than one, and the mean value and the standard deviation are 0.35 ± 0.21 . This result means we may overestimate the core mass by \sim three times when we do not subtract the background column

density.

According to the results of virial analysis, we have 684 gravitationally bound starless cores and 25 unbound starless cores in the final core catalog. Most starless cores are classified as gravitationally bound starless cores, and we constructed CMF as Figure 1.21. The completeness corrected CMF is also shown in the figure. The completeness is calculated by calculating the detection probability of inserted artificial cores which have masses of the center of mass bins of CMF. Although observed CMF has a turnover as $\sim 0.3 M_{\odot}$, the completeness corrected CMF does not have a turnover there, and it has a peak at a smaller mass. Then, we concluded that we could not detect a turnover of CMF with the map resolution; the higher spatial resolution is required to detect them.

1.6 Comparison of IMF and CMF in the Orion Nebula Cluster (ONC) Region

We performed a dense core survey in the central region of Orion A called the Orion Nebula Cluster (ONC) region with higher spatial resolution than NRO45-m data in Section 1.5. We reported this result in [Takemura, Nakamura, Kong, et al. \(2021\)](#). The map is a combined data of Combined Array for Research in Millimeter-wave Astronomy (CARMA) and NRO45-m ([Kong, Arce, Feddersen, et al. 2018](#)). The observed line is the same as $C^{18}O$ ($J=1-0$), the same as our previous study, but the angular resolution is \sim three times better than the data used in it. The map achieved an angular resolution of $8''$, which is ~ 3300 au at Orion A. In addition

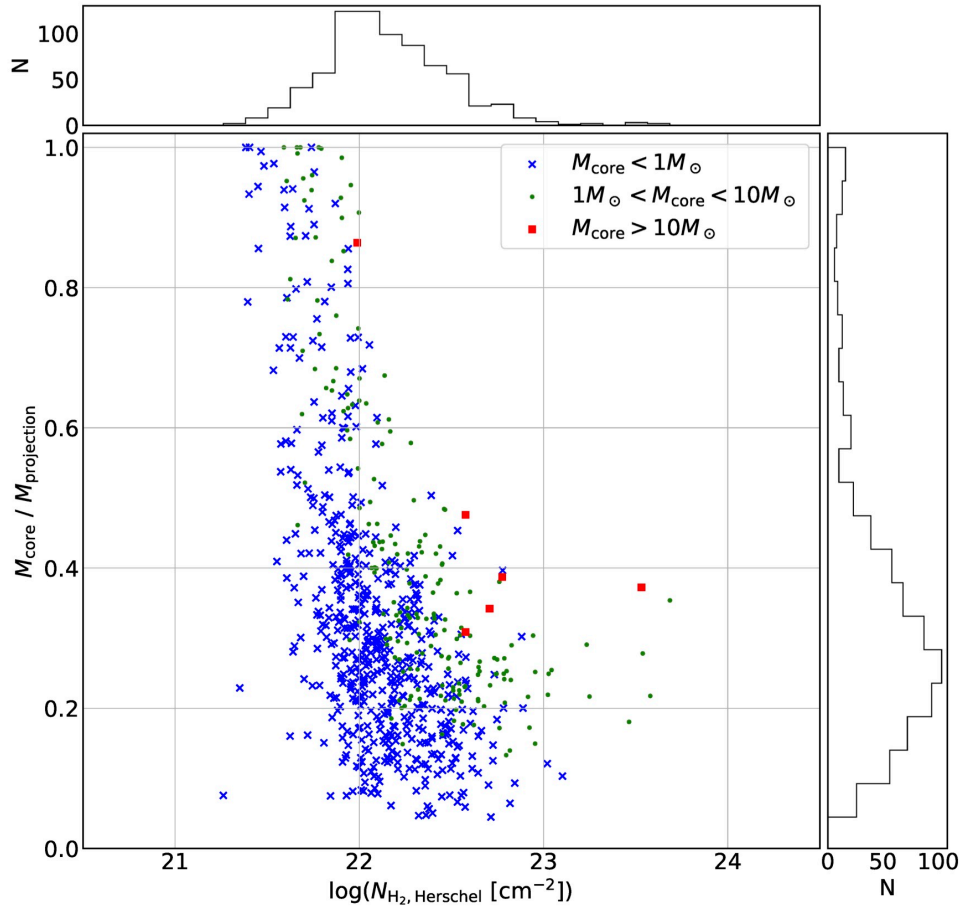


Figure 1.20: The relation between the mass ratio $M_{\text{core}}/M_{\text{projection}}$ and mean core column density in Takemura, Nakamura, Ishii, et al. (2021). The $M_{\text{projection}}$ is calculated using total column density at the core. The red squares, the green dots, and the blue crosses represent the core with a mass of $M_{\text{core}} > 10M_{\odot}$, $1M_{\odot} < M_{\text{core}} < 10M_{\odot}$, and $M_{\text{core}} < 1M_{\odot}$, respectively. The top and right histograms show the distribution along horizontal and vertical axes.

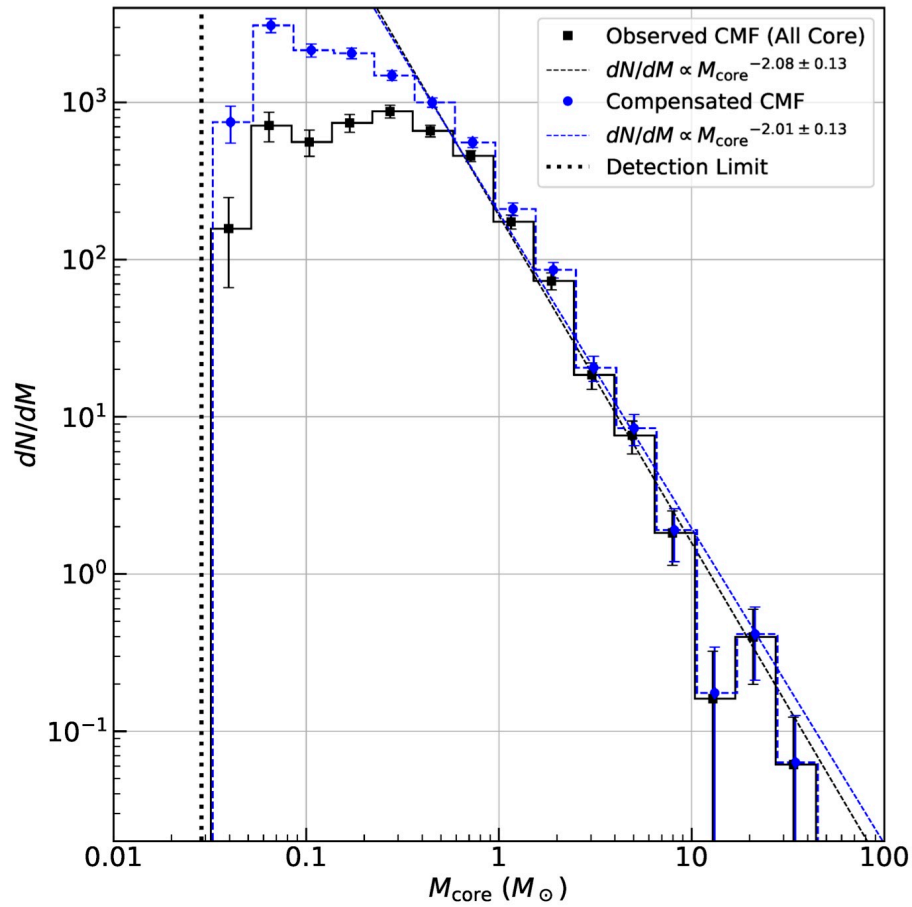


Figure 1.21: The observed CMF for all identified cores (black) and the completeness corrected CMF (blue) in Takemura, Nakamura, Ishii, et al. (2021).

to the dense core survey, we directly compared our CMF and IMF constructed with the stellar catalog of Da Rio, Robberto, L. A. Hillenbrand, et al. (2012), which has 1619 stars of the ONC region. Following the procedure of core identification in Takemura, Nakamura, Ishii, et al. (2021), we identified 151 gravitationally bound starless cores, 529 unbound starless cores, and 12 protostellar cores. The fact that the significant part of starless cores is classified as gravitationally unbound cores is consistent with the results of the dense core survey of ρ Ophiuchus with the H^{13}CO^+ ($J=1-0$) emission (Maruta et al. 2010) and Orion A with NH_3 (Kirk et al. 2017). Kirk et al. (2017) mentioned that external pressure is essential in maintaining dense cores. Then, the distributions of cores and stars are shown in Figure 1.22. We also updated the H_2 column density map from our previous study; we adopted a high-angular resolution ($18''$) H_2 column density map (Kong, Arce, Feddersen, et al. 2018).

Figure 1.23 shows the CMFs for all starless cores and bound starless cores and IMF in the ONC region. As seen in the figure, the CMF for bound starless cores and IMF have turnovers at similar masses of $\sim 0.1 M_{\odot}$, and both mass functions also have similar slopes above the turnovers. The observed relationship of CMF and IMF differs from that reported in previous studies in Section 1.3 except for the results in ρ Ophiuchus (Bontemps, P. André, et al. 2001), which also showed that CMF resembles MF of Class-II objects. When CMF and IMF have similar turnover masses, CMF is no longer reproduced by shifting IMF with SFE of smaller than unity. Bontemps, P. André, et al. (2001) conclude that SFE should be larger than 50-70% at least. However, high SFE such as $\sim 100\%$ is not justified physically

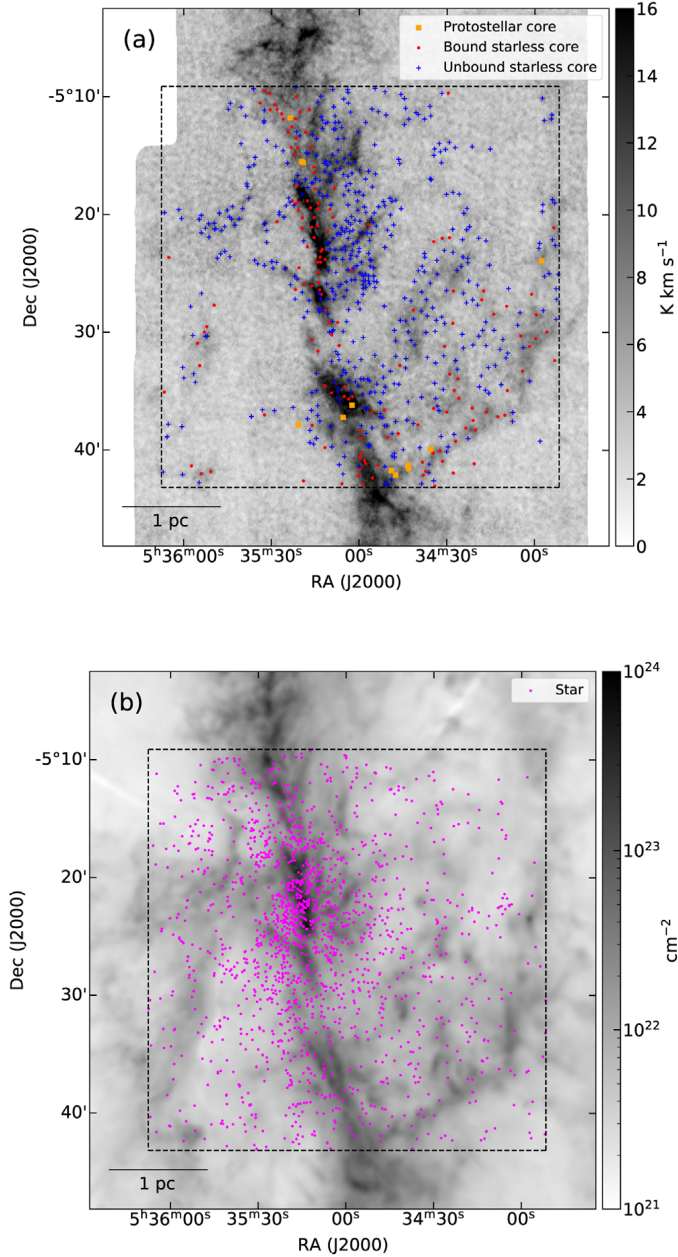


Figure 1.22: (a) The identified cores are plotted onto the integrated intensity map of the $C^{18}O$ ($J=1-0$) emission. The bound, unbound, and protostellar cores are plotted as red dots, blue crosses, and orange squares. (b) The stars are plotted onto the H_2 column density map. The observed region in [Da Rio, Robberto, L. A. Hillenbrand, et al. \(2012\)](#) is represented as a dotted square in both panels, and we analyzed cores in this region. (Figure 1 in [Takemura, Nakamura, Kong, et al. \(2021\)](#) but the configuration of panels are changed).

because the protostellar outflow/jet is a necessary process when mass accretion to a protostar takes place (Machida and Matsumoto 2012, see also Section 1.2). The previous observations, numerical simulations, and theoretical models suggest that $\sim 30\%$ of an accreting mass is blown off by the feedback of a protostar (Pudritz et al. 2007). Then, we guess that mass accretion of the surrounding material of a core can explain the observed relation of CMF and IMF in this study.

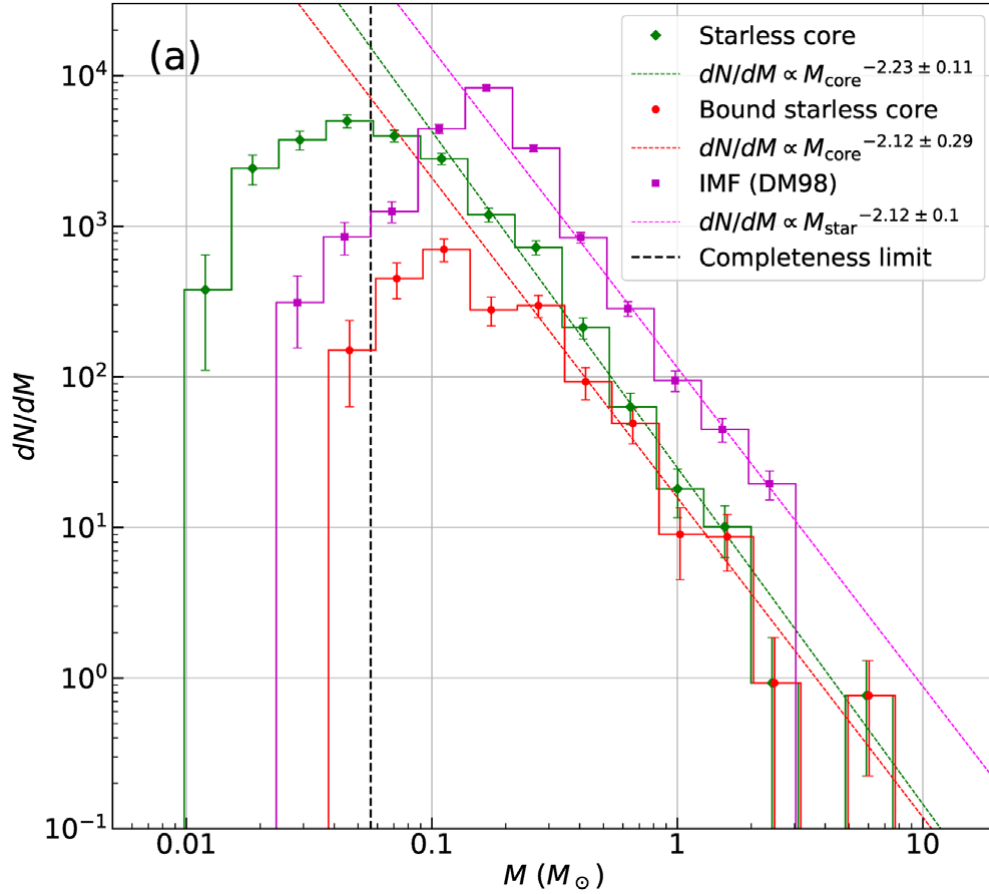


Figure 1.23: The CMF for starless cores (green) and bound starless cores (red) and IMF (magenta) in Takemura, Nakamura, Kong, et al. (2021).

To test whether our identified cores can form stars with mass accretion, we calculated the SFE of the cloud, which is different from the SFE of a core discussed in the previous paragraph and SFR. For the SFE of the cloud, it is estimated as $\sim 4\%$ (Nakano, Hasegawa, and Norman 1995). To estimate the SFE of the cloud when our starless cores evolve into stars, we calculated the ratio of the sum of bound starless core masses and total gas mass of the ONC region as Equation 1.7. Here we assumed that all bound starless cores form a star and SFE of a core is 100% due to mass accretion.

$$\frac{\sum_{\text{bound starless core}} M_{\text{core}}}{M_{\text{cloud,ONC}}} \sim 0.034 \quad (1.7)$$

This value is consistent with the fiducial value of a few percent. The ratio becomes 0.074 when we use the total mass of identified starless cores instead of bound ones. Then, we will obtain reasonable SFE of a cloud even if all starless cores, including unbound starless cores, form stars with mass accretion.

Next, we compared the SFR estimated with stellar catalog (Da Rio, Robberto, L. A. Hillenbrand, et al. 2012) and our core samples. The former is the mean SFR in 2 Myr calculated as Equation 1.8.

$$\text{SFR}_{2 \text{ Myr}} = \frac{\sum_{2 \text{ Myr}} M_{\text{star}}}{2 \text{ Myr}} \sim 1.5 \times 10^{-4} M_{\odot} \text{ yr}^{-1} \quad (1.8)$$

Then, the latter is derived as below.

$$\text{SFR}_{\text{core}} = \frac{\sum_{\text{bound starless core}} M_{\text{core}}}{3\bar{t}_{ff}} \sim 1.0 \times 10^{-4} M_{\odot} \text{ yr}^{-1} \quad (1.9)$$

where \bar{t}_{ff} is a mean free-fall time of bound starless cores. To calculate this value, we assumed two things; SFE of a core is 100% due to mass accretion, and all bound starless cores evolve into the core within three times a mean free fall time. As Equations 1.8 and 1.9, SFRs computed with a stellar catalog, and our core sample has similar values.

Therefore, we concluded that our cores could be birthplaces of stars, and mass accretion is a critical process for cores to gain masses. Figure 1.24 is a standard star formation scenario. Mass accretion is not considered, and the parental core mass determines stellar mass. On the other hand, our star formation model considers the mass accretion from the surrounding cloud to the cores as Figure 1.25. The cores grow due to mass accretion, and gravitationally unbound cores may evolve into bound starless cores or stars by obtaining enough mass.

1.7 Growth of Core Mass and CMF

In Section 1.6, we have pointed out the possibility of core growth with mass accretion from the surrounding cloud. The core growth will greatly influence the final stellar mass and mapping from CMF to IMF. As we mentioned in Section 1.6, Then, we introduce an observation, numerical simulation, and analytical study,

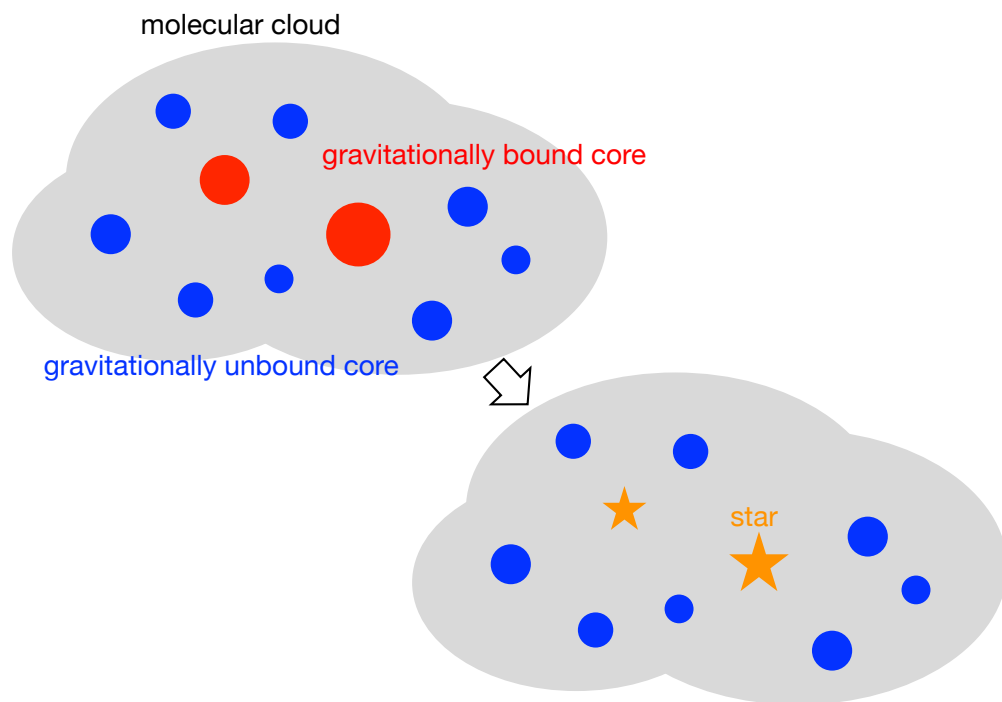


Figure 1.24: The schematic diagram of a current standard star formation scenario.

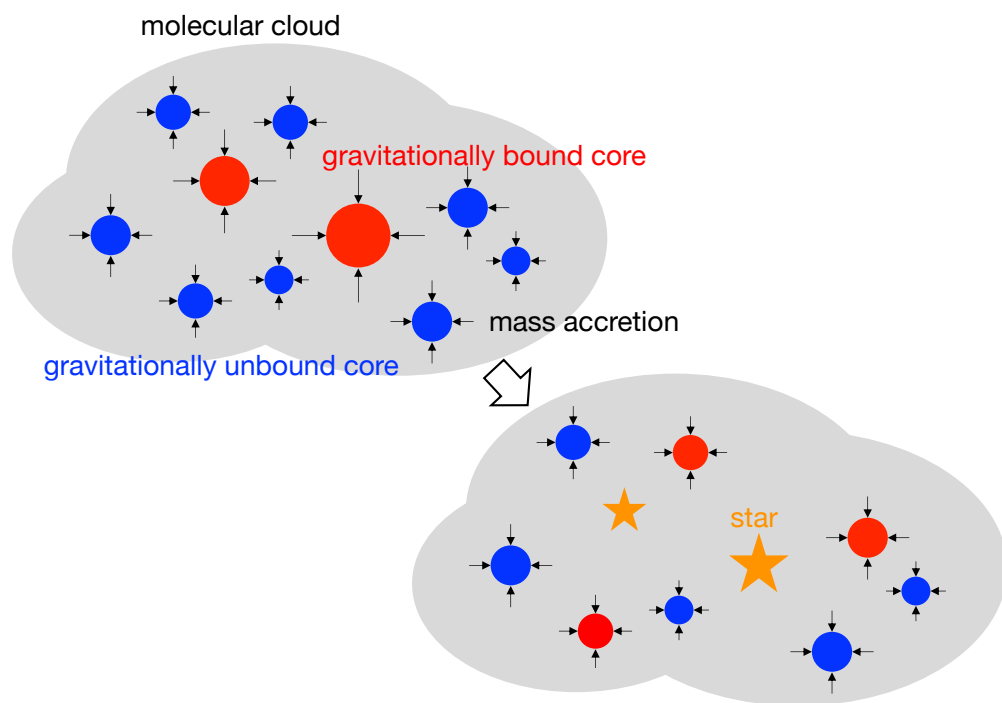


Figure 1.25: The schematic diagram of a new star formation model considers the mass accretion and core growth with it.

which suggests a core growth in this section.

1.7.1 Observational Study

Kong (2019) observed the Dragon Infrared Dark Cloud with ALMA 1.3 mm continuum and performed a dense core survey. The author also investigated outflows with ALMA CO ($J=2-1$) image of the same region in Kong, Arce, Maureira, et al. (2019). Then, the core properties of cores with and without outflow, corresponding to protostellar and starless cores, are compared in Kong, Arce, Shirley, et al. (2021). Here, the starless cores do not have any infrared sources and no CO and SiO outflows. The comparison of their core mass histograms is shown in Figure 1.26. The top two panels are for cores identified with *astrograph*, and the bottom two panels are for cores identified with *astrodendro* (Dendrogram). The core masses are calculated with the continuum flux and constant dust temperature of 20 K in panels (a) and (c) and NH_3 kinetic temperature for each core (> Wang 2018) in panels (b) and (d). Whichever core identification algorithm and temperature are used, the cores with outflow tend to have larger masses than those without outflow. In Figure 1.26 (a), the median values of protostellar and starless core masses are $2.1 M_{\odot}$ and $0.37 M_{\odot}$, respectively. The authors conclude that the mass gap of cores is due to continuous core growth.

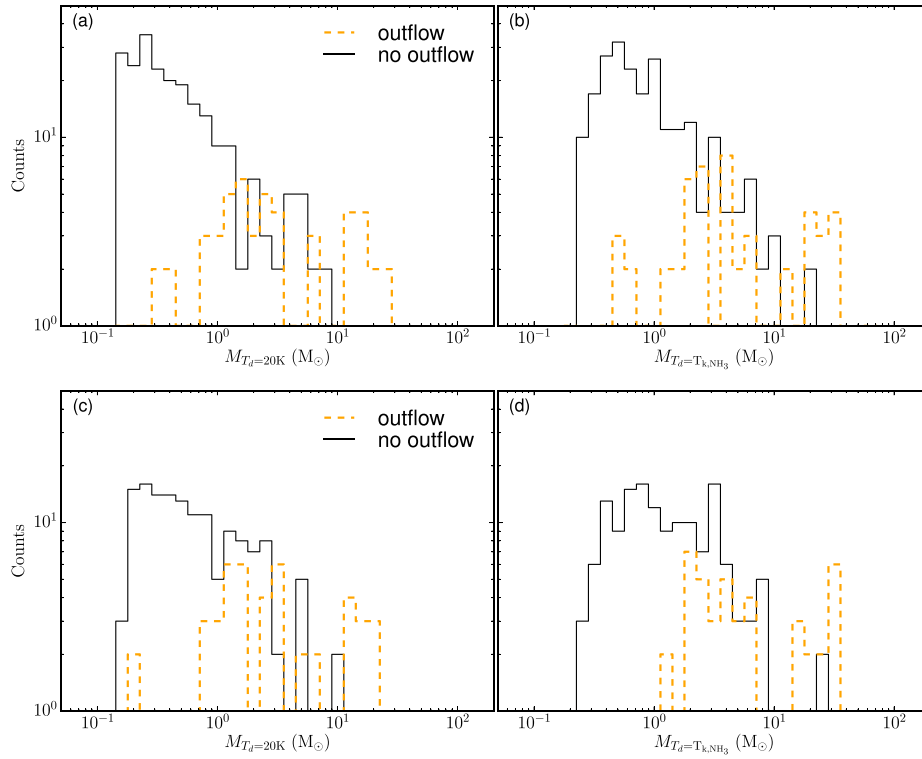


Figure 1.26: The mass histograms of protostellar cores (orange dashed histograms) and starless cores (solid black histograms) of the Dragon IRDC from [Kong, Arce, Shirley, et al. \(2021\)](#). (a) *astrograph* cores with dust temperature of 20 K, (b) *astrograph* cores with NH_3 kinetic temperature, (c) *astrodendro* cores with dust temperature of 20 K, and (d) *astrodendro* cores with NH_3 kinetic temperature.

1.7.2 Numerical Simulation

From the point of view of numerical simulation, [Pelkonen et al. \(2021\)](#) compared IMF and CMF of the progenitor cores considering the mass accretion to the cores. The authors used the cloud scale three-dimensional adaptive-mesh-refinement (AMR) and magneto-hydrodynamic (MHD) simulation done by [Hennebelle \(2018\)](#). In the simulation, the turbulent state is calculated for ~ 20 dynamical times without the self-gravity under the conditions of the periodic boundaries and an isothermal equation of state. After that, the self-gravity is introduced, and the cloud evolution is computed for another ~ 2.6 Myr with a snapshot of every 22 kyr. The box size is $L_{\text{box}} = 4$ pc, and the total mass in the box is $M_{\text{box}} = 3000 M_{\odot}$. The data have $8,192^3$ resolution for 4 pc simulation box, corresponding to ~ 100 au. Then, a sink particle (hereafter called star) is placed at a local gravitational potential minimum with a density above the critical density of $1.7 \times 10^9 \text{ cm}^{-3}$. There are 413 stars formed at the end of the simulation. After the sink particles form, half of the accreted mass is given to the stellar mass, and the authors reproduced the situation that the stars grow with mass accretion from the surrounding cloud.

[Pelkonen et al. \(2021\)](#) applied Clumpfind algorithm ([Padoan, Nordlund, et al. 2007](#)) to the data to identify the progenitor cores of stars, and they identified 382 unambiguously matched progenitors. The authors divided the samples into three categories based on the number and age of stars in progenitor cores as follows.

[category a] A single star in a progenitor core (312 progenitor cores)

[category b] Multiple stars that birthed in the same snapshot in a progenitor core
(32 progenitor cores)

[category c] There is more than one older star in addition to the primary star in the same progenitor core (38 progenitor cores)

Since the older stars are fed by the progenitor core rather than the primary star, the samples of [category c] are removed from the samples, and the final sample consists of 344 stars and cores. Figure 1.27 shows the mass histograms of stars and progenitor cores. The figure shows they have peaks at the same mass bin of $0.29 M_{\odot}$ and similar slopes above the peaks. Then, the shape of CMF remains even if we consider the mass accretion to the cores while they evolve. However, the stellar and core mass do not correspond as shown in Figure 1.28. The massive cores with $M_{\text{prog}} > 5 M_{\odot}$ are extracted, and the authors follow where the mass goes during the star formation. There are three possible states for a core mass: unaccreted mass, mass accreted by the internal star in the progenitor core, and mass accreted by other stars. The fractions of the three masses vary among cores. The motivation of their study is to test the core collapse scenario of star formation. In this model, a stellar mass is defined by its parental core mass as $M_{\text{star}} = \epsilon_{\text{core}} M_{\text{core}}$ but the figure suggests it is not. Then, the core collapse scenario is not preferred by their simulation. In addition, the authors claimed that the variation of a mass fraction means that the shape of CMF remains during star formation in a statistical sense only.

The authors also trace the mass accretion rate as Figure 1.29. In the competitive accretion scenario, the cores grew with Bondi-Hoyle accretion, and dashed and dotted lines represent the mass accretion rate. Each line is for the median and mean of the accretion rate. On the other hand, the mass accretion rate calculated in the

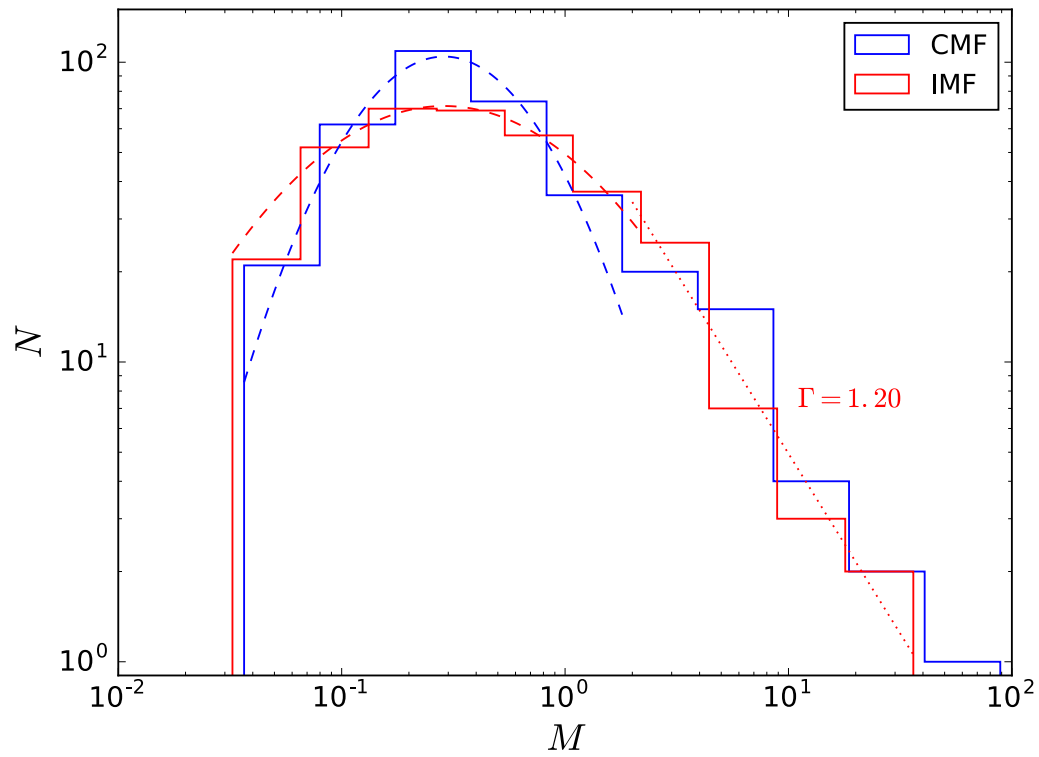


Figure 1.27: The histograms of stellar mass (red) and progenitor core mass (blue) from Pelkonen et al. (2021). The dashed lines are lognormal fits of histograms with masses $\leq 2 M_{\odot}$.

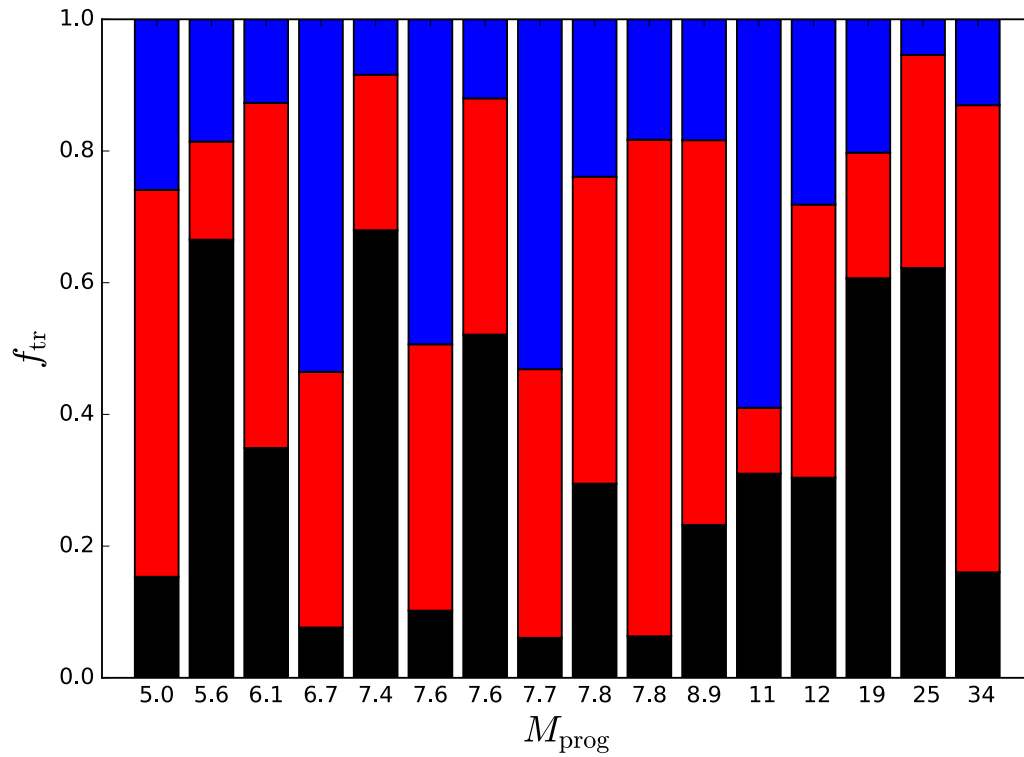


Figure 1.28: The fraction of the final stages of mass of each massive ($> 5M_{\odot}$) progenitor core: unaccreted mass (black), and mass accreted by the internal star in the progenitor core (blue), and mass accreted by other stars (red) from [Pelkonen et al. \(2021\)](#).

simulation is drawn with the other lines, which are higher than the predicted mass accretion rate of Bondi-Hoyle accretion by a few orders. The bright solid, faint solid, and dot-dashed lines are for the median values, mean values, and accretion rate of chosen two cores, respectively. Therefore, mass accretion in the simulation is more effective than Bondi-Hoyle accretion, which differs from the competitive accretion scenario.

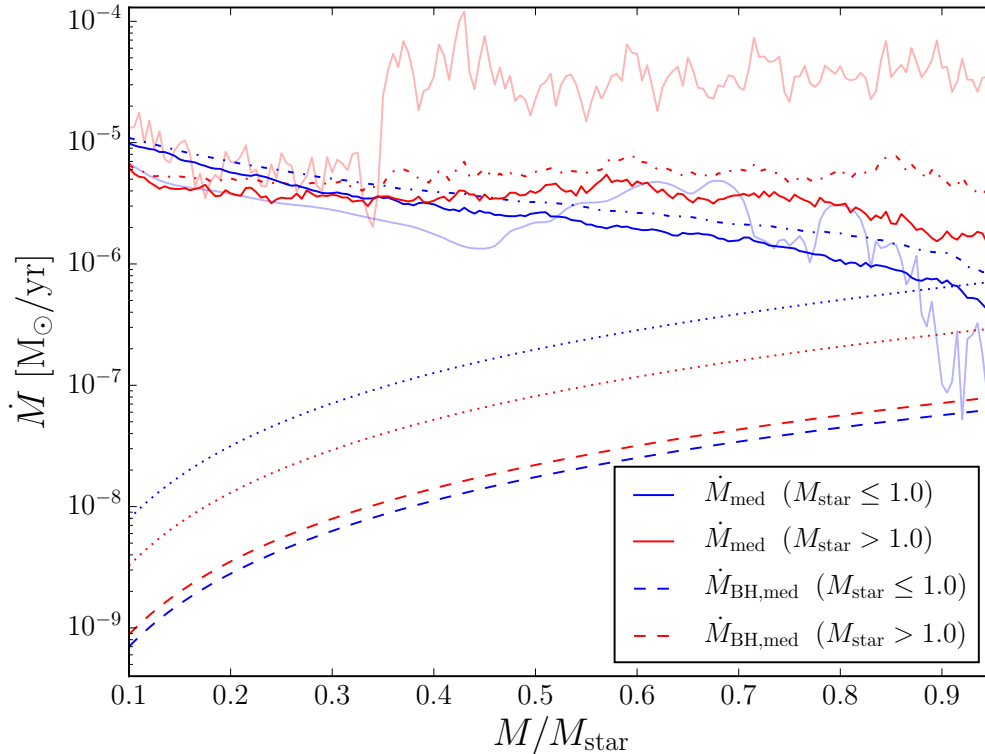


Figure 1.29: The time evolution of mass accretion rate calculated in [Pelkonen et al. \(2021\)](#). The bright solid lines show the median value calculated in the simulation for stellar masses of $M_{\text{star}} \leq 1.0 M_{\odot}$ (blue) and $M_{\text{star}} > 1.0 M_{\odot}$ (red). The dot-dashed lines are the mean values for each stellar mass. The faint lines are for two chosen stars from each stellar mass group. The predicted Bondi-Hoyle mass accretion rate is drawn with dashed (median values) lines and dotted lines (mean values), respectively.

1.7.3 Analytical Study

[S.-i. Inutsuka \(2001\)](#) derived CMF as a function of the power spectrum of the density distribution of the parental filamentary molecular cloud analytically as [Figure 1.30](#). The fragmentation of filaments forms the cores, and materials are given to cores along the filament. Then, core growth with mass accretion is taken into account in this study. The author predicted that CMF has a Salpeter-like slope when the initial index of the filament power spectrum is -1.5 . The CMF has a shallower slope than IMF during the first one free-fall time, and the slope becomes steeper until it reaches to Salpeter-like slope, to be precise. The filament power spectra are derived as -1.6 ± 0.3 from observation ([Roy et al. 2015](#)), similar to the predicted value by [S.-i. Inutsuka \(2001\)](#). However, the relation between this study and shallower slopes of CMF is still unclear (see [Figure 1.13](#) and [Section 1.3.3](#)).

1.8 Binning of CMF

To derive IMF and CMF, we count the number of stars or cores in a specific mass range called a mass bin. There are two main ways of binning to construct mass functions. The one is called "uniform sized logarithmic bins of mass (hereafter called uniform sized bins)." In this method, the sizes of mass bins are uniform on a log scale, and the number of objects in each mass bin is variable. To date, this binning way is usually used, and we also adopted this in our previous study ([Takemura, Nakamura, Kong, et al. 2021](#); [Takemura, Nakamura, Ishii, et al. 2021](#)). The other is named "variably sized logarithmic bins of mass (hereafter called

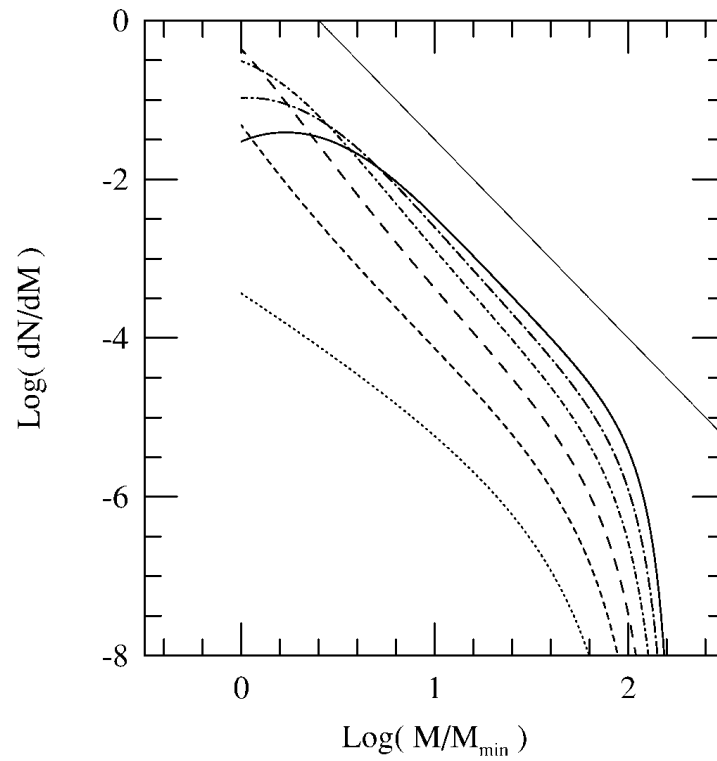


Figure 1.30: The time evolution of CMF when the filament power spectrum is -1.5 derived in [S.-i. Inutsuka \(2001\)](#). The evolution starts at $t/t_{ff}=0$ (dotted line), and CMFs at $t/t_{ff}=2, 4, 6, 8, 10$ (solid line) are also shown, where t/t_{ff} is a time scale of free fall time.

variably sized bins)." Contrary to another method, the number of objects in each mass bin is fixed, and the sizes of mass bins are variable in this method. The CMF is constructed in this way in [Motte, Nony, et al. \(2018\)](#) (see [Figure 1.13](#)).

[Maíz Apellániz and Úbeda \(2005\)](#) compared the slopes of mass functions with the two binning methods statistically. The authors constructed mass functions by changing the number of mass bins and stars that were randomly generated from IMF with a Salpeter-like slope. Then, they investigated whether we could obtain the Salpeter-like slope. The bias of a power-law slope normalized with respect to the uncertainty is calculated as [Equation 1.10](#).

$$b = \frac{1}{N_{\text{star}}} \sum_k^{N_{\text{star}}} \frac{\gamma_k + 2.35}{\sigma_k} \quad (1.10)$$

where N_{star} , γ , and σ are the number of stars, a power-law slope of mass function in the form of $dN/dM \propto M_{\text{star}}^\gamma$, and the uncertainty of the power-law index, respectively. When we get Salpeter-like slope of $\gamma = 2.35$, $(\gamma + 2.35)/\sigma$ the absolute value of b becomes zero. Then, if the binning and the fitting methods are not biased, $|b| \ll 1$. In contrast, the large value of $|b|$ means that the binning and fitting are biased.

[Figure 1.31](#) shows the histograms of distributions of $(\gamma + 2.35)/\sigma$ value for two binning cases: uniform sized bins case in panel (a) and variably sized bins case in panel (b). In both cases, a mass function is derived with 300 stars and 50 mass bins 1000 times. They constructed mass functions with 30, 100, 300, and 1000 stars, and each has 3, 5, 10, 30, and 50 mass bins in the paper. As the figure, there

is a systematic error in the case of the uniform sized bins, but such error is not seen in the case of the variably sized bins. The error in uniform sized bins cases becomes significant when the number of stars is small. Thus, the authors conclude that variably sized bins are the preferred way of binning, especially when we do not have enough stars or cores. However, according to their parameter study of the number of stars, the error is small even in the uniform sized bins case when the number of stars is 1000.

In this thesis, we mainly adopt the uniform sized bins case since we usually have objects of $g \geq 1000$, and this binning method has been used in many previous studies, as we mentioned above.

1.9 Summary of This Chapter

In this chapter, Chapter 1, we described the overview of the star formation study focusing on CMF and IMF. The properties of molecular clouds and their dense cores have been extensively studied observationally and theoretically as Sections 1.2 and 1.1. Since stars are formed in the dense cores, and the evolutionary process of a star, the core mass, and CMF are the notable targets of the star formation field. Many previous observations of IMFs and CMFs have reported the universality of IMF and self-similar mapping of CMF to IMF with SFE smaller than unity. The numerical simulations of prestellar cores showed that a large amount of initial core mass is blown off protostellar outflow. Based on such results, the core-collapse scenario of star formation is proposed. In the scenario, the final stellar mass is

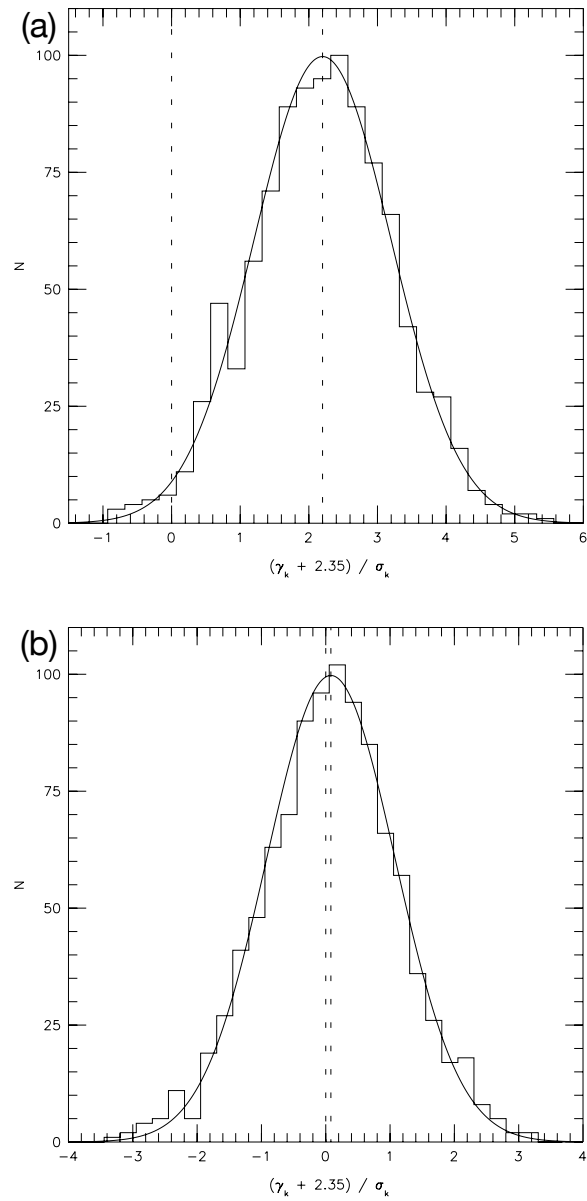


Figure 1.31: The histograms of $(\gamma + 2.35)/\sigma$ values in [Maíz Apellániz and Úbeda \(2005\)](#). (a) The mass function is constructed with uniform sized logarithmic bins of mass method and (b) variable sized logarithmic bins of mass method.

determined only by the parental core mass, and the mass ratio of the star and parental core, SFE, is uniform and does not depend on the core mass. We also represented the previous studies which mentioned that the effects of variable SFE, multiplicity, and fragmentation of the core on the mapping from CMF to IMF are small. The authors said that the low- and high-mass ends of mass functions imprint the information of the above processes, but such observations are not possible with the observational accuracy at that time. See Section 1.3 for details.

However, core growth with mass accretion, which is not considered in the core-collapse scenario, is also studied. We pointed out the importance of core growth from observation of CMF in the ONC region, which is a central region of Orion A as Section 1.6. We have compared the CMF with IMF constructed with a star catalog provided by previous observation. Then, we found that the CMF resembles IMF: CMF and IMF have similar turnover masses and power-law indices at the high-mass ends. This result indicates that mass accretion to cores is required to match the turnover masses of CMF and IMF because the protostellar outflow decreases the SFE of the individual core. This result is reported in the published refereed paper of [Takemura, Nakamura, Kong, et al. \(2021\)](#). In Section 1.7, we have introduced the observational, theoretical, and analytical studies of core growth. The analytical study predicted that the slope of CMF is reproduced from the fragmentation of filaments which have a specific index of the power spectrum, and the CMF slope does not change with time even if mass accretion along the filament is considered.

Besides, we also presented technical issues of CMF studies, such as the core

identification method and binning procedure to construct CMFs in Sections 1.4 and 1.8. In addition, we found that background column density should be subtracted to calculate accurate core masses with two-dimensional column density data based on a dense core survey in Orion A. Section 1.5 and the published refereed paper of Takemura, Nakamura, Ishii, et al. (2021) show more details.

1.10 Purpose and Structure of This Thesis

The relationship between CMF and IMF and CMF properties are expected to have information on the star formation processes, such as core growth with mass accretion, SFE, stellar multiplicity, and fragmentation of the core. The processes may affect the mapping from CMF to IMF. In the case of mass accretion, although S.-i. Inutsuka (2001) found that the slope does not evolve with time, we cannot rule out the possibility of the time evolution of CMF caused by mass accretion.

For the other three processes, the influences on the mapping were evaluated in (Swift and Jonathan P. Williams 2008) and concluded that they are negligible except for low- and high-mass ends of CMF. However, the accuracy of observations at that time was not enough to observe the edges of CMF.

Today, high-spatial resolution and sensitivity observations towards various star-forming regions have become available thanks to ALMA and other interferometers. Actually, precise observations of star-forming regions, including distant high-mass star-forming regions, are in progress, such as one of the ALMA large programs of ALMA-IMF. Then, as we have shown in Section 1.3.3, the top-heavy CMFs are

reported in high-mass star-forming regions. Comparing CMF covers from low- to high-mass ends in various cloud environments and stages of star formation becomes possible. In order to conduct such studies, the following two will be necessary.

[Remaining task 1] Construct the method to construct accurate CMF from observations.

[Remaining task 2] Establish the fiducial core catalog.

The CMF properties are affected not only by the star formation process but also observation method. We do not know the structure of molecular clouds in position-position-position three-dimensional space. We can obtain the column density of the molecular cloud from continuum observation or column density at each velocity along the line of sight from molecular line observation. The limitation will cause an artificial effect on CMF properties which should be removed to compare CMFs in different regions. Then, in Chapter 2, we conduct a dense core survey to construct CMFs with three-dimensional numerical simulation data of molecular cloud. Since we know a three-dimensional structure of the simulated cloud, we can construct the true CMF and compare it with CMFs from core samples assuming continuum and molecular line observations. We aim to evaluate the influence of each observation method on the CMF property and investigate to derive true CMF to achieve [Remaining task 1].

After we obtain the true CMFs and core catalogs from observations, the core catalog of a well-known cloud will be helpful to compare. Then, we conducted a dense core survey in Orion A and provided the core catalog and the analysis results of the core properties such as CMF in Chapter 3. Based on the results of Chapter

2, especially the discussion of PPV data, we constructed CMFs with molecular line data. The data covers a wide area of this cloud with a high spatial resolution comparable to the spatial resolution toward distant high-mass star-forming regions at a few kpc with ALMA. In addition, since Orion A is the nearest giant molecular cloud, many observations in various wavelengths have been performed so far, like NRO45-m, CARMA, ALMA, Herschel, and Spitzer. Thus, our core catalog is considered one of the most suitable for [Remaining task 2]. Detailed information and discussion are provided in [Takemura, Nakamura, Arce, et al. \(2023\)](#).

Finally, we summarise this thesis and show prospects in Chapter 4.

2. Dense Core Survey with Numerical Simulation Data

When conducting a dense core survey and constructing CMF, two-dimensional PP (position-position) data and three-dimensional PPV (position-position-velocity) data are usually used. The former data is constructed with a continuum observation, and the latter is derived from a molecular line observation. In practice, however, molecular clouds and dense cores have a structure in PPP (position-position-position) space. In this chapter, we conduct a dense core survey with numerical simulation data (see Section 2.1 for detailed information) to compare CMFs from three-dimensional PPP (position-position-position) volume density data, two-dimensional PP column density data, and three-dimensional PPV column density data. The PP CMF seems to be affected by the overlap effect and background column density of a core. First, when several cores overlap along the line of sight, only the most massive and extended core will be identified as a core; then, we may miss low-mass cores. Second, the observed column density is the sum of the column densities of a core and an ambient material along the line of sight. The

later column density is needed to be extracted from the observed column density to derive an accurate core mass; otherwise, we overestimate a core mass. In the case of PPV CMF, core masses are underestimated due to a line broadening, even if we chose an optically thin line. Because the structures are resolved along the line of sight velocity, the influences of overlap effect and background column density are likely less severe than PP data. Instead of that, the line width of a structure is broadened with the thermal and turbulent motion of a gas, and we need to set a cut-off velocity to decide a boundary of a core. Then we aim to evaluate the above effects of observational data and investigate a way to obtain a true CMF from observational data by comparing the CMFs of PPP, PP, and PPV data created with the result of the numerical simulation.

In addition, we conducted a dense core survey with various `min_delta` one of the parameters of Dendrogram (see Section 1.4) and studied how the resultant CMF's parameters change. Since a high-spatial-resolution observation of a molecular cloud, such as it performed by ALMA, tends to have a small field of view, it is difficult to cover the entire cloud and its dense cores. We reproduced such a situation by constructing CMFs only with cores at a certain distance from the peak of column density, and then, we studied the CMF's properties. In this section, we calculate the number of mass bins of CMFs as $\sqrt{N_{\text{core}}}$, where N_{core} is the total number of identified cores.

From one PPP data cube, we can obtain three PP data and PPV data by changing the line of sight direction: x , y , and z axes. In this chapter, we focus on analyzing the PP and PPV data with the line of sight direction of the z axis. Then, we show

the results of other data in Appendix A.

2.1 Numerical Simulation Data

We used the three-dimensional AMR, MHD simulation of the collision of two GMCs done by Wu, Benjamin (the second author of the reference paper) with the same setup of Model 2 in Table 2 of [Christie, Wu, and Jonathan C. Tan \(2017\)](#). We briefly describe the initial condition and setup of the simulation. The simulation box size is $L_{\text{box}} = 128$ pc, and the box is filled with the uniform ambient gas whose density is $n_{\text{H,ambient},0} = 10 \text{ cm}^{-3}$. In the simulation box, two GMCs that have the same radii and densities of $R_{\text{GMC}} = 20$ pc and $n_{\text{H,GMC},0} = 100 \text{ cm}^{-3}$ are placed. The offsets between the two clouds are $b = 0.5R_{\text{GMC}}$ and this is an impact parameter of the collision which has a relative velocity of $v_{\text{rel}} = 10 \text{ km s}^{-1}$. The internal velocity dispersion is yielded in both GMCs, and the velocity of the virial scale Mach number is $\mathcal{M}_s = \sigma/c_s = 23$ at $T = 15$ K. Here the velocity field of the turbulence is initialized with a spectrum of $v_k^2 \propto k^4$, where k is a wavenumber; the k -modes are in the range of $2 < k/(\pi/L) < 20$. In addition, a uniform magnetic field with field strength and angle respect to the collision axis of $B = 10 \mu\text{G}$ and $\theta_B = 60^\circ$ is inserted in the box. Using the Grackle chemistry and cooling library ([Smith et al. 2017](#)) is adopted to implement the heating and cooling effect. We used the data that was calculated for 4 Myr after the gravity is switched on.

The resolution is the difference between our data and [Christie, Wu, and Jonathan C. Tan \(2017\)](#). The maximum of their data is from four levels of refinement of (128

$\text{pc})^3$ box, and the grid size is $\Delta x_{\text{Christie et al.}} = 0.0625$ pc. On the other hand, our data achieved the grid size of $\Delta x = 0.03125$ pc with five levels of refinement of the box. In this thesis, we analyzed the central $(64 \text{ pc})^3$ region. This spatial resolution is comparable to the observation data of distant star-forming regions as a few kpc with ALMA.

2.2 Preparation of Data Set: PP data and PPV data

We created PP column density data by calculating the sum of the volume density of the simulated PPP data along one of the axes as Equation 2.1. Since the density of ambient gas is set to $n_{\text{H},0} = 100 \text{ cm}^{-3}$ as an initial condition, we calculated the column density of the molecular cloud itself using pixels with a density larger than $\rho_{\text{ambient}} = \mu m_{\text{H}} n_{\text{H},0} \simeq 4.68 \times 10^{-22} \text{ g cm}^{-3}$. Here, $\mu = 2.8$ is a mean molecular weight per H. The direction of line-of-sight is selected from three axes (x , y , and z axes in this study), and three PP data and PPV data are made from one PPP data. In Equation 2.1, line-of-sight is set to z axes.

$$N_{\text{PP}}(x, y) = \sum \rho(x, y) dz [\text{g cm}^{-2}] \quad (2.1)$$

Next, we constructed PPV column density data from PPP volume density data considering a thermal broadening and a small-scale velocity gradient (Brunt and Heyer 2002; Miville-Deschênes, Levrier, and Falgarone 2003). We assume that

the density of a cell, $\rho(x, y, z)$, has a gaussian line profile centered at the velocity at (x, y, z) , $u(x, y, z)$, in (x, y, v) space which computed with velocity dispersion of Equation 2.2. Three PPV data are given from one PPP data as well as PP data, and we describe the equations when the line of sight is set to the z axis.

$$\sigma_{\text{PPV}}(x, y, z) = \left[\frac{k_{\text{B}} T(x, y, z)}{m} + \left(\frac{\partial u(x, y, z)}{\partial z} dz \right)^2 \right]^{1/2} \quad [\text{km s}^{-1}] \quad (2.2)$$

where k_{B} , $T(x, y, z)$, and m are the Boltzmann constant, a gas temperature, and a mass of species we are focusing on, respectively. Then, the column density of PPV data is calculated as Equation 2.3. The column density of a specific velocity channel is a sum of the Gaussian line profile of each velocity.

$$N_{\text{PPV}}(x, y, v) = \sum_z \rho(x, y, z) dz \times \frac{1}{\sqrt{2\pi}\sigma_{\text{PPV}}(x, y, z)} \exp\left(\frac{v - u(x, y, z)}{2\sigma_{\text{PPV}}(x, y, z)}\right) \quad [\text{g cm}^{-2}] \quad (2.3)$$

In this study, the volume density, temperature, and velocity along three axes in three-dimensional space are calculated by numerical simulation. Since we conduct a dense core survey with the C^{18}O ($J=1-0$) data of Orion A molecular cloud, which has a velocity resolution of 0.1 km s^{-1} in Chapter 3, we constructed the PPV data of C^{18}O by setting the velocity resolution to 0.1 km s^{-1} to compare each other. Moreover, the C^{18}O ($J=1-0$) emission is emitted from not everywhere in a cloud but a region with a higher density than its critical density. The critical densities of CO and its isotopologues are $\sim 10^3 \text{ cm}^{-3}$. Then, we converted dense regions above the critical density in PPP data to PPV data in this study.

2.3 Core Identification

We applied the Dendrogram algorithm (E. W. Rosolowsky et al. 2008) to PPP, PP, and PPV data to identify the hierarchical structures of the data. The input parameters for each data are calculated as follows.

For PPP data, we set $\text{min_value} = 10^4 \text{ cm}^{-3} \simeq 4.68 \times 10^{-20} [\text{g cm}^{-3}]$ which is a typical density of a dense core and min_delta is one tenth of min_value . Then, we computed min_npix using jeans length λ_J as $\text{min_npix} = 4\pi/3(\lambda_J/2)^3$ pixels. The jeans length is uniform in the entire data and calculated with density and sound speed of 10^4 cm^{-3} and 0.2 km s^{-1} (Equation 2.4).

$$\lambda_J = \frac{c_s}{\sqrt{G\rho}} \simeq 0.13 \left(\frac{c_s}{0.2 \text{ km s}^{-1}} \right) \left(\frac{n}{10^4 \text{ cm}^{-3}} \right)^{1/2} [\text{pc}] \quad (2.4)$$

where G and c_s are universal gravitational constants and sound speed.

There are two classes in the `astrodendro.analysis` module to derive the properties of each Dendrogram's hierarchy. One is the `PPStatistic` for PP data, and the other is the `PPVStatistic` for PPV data. Then, to analyze PPP data with Dendrogram, we used the latter class for PPP data by setting one of the three axes as a line of sight corresponding to the velocity axis of PPV data. We call the axis z axis and the other axes x and y axes, respectively.

In the case of PP data, min_value is a typical column density of a filamentary structure of the data which is 10^{22} cm^{-2} and min_delta is one-tenth of it as well. The area with a radius of half of the jeans length, which is the same as the PPP case, is applied as min_npix .

Lastly, we assumed that a core has an ellipsoidal shape in PPV space to calculate Dendrogram's parameters: `min_value`, `min_delta`, `min_npix`. The lengths of two axes in the PP plane are jeans length, and the length along the velocity axis is a velocity width Δv calculated from Larson's law of [Heyer and Brunt \(2004\)](#) as Equation 2.5.

$$\Delta v = 0.87 \left(\frac{\lambda_J}{\text{pc}} \right)^{0.65} [\text{km s}^{-1}] \quad (2.5)$$

where the jeans length is calculated with Equation 2.4 and $\Delta v = 0.21 \text{ km s}^{-1}$ at $\lambda_J = 0.13 \text{ pc}$. We used the volume as `min_npix`.

Then, we drive the column density of each channel as `min_value` when a core has a uniform density of 10^4 cm^{-3} using Equation 2.6.

$$N_{\text{H}_2, \text{ channel}} \simeq 1.67 \times 10^{21} \left(\frac{n_{\text{core}}}{10^4 \text{ cm}^{-3}} \right) \left(\frac{\lambda_J}{0.13 \text{ pc}} \right) \times \left[\left(\frac{\Delta v}{0.21 \text{ kms}^{-1}} \right) \left(\frac{v_{\text{res}}}{0.1 \text{ km s}^{-1}} \right)^{-1} \right]^{-1} [\text{cm}^{-2}] \quad (2.6)$$

One-tenth of this value is `min_delta` like PPP and PP cases. In addition, we set a selection threshold to the output of the Dendrogram for PPV data to identify spatial and velocity coherent structures as cores. The threshold is that at least three consecutive channels have more than 4 pixels in each channel. This threshold eliminates leaves with a too-small projected area or a narrow velocity width to be classified as a real core.

In this section, we call the above parameters fiducial values for PPP, PP, and PPV data. In addition, we also conducted a dense core survey with various `min_delta` to check its dependence on the core properties, especially CMF properties, since

the fineness of identification is considered to have a significant influence on the resultant core properties and CMFs. When we use Dendrogram to identify compact structures such as dense cores, min_npix is usually set to \sim map resolution except for the case that map resolution is much smaller than the typical size of the target structure. What the least one parameter min_value define is volume density (PPP data), column density (PP and PPV case), or observed flux (actual observations) of *trunks*, and it seems not to affect the properties *leaves*. We summarize the input parameters for PPP, PP, and PPV data in Tables 2.1, 2.2, and 2.3, respectively.

Table 2.1: The Input Parameters of Dendrogram for PPP data

Case No.	min_value	min_delta		min_npix pc ³
	cm ⁻³	cm ⁻³	(min_delta) _{fiducial}	
1	10 ⁴	2 × 10 ³	2	4π/3 × (0.13/2) ³
2 (fiducial)	10 ⁴	10 ³	1	0.13
3	10 ⁴	4 × 10 ²	0.4	0.13
4	10 ⁴	2 × 10 ²	0.2	0.13
5	10 ⁴	1.3 × 10 ²	0.13	0.13
6	10 ⁴	10 ²	0.1	0.13

Table 2.2: The Input Parameters of Dendrogram for PP data

Case No.	min_value	min_delta		min_npix pc ²
	cm ⁻²	cm ⁻²	(min_delta) _{fiducial}	
1	10 ²²	2 × 10 ²¹	2	π(0.13/2) ²
2 (fiducial)	10 ²²	10 ²¹	1	π(0.13/2) ²
3	10 ²²	4 × 10 ²⁰	0.4	π(0.13/2) ²
4	10 ²²	2 × 10 ²⁰	0.2	π(0.13/2) ²
5	10 ²²	1.3 × 10 ²⁰	0.13	π(0.13/2) ²
6	10 ²²	10 ²⁰	0.1	π(0.13/2) ²

Table 2.3: The Input Parameters of Dendrogram for PPV data

Case No.	min_value	min_delta		min_npix
	cm ⁻²	cm ⁻²	(min_delta) _{fiducial}	cm ⁻² km s ⁻¹
1	1.67 × 10 ²¹	3.34 × 10 ²⁰	2	4π/3 × (0.13/2) ² (0.21/2)
2 (fiducial)	1.67 × 10 ²¹	1.67 × 10 ²⁰	1	4π/3 × (0.13/2) ² (0.21/2)
3	1.67 × 10 ²¹	6.67 × 10 ¹⁹	0.4	4π/3 × (0.13/2) ² (0.21/2)
4	1.67 × 10 ²¹	3.34 × 10 ¹⁹	0.2	4π/3 × (0.13/2) ² (0.21/2)
5	1.67 × 10 ²¹	2.22 × 10 ¹⁹	0.13	4π/3 × (0.13/2) ² (0.21/2)
6	1.67 × 10 ²¹	1.67 × 10 ¹⁹	0.1	4π/3 × (0.13/2) ² (0.21/2)

2.4 Dense Core Survey and Construction of CMFs - PPP data -

We show the number of identified cores in Table 2.4 and the spatial distribution of cores for fiducial parameters case (case 2) in Figure 2.1. The cores are plotted onto the column density map, and each panel corresponds to the different projection directions to calculate column density. Then, a fiducial case's minimum, maximum, mean, and standard deviation of core physical properties such as the diameter, mass, density, and temperature are summarized in Table 2.5. We calculated a core diameter $2R_{\text{core}}$ from its projected area A_{core} to the plane perpendicular to z axis as Equation 2.7. The core area is one of the outputs of the Dendrogram.

$$2R_{\text{core}} = \left(\frac{A_{\text{core}}}{\pi} \right)^{1/2} \quad (2.7)$$

Figure 2.2 and Table 2.6 show the derived CMFs and their properties, such as peak mass and power-law indices at the high-mass ends. The number of mass

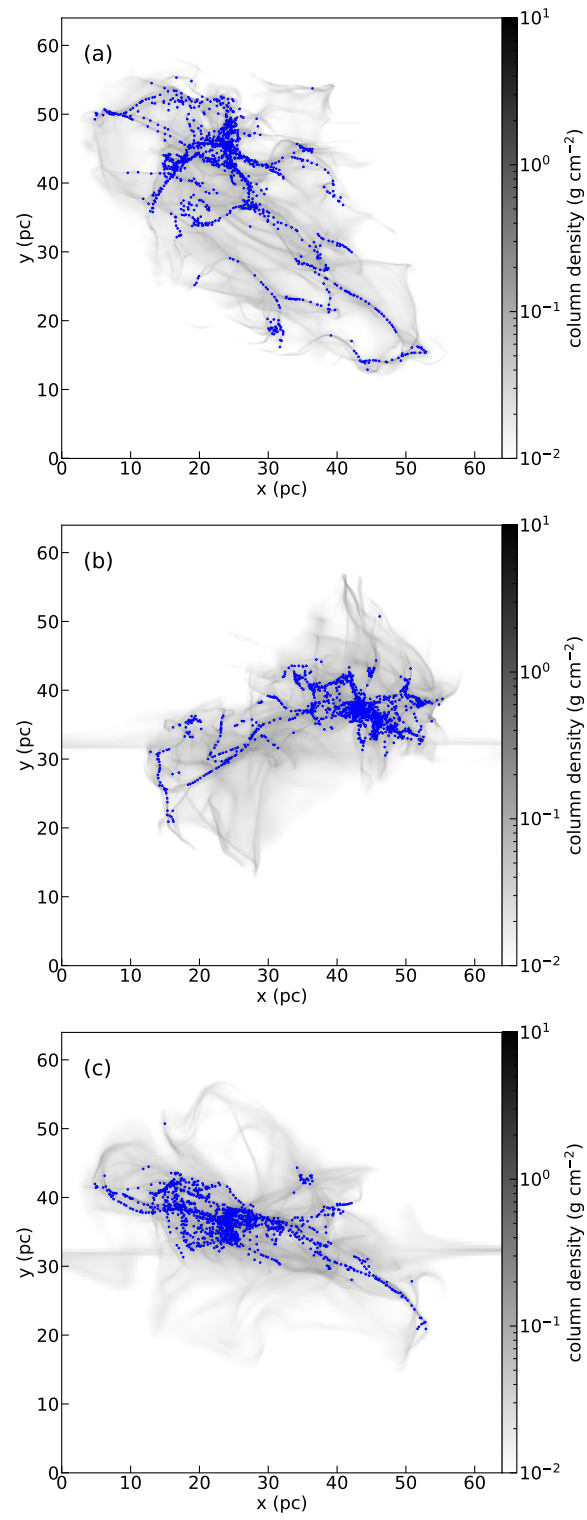


Figure 2.1: The identified cores are potted onto the column density map in xy plane (panel (a)), yz plane (panel (b)), and zx plane (panel (c)).

Table 2.4: The Results of Dense Core Survey with PPP Data

Case No.	Number of Identified Cores
1	1197
2 (fiducial)	1182
3	1188
4	1364
5	1188
6	1229

Table 2.5: The Results of Dense Core Survey with PPP Data

Core property		minimum	maximum	mean \pm std.
$2R_{\text{core}}$ (pc)	xy plane	0.08	0.7	0.21 ± 0.09
	yz plane	0.06	0.69	0.2 ± 0.08
	zx plane	0.07	0.83	0.22 ± 0.09
Mass (M_{\odot})		0.62	1413.66	19.93 ± 60.74
Number density (10^{-19} g cm $^{-3}$)		0.49	188.86	5.07 ± 11.32
Temperature (K)		7.84	46.26	15.42 ± 4.01

bins and error bar of each mass bin is set to the square root of the number of total identified cores and cores in each mass bin and calculated as $\sim \sqrt{N_{\text{core}}}$ and $\sim \sqrt{N_{\text{core, bin}}}$. Then, we estimate the mass detection limit as the smallest core mass that can be identified as a leaf with the Dendrogram. It is a core mass with a diameter and a density of 0.13 pc and 1.1×10^4 cm $^{-3}$ (min_value + min_delta) for the fiducial parameter case. When we conduct a dense core survey with fiducial input of Dendrogram parameters, CMF has a turnover at $1.31 M_{\odot}$ and a power-law index of -1.87 ± 0.06 . Even if we conduct a dense core survey with finer values of min_delta, such as case No.6, turnover masses are similar to the fiducial case (case No.2). We suppose that we can achieve a turnover mass of our simulation data. However, the future numerical simulation with higher resolution will identify

a proper turnover of an actual CMF, but it is out of the scope of this study, and we will not go into detail. We treat this CMF as a "true CMF" of the simulated molecular cloud and compare it with CMFs from PP and PPV data in Section 2.5 and 2.6.

Table 2.6: The CMF Properties with PPP Data

Case No.	Turnover Mass M_{\odot}	$\alpha \pm \sigma_{\alpha}$
1	1.71	-1.92 ± 0.06
2 (fiducial)	1.31	-1.87 ± 0.06
3	1.32	-1.87 ± 0.06
4	1.27	-1.92 ± 0.06
5	1.32	-1.87 ± 0.06
6	1.29	-1.91 ± 0.05

We also show the PPP CMFs with variably sized bins for all Dendrogram's parameter cases in Figure 2.3. Their properties are presented in Table 2.7. Although the binning method less affects the turnover masses, the slopes above the turnovers become shallower when we use variably sized bins. Since the trend when we change the Dendrogram's parameter does not change among CMFs with each binning method, we should unify the binning method. We note that most observed IMFs are derived with uniform sized bins (see Section 1.3.1).

2.4.1 Overlap Effect

Next, we investigate the overlap effect using the PPP data since dense cores and other dense structures, such as filaments, are spread out in three-dimensional space. With parameter case No.2, 48%, 60%, 65% of cores overlap each other along x , y ,

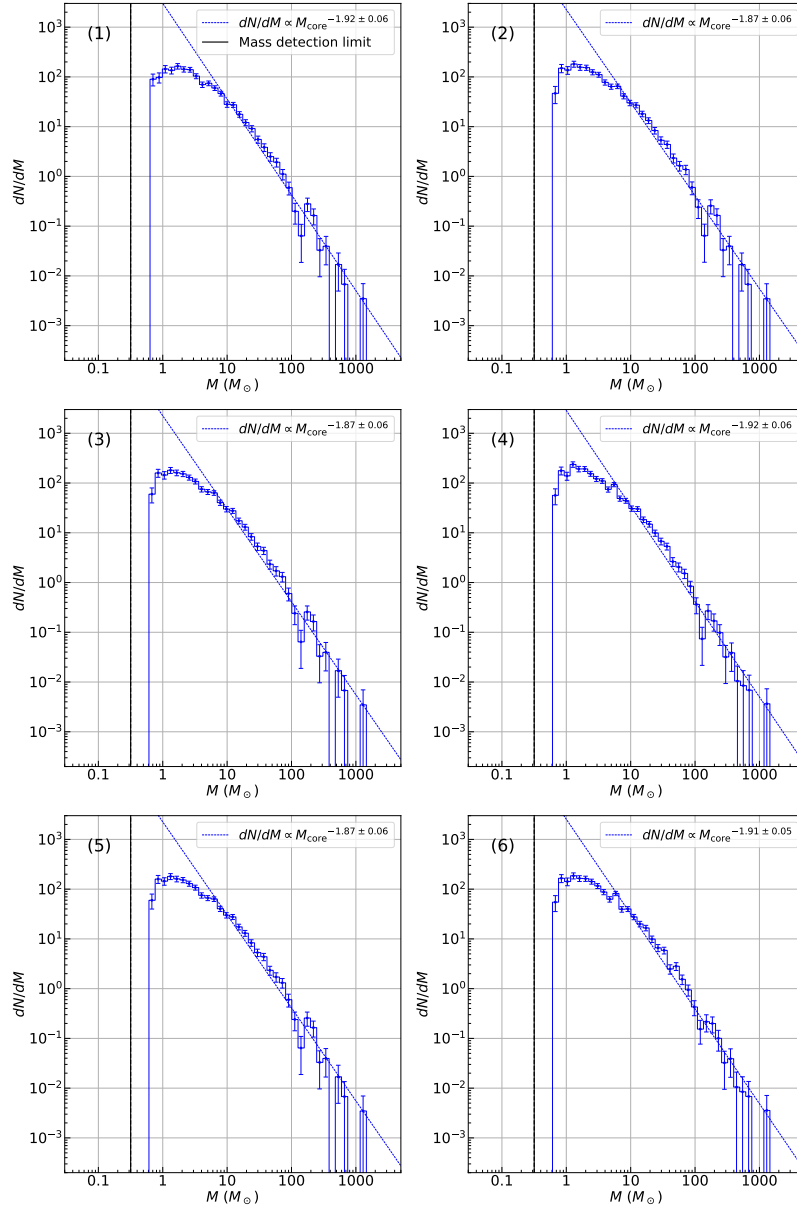


Figure 2.2: The PPP CMFs for all parameter cases. Each panel represents each Dendrogram’s parameter in Table 2.1, and the case numbers are shown at the top left corners. The error bars show the statistical uncertainty calculated as the square root of the number of cores in each mass bin, $\sqrt{N_{\text{core}}}$. The dashed line shows the best-fit single power-law functions for each CMF between five mass bins above the turnover and the high-mass end.

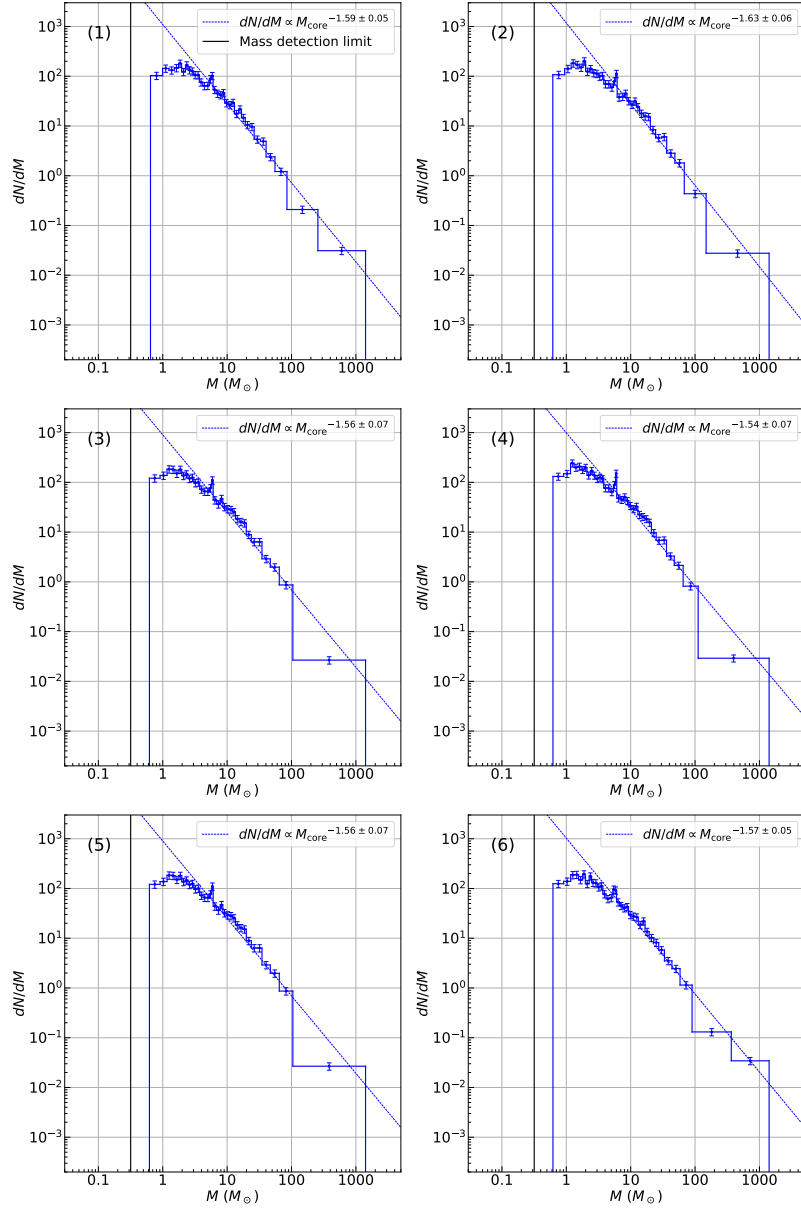


Figure 2.3: The same as Figure 2.2 but CMF with variably sized bins.

Table 2.7: The CMF Properties of Variably Sized Bins with PPP Data

Case No.	Turnover Mass M_{\odot}	$\alpha \pm \sigma_{\alpha}$
1	1.86	-1.59 ± 0.05
2 (fiducial)	1.9	-1.63 ± 0.06
3	1.26	-1.56 ± 0.07
4	1.24	-1.54 ± 0.07
5	1.26	-1.56 ± 0.07
6	1.88	-1.57 ± 0.05

and z axes respectively. Here, if the distance between the centers of two cores in the projected plane is smaller than the sum of the radii of two cores, we think these two cores overlap. The overlap effect seems to be more severe in PP data than in PPV data as long as enough velocity resolution is achieved. Only the densest and most massive core will be observable when several cores overlap along the line of sight. Even if cores do not overlap, a core and density fluctuation of denser structures may be mixed up if a core overlaps with denser structures. In both cases, low-mass cores are thought to be more influenced than high-mass cores, and this effect will change the turnover mass and slopes. Figure 2.4 shows the density profiles at peaks of cores along the z axis. The core peaks are fixed at 0 of the horizontal axis in each panel. The density profiles of cores that do and do not locate the peaks of the profiles in Figure 2.4. In the figure, we show the density profiles of three cores from each of the two groups: there are one or denser structures along the line of sight (panels (a), (c), and (e)), and the core is a peak of density profile along line of sight (panels (b), (d), and (f)). In Figure 2.5, we present the R_z -mass relation (panel (a)) and the $R_{z,2nd}$ -mass relation (panel (b)). Here R_z is the

normalized peak density along the z axis with a core peak density, and $R_{z,2nd}$ is the normalized density of a second peak along z axis with a core peak density. Only relatively low-mass cores (94 cores) have R values larger than unity, which means they have other density peaks along z axis, and they will not be observed in column density map (Figure 2.5 (a)). In addition, higher-mass cores tend to have smaller $R_{z,2nd}$ as Figure 2.5 (b), and they seem less affected by the overlap effect. We constructed CMFs with $R_{z,2nd}$ values as Figure 2.6: CMF with all identified cores, CMF of cores with $R_{z,2nd} < 0.8$, and CMF of cores with $R_{z,2nd} < 0.5$. The properties are shown in Table 2.8. When excluding cores with large peaks except for cores with large $R_{z,2nd}$, plateaus around turnovers appear. Since we exclude the five mass bins above the turnover to derive the best-fit function to exclude the plateaus, the power-law index does not so change. Then, this effect probably makes CMF slope shallower. When the overlap effect is severe, like PP data, CMF is expected to be shallower than PPP CMF.

Table 2.8: The CMF Properties with PPP Data and $R_{z,2nd}$ Values

Category	Number of Cores	Turnover Mass M_{\odot}	$\alpha \pm \sigma_{\alpha}$
All cores	1182	1.31	-1.87 ± 0.06
$R_{z,2nd} < 0.8$	619	2.45	-1.99 ± 0.08
$R_{z,2nd} < 0.5$	267	1.89	-1.97 ± 0.09

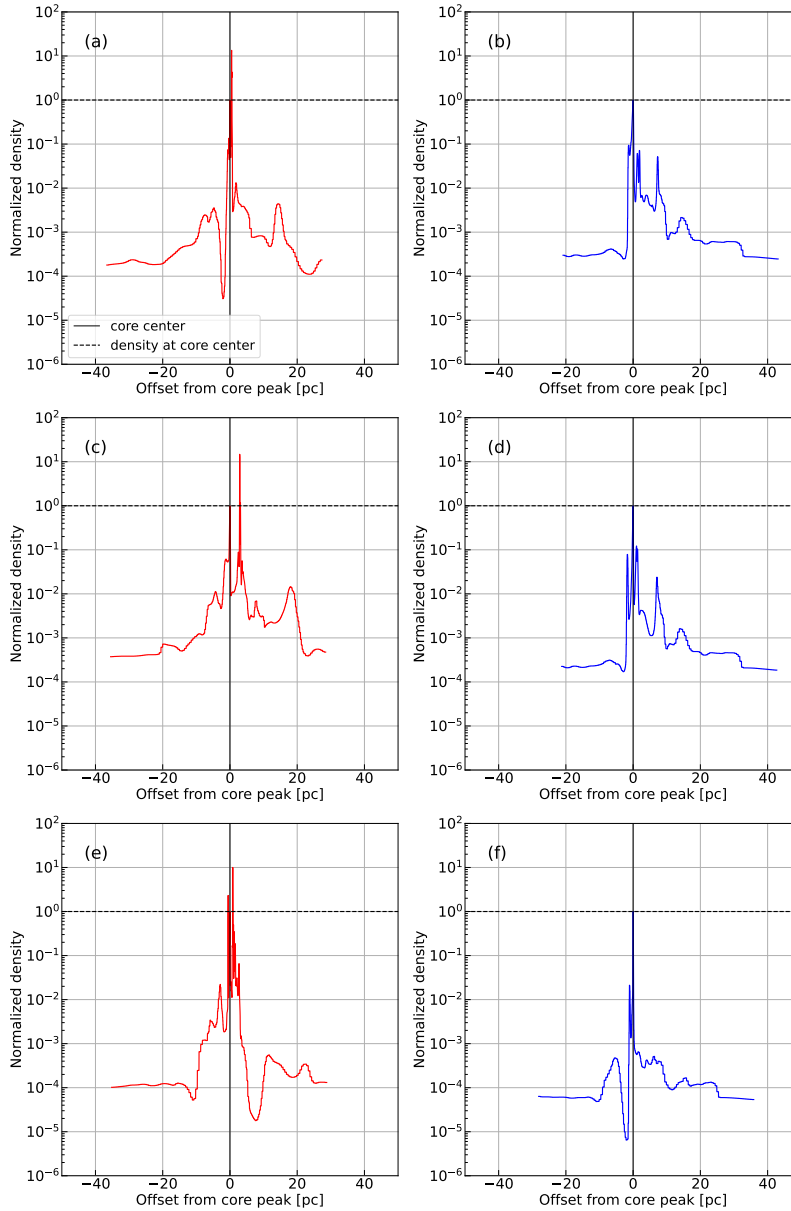


Figure 2.4: The normalized density profiles with the core peak density at core peaks along z axis for six selected cores. (a), (c), and (e) The profiles of cores that have other peaks along the line of sight. (b), (d), and (f) The profiles of cores that locate the density peaks along the line of sight. The positions of cores are fixed to zero on the vertical axis, and the vertical axis is offset from the core.

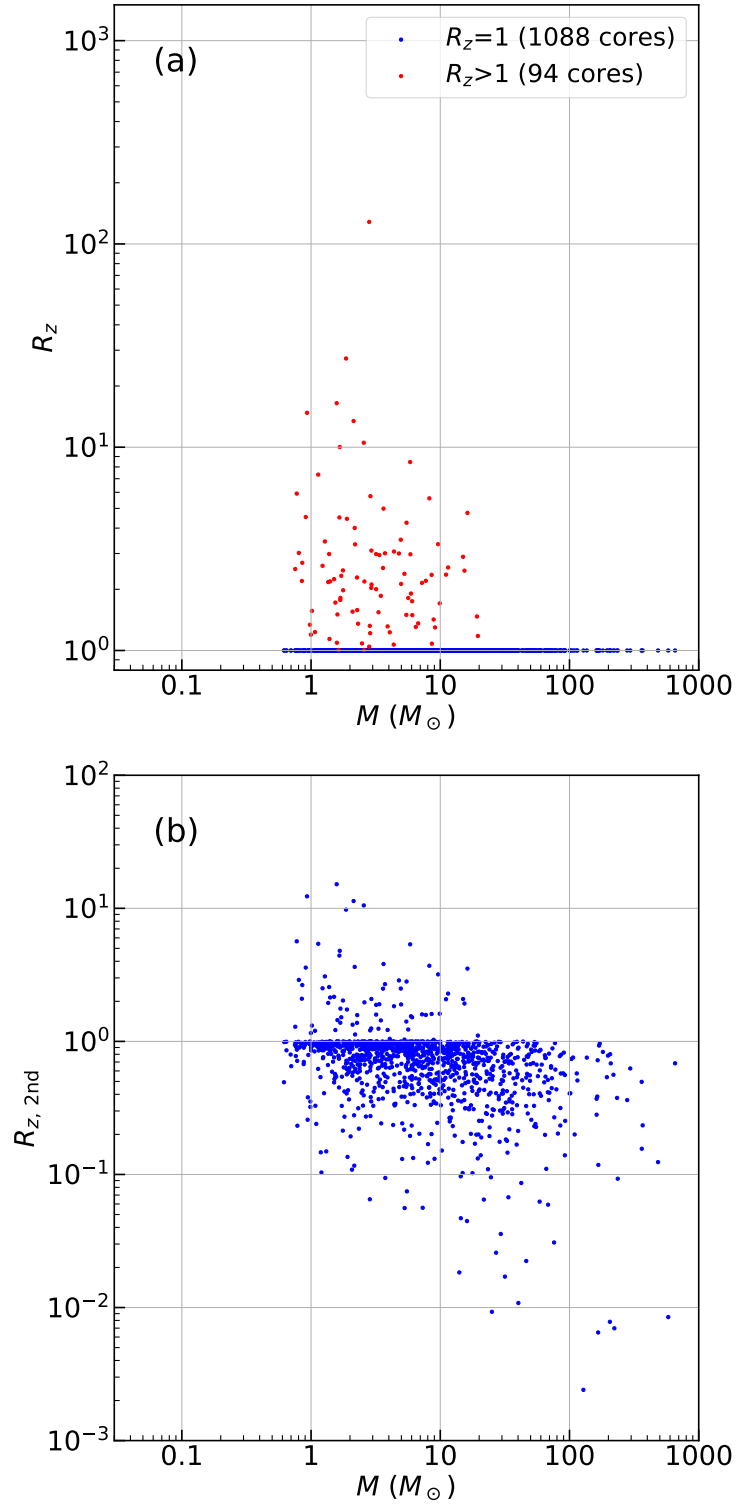


Figure 2.5: (a) The relationship between R_z and core mass. Out of 1182 identified cores, R_z values of 94 cores are larger than unity. (b) The relationship between $R_{z,2nd}$ and core mass.

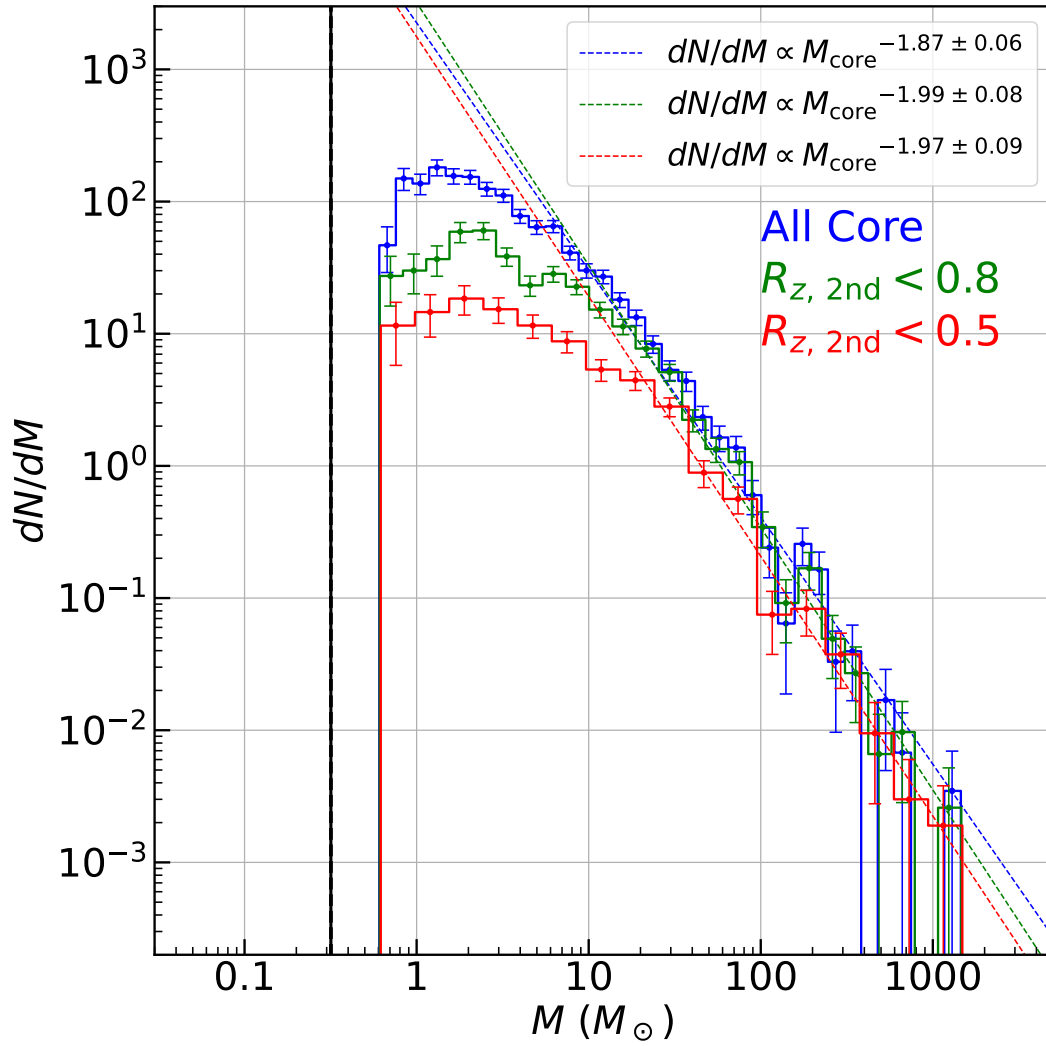


Figure 2.6: The CMFs for various $R_{z,2\text{nd}}$ values: all $R_{z,2\text{nd}}$ (blue), $R_{z,2\text{nd}} < 0.8$ (green), $R_{z,2\text{nd}} < 0.5$ (red).

2.5 Dense Core Survey and Construction of CMFs - PP data -

As mentioned, we discuss the core physical properties and CMFs based on the analysis with the column density map in the xy plane in the main text. Then, we show the result of the analyses of PP data projected onto yz and zx planes in Appendix A.1.1.

The number of cores with each Dendrogram's input parameter (see Table 2.2) is shown in Table 2.9, and it becomes smaller than the PPP case. We note that we cannot make one Dendrogram's parameter set for PP data correspond with that for PPP data. We need to conduct a dense core survey with various parameter sets to investigate the similarities and differences between PPP and PP data. We should take this into account when we use PPV data as well. In the fiducial case, we identified 826 cores, and we plot them in Figure 2.7. Most cores distribute along filamentary structures, and this trend is seen in the projected images of PPP data in Figure 2.1.

Table 2.9: The Results of Dense Core Survey with PP Data (xy Plane)

Case No.	Number of Identified Cores
1	730
2 (fiducial)	826
3	900
4	927
5	942
6	942

We calculate the core masses from PP data as a sum of the column density of

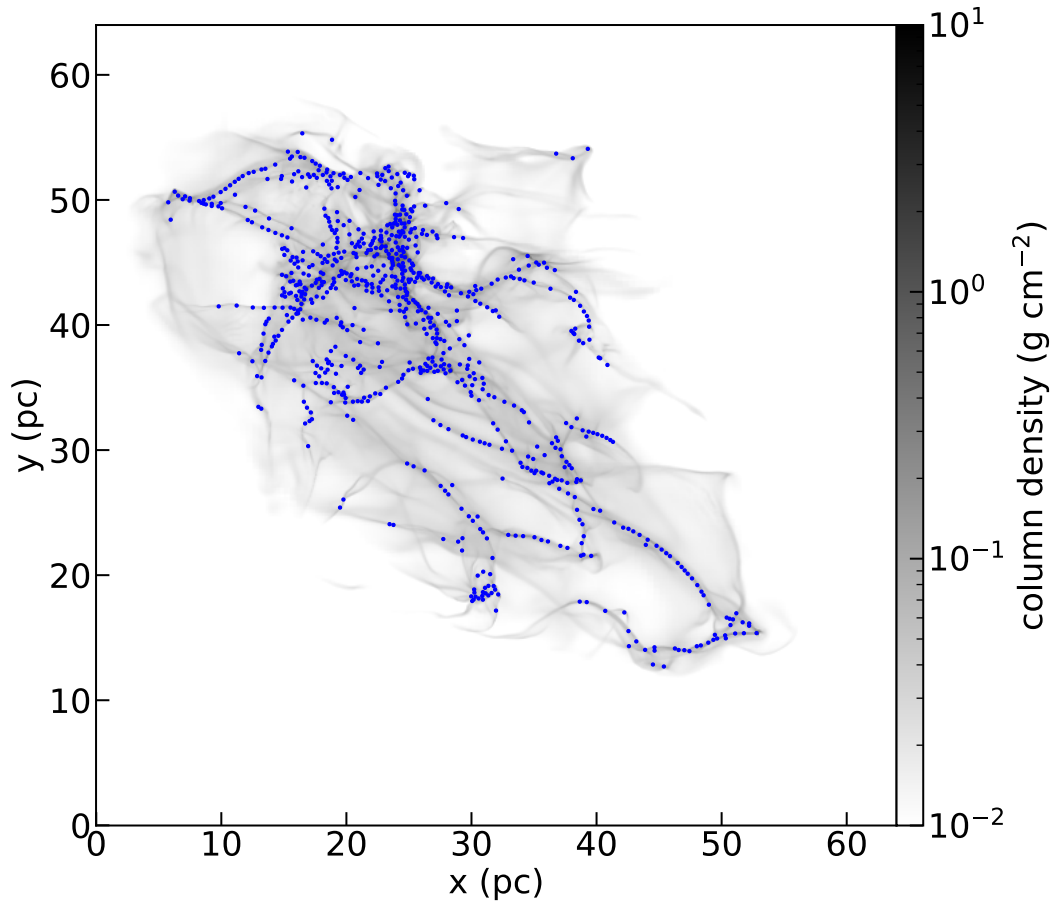


Figure 2.7: The identified cores with xy PP data are potted onto the column density map in xy plane.

identified leaves. Since cores are deeply embedded into the cloud, we conduct background subtraction to extract the column density of a core from the column density of the cloud, which is calculated with Equation 2.1. We call the column density of the cloud in front of and behind the core as background column density. To do background subtraction, we use Dendrogram's hierarchy as follows.

1. Search a branch one level below the focusing leaf (core). Here, the branch includes two substructures, and one is the core.
2. Calculate the mean column density of the branch excluding the two substructures as a background column density and the mass in the area of the core using the column density as a background mass.
3. Subtract the background mass from the core mass as a background subtracted core mass.

If a core is identified as an isolated leaf and does not have a structure at the lower level, we used the mean column density of one pixel around the core as a background column density. We show the minimum, maximum, mean, and standard deviation of core properties of a fiducial parameter, including core mass with and without subtraction, in Table 2.10.

Table 2.10: The Summary of Core Properties Identified with PP Data (xy Plane)

Core property	minimum	maximum	mean \pm std.
$2R_{\text{core}}$ (pc)	0.12	0.93	0.2 ± 0.09
M_{core} (M_{\odot})	2.84	1426.24	41.32 ± 83.81
$M_{\text{core,sub}}$ (M_{\odot})	0.13	1310.45	20.65 ± 68.15
$N_{\text{core,mean}}$ (g cm^{-2})	0.05	11.73	0.28 ± 0.58
$N_{\text{core,peak}}$ (g cm^{-2})	0.05	157.57	1.2 ± 6.2

We constructed CMFs for all parameter cases as Figure 2.8 summarize their

properties in Table 2.11. When we compare the CMFs with and without subtraction, turnover masses and power-law indices at high-mass ends differ for each parameter case. For turnover masses, a power-law-like shape continues to the lower-mass regime in CMF with subtraction compared to CMF without subtraction. This is natural since we subtract the mass of the column density of material outside the core along the line of sight. We note that, however, the power-law-like shape continues to be near the mass detection limit estimated in the PPP case (Section 2.4), and we cannot judge whether this turnover mass is real or artificial with our data. Some CMFs with subtraction have plateaus at low-mass ends, and these are thought to be artificially created with low completeness because these are also close to the mass detection limit. Then, the power-law indices of CMF with subtraction become shallower with background subtraction. This seems to be because lower-mass cores are more affected by background mass than higher-mass cores, and background makes CMF steeper. Compared to PPP CMF in Figure 2.8, which is the true CMF of the simulated cloud, PP CMFs with subtraction have shallower, and PP CMFs without subtraction have steeper slopes, respectively. Although we cannot reproduce the true CMF from PP CMF even if we conduct background subtraction, the slope of PP CMF with subtraction becomes shallower as we expected in Section 2.4. Therefore background subtraction and compensation of completeness would be a way to obtain true CMF from PP accurate column density data. Besides background subtraction, convolution with some function, such as gaussian, might also work to derive actual core masses from PP data.

The PP CMFs with variably sized bins and their properties are shown in Figure

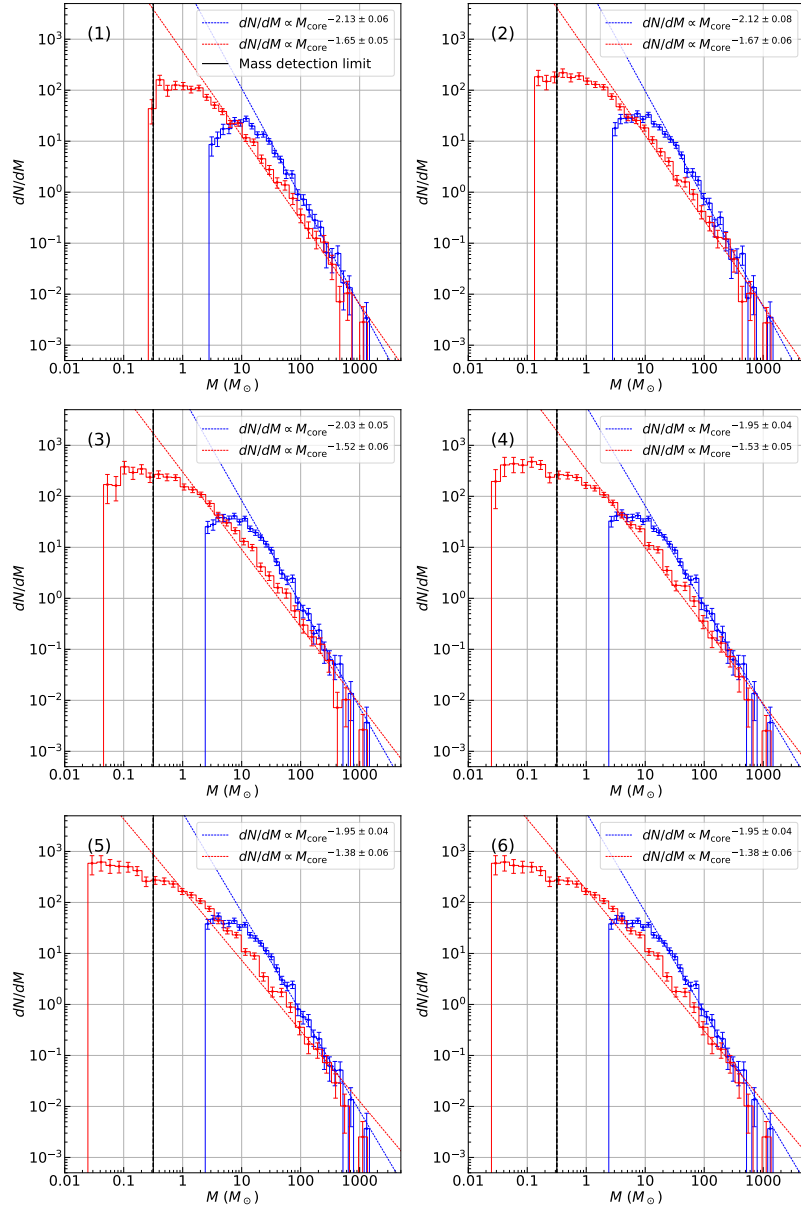


Figure 2.8: The PP CMFs for all parameter cases in xy plane. Each panel represents each Dendrogram's parameter in Table 2.2, and the case numbers are shown at the top left corners as Figure 2.2. The details are the same as Figure 2.2.

Table 2.11: The CMF Properties with PP Data in xy Plane

Case No.	Category	Turnover Mass M_{\odot}	$\alpha \pm \sigma_{\alpha}$
1	w/o subtraction	11.9	-2.13 ± 0.06
	w/ subtraction	0.41	-1.65 ± 0.05
2	w/o subtraction	7.34	-2.12 ± 0.08
	w/ subtraction	0.4	-1.67 ± 0.06
3	w/o subtraction	7.48	-2.03 ± 0.05
	w/ subtraction	0.1	-1.52 ± 0.06
4	w/o subtraction	4.02	-1.95 ± 0.04
	w/ subtraction	0.12	-1.53 ± 0.05
5	w/o subtraction	4.02	-1.95 ± 0.04
	w/ subtraction	0.04	-1.38 ± 0.06
6	w/o subtraction	4.02	-1.95 ± 0.04
	w/ subtraction	0.04	-1.38 ± 0.06

2.9 and Table 2.12. The overall trend is the same as the analysis of PPP data in Section 2.4.

In continuum observations of molecular clouds, we convert continuum flux F_{ν} to core or cloud mass M using Equation 2.8 when the observing frequency or wavelength is optically thin.

$$M = \mathbb{R} \frac{F_{\nu} D^2}{\kappa_{\nu} B(T_{\text{dust}})} \quad (2.8)$$

where \mathbb{R} , D , κ_{ν} , and $B(T_{\text{dust}})$ are the gas-to-dust mass ratio, the source distance, the dust opacity per gram of dust, and the Planck function at dust temperature T_{dust} , respectively. We can easily convert the mass to column density with mean molecular weight and spatial scale. The accurate value at each position in the cloud is required to calculate the accurate column density and apply the above

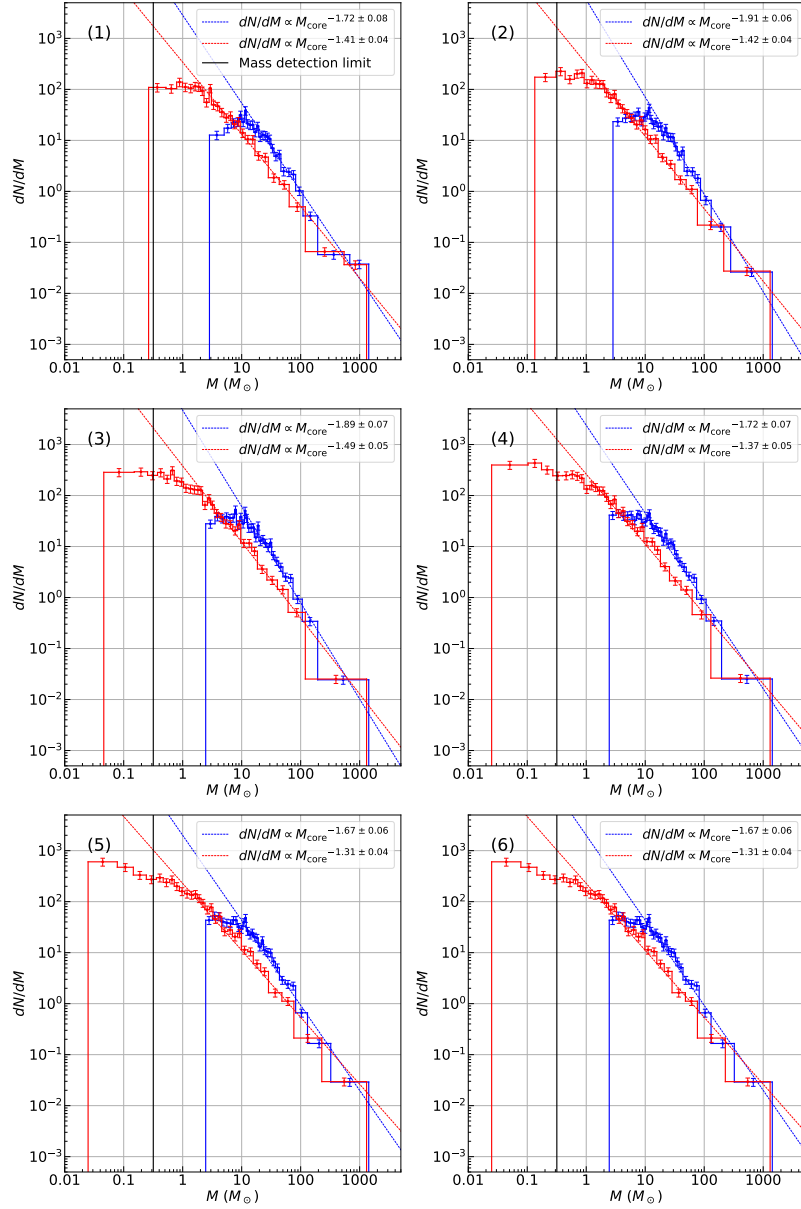


Figure 2.9: The same as Figure 2.8 but CMF with variably sized bins.

Table 2.12: The CMF Properties of Variably Sized Bins with PP Data in xy Plane

Case No.	Category	Turnover Mass M_{\odot}	$\alpha \pm \sigma_{\alpha}$
1	w/o subtraction	11.6	-1.72 ± 0.08
	w/ subtraction	0.89	-1.41 ± 0.04
2 (fiducial)	w/o subtraction	11.66	-1.91 ± 0.06
	w/ subtraction	0.37	-1.42 ± 0.04
3	w/o subtraction	7.86	-1.89 ± 0.07
	w/ subtraction	0.67	-1.49 ± 0.05
4	w/o subtraction	3.53	-1.72 ± 0.07
	w/ subtraction	0.13	-1.37 ± 0.05
5	w/o subtraction	3.49	-1.67 ± 0.06
	w/ subtraction	0.04	-1.31 ± 0.04
6	w/o subtraction	3.49	-1.67 ± 0.06
	w/ subtraction	0.04	-1.31 ± 0.04

discussion in this section. Despite that, \mathbb{R} is set to 100, and κ_{ν} is calculated from the relation between the dust opacity and observing frequency of [Ossenkopf and Henning \(1994\)](#) in many observations. Besides, the mean temperature of a parental cloud derived from the results of a prior clump survey or the typical temperature of a dense core is used in the calculation. It is necessary to evaluate the effect arises from the assumption that a cloud has uniform \mathbb{R} , κ_{ν} , and T_{dust} on the CMF properties to compare our simulated CMF and other observational CMFs. To do so, we estimated the continuum flux of the simulated cloud. We derived column density with Equation 2.8 and CMF to reproduce the situation of actual continuum observation as much as we can in Section 2.5.1.

2.5.1 CMFs with Simulated Radio Flux and Constant Temperature

In this section, we investigate the influence on CMF properties when we apply the constant temperature to calculate core mass using 2.8 in continuum observation. It is not easy to obtain the temperature of distant star-forming regions with high-spatial resolutions of a core scale. In the actual observations, the observed clump temperature is often applied to all identified cores to derive core masses and construct CMFs (e.g., Sanhueza et al. 2019). Guzmán et al. (2015) provides dust column densities and dust temperatures for about 3000 young and high-mass molecular clumps. They are obtained from two infrared surveys with wavelengths of between $160 \mu\text{m}$ and $870 \mu\text{m}$: Herschel Infrared Galactic Plane Survey (Hi-Gal) and APEX Telescope Large Area Survey of the Galaxy (ATLASGAL) surveys. The average temperatures of clumps without mid-infrared detection, clumps with mid-infrared detection, clumps with H II region, and clumps with photo-dissociation regions are $16.8 \pm 0.2 \text{ K}$, $18.6 \pm 0.2 \text{ K}$, 23.7 ± 0.2 , and $28.1 \pm 0.3 \text{ K}$, respectively. Then, we set 20 K as a typical clump temperature to derive core masses in this study.

Since the CMF properties do not differ significantly from the three projection directions, we use PP data projected onto the xy plane. Then, we compare the results of the dense core survey with true PP data in Section 2.5 and PP data with a constant temperature. The procedure of analysis is as follows.

1. Calculate the 224 GHz ($\sim 1.34 \text{ mm}$) continuum flux as a function of source

distance and the dust opacity by solving Equation 2.8 about $F_{224 \text{ GHz}}$. Here we assumed that the 224 GHz continuum is optically thin.

2. Derive the column density map using Equation 2.8 with the continuum flux and uniform temperature of 20 K.
3. Conduct the dense core survey with Dendrogram and construct CMFs. The input parameters of the Dendrogram are the same as Section 2.5.

Then, the column density with a uniform temperature of 20 K is calculated with the simulated column density as Equation 2.9

$$N_{\text{H}_2, 20 \text{ K}} = \frac{B_{224 \text{ GHz}}(20 \text{ K})}{B_{224 \text{ GHz}}(T_{\text{simulation}})} \times N_{\text{H}_2, \text{simulation}} \quad (2.9)$$

where $T_{\text{simulation}}$ and $N_{\text{H}_2, \text{simulation}}$ are the true temperatures in the simulation and column density calculated with Equation 2.1.

The core properties and CMFs are shown in Table 2.13 and Figure 2.10, respectively. The cores tend to have a larger mass, and CMFs with background subtraction have steeper slopes in the uniform temperature case than in the true temperature case. This seems to be reasonable because the temperature in dense regions is usually lower than in less dense regions. On the other hand, the mean mass and mass functions without subtraction are similar to them with true column density data in Section 2.5. This implies that the temperature of the bulk of the cloud is $\sim 20 \text{ K}$ in our simulation, and the total column density of the cloud does not change significantly even if dense cores have a lower temperature than outside them. Inversely, we probably overestimate the column density of the background

when we use a lower temperature such as that of a typical core instead of 20 K. This will make a core mass small and CMF shallow compared to the results of a true PP image.

Table 2.13: The CMF Properties with PP Data with Uniform Temperature in xy Plane

Case No.	Category	Turnover Mass M_{\odot}	$\alpha \pm \sigma_{\alpha}$
1	w/o subtraction	6.04	-1.87 ± 0.13
	w/ subtraction	0.44	-1.62 ± 0.04
2	w/o subtraction	4.05	-1.85 ± 0.08
	w/ subtraction	0.42	-1.65 ± 0.06
3	w/o subtraction	4.92	-1.79 ± 0.06
	w/ subtraction	0.12	-1.59 ± 0.04
4	w/o subtraction	4.89	-1.79 ± 0.06
	w/ subtraction	0.12	-1.57 ± 0.03
5	w/o subtraction	4.89	-1.79 ± 0.06
	w/ subtraction	0.12	-1.57 ± 0.03
6	w/o subtraction	4.89	-1.79 ± 0.06
	w/ subtraction	0.18	-1.58 ± 0.03

As discussed above, temperature selection impacts the core and CMF properties. Therefore, we should compensate for the effect arising from temperature variation in addition to the completeness of core identification (see Section 2.5) to derive a true CMF in continuum observation. However, it is noted that both effects may strongly depend on the cloud environment, and we guess that there is no universal value of the compensations.

The top-heavy CMFs are reported in various high-mass star-forming regions with ALMA continuum observations as we presented in Section 1.3.3. However, it is unclear how severe the effects of overlapping among cores along the line of sight,

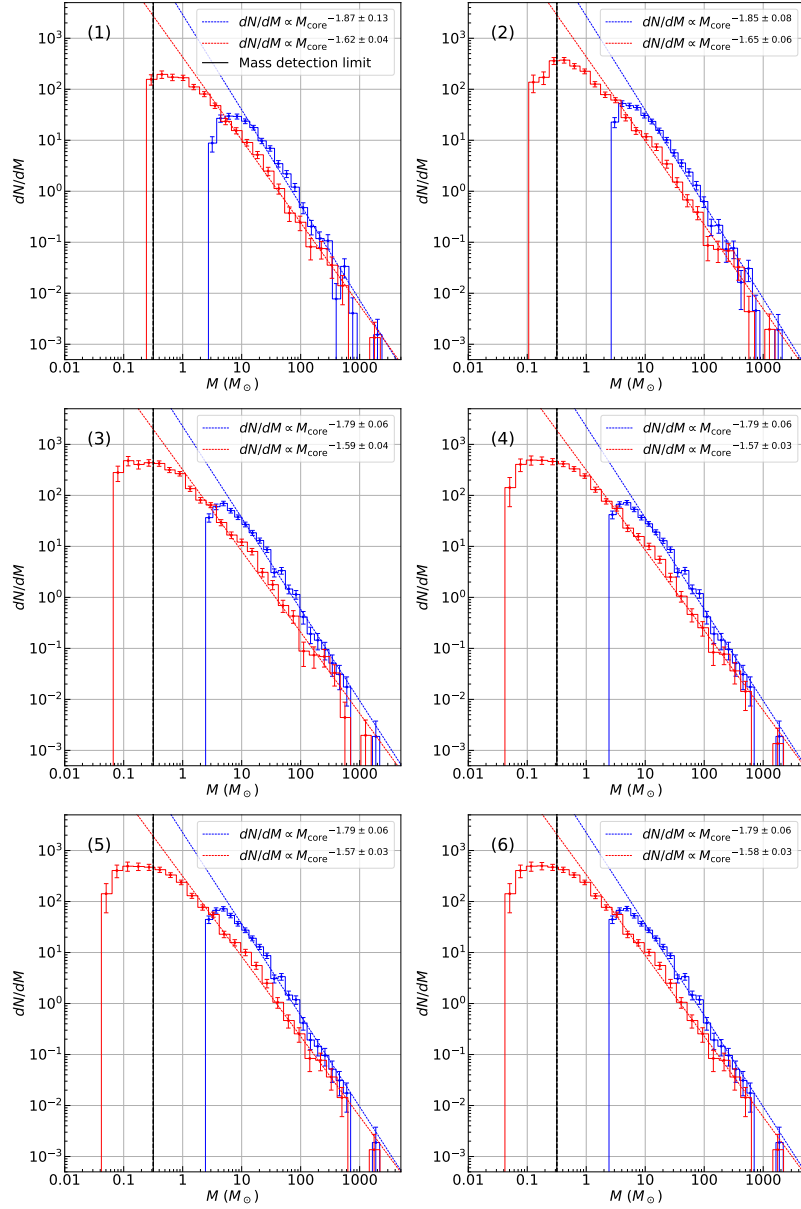


Figure 2.10: The PP CMFs for all parameter cases with uniform temperature in xy plane. Each panel represents each Dendrogram's parameter in Table 2.2, and the case numbers are shown at the top left corners as Figure 2.2.

background column density, field of view selection, and missing flux on the CMF properties are. In fact, how extended the core is varied, and several significantly extended cores seem to be missed in interferometer observations depending on the observation setup. Indeed, there is a possibility that top-heavy CMFs are real, and some physical processes make CMFs shallow. However, it is also possible that CMFs are affected by the above influences and appear to be top-heavy. We suggest that the compensation of CMFs with the effects should be conducted for careful comparison of CMFs in various regions and discussion on mapping from CMF to IMF.

2.5.2 CMFs with Various Distances from the Peak of Column Density

We have discussed the CMF properties with dense cores in the entire cloud. However, it is difficult to cover the whole cloud in actual observations, and only the central regions are often observed. If mass segregation occurs, i.e., massive cores are concentrated in the cloud center, CMF properties may be affected by the selection bias of the observing area. We investigate whether the selection bias influences the CMF properties with true PP data in the xy plane. We extract the cores within various distances from the peak of column density in xy plane as Figure 2.11 and constructed CMFs with them as Figure 2.12. The CMF properties without and with background subtraction are shown in Tables 2.14 and 2.15. Here, we derived best-fit functions with mass bins above three bins above turnovers instead of five

bins to do so with as many mass bins as we have. As the figures and tables show, the CMF becomes shallower when we construct CMF with cores closer to the peak of column density. The trend is more clearly seen in the background subtracted case. This may occur in real observations, and we should be careful in selecting the observation area; a shallower CMF than a cloud CMF can be observed if the field of view is limited to only the central region of the cloud.

Table 2.14: The CMF Properties for Cores in Various Distances from Column Density Peak without Subtraction

Category	Turnover Mass M_{\odot}	$\alpha \pm \sigma_{\alpha}$
Central 20%	12.71	-1.88 ± 0.12
Central 40%	12.96	-1.97 ± 0.1
Central 60%	7.2	-1.9 ± 0.08
Central 80%	10.45	-1.97 ± 0.05
All cores	7.34	-2.01 ± 0.07

Table 2.15: The CMF Properties for Cores in Various Distances from Column Density Peak with Subtraction

Category	Turnover Mass M_{\odot}	$\alpha \pm \sigma_{\alpha}$
Central 20%	0.25	-1.35 ± 0.09
Central 40%	0.34	-1.45 ± 0.07
Central 60%	0.3	-1.42 ± 0.06
Central 80%	0.16	-1.35 ± 0.06
All cores	0.4	-1.55 ± 0.06

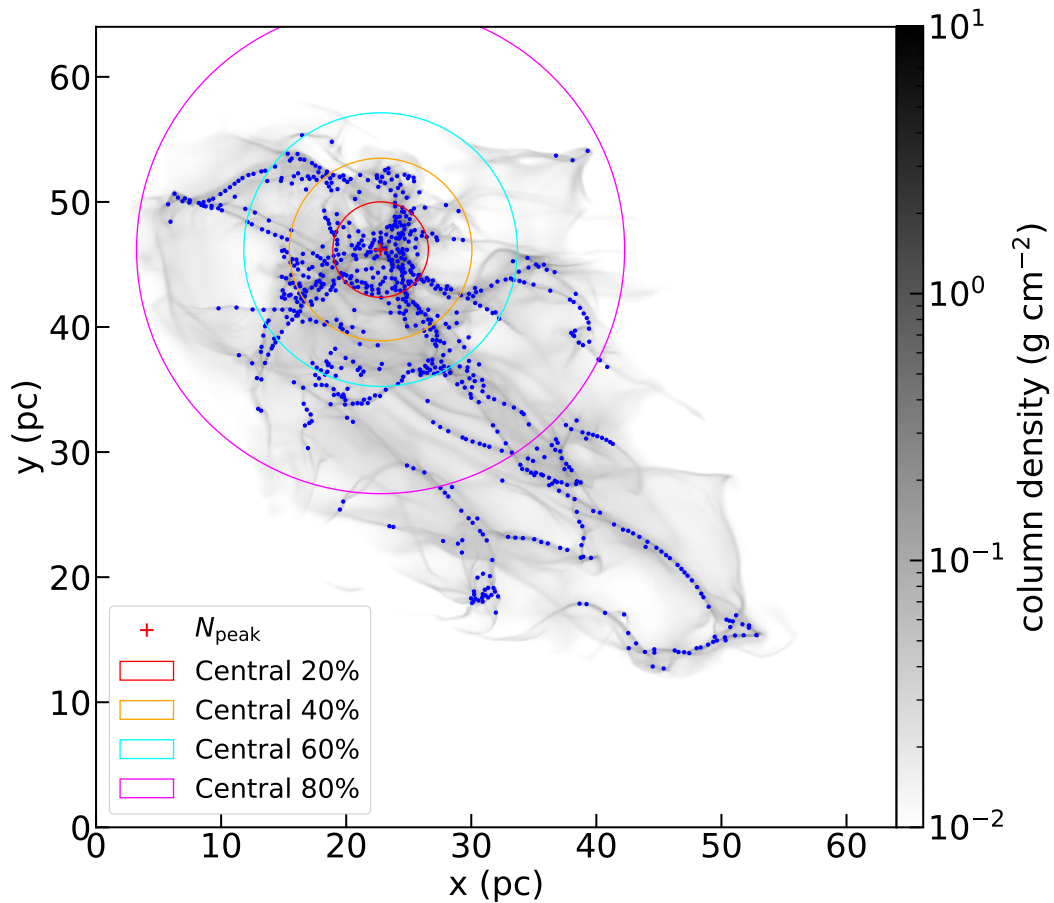


Figure 2.11: The distribution of identified cores with PP data in xy plane and concentric circles centers at the peak of column density, N_{peak} , (a red cross). The cores are the same as Figure 2.7. The red, orange, cyan, and magenta concentric circles represent the distance from the N_{peak} , which involve 20%, 40%, 60%, and 80% cores, respectively.

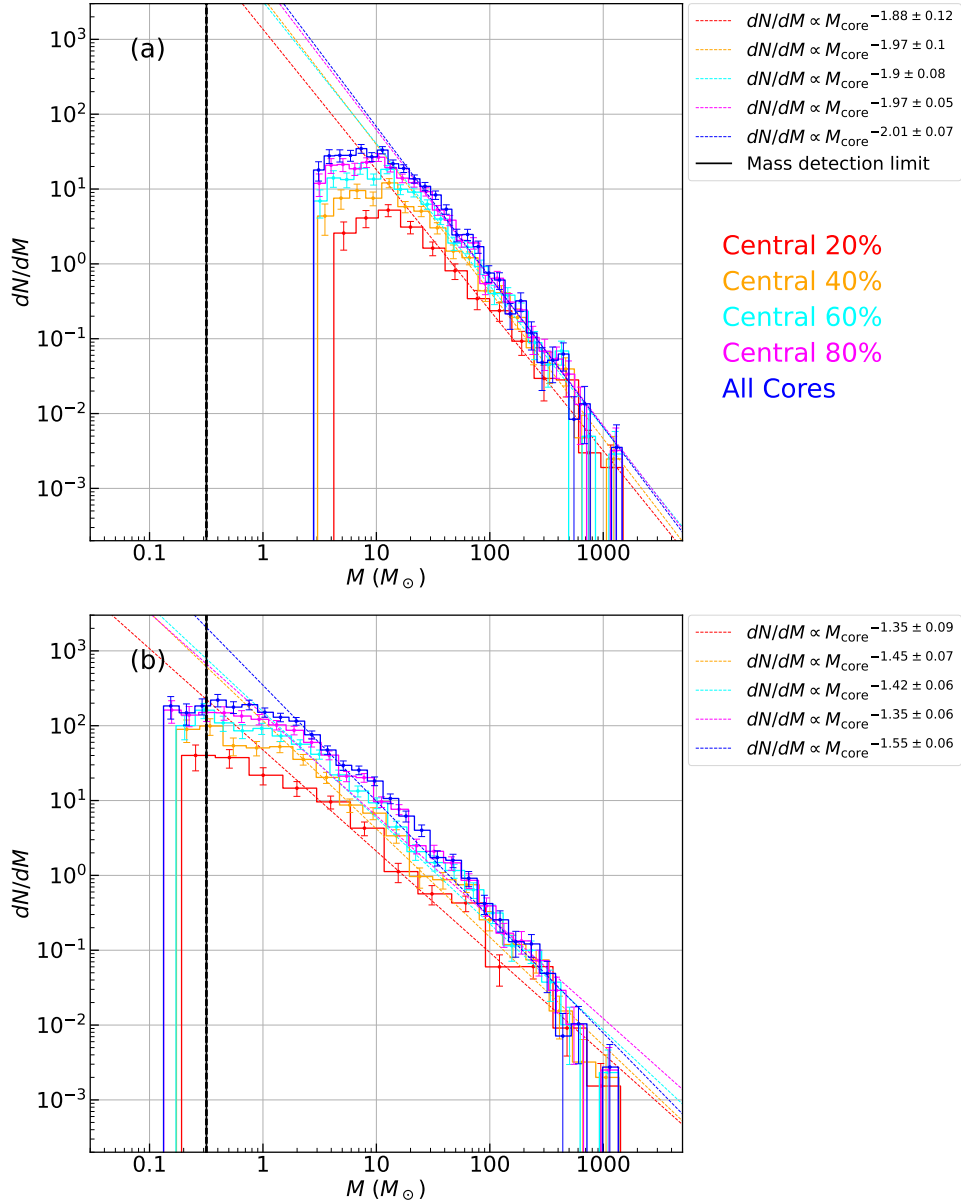


Figure 2.12: (a) The CMFs for cores in various distances from the column density peak without background subtraction. The blue CMF is the same as Figure 2.8 (b), and the other colored CMFs are the same as Figure 2.11. (b) The CMFs for cores with background subtraction.

2.6 Dense Core Survey and Construction of CMFs - PPV data -

As the analysis of PP data in Section 2.5, we focus on the PPV data in the xyv plane in the main text. Then, we show the result of the analyses of PPV data in yzv and zxv spaces in Appendix A.1.1. Because PPV data can resolve the structure along the line of sight with its velocity, the overlap effect discussed in Section 2.5 is expected to be less severe in PPV data than in PP data.

We identified 1698 cores with a fiducial parameter in Table 2.3 as shown in Table 2.16. Then, Table 2.17 presents the physical parameters of identified cores with fiducial parameter case (case 2). The CMFs with cores with all parameter sets are shown in Figure 2.13, and the CMF properties are listed in Table 2.18.

Table 2.16: The Results of Dense Core Survey with PPV Data (xyv Space)

Case No.	Number of Identified Cores
1	1074
2 (fiducial)	1075
3	1075
4	1086
5	1086
6	1086

Following the analysis of PPP and PP data, we show the CMFs with variably sized bins in Figure 2.9 for reference (see Table 2.12 for their properties). The PP CMFs with variably sized bins and their properties are shown in Figure 2.9 and Table 2.19. As described in Section 2.4, the effect on the CMF properties of changing parameters does not depend on the binning method. Then, we use PPV

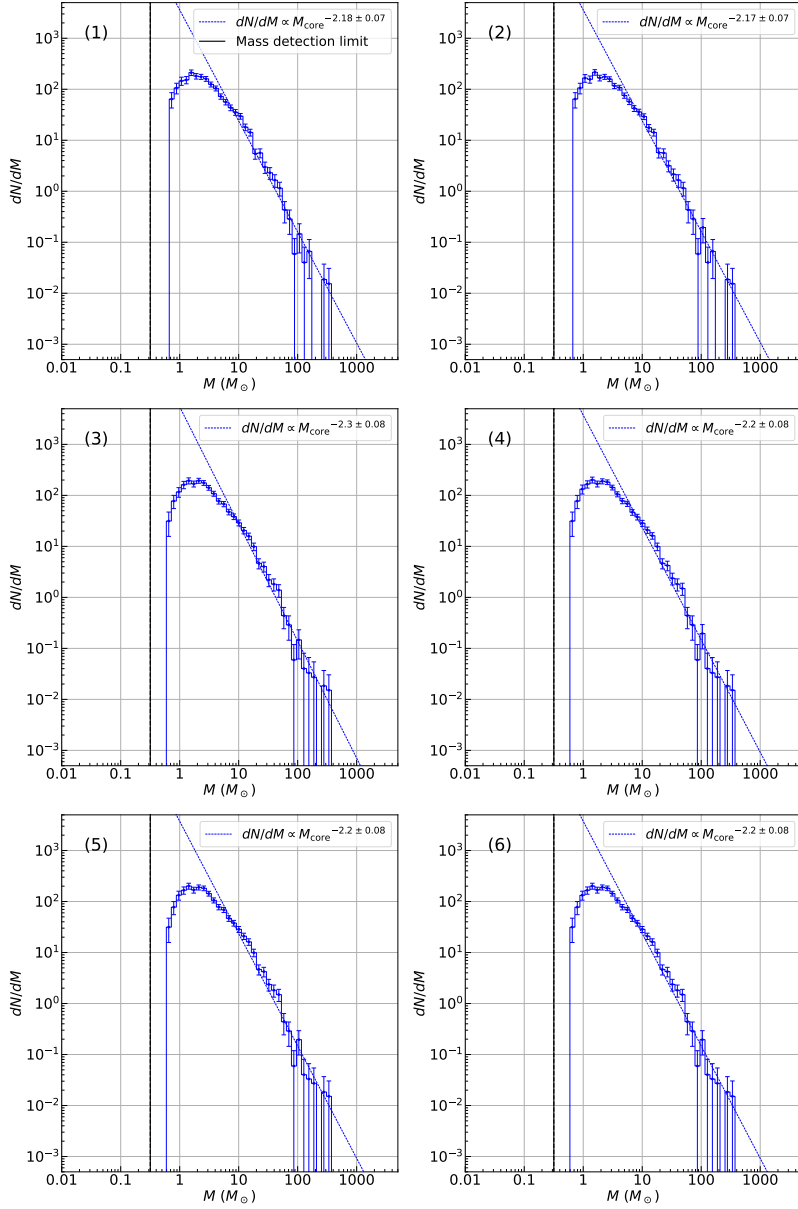


Figure 2.13: The PPV CMFs for all parameter cases in xyv space. Each panel represents each Dendrogram's parameter in Table 2.2, and the case numbers are shown at the top left corners as Figure 2.2.

Table 2.17: The Summary of Core Properties Identified with PPV Data (xyv space) Using Fiducial Parameter

Core property	minimum	maximum	mean \pm std.
$2R_{\text{core}}$ (pc)	0.07	0.47	0.16 ± 0.06
$\text{FWHM}_{\text{core}}$ (km s^{-1})	0.11	9.05	0.58 ± 0.64
M_{core} (M_{\odot})	0.68	364.17	9.45 ± 19.6
$n_{\text{core,mean}}$ ($10^{-19} \text{ g cm}^{-3}$)	0.16	474.47	6.59 ± 23.85

Table 2.18: The CMF Properties with PPV Data in xyv Space

Case No.	Turnover Mass M_{\odot}	$\alpha \pm \sigma_{\alpha}$
1	1.57	-2.18 ± 0.07
2 (fiducial)	1.57	-2.17 ± 0.07
3	2.11	-2.3 ± 0.08
4	1.42	-2.2 ± 0.08
5	1.42	-2.2 ± 0.08
6	1.42	-2.2 ± 0.08

CMFs with uniform sized bins in the following discussion.

With the fiducial parameter, the turnover mass and the power-law index at the high-mass end are $1.09 M_{\odot}$, and 2.1 ± 0.06 , and there are no significant differences with Dendeogram's parameters in our parameter range. Here, we cannot judge whether the turnovers are real or not, but they are probably created with worth completeness of core identification that is mainly decided by the map spatial resolution. In addition, PPV CMFs have similar turnover masses, and slightly steeper slopes compare to PPP CMFs in Section 2.4. Figure 2.15 is the normalized histograms of PPP masses (case 2) and PPV masses (case 2) in the cumulative form. The p-value of the two-sample Kolmogorov-Smirnov test of the two masses is $\sim 2.09 \times 10^{-27}$. So then, the null hypothesis that PPP and PPV mass have

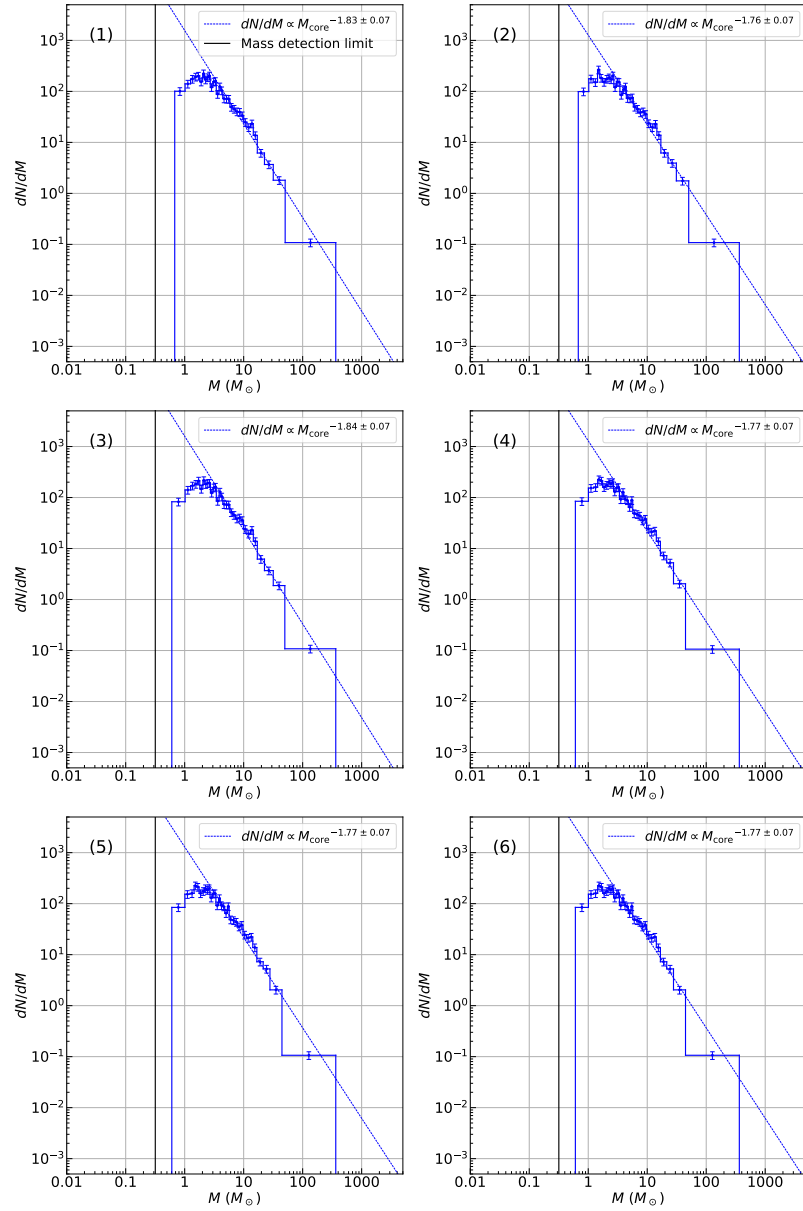


Figure 2.14: The same as Figure 2.13 but CMF with variably sized bins.

Table 2.19: The CMF Properties of Variably Sized Bins with PPV Data in xyv Space

Case No.	Turnover Mass M_{\odot}	$\alpha \pm \sigma_{\alpha}$
1	2.09	-1.83 ± 0.07
2 (fiducial)	1.5	-1.76 ± 0.07
3	2.11	-1.84 ± 0.07
4	1.52	-1.77 ± 0.07
5	1.52	-1.77 ± 0.07
6	1.52	-1.77 ± 0.07

identical distributions is rejected with a significance level of 5%. The steeper slope of PPV CMF seems to arise because the PPV masses tend to be smaller than the PPP masses.

PPV mass is smaller than PPP mass because the density profile along the line of sight in PPV data is broadened with the velocity dispersion. Figure 2.16 shows the mass–velocity width in FWHM relation for cores with case 2 parameter set. As seen in the figure, the best-fit function is $\text{FWHM} \propto M_{\text{core}}^{0.45 \pm 0.01}$, meaning that a more massive core has a large FWHM.

We estimate how much a core mass is underestimated in the steeper CMF (PPV CMF) than the true CMF (PPP CMF). To do so, we think of a simple case that the two CMFs' slopes cross at the turnovers of them as Figure 2.17. This means that both CMFs have the same turnover masses and peak values. Since velocity width is larger for massive cores and low-mass cores around a turnover are less affected by the line broadening, the assumption seems reasonable for a rough estimation. Then, the core mass with PPV data M_{PPV} is calculated with core mass with PPP

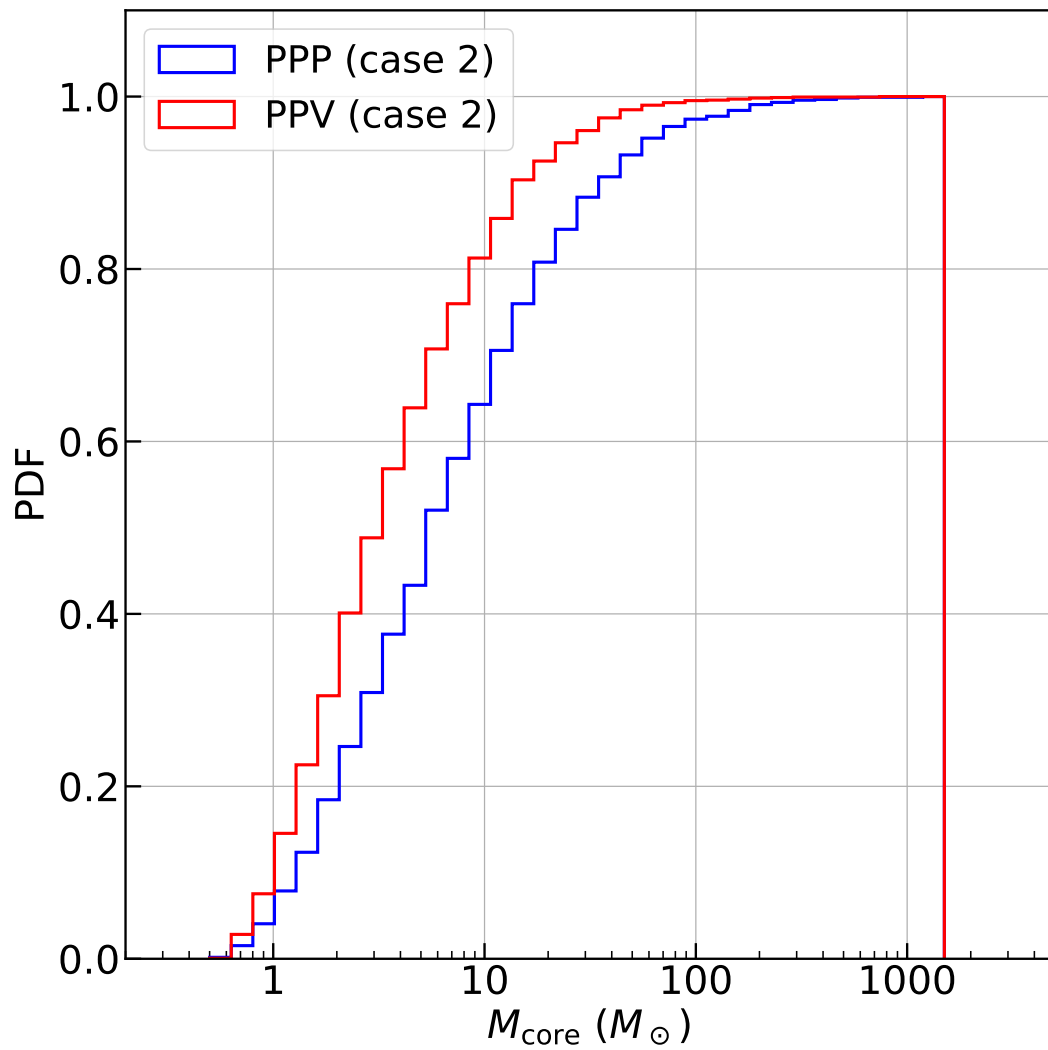


Figure 2.15: The normalized histograms of PPP masses (blue) and PPV masses (red). The cores are identified with parameter case 2 for PPP and PPV data.

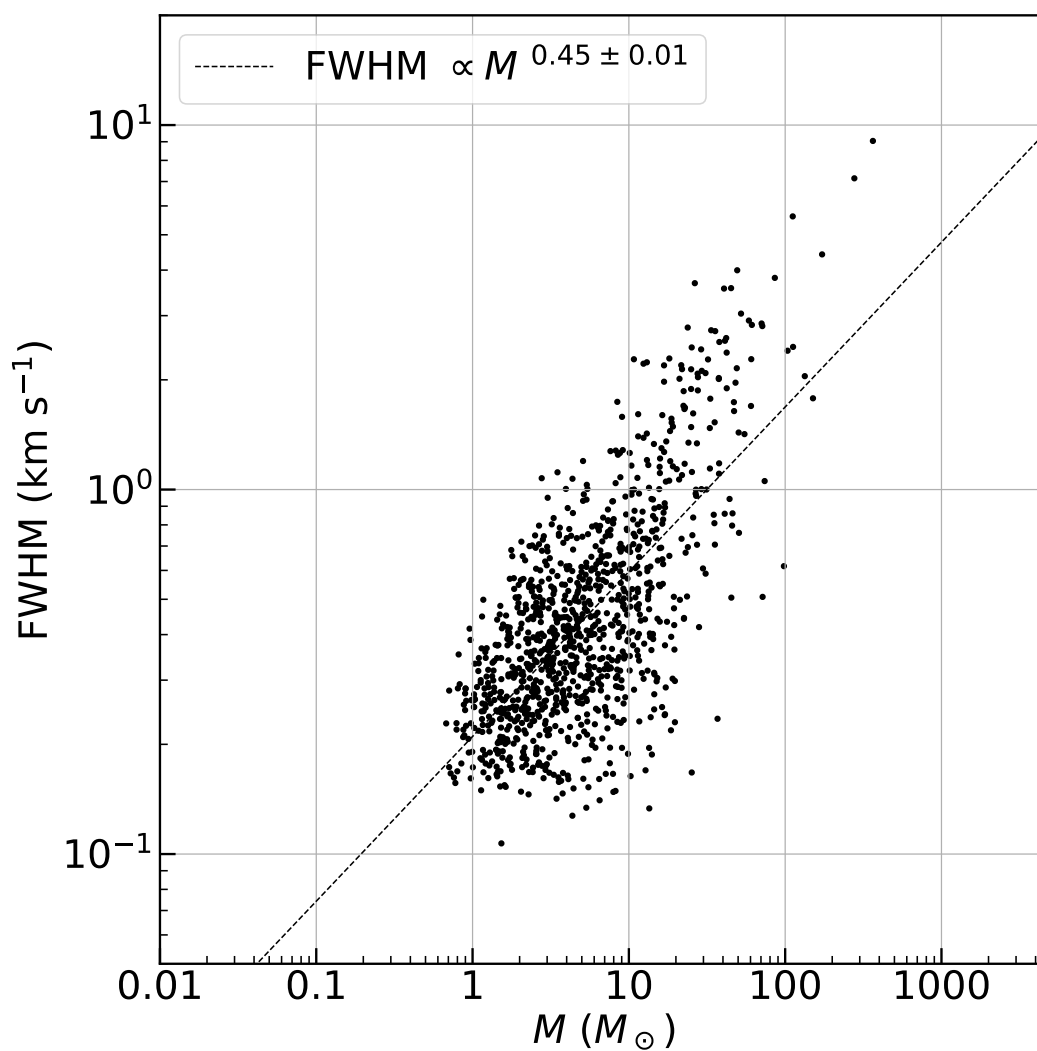


Figure 2.16: The mass–velocity width in FWHM relation for PPV cores with case 2 parameter set. The best-fit function is $\text{FWHM} \propto M_{\text{core}}^{0.45 \pm 0.01}$.

data M_{PPP} as Equation 2.10.

$$M_{\text{PPV}} = \frac{\alpha_{\text{PPP}}}{\alpha_{\text{PPV}}} \times M_{\text{PPP}} \quad (2.10)$$

where α_{PPP} and α_{PPV} are the power-law indices of PPP CMF and PPV CMF, respectively. For example, when $\alpha_{\text{PPP}} = 1.87$ (Figure 2.2 (b)) and α_{PPV} (Figure 2.13 (b)), $M_{\text{PPV}} \simeq 0.86M_{\text{PPP}}$.

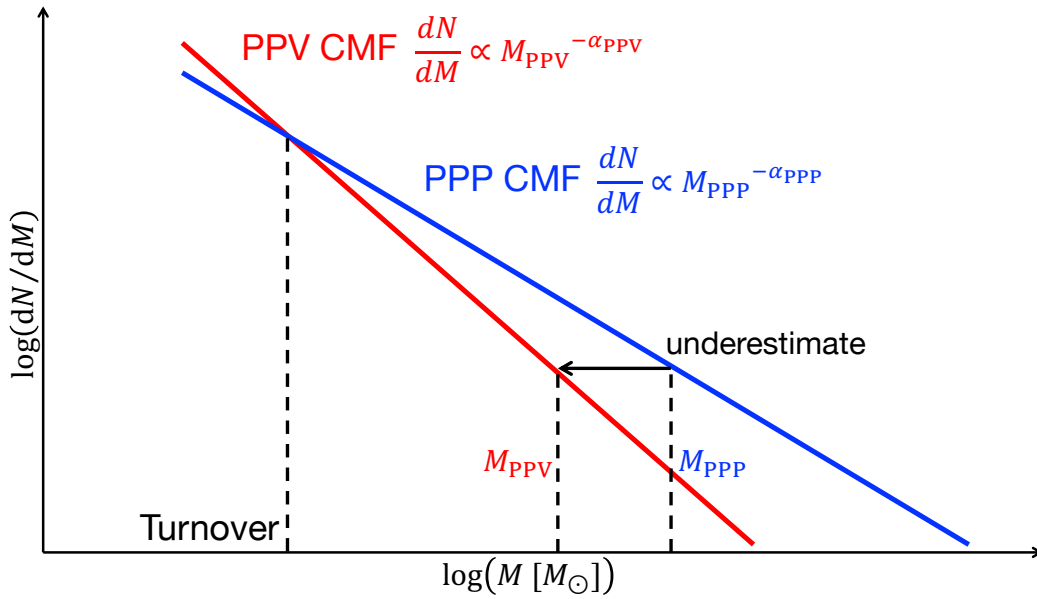


Figure 2.17: The schematic figure of PPP slope (blue) and PPV slope (red) that have power-law indices of α_{PPP} and α_{PPV} .

However, the situation is not always achieved in actual molecular line observations since they are more severely affected by chemical reactions than continuum observations. There are optically thick molecular lines and their transitions in molecular clouds, unlike the continuum. Even if we chose optically thin molecular

lines, H_2 column density estimated from molecular line observations depends on the excitation temperature of observing molecule $T_{\text{ex, molecule}}$ and its abundance ratio to molecular hydrogen X_{molecule} . Then, the variations of excitation temperature and abundance ratio in the plane of the sky and a long line of sight will arise the artificial variation of H_2 column density. It probably makes PPP true CMF and PPV observed CMF different.

The core or cloud mass from $C^{18}O$ ($J=1-0$) observations is computed as Equation 2.11 in (iked09) by assuming the local thermodynamic equilibrium (LTE) condition and the H_2 column density is calculated with the mass.

$$M_{\text{LTE}} = 5.0 \times 10^{-2} \left(\frac{X_{C^{18}O}}{1.7 \times 10^{-7}} \right)^{-1} T_{\text{ex}} e^{5.27/T_{\text{ex}}} \left(\frac{D}{480 \text{ pc}} \right)^2 \times \left(\frac{\Delta\theta_{\text{eff}}}{26''.4} \right)^2 \left(\frac{\eta}{0.4} \right)^{-1} \left(\frac{\sum_i T_{A,i}^* \Delta v_i}{\text{K km s}^{-1}} \right) M_{\odot} \quad (2.11)$$

where $\Delta\theta_{\text{eff}}$ and $\sum_i T_{A,i}^* \Delta v_i$ are grid size and integrated intensity of the object. In Figure 2.18, we fixed the flux ratio of dense cores and ambient gas in the cloud to 3:7 and calculated their column density ratio by changing the temperature and abundance ratio. If there are no variations of excitation temperature and abundance ratio along the line of sight, the column density ratio of dense cores and ambient gas in the cloud resembles the $C^{18}O$ flux ratio of them. Nevertheless, in many cases, the abundance ratio of $C^{18}O$ to H_2 is thought to be smaller inside the cores than outside due to the depletion effect since dense cores have larger density and lower temperature compared to the other region in a molecular cloud. According to Equation 2.11, the variations of temperature and abundance ratio cancel out each

other, which is also shown in Figure 2.18. For example, when $T_{\text{ambient}}/T_{\text{core}} = 2$ and $X_{\text{C}^{18}\text{O, ambient}}/X_{\text{C}^{18}\text{O, core}} = 2$, we overestimate the core column density by $\sim 15\%$ in C^{18}O observation compared to true core column density. Therefore, the temperature and abundance ratio variations do not have much impact on the column density in C^{18}O observations. We expect the C^{18}O CMF to have similar properties to PPP true CMF. The observed CMFs with molecules that do not have temperature and abundance ratio variations or have similar variations to C^{18}O also resemble a true CMF. We note that the molecular lines should be optically thin everywhere in molecular clouds.

2.7 Summary of This Chapter

We conducted dense cores surveys and constructed CMFs with three-dimensional numerical simulation data, PP data, and PPV column density data which are obtained from the simulation data. Then, the following lists are the main results and discussions of this Chapter and [Remaining task 1] of Section 1.10.

1. The overlap effect decreases the number of observed low-mass cores and makes CMF shallower. This effect is much more severe in PP data than in PPV data. Compensation of observed CMF with estimated core detection probability suppose to ease the undercount of low-mass cores.
2. As we reported in [Takemura, Nakamura, Ishii, et al. \(2021\)](#), background column density should be subtracted to derive a true CMF from continuum data otherwise the core masses and the slope of CMF above the turnover becomes

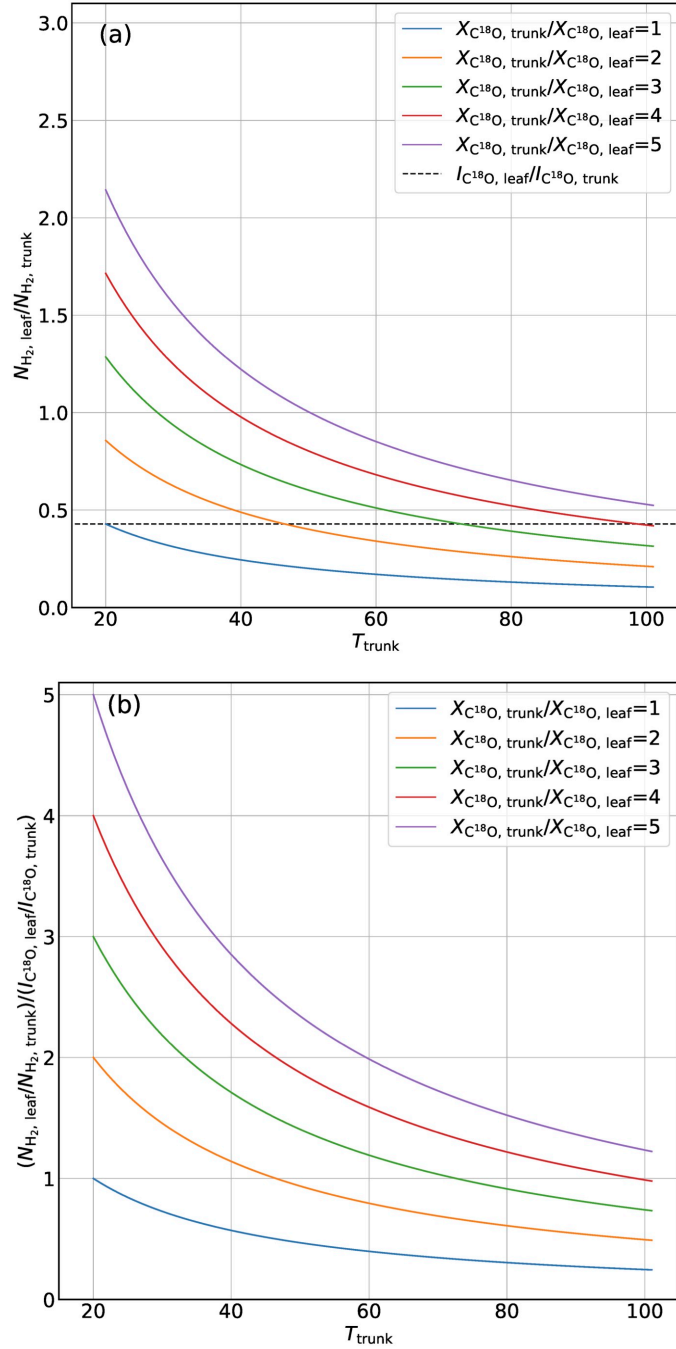


Figure 2.18: (a) The relationship between column density ratio of trunk and leaf, $N_{\text{H}_2, \text{leaf}}/N_{\text{H}_2, \text{trunk}}$, the temperature of trunk T_{trunk} . The abundance ratio fractions of leaf and trunk are $X_{\text{C}^{18}\text{O}, \text{leaf}}/X_{\text{C}^{18}\text{O}, \text{trunk}} = 1$ (blue), 2, 3, 4, 5 (magenta). The horizontal dashed line represents the fixed intensity ratio of the trunk and leaf $I_{\text{C}^{18}\text{O}, \text{leaf}}/I_{\text{C}^{18}\text{O}, \text{trunk}}$. (b) The column density ratio of trunk and leaf, $N_{\text{H}_2, \text{leaf}}/N_{\text{H}_2, \text{trunk}}$ normalized with the fixed intensity ratio of the trunk and leaf $I_{\text{C}^{18}\text{O}, \text{leaf}}/I_{\text{C}^{18}\text{O}, \text{trunk}}$ with various abundance ratio fractions as panel (a). This figure is from Takemura, Nakamura, Ishii, et al. (2021).

larger and steeper, respectively. In addition, As long as the background subtraction is performed, the slope of the CMF remains almost the same when we use clump typical temperature to derive core mass. Convolution using some function like gaussian seems to work well to derive true core masses and turnover masses from continuum data.

3. According to the analyses of PP data, CMF only with cloud center has a shallower slope than cloud CMF.
4. The turnover mass of PPV CMF resembles that of PPP CMF. On the other hand, the power-law index at the high-mass end of PPV CMF is steeper than that of PPP CMF. This supposes to arise from an underestimation of core mass in PPV data due to the line broadening. The magnitude of the influence depends on the slope of the line width – mass relation. Then, it is thought to be less severe when the slope is shallower in the actual observation than in our simulation data.
5. The slope of CMF with variably sized bins is systematically shallower than it of CMF with uniform sized bins. Thus, the binning method needs to be fixed, when we discuss the mapping from CMF to IMF and the comparison of CMFs in various star-forming regions.

3. Dense Core Survey with Observational Data

We extended our previous studies (Takemura, Nakamura, Ishii, et al. 2021; Takemura, Nakamura, Kong, et al. 2021, see Sections 1.5 and 1.6), we performed a dense core survey in Orion A using wide and high-spatial-resolution C18O ($J=1-0$) data (see Section 3.1.1). In Takemura, Nakamura, Kong, et al. (2021), we focused on the ONC region, but we analyzed the whole data in this study. The wide observation area makes us separate the data into subregions to investigate and compare the core properties in a different environment. Besides, our core catalog covers various cloud environments, and it will be helpful to investigate newly observed star-forming regions in the future. Applying the Dendrogram algorithm to the data, we identified dense cores in Section 3.2 and investigated their physical quantities in Section 3.3. Then, we constructed CMFs in 3.4 and discussed the core growth with mass accretion based on the observed CMFs in Section 3.5. This study is presented in (Takemura, Nakamura, Arce, et al. 2023). According to the dense core survey with numerical simulation data in Section 2.6, PPV CMF tends to be steeper than

true CMF due to the line-broadening effect. Then, we discuss the application of the result to this observational data in Section 3.3.2.

3.1 Observational Data

We utilized three datasets of Orion A in this study: CARMA+NRO45-m combined C18O ($J=1-0$) data, *Herschel* H₂ column density data, and YSO catalog. In this section, we introduce the information of each dataset.

3.1.1 CARMA+NRO45-m Combined C18O ($J=1-0$) Data

We use the CARMA+NRO45-m combined C18O ($J=1-0$) data to identify dense cores, and this new map has a larger area than Kong, Arce, Feddersen, et al. (2018). The detailed information, such as the process of data production, is described in Kong, Arce, Feddersen, et al. (2018). The C18O ($J=1-0$) data covers $1^\circ \times 2^\circ$ area which contains OMC-1/2/3/4/5, L1641-N, V380 Ori, and L1641C regions with angular and velocity resolutions of $8''$ and 0.1 km s^{-1} . The resolutions are the same as our previous study in the ONC region. However, we updated the distance to the cloud from 414 pc (Menten et al. 2007) to 390 pc based on the recent Gaia analysis (Großschedl et al. 2018). Then, the spatial resolution of the map is ~ 3100 au. We note that the L1641C area does not include in the previous map. The mean RMS noise level is $\sim 0.68 \text{ K}$ ($1 \sigma_{\text{rms}}$) in units of T_{MB} , and this is almost the same as the previous map.

We divided the data of the observation into four subregions based on their

declination, and we named the regions as listed below.

subregion (a) OMC-1/2/3 ($-5^{\circ}30' \lesssim \delta$)

subregion (b) OMC-4/5 ($-6^{\circ}10' \lesssim \delta \lesssim -5^{\circ}30'$)

subregion (c) L1641N/V380 Ori ($-6^{\circ}50' \lesssim \delta \lesssim -6^{\circ}10'$),

subregion (d) L1641C ($\delta \lesssim -6^{\circ}45'$)

These subregions and the ONC region studied in (Takemura, Nakamura, Kong, et al. 2021) are shown as dashed rectangles and a solid square in Figure 3.1. Even though we only referred to the declination to define subregions, each region has a different cloud environment. For example, there are massive stars such as θ^1 Ori C in the Trapezium star cluster (Pabst et al. 2019) in OMC-1. This region is considered to be affected by UV radiation from the star cluster. In addition, Yasuo Fukui, Torii, et al. (2018) suggested that the O-type star formation of this region is triggered by a cloud-cloud collision (see also Lim et al. (2021)). Another feature of the OMC-1/2/3 area is a single dense filamentary ridge, and several faint filamentary structures are seen. Except for several tiny filaments in OMC-4/5, there is no filamentary ridge in other subregions. In contrast to the massive star formation in OMC-1, L1641N, and L1641C are likely to be more quiescent. Nevertheless, protostars or protostellar outflows are detected in L1641N (Ali and Noriega-Crespo 2004; Nakamura, Miura, et al. 2012; Tanabe et al. 2019; Feddersen et al. 2020) and L1641C (Y. Fukui et al. 1986; Chen et al. 1993).

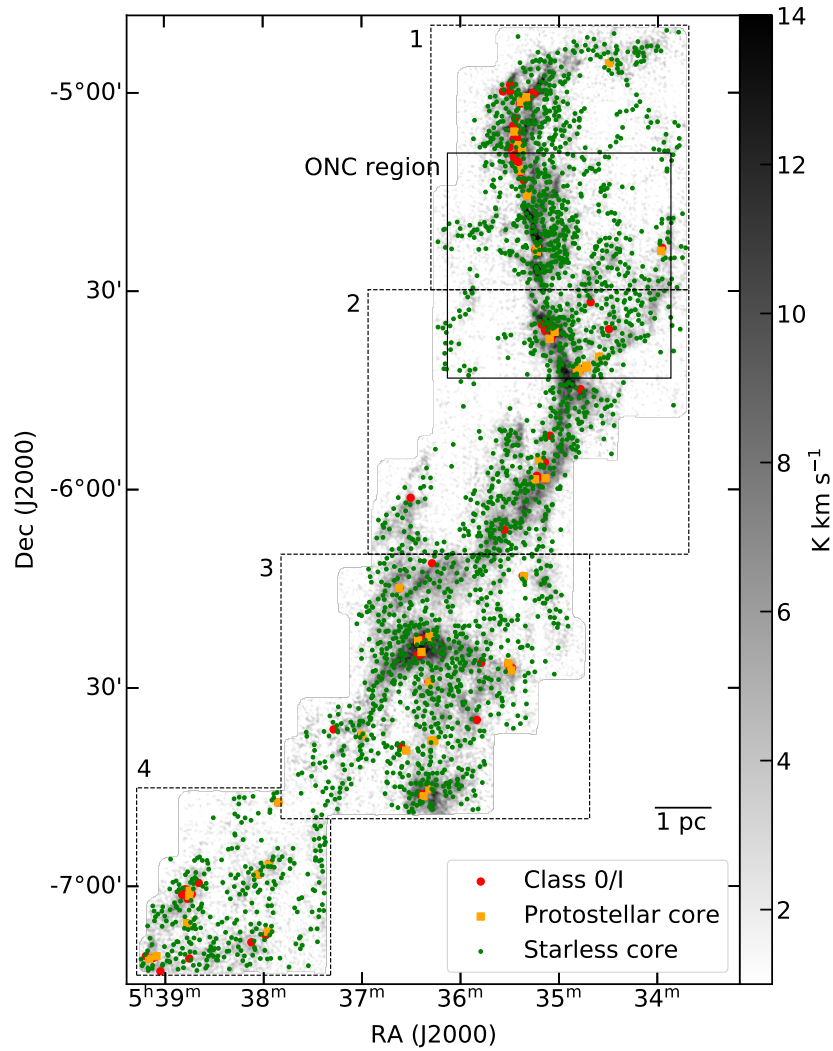


Figure 3.1: The identified starless cores (green dots) and protostellar cores (orange squares) are plotted on the integrated intensity map of the C18O ($J=1-0$) line (see Section 3.2.1). The dashed rectangles represent the subregions of Orion A: OMC-1/2/3 area, OMC-4/5 area, L1641N/V380 Ori area, and L1641C area from north to south. The analyzed ONC region by [Takemura, Nakamura, Kong, et al. \(2021\)](#) is surrounded by solid lines. The red circles are Class-0/I objects of VISION catalog ([Meingast et al. 2016](#), see Section 3.1.3).

3.1.2 *Herschel* H₂ Column Density Data

We used *Herschel* H₂ column density data to derive a core mass as done by (Takemura, Nakamura, Kong, et al. 2021). The data is obtained with the *Herschel* observation of Orion A within Gould Belt keyprogram (Ph. André, Men'shchikov, et al. 2010). Using a deconvolution method based on the Richardson-Lucy algorithm (Richardson 1972; Lucy 1974) in addition to the standard pipeline, the map achieved an angular resolution of 18". Although the map resolution is approximately twice worse than that of C18O ($J=1-0$) data, we regridded the column density data to match the grid of C18O ($J=1-0$) data with CASA task of *imregrid* to derive a core mass. Figure 3.2 shows the H₂ column density map. The details of data production are in Section 2.2 of (Takemura, Nakamura, Arce, et al. 2023).

3.1.3 YSO Catalog

To classify the identified cores C18O into starless cores and protostellar cores, we used the YSO catalog of Vienna survey in Orion (VISION) with the European Southern Observatory's (ESO) Visible and Infrared Survey Telescope for Astronomy (VISTA) (Meingast et al. 2016). This catalog includes 40 Class 0, 61 Class I, and 264 Class II objects in the observation area of C18O ($J=1-0$) data. It is noted in Meingast et al. (2016) that an $11' \times 11'$ area around OMC-1 is excluded from the analysis since the background emission of this region on a tiny scale is too large to allow source detection. So then, this catalog may not complete YSOs in Orion A and we probably undercount the protostellar cores in the OMC-1/2/3 area.

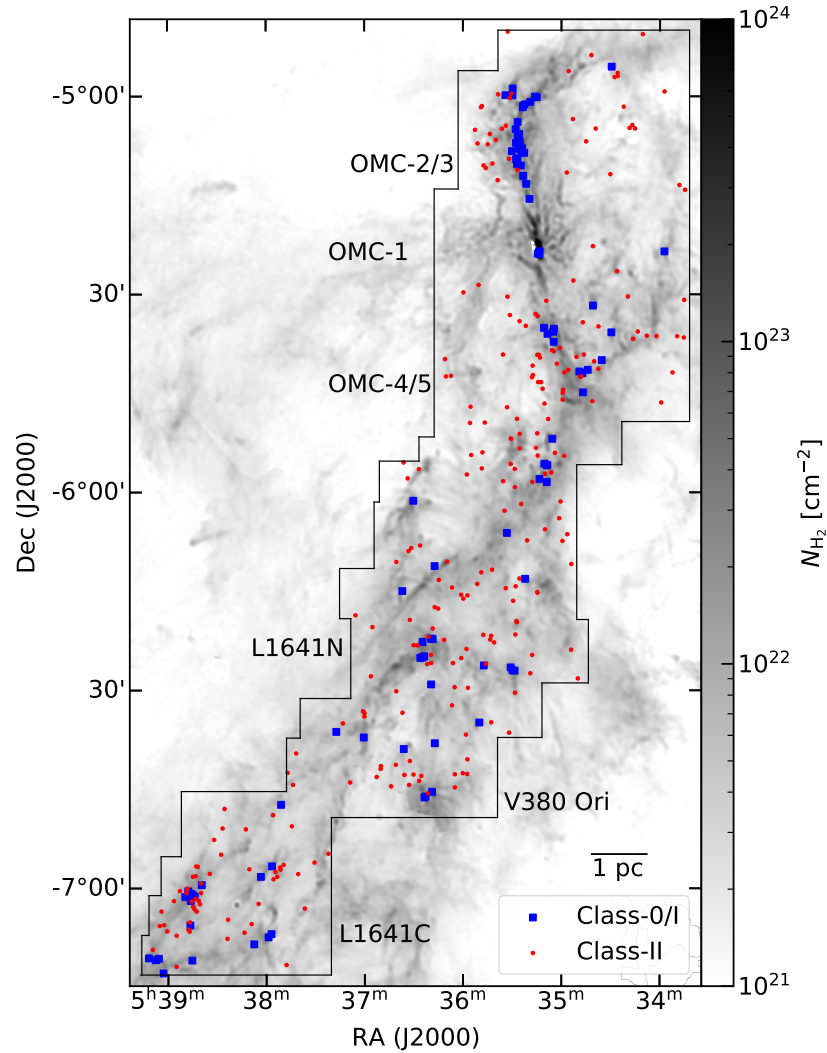


Figure 3.2: The *Herschel* H₂ column density with Class-0/I objects (blue squares) and Class-II objects (red dots) of VISION catalog (Meingast et al. 2016, see Section 3.1.3). The observed area with the CARMA+NRO45-m combined C18O ($J=1-0$) data is shown as solid lines.

Figure 3.2 shows the distributions of Class-0/I objects and Class-II objects.

We also used the Class II objects in the YSO catalog to estimate the core lifetime. Here, we extracted the objects with spectral indices of $-1.6 < \alpha < -0.3$ as the Class II objects.

3.2 Dense Core Survey in Orion A

3.2.1 Core Identification

We applied Dendrogram algorithm to the C18O ($J=1-0$) PPV data with input parameters of $\text{min_delta} = 2\sigma_{\text{rms}}$, $\text{min_value} = 2\sigma_{\text{rms}}$, and $\text{min_npix} = 60$ (≈ 1 beam $\times 3$ channels). [E. W. Rosolowsky et al. \(2008\)](#) suggested that the hierarchical structure with amplitude changes larger than $\sim 2\sigma_{\text{rms}}$ can only be considered to be reliable. Following this, we set min_delta to $2\sigma_{\text{rms}}$. In order to minimize the effect of the noise on the core sample, we set three additional selection criteria for the output of the Dendrogram as follows. We also used these criteria in a dense core survey in the ONC region ([Takemura, Nakamura, Kong, et al. 2021](#)).

criterion (1) The peak C18O ($J=1-0$) intensity of a leaf should be larger than

$4\sigma_{\text{rms}}$ at the corresponding spatial position.

criterion (2) More than three consecutive channels have more than 20 pixels (\approx the map angular resolution) for each channel.

criterion (3) An identified core does not contain any pixels located at the edge of the observation area.

We identified 2342 C18O cores, but one of them in OMC-1/2/3 is not covered with

H_2 column density map because of the saturation of the *Herschel* observations. Then, our final core sample consists of 2341 cores. Approximately 55% of them overlap each other along the line of sight.

The output of the Dendrogram has information about which pixels are assigned to cores, and we know the positions of YSOs in the plane of the sky. We classified a core as a protostellar core if it overlaps with one or more YSOs along the line of sight, ignoring a velocity. After that procedure, we identified 2295 starless cores and 46 protostellar cores, and we show their distribution and VISION objects in Figure 3.1. Although most of the VISION Class 0/I objects are associated with identified leaves, about half of such leaves do not satisfy an additional selection criterion (2). In addition to this, the VISION catalog may not cover all YSOs in Orion A as described in Section 3.1.3. For these two reasons, we may underestimate the number of protostellar cores and overestimate the number ratio of starless cores and protostellar cores. The results of the dense core survey are summarised in Table 3.1.

3.2.2 Calculation of the Core Physical Properties

We explain how we calculate each core physical property in this section. The positions and the line of sight velocity of a core are in the output of the Dendrogram. The definitions are the mean positions of the structure identified and the intensity-weighted first-moment velocity. The core area projected onto the plane of sky A_{core} is also calculated by Dendrogram, and we define the core radius using the core

Table 3.1: The summary of identified cores in Orion A and its subregions

Region	Category	Total	Bound Cores	Unbound Cores
Entire region	Identified Core	2341	1087	1254
	Starless Core	2295	1045	1250
	Protostellar Core	46	42	4
(a) OMC-1/2/3 area	Identified Core	716	223	493
	Starless Core	705	212	493
	Protostellar Core	11	11	0
(b) OMC-4/5 area	Identified Core	605	299	306
	Starless Core	595	291	304
	Protostellar Core	10	8	2
(c) L1641N area	Identified Core	726	335	391
	Starless Core	710	321	389
	Protostellar Core	16	14	2
(d) L1641C area	Identified Core	294	230	64
	Starless Core	285	221	64
	Protostellar Core	9	9	0

area as

$$R_{\text{core}} = \left(\frac{A_{\text{core}}}{\pi} \right)^{1/2}. \quad (3.1)$$

Most of the cores have some elongation in the PP plane. The major and minor axes are computed in the Dendrogram as the intensity-weighted second moment in the direction of maximum elongation and perpendicular to the major axis. From the intensity-weighted second moment of velocity v_{rms} included in the Dendrogram output, we calculated the velocity width in FWHM dV_{core} as

$$dV_{\text{core}} = 2\sqrt{2\ln 2} \times v_{\text{rms}}. \quad (3.2)$$

To calculate core mass, we used *Herschel* H₂ column density and Dendrogram's hierarchy as our previous studies (Takemura, Nakamura, Ishii, et al. 2021;

Takemura, Nakamura, Kong, et al. 2021, see Sections 1.5 and 1.6). When the intensities of a leaf and a trunk at (i, j) pixel are $I_{\text{leaf}}(i, j)$, $I_{\text{trunk}}(i, j)$, the core mass is calculated as

$$M_{\text{core}} = \mu m_{\text{H}} \sum N_{\text{H}_2}^{\text{Herschel}}(i, j) \times \frac{I_{\text{leaf}}(i, j)}{I_{\text{trunk}}(i, j)}. \quad (3.3)$$

This is a different form of Equation 1.6. The total column density of a core and an ambient gas at (i, j) pixel is fixed to *Herschel* H_2 column density at the pixel, but the column density ratio is influenced by the variation of excitation temperature, and the abundance ratio of C^{18}O to H_2 . Nevertheless, as we discussed in Section 2.6 and Takemura, Nakamura, Ishii, et al. (2021), the influence does not so much affect a core mass estimation.

Using the core mass, we performed a simple virial analysis with an assumption of a centrally condensed sphere without magnetic support and external pressure as

$$M_{\text{vir}} = 126 \left(\frac{R_{\text{core}}}{\text{pc}} \right) \left(\frac{\Delta V_{\text{core}}}{\text{km s}^{-1}} \right)^2, \quad (3.4)$$

and

$$\alpha_{\text{vir}} = \frac{M_{\text{vir}}}{M_{\text{core}}}. \quad (3.5)$$

where the core is assumed to be a centrally condensed sphere without magnetic support and external pressure. We define a core with a virial ratio of smaller than 2 ($\alpha_{\text{vir}} < 2$) gravitationally-bound core (hereafter referred to as a bound core) and that with a virial ratio of larger than 2 ($\alpha_{\text{vir}} \geq 2$) gravitationally-unbound core (hereafter

referred to as an unbound core), respectively. We identified 1045 bound cores in Orion A, which is $\sim 46\%$ of identified starless cores. Figure 3.3 shows the spatial distribution of bound and unbound cores. The figure shows that most of the bound cores are located in the inner regions of the main filamentary structure. In Appendix B.1, we discuss the core and CMF properties when we set the boundary of bound and unbound cores to $\alpha_{\text{vir}} = 1$.

We computed a free-fall time of a core as

$$t_{\text{ff}} = \sqrt{\frac{3\pi}{32G\rho_{\text{core}}}}, \quad (3.6)$$

where ρ_{core} is a core density derived with a uniform sphere which has a radius and a mass of R_{core} and M_{core} . Here we used a mean molecular weight of $\mu = 2.8$.

As we mentioned in Section 3.1.3, we estimated a core lifetime with the number ratio of Class II objects and identified cores. This statistical estimation of a core lifetime using the number ratio has already been done in previous unbiased core surveys (Beichman et al. 1986; Lee and Myers 1999; Jessop and Ward-Thompson 2000; Onishi et al. 2002; Tokuda et al. 2020; Das, Basu, and Philippe André 2021) and we followed them. Assuming all Class II objects have the same lifetime of 2×10^6 yr (Evans et al. 2009) and the star formation rate is constant over the cloud lifetime, we estimated the core lifetime as

$$\tau_{\text{SF}} = \frac{\text{number of prestellar cores}}{\text{number of Class II objects}} \times (2 \times 10^6 \text{ yr}) \quad (3.7)$$

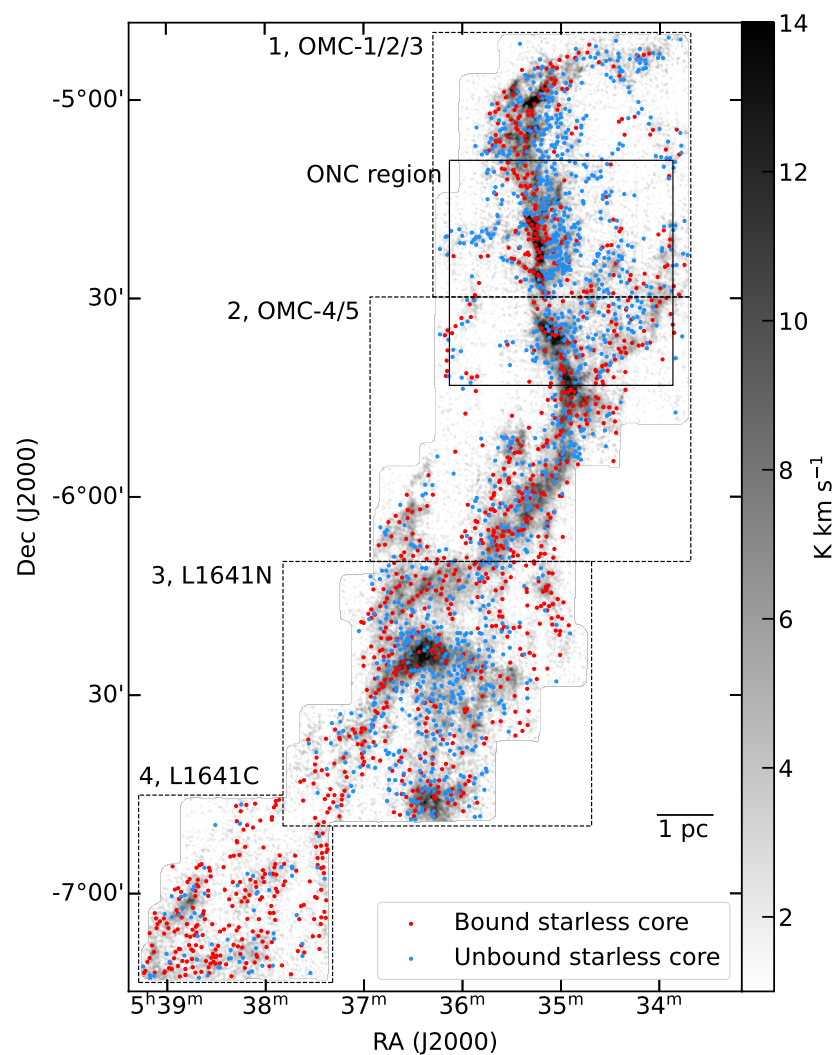


Figure 3.3: The bound starless cores (red) and unbound cores (blue) are plotted on the integrated intensity map of the C18O ($J=1-0$) line. The details are the same as Figure 3.1.

The derived core properties are summarised in Table 3.2.

Table 3.2: The summary core physical properties in Orion A

Property	Category	Minimum	Maximum	Mean \pm Std.
Diameter (pc)	Identified Core	0.030	0.260	0.076 ± 0.027
	Starless Core	0.030	0.260	0.076 ± 0.027
	Protostellar Core	0.040	0.173	0.081 ± 0.033
Aspect Ratio	Identified Core	1.01	5.45	1.89 ± 0.62
	Starless Core	1.01	5.45	1.89 ± 0.62
	Protostellar Core	1.11	3.39	1.80 ± 0.50
FWHM (km s^{-1})	Identified Core	0.11	1.04	0.30 ± 0.11
	Starless Core	0.11	1.04	0.30 ± 0.11
	Protostellar Core	0.18	0.80	0.32 ± 0.11
Mass (M_{\odot})	Identified Core	0.02	72.2	0.35 ± 1.85
	Starless Core	0.02	72.2	0.32 ± 1.70
	Protostellar Core	0.08	34.4	2.05 ± 5.10
Number Density (10^4 cm^{-3})	Identified Core	0.16	615	2.79 ± 21.43
	Starless Core	0.16	508	2.34 ± 16.37
	Protostellar Core	0.62	615	25.21 ± 97.44
Virial Ratio	Identified Core	0.04	39.2	3.03 ± 3.06
	Starless Core	0.04	39.2	3.07 ± 3.08
	Protostellar Core	0.06	3.21	0.81 ± 0.71

3.3 Analysis of the Core Physical Properties

3.3.1 Histograms of the Core Physical Properties

We show the histograms of core diameter, aspect ratio, velocity width in FWHM, core mass, core number density, and the virial ratio of starless and protostellar cores in Orion A in Figure 3.4. The protostellar cores tend to be more massive, denser, and more virialized compared to starless cores. The fact that protostellar cores have larger masses than starless cores is consistent with previous observations (Kong,

Arce, Shirley, et al. 2021, see Section 1.7.1). Figure 3.5 also shows the histograms of core properties but for starless cores, classifying them into bound and unbound cores. We see the differences in velocity width, core mass, and density; the velocity width of bound cores is smaller, and the mass and density are larger than unbound cores. In addition to the above quantitative comparisons, we performed a two-sample Kolmogorov – Smirnov (KS) test of the physical properties for statistical comparisons as Table 3.3. In a two-sample KS test, the null hypothesis that two core properties have identical distributions is rejected with the significance level of 5% when the p-value is less than 0.05. Even if a p-value is larger than 0.05, we cannot conclude that the two properties have identical distributions. A proper explanation of a large p-value is that it is not clear whether the two core properties have the same distribution or not. According to the results of the KS test, the different distributions of a velocity width, a core mass, and a density of bound and unbound cores are confirmed statistically. In addition, the p-value between the core radii of bound and unbound cores is also much smaller than 0.05, and bound cores tend to be smaller than unbound cores.

Next, we compare the core physical properties in subregions in Orion A. The minimum, maximum, mean, and standard deviation of core properties in subregions are shown in Tables 3.4, 3.5, 3.6, and 3.7. We show the histograms of core properties in four subregions in Figures 3.6 (diameter), 3.7 (aspect ratio), 3.8 (velocity width in FWHM), 3.9 (mass), 3.10 (density), and 3.11 (virial ratio). Besides, as in Orion A, we performed the two-sample KS test of core physical properties among subregions and showed the results in Appendix B.2 for quantitative comparison.

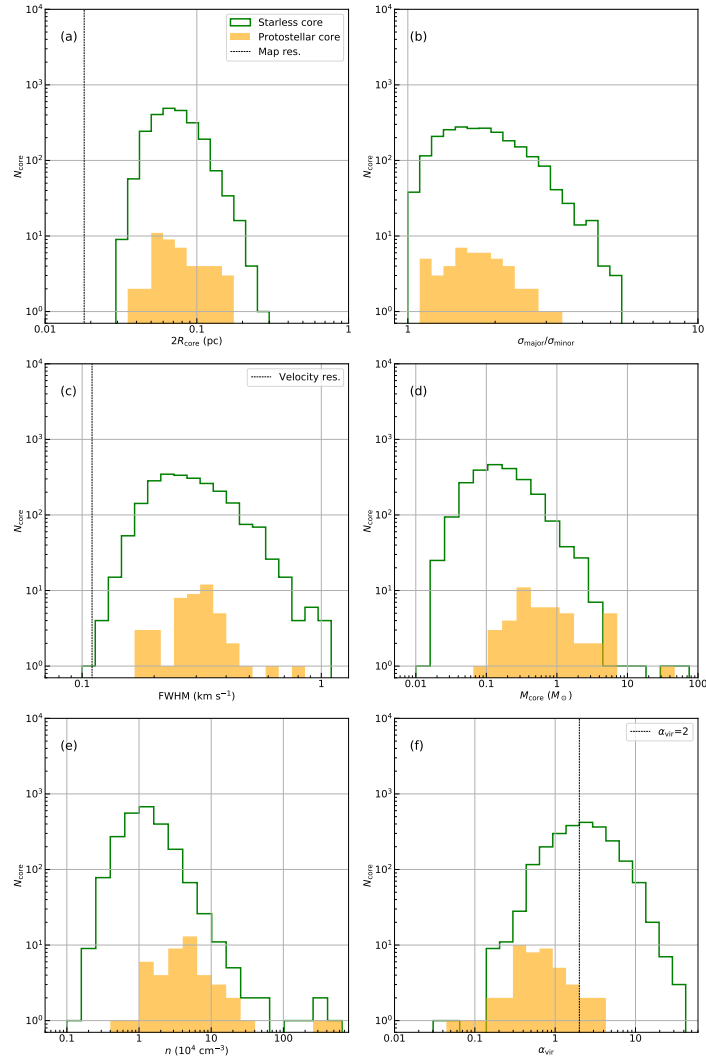


Figure 3.4: The histograms of a core diameter (panel (a)), an aspect ratio (panel (b)), a velocity width in FWHM (panel (c)), a core mass (panel (d)), a core number density (panel (e)), and virial ratio (panel (d)) of starless cores and protostellar cores in Orion A. The green and orange histograms are for starless cores and protostellar cores.

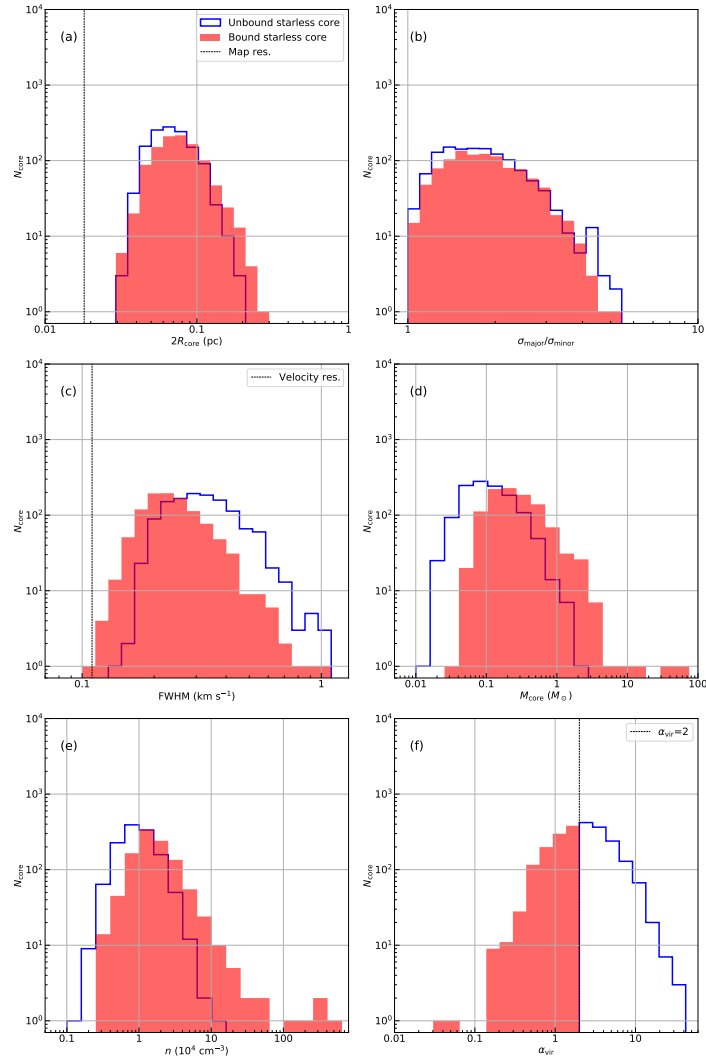


Figure 3.5: The histograms of core physical properties of bound starless cores (red) and unbound starless cores (blue). The details are the same as Figure 3.4.

Table 3.3: The Results of Two-Sample KS Test of Core Properties in Orion A

Core Property	Category	p-value
Diameter (pc)	Starless Core & Protostellar Core	4.36×10^{-1}
	Bound Starless Core & Unbound Starless Core	1.61×10^{-10}
	Bound Starless Core & Protostellar Core	5.37×10^{-1}
Aspect Ratio	Starless Core & Protostellar Core	6.94×10^{-1}
	Bound Starless Core & Unbound Starless Core	1.96×10^{-2}
	Bound Starless Core & Protostellar Core	4.34×10^{-1}
FWHM (km s^{-1})	Starless Core & Protostellar Core	3.97×10^{-3}
	Bound Starless Core & Unbound Starless Core	3.77×10^{-15}
	Bound Starless Core & Protostellar Core	5.19×10^{-9}
Mass (M_{\odot})	Starless Core & Protostellar Core	7.33×10^{-15}
	Bound Starless Core & Unbound Starless Core	3.77×10^{-15}
	Bound Starless Core & Protostellar Core	4.73×10^{-8}
Number Density (10^4 cm^{-3})	Starless Core & Protostellar Core	4.18×10^{-17}
	Bound Starless Core & Unbound Starless Core	3.77×10^{-15}
	Bound Starless Core & Protostellar Core	9.42×10^{-12}
Virial Ratio	Starless Core & Protostellar Core	3.73×10^{-16}
	Bound Starless Core & Unbound Starless Core	-
	Bound Starless Core & Protostellar Core	3.20×10^{-8}

This study mainly focuses on noticeable differences in core properties among the subregions based on the above analyses, especially the histograms.

The average core diameter in the OMC-1/2/3 region tends to be smaller than those in the other regions. The trend is more explicit in bound cores compared to unbound cores. Except for this point, significant differences are not seen in core diameters and aspect ratios among subregions from the histograms.

In the FWHM velocity widths, There is a noticeable difference among subregions; the bound cores with large velocity widths larger than 0.5 km s^{-1} are only in OMC-1/2/3 area, and the cores with large velocity widths are classified as unbound cores in the other regions. However, the peaks of the histograms resemble each other, and they have peaks at $\sim 0.2 \text{ km s}^{-1}$. The p-values between the OMC-1/2/3 area and the other areas are smaller than 0.01, which means that the differences are confirmed with the significance level of 5%.

The massive starless cores ($\geq 5 - 10 M_{\odot}$) centrally distributed in OMC-1/2/3 area. Although one high-mass core has a mass of $\sim 10 M_{\odot}$ in L1641N, only OMC-1/2/3 has multiple massive cores of $M_{\text{core}} > 2 M_{\odot}$. We note that the p-values between the OMC-1/2/3 and other areas are not smaller than 0.05. Then, in the case of mass distribution of bound cores, we cannot judge whether OMC-1/2/3 differs from the other subregions in this study. For another difference, the fraction of low-mass ($\leq 0.04 M_{\odot}$) cores in L1641C is small compared to other areas.

Since the starless cores in OMC-1/2/3 tend to be more massive than the other regions and are comparable in size to the other regions, the cores are expected to be dense. The trend is seen in the density histograms. Only the OMC-1/2/3 area

contains the dense cores with $n_{\text{core}} > 10^5 \text{ cm}^{-3}$ and the number of cores gradually decreases as the density increases while there are steep slopes above peaks in the other subregions. Conversely, the range of the density distribution is narrower in the L1641C area. The intermediate density range is seen in the OMC-4/5 and L1641N/V380 Ori areas, and their distributions resemble each other.

The fraction of unbound cores in starless cores looks slightly larger than the other region in the OMC-1/2/3 area compared to the other areas. Inversely, bound cores are more abundant in the L1641C area, and the peak of the distribution is at $\sim \alpha_{\text{vir}} = 1$. Except for the L1641C area, the distributions have peaks at around $\alpha_{\text{vir}} = 2 - 3$.

Table 3.4: The Summary Core Properties in OMC-1/2/3 Area

Property	Category	Minimum	Maximum	Mean \pm Std.
Diameter (pc)	Identified Core	0.030	0.159	0.066 ± 0.020
	Starless Core	0.030	0.159	0.065 ± 0.020
	Protostellar Core	0.040	0.156	0.071 ± 0.034
Aspect Ratio	Identified Core	1.02	5.45	1.91 ± 0.64
	Starless Core	1.02	5.45	1.91 ± 0.64
	Protostellar Core	1.38	3.39	1.97 ± 0.54
FWHM (km s^{-1})	Identified Core	0.15	1.04	0.34 ± 0.13
	Starless Core	0.15	1.04	0.33 ± 0.13
	Protostellar Core	0.18	0.80	0.38 ± 0.17
Mass (M_{\odot})	Identified Core	0.02	72.2	0.47 ± 3.26
	Starless Core	0.02	72.2	0.39 ± 3.00
	Protostellar Core	0.17	34.4	5.55 ± 9.42
Number Density (10^4 cm^{-3})	Identified Core	0.33	615	5.94 ± 38.54
	Starless Core	0.33	508	4.59 ± 29.38
	Protostellar Core	2.29	615	92.13 ± 183.81
Virial Ratio	Identified Core	0.04	32.7	3.82 ± 3.32
	Starless Core	0.04	32.7	3.87 ± 3.32
	Protostellar Core	0.06	1.48	0.49 ± 0.50

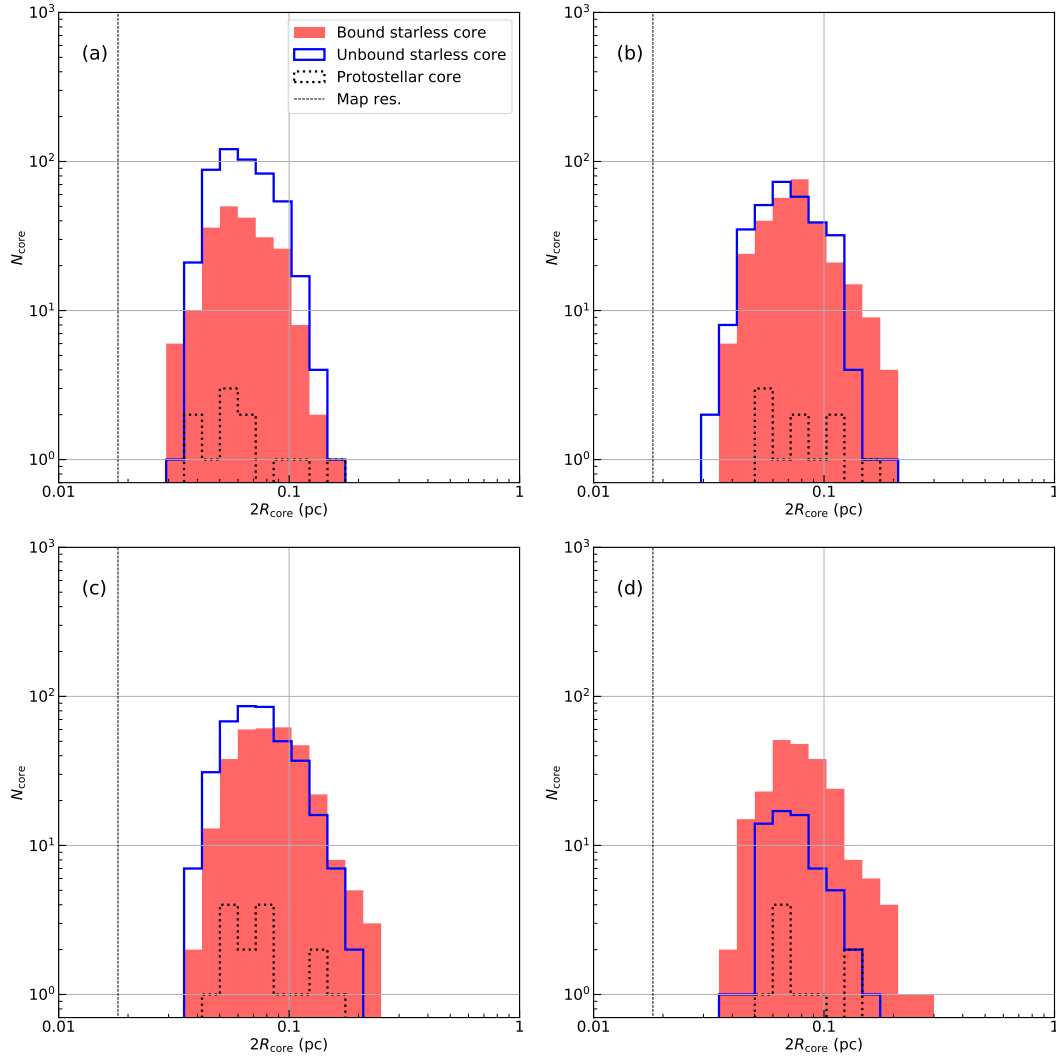


Figure 3.6: The histograms of core size in four subregions. The panels correspond to the subregions in Orion A: (a) OMC-1/2/3 area, (b) OMC-4/5 area, (c) L1641N/V380 Ori area, and (d) L1641C area. The red, blue, and black histograms are for bound, unbound, and protostellar cores.

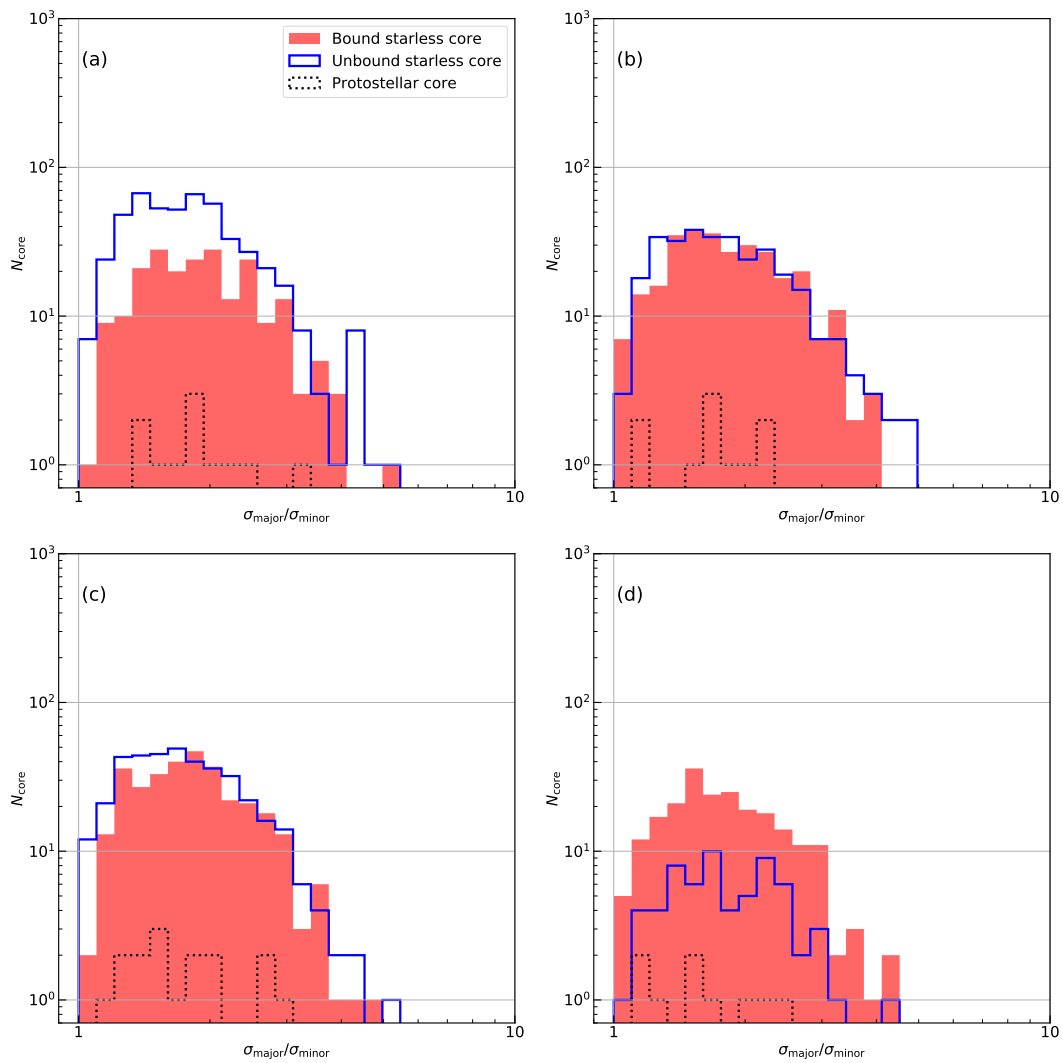


Figure 3.7: The same figure as Figure 3.6 but for aspect ratio.

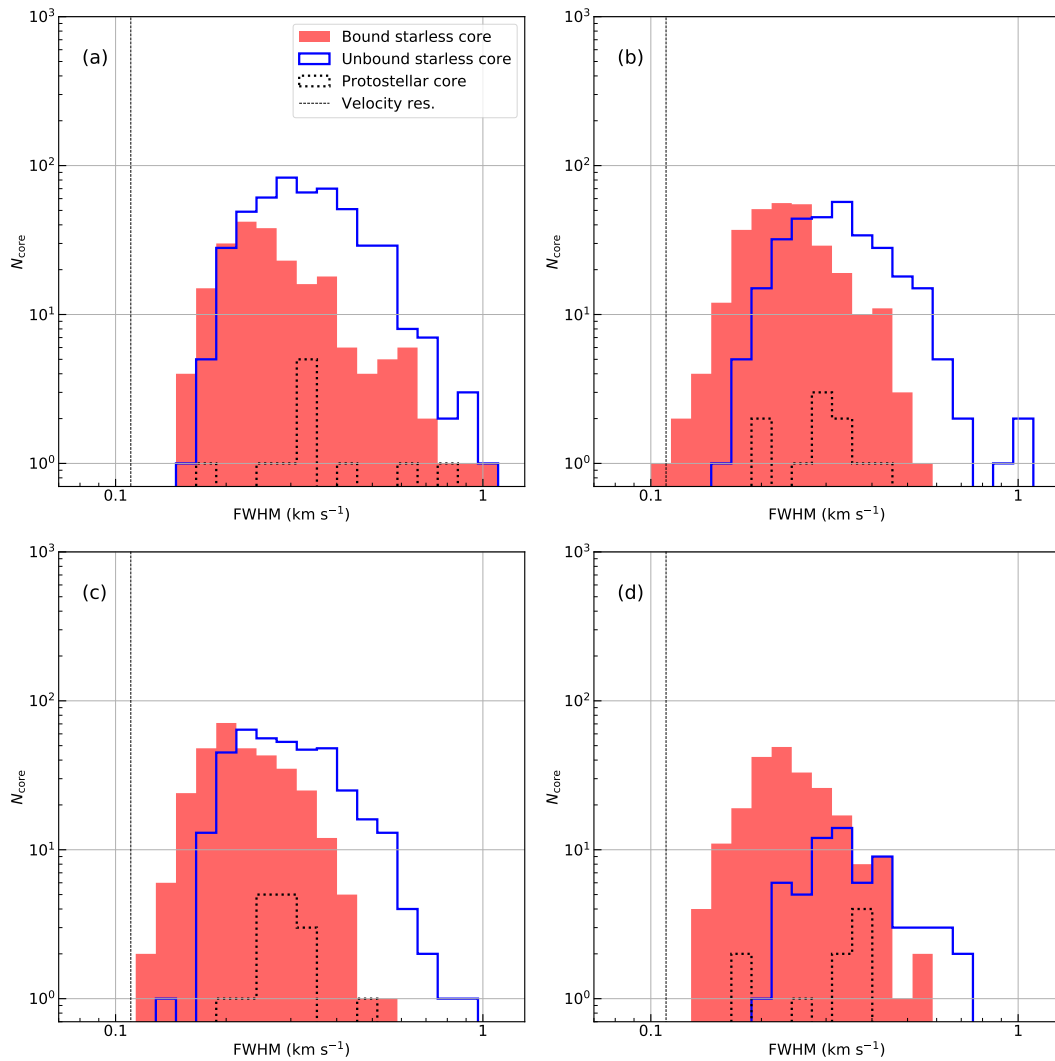


Figure 3.8: The same figure as Figure 3.6 but for velocity width in FWHM.

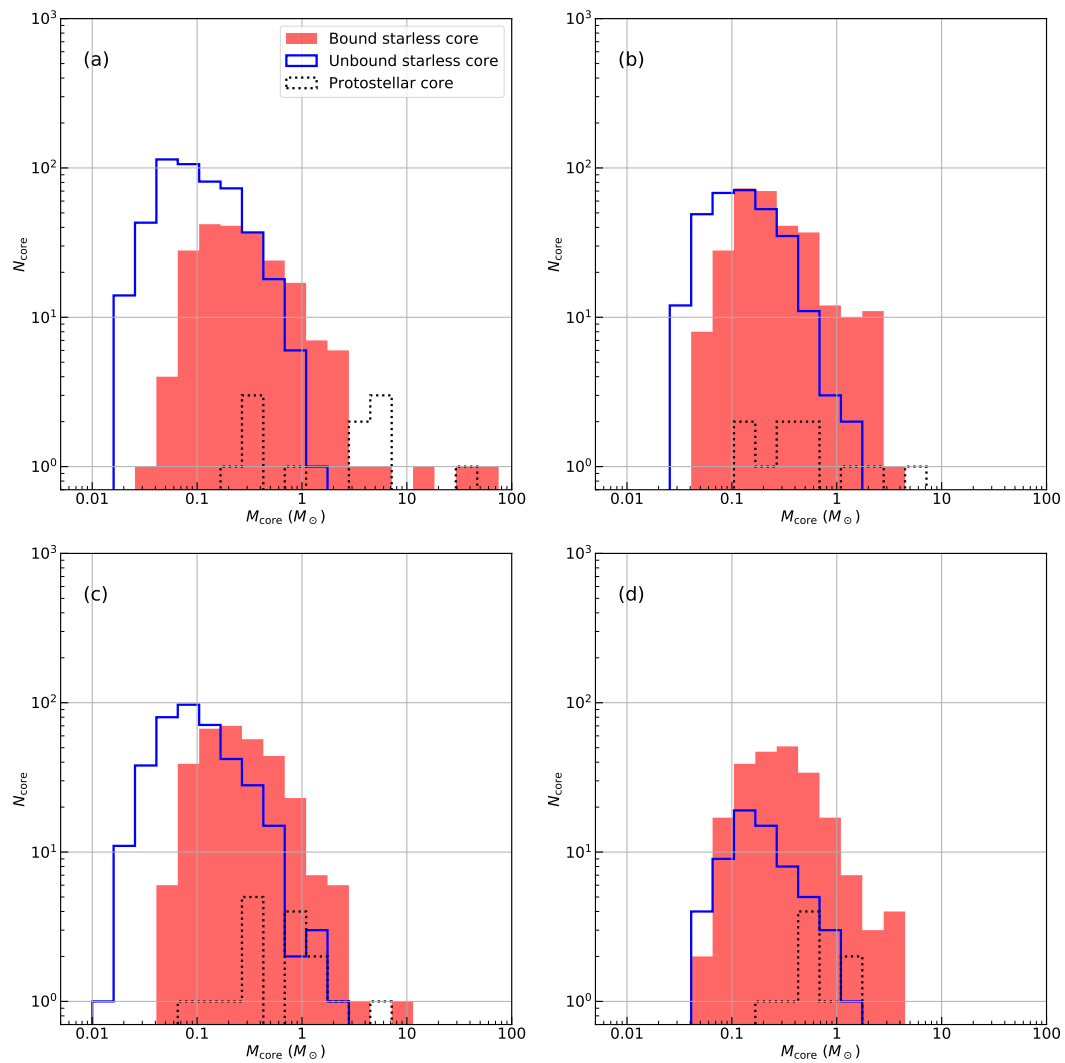


Figure 3.9: The same figure as Figure 3.6 but for core mass.

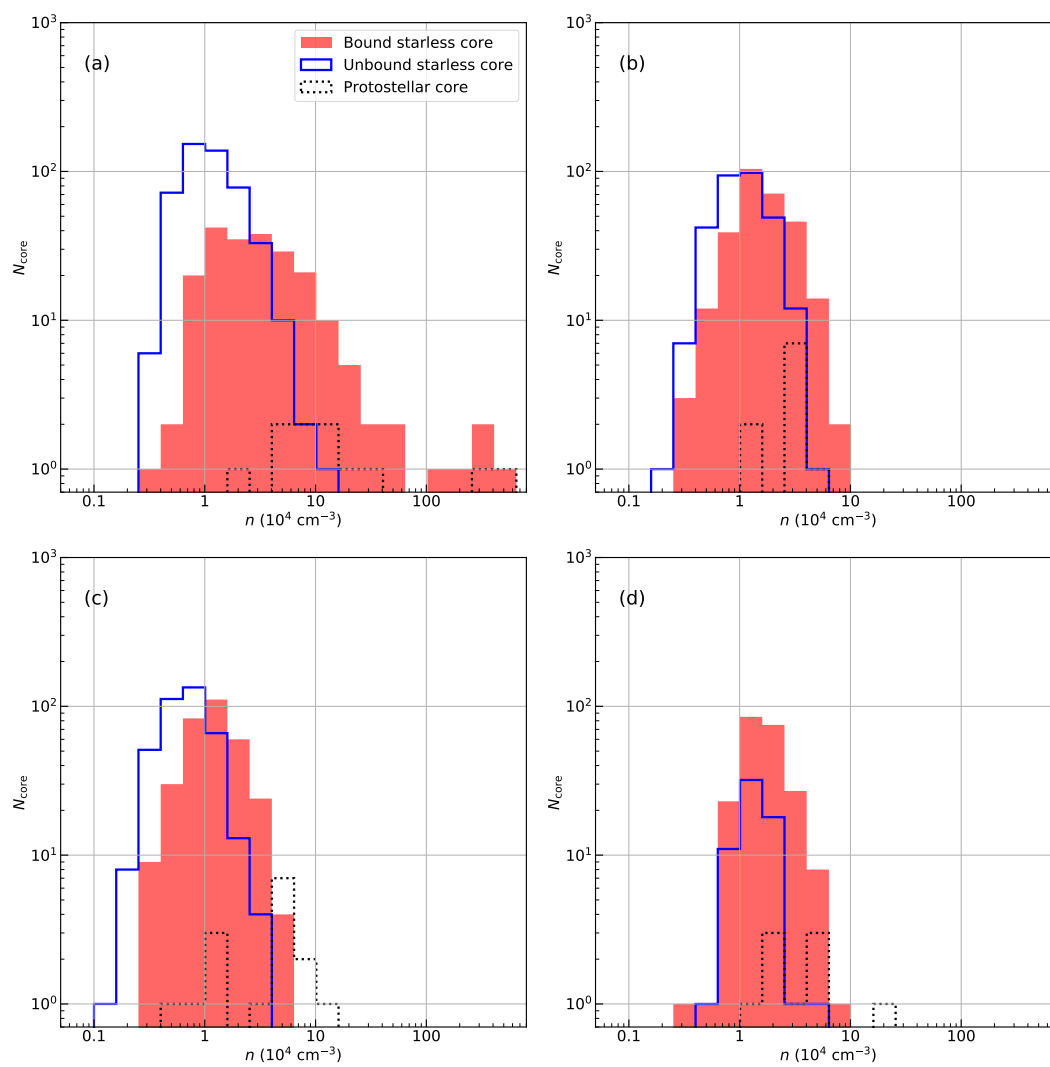


Figure 3.10: The same figure as Figure 3.6 but a core number density.

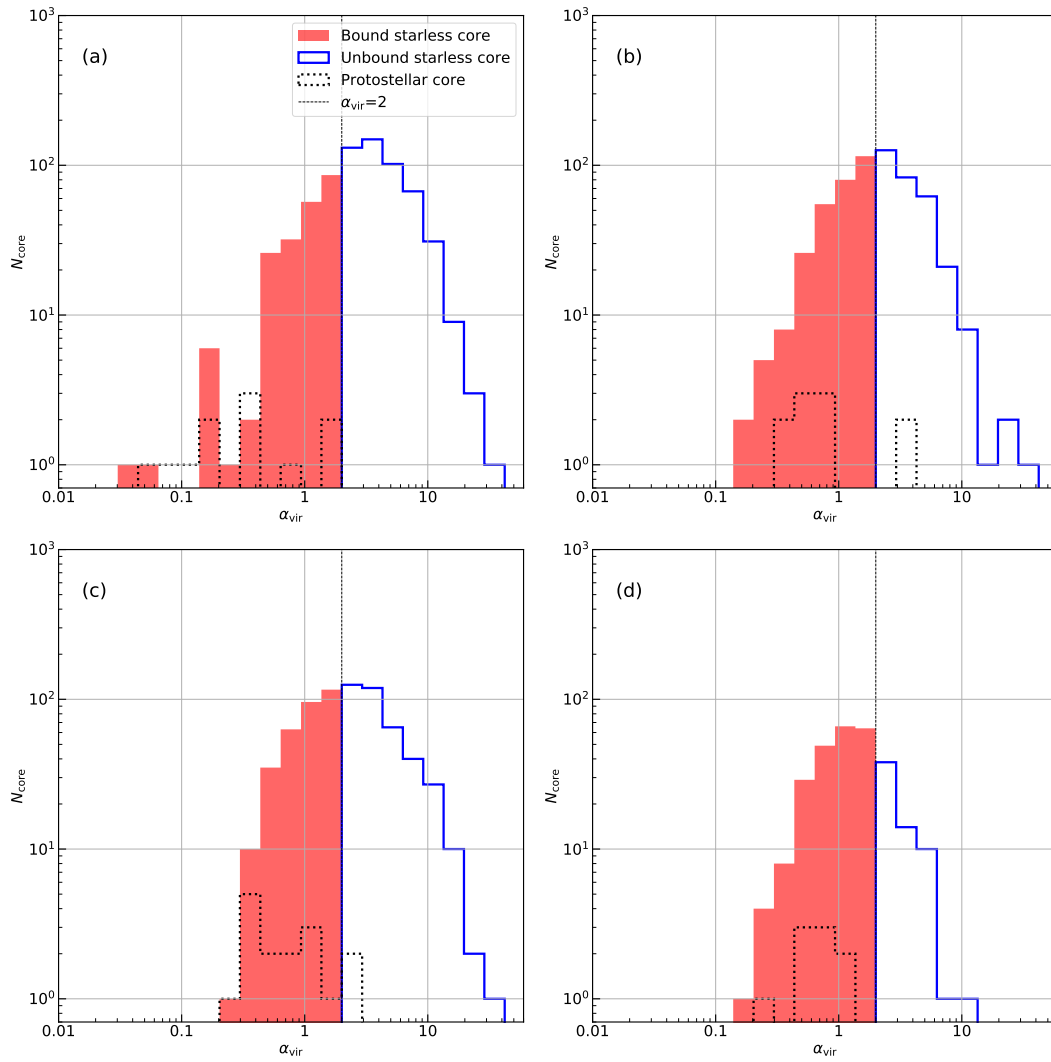


Figure 3.11: The same figure as Figure 3.6 but for virial ratio. The vertical dashed line is a boundary of bound and unbound cores at $\alpha_{\text{vir}} = 2$.

Table 3.5: The Summary Core Properties in OMC-4/5 Area

Property	Category	Minimum	Maximum	Mean \pm Std.
Diameter (pc)	Identified Core	0.034	0.206	0.077 ± 0.027
	Starless Core	0.034	0.206	0.077 ± 0.026
	Protostellar Core	0.053	0.173	0.088 ± 0.036
Aspect Ratio	Identified Core	1.03	4.97	1.90 ± 0.62
	Starless Core	1.03	4.97	1.90 ± 0.63
	Protostellar Core	1.13	2.21	1.71 ± 0.36
FWHM (km s^{-1})	Identified Core	0.11	1.04	0.30 ± 0.11
	Starless Core	0.11	1.04	0.30 ± 0.11
	Protostellar Core	0.19	0.44	0.30 ± 0.07
Mass (M_{\odot})	Identified Core	0.03	4.88	0.29 ± 0.43
	Starless Core	0.03	3.31	0.28 ± 0.38
	Protostellar Core	0.11	4.88	1.08 ± 1.40
Number Density (10^4 cm^{-3})	Identified Core	0.23	7.66	1.53 ± 0.98
	Starless Core	0.23	7.66	1.51 ± 0.96
	Protostellar Core	1.12	6.18	3.03 ± 1.31
Virial Ratio	Identified Core	0.19	39.2	2.67 ± 2.73
	Starless Core	0.19	39.2	2.69 ± 2.74
	Protostellar Core	0.31	3.21	1.10 ± 1.05

Table 3.6: The Summary Core Properties in L1641N/V380 Ori Area

Property	Category	Minimum	Maximum	Mean \pm Std.
Diameter (pc)	Identified Core	0.037	0.234	0.082 ± 0.029
	Starless Core	0.037	0.234	0.082 ± 0.029
	Protostellar Core	0.049	0.157	0.083 ± 0.031
Aspect Ratio	Identified Core	1.01	5.02	1.87 ± 0.60
	Starless Core	1.01	5.02	1.87 ± 0.60
	Protostellar Core	1.11	2.88	1.80 ± 0.51
FWHM (km s^{-1})	Identified Core	0.12	0.86	0.28 ± 0.10
	Starless Core	0.12	0.86	0.28 ± 0.10
	Protostellar Core	0.20	0.47	0.29 ± 0.06
Mass (M_{\odot})	Identified Core	0.02	8.39	0.27 ± 0.48
	Starless Core	0.02	8.39	0.25 ± 0.44
	Protostellar Core	0.08	4.93	0.98 ± 1.15
Number Density (10^4 cm^{-3})	Identified Core	0.16	11.3	1.13 ± 0.98
	Starless Core	0.16	6.05	1.05 ± 0.73
	Protostellar Core	0.62	11.3	4.51 ± 2.87
Virial Ratio	Identified Core	0.26	33.1	3.16 ± 3.30
	Starless Core	0.27	33.1	3.21 ± 3.32
	Protostellar Core	0.26	2.18	0.89 ± 0.64

Table 3.7: The Summary Core Properties in L1641C Area

Property	Category	Minimum	Maximum	Mean \pm Std.
Diameter (pc)	Identified Core	0.036	0.260	0.082 ± 0.031
	Starless Core	0.036	0.260	0.082 ± 0.031
	Protostellar Core	0.053	0.136	0.083 ± 0.029
Aspect Ratio	Identified Core	1.03	4.37	1.88 ± 0.60
	Starless Core	1.03	4.37	1.88 ± 0.61
	Protostellar Core	1.12	2.55	1.67 ± 0.48
FWHM (km s^{-1})	Identified Core	0.14	0.71	0.28 ± 0.10
	Starless Core	0.14	0.71	0.28 ± 0.10
	Protostellar Core	0.18	0.39	0.30 ± 0.08
Mass (M_{\odot})	Identified Core	0.05	4.46	0.42 ± 0.55
	Starless Core	0.05	4.46	0.41 ± 0.54
	Protostellar Core	0.24	1.59	0.75 ± 0.45
Number Density (10^4 cm^{-3})	Identified Core	0.36	17.4	1.85 ± 1.33
	Starless Core	0.36	7.00	1.75 ± 0.92
	Protostellar Core	1.55	17.4	4.86 ± 4.63
Virial Ratio	Identified Core	0.19	11.8	1.52 ± 1.19
	Starless Core	0.19	11.8	1.55 ± 1.19
	Protostellar Core	0.28	1.36	0.74 ± 0.32

3.3.2 Correlations Among the Core Physical Properties

The correlations of the physical properties of starless cores in Orion A are shown in Figure 3.12. In the figure, we present (a) velocity width – diameter relation, (b) diameter – mass relation, (c) velocity width – mass relation, and (d) virial ratio – mass relation. Despite the large dispersion, bound cores tend to have smaller velocity widths and larger masses when we compare them at the same core diameter. The best-fit functions of the velocity width – mass relations for bound and unbound cores are $\text{FWHM} \propto M_{\text{core}}^{0.23 \pm 0.01}$ and $\text{FWHM} \propto M_{\text{core}}^{0.26 \pm 0.01}$, respectively. The slopes are shallower than a dense core survey result with PPV data from numerical simulation data in Section 2.6. In the simulated PPV data analysis, core masses are underestimated due to the line-broadening. However, the effect seems to be smaller in our observed data because of the shallow slope of the velocity width – mass relation and the constructed CMFs are expected to be closer to the true CMF compared to the relation of PPP CMF and PPV CMF. From the virial ratio – mass relation, the virial ratio becomes smaller as the core mass increases.

The four relations between core properties in Figure 3.12 of four subregions are shown in Figures 3.13, 3.14, 3.15, and 3.16.

The several massive cores in the OMC-1/2/3 area significantly deviate from the relation of $R_{\text{core}} \propto M_{\text{core}}^{1/3}$ for uniform core density as seen in Figure 3.14. This might imply that the massive cores are formed by different processes other than low-mass cores, like global compressional processes. Such processes are thought to be related to global gravitational collapse, global colliding flows, cloud-cloud

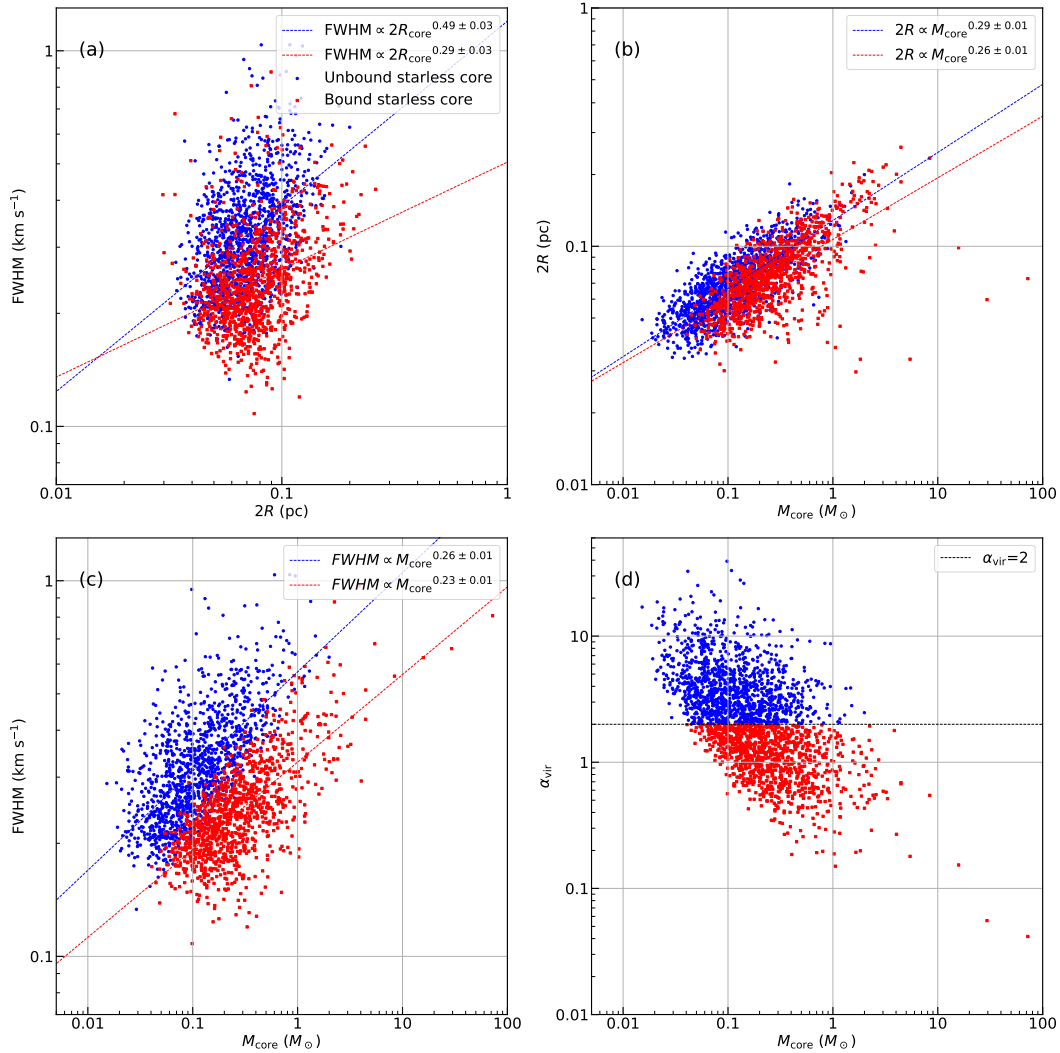


Figure 3.12: The correlations between core physical properties in Orion A: (a) The velocity width – diameter relation, (b) diameter – mass relation, (c) velocity width – mass relation, and (d) virial ratio – mass relation. The red and blue dots represent the properties of bound and unbound cores. In panels (a), (b), and (c), the best-fit functions are shown as dashed lines. In panel (d), the horizontal dashed line is drawn at $\alpha_{\text{vir}} = 2$.

collisions, or stellar feedback from supernovae and stellar winds from massive stars.

The velocity width – mass relation in each region (Figure 3.15) is still shallower than the result of analysis of simulated PPV data. Then, the CMFs in each region are also expected to resemble the true CMF.

Figures 3.17 and 3.18 show the core free-fall time – mass relation in Orion A and the subregions. Although the dispersion is large, unbound cores will likely have almost the same free-fall time. In contrast, several bound cores have small free-fall times than the other cores in Orion A. Such cores are concentrated in the OMC-1/2/3 area. Therefore, the free-fall times of bound and unbound cores in the other area also look the same. Since the number of cores with small free-fall times is small compared to the total sample size, we treat all cores as having the same free-fall time when we discuss the core evolution process.

Next, we show the core lifetime as a function of a minimum core density in Figure 3.19 following the analysis of Könyves, Ph. André, Men'shchikov, Palmeirim, et al. (2015). We used cores with a density of $> n_{\text{core}}$ on the horizontal axis and calculated the core lifetime with Equation 3.7. In Könyves, Ph. André, Men'shchikov, Palmeirim, et al. (2015), the estimated core lifetimes lie between 5 and 30 times a free-fall time. When we focus on the bound cores, the range of core lifetime is 5-30 free-fall times as the shaded regions in all subregions, which is not so much different from the results of the previous study. As described in Section 3.1.3, the number of Class II objects may be undercounted, and the core lifetime can be overestimated in the OMC-1/2/3 area. This makes our core lifetime

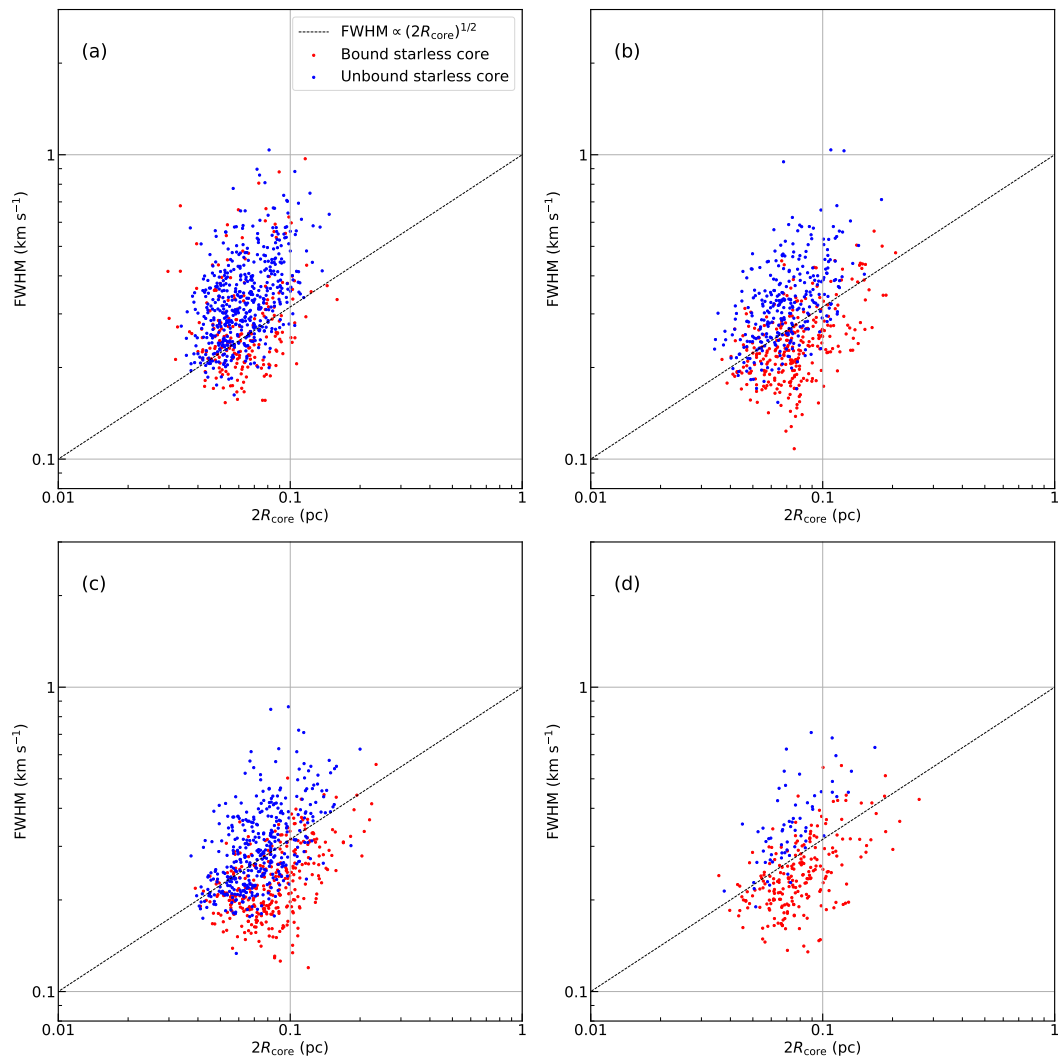


Figure 3.13: The velocity width – diameter relations of four subregions. Each panel corresponds to each subregion as Figure 3.6.

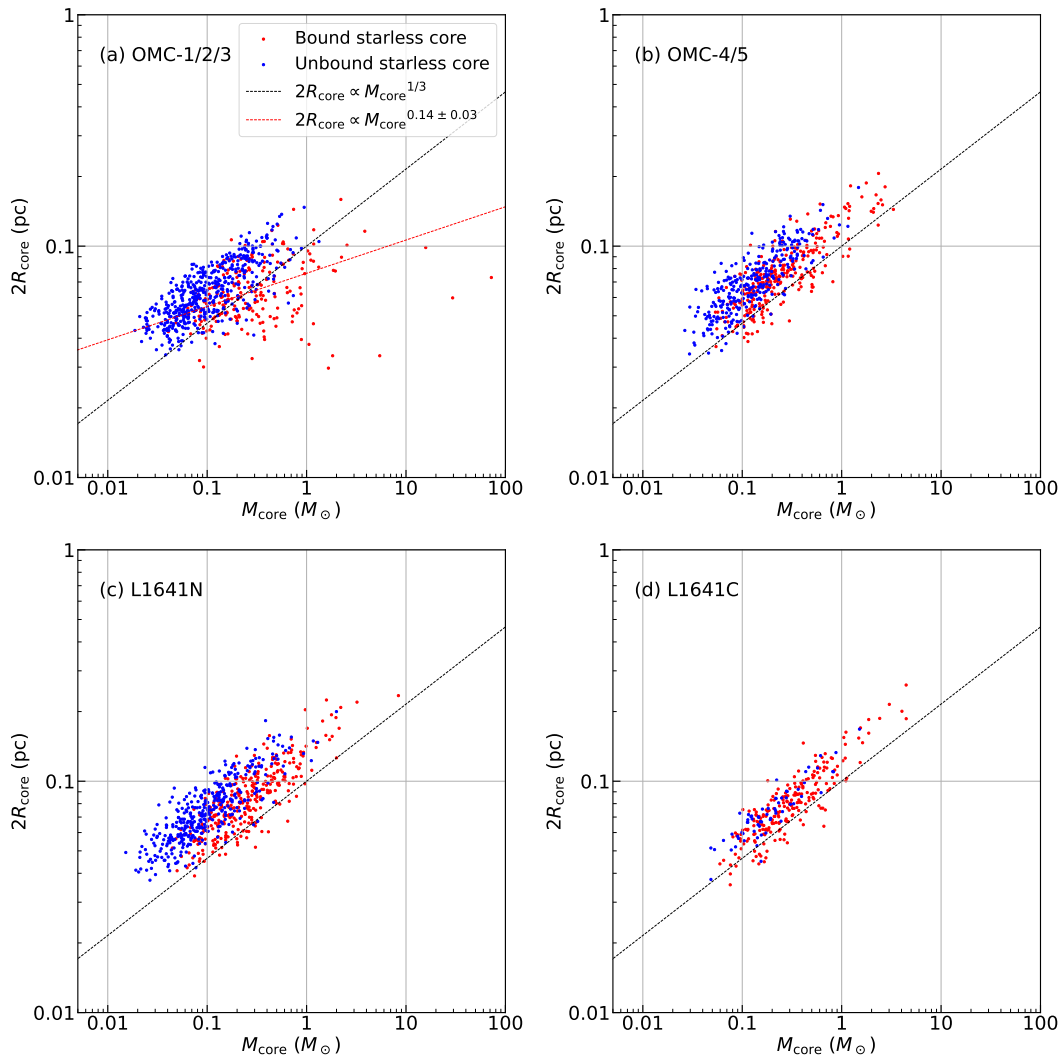


Figure 3.14: The diameter – mass relations of four subregions. The details are the same as Figure 3.13.

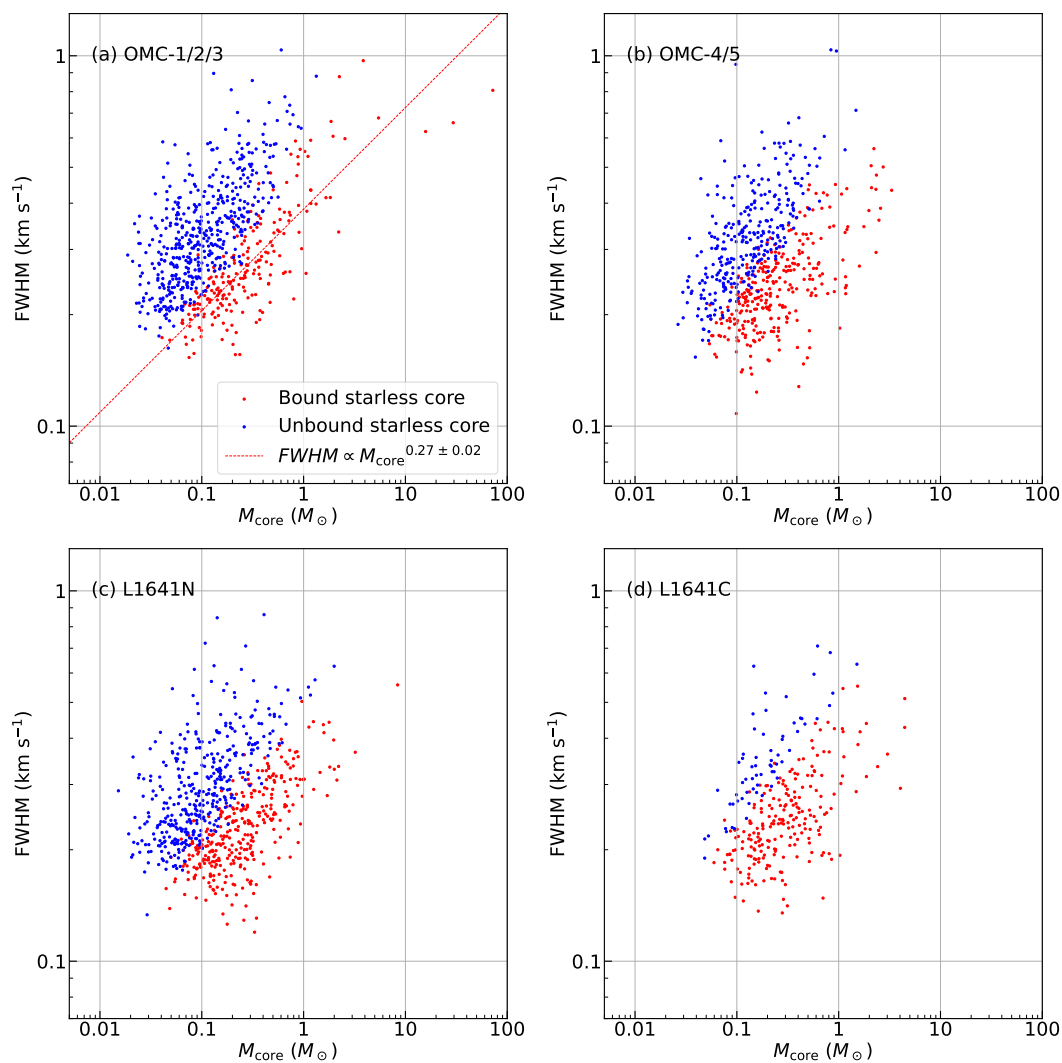


Figure 3.15: The FWHM – mass relations of four subregions. The details are the same as Figure 3.13.

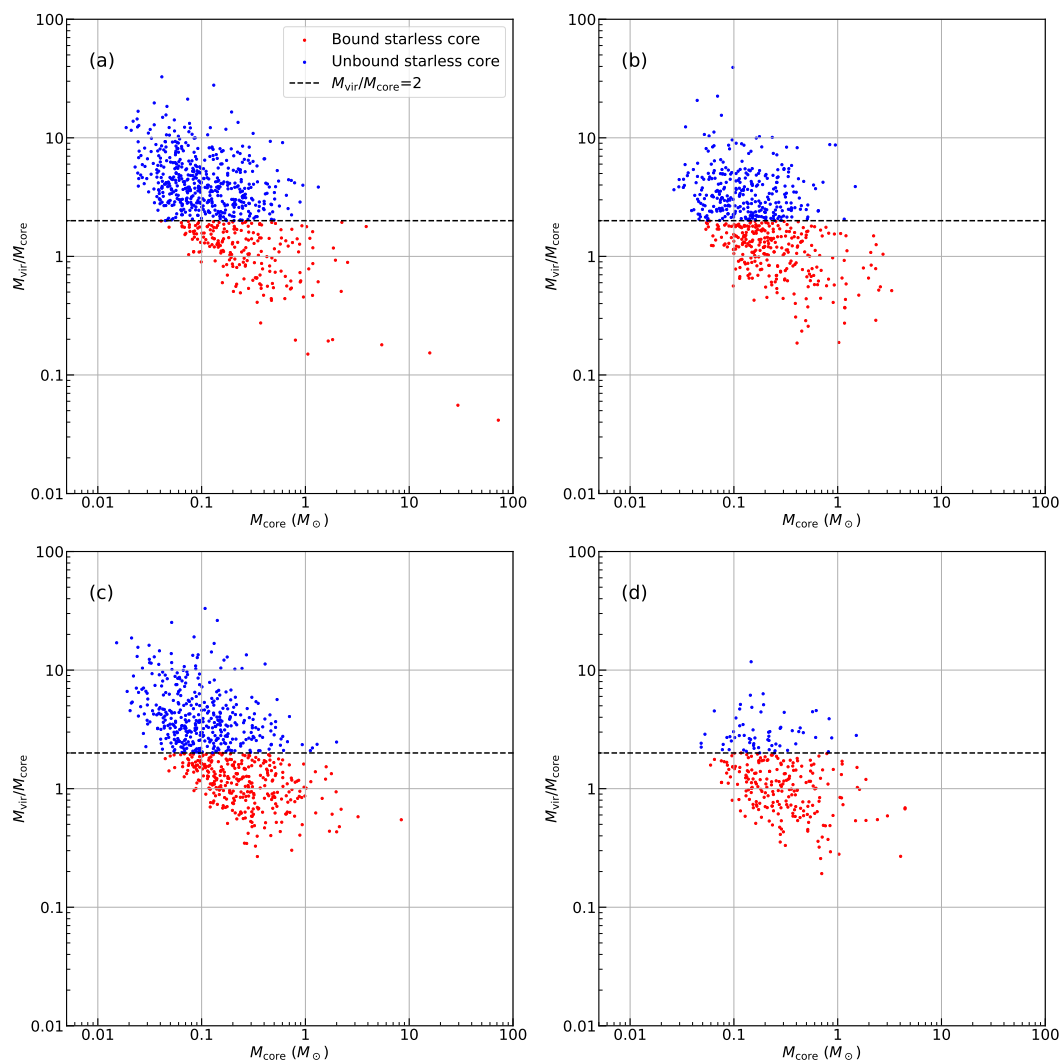


Figure 3.16: The virial ratio – mass relations of four subregions. The details are the same as Figure 3.13.

closer to the result of the previous observation. Since there are a few dense cores of $n_{\text{core}} > 10^5 \text{ cm}^{-3}$ in subregions other than OMC-1/2/3 area, the core lifetimes become shorter for such dense cores when we use all core samples in the entire cloud as shown in Figure 3.20.

For dense unbound cores of $n_{\text{core}} > 10^4 \text{ cm}^{-3}$, they have short lifetimes similar to or shorter than a core free-fall time. We think this mainly arises from the lacking of dense unbound cores. From this result, we guess the majority of unbound cores may not form stars unless they first become gravitationally bound due to mass accretion and/or external pressure.

Although our results seem to be qualitatively consistent with earlier studies, our estimated core lifetimes are slightly longer than theirs. Könyves, Ph. André, Men'shchikov, Palmeirim, et al. (2015) found that the lifetime of high-density cores of $>10^5 \text{ cm}^{-3}$ reaches one free-fall time in Serpens south region. Similar results are also shown in the Taurus region by Tokuda et al. (2020). The core lifetime estimated in Aquila Rift by Das, Basu, and Philippe André (2021) is well-fitted with the magnetically critical model. The possible reason why our estimated core lifetime becomes longer than previous observations is that cores in Orion A are more strongly magnetized than those in Aquila Rift. Actually, Hwang et al. (2021) reported that the mass-to-magnetic flux ratio is smaller than its critical value for the outer parts of the ridge in OMC-1 based on polarization observations.

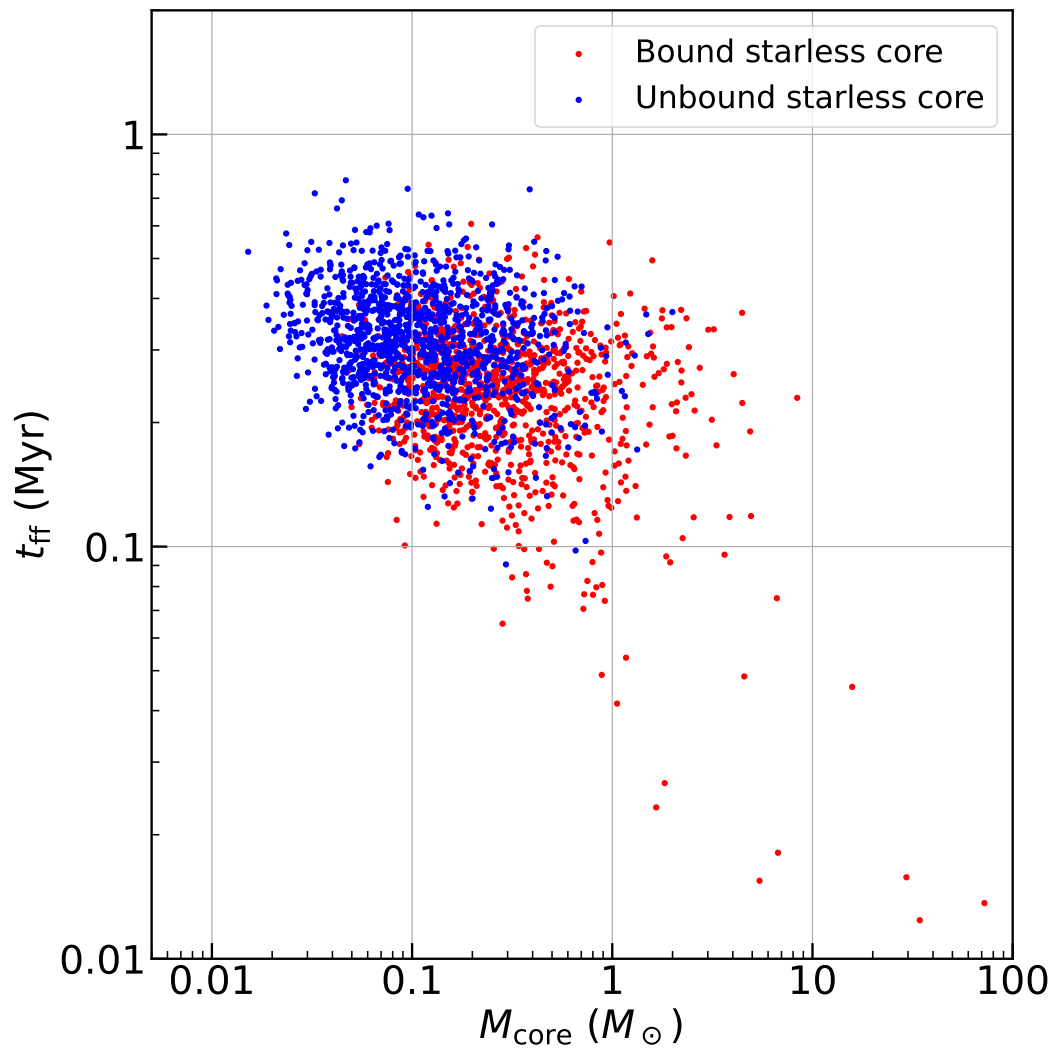


Figure 3.17: The core free-fall time – mass relation in Orion A. The red and blue dots represent bound and unbound cores.

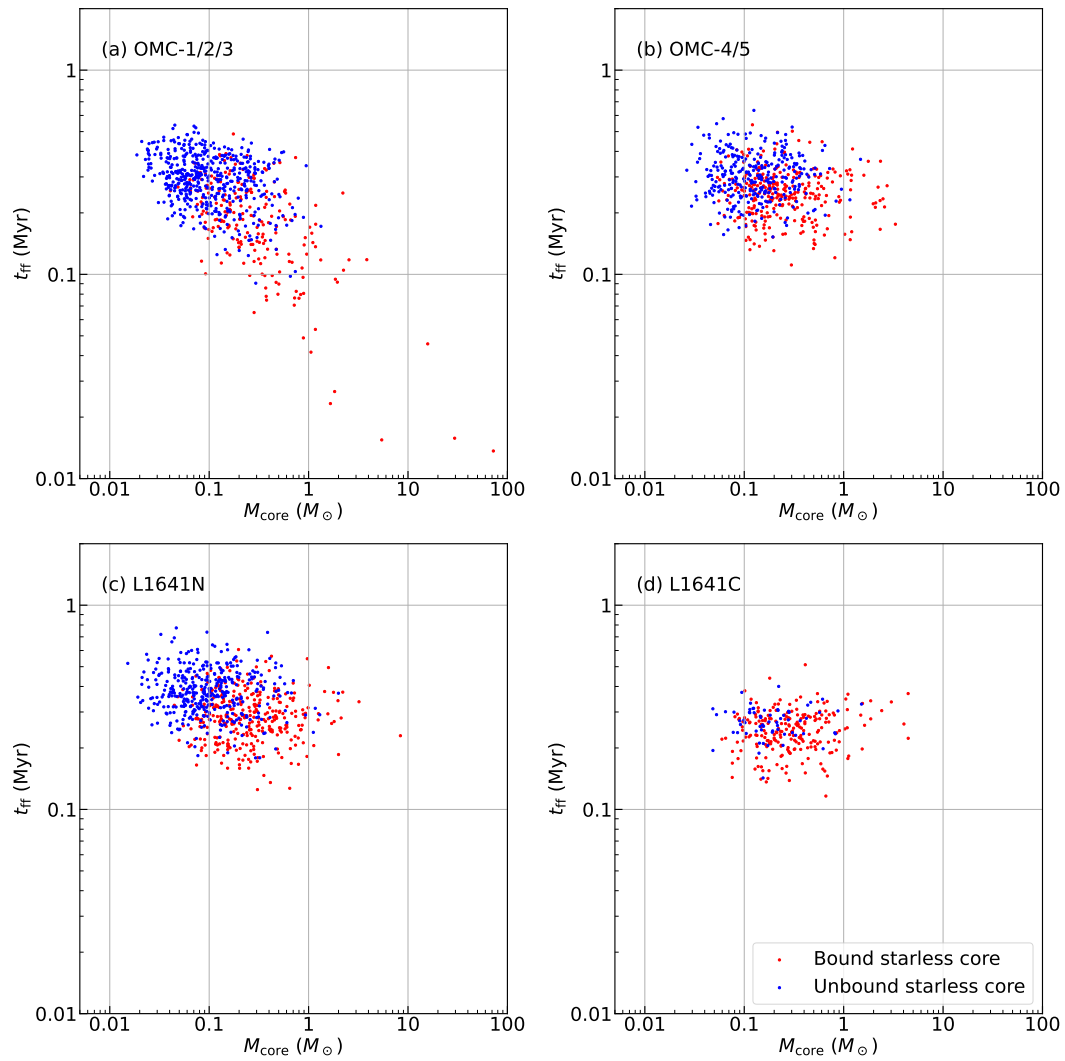


Figure 3.18: The core free-fall time – mass relation in four subregions in Orion A.

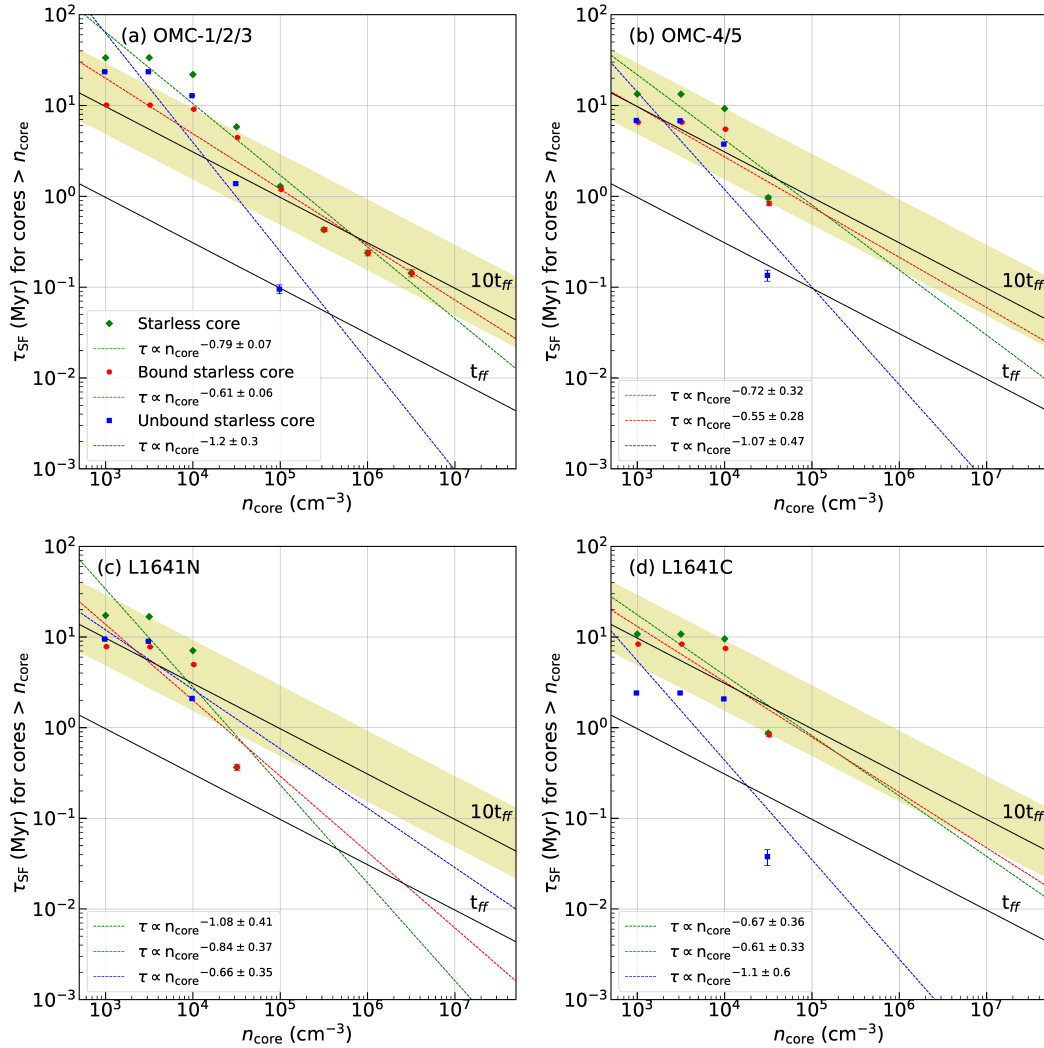


Figure 3.19: The core lifetime as a function of a minimum core density in four subregions. The green diamonds, red circles, and blue squares are for starless, bound, and unbound cores, respectively. The best-fit function of each core category is shown as a dashed line. The black lines represent $\tau_{\text{SF}} = 1 t_{\text{ff}}$ and $10 t_{\text{ff}}$ at each core density. The shaded area presents the range of τ_{SF} of $5t_{\text{ff}} \leq \tau_{\text{SF}} \leq 30t_{\text{ff}}$.

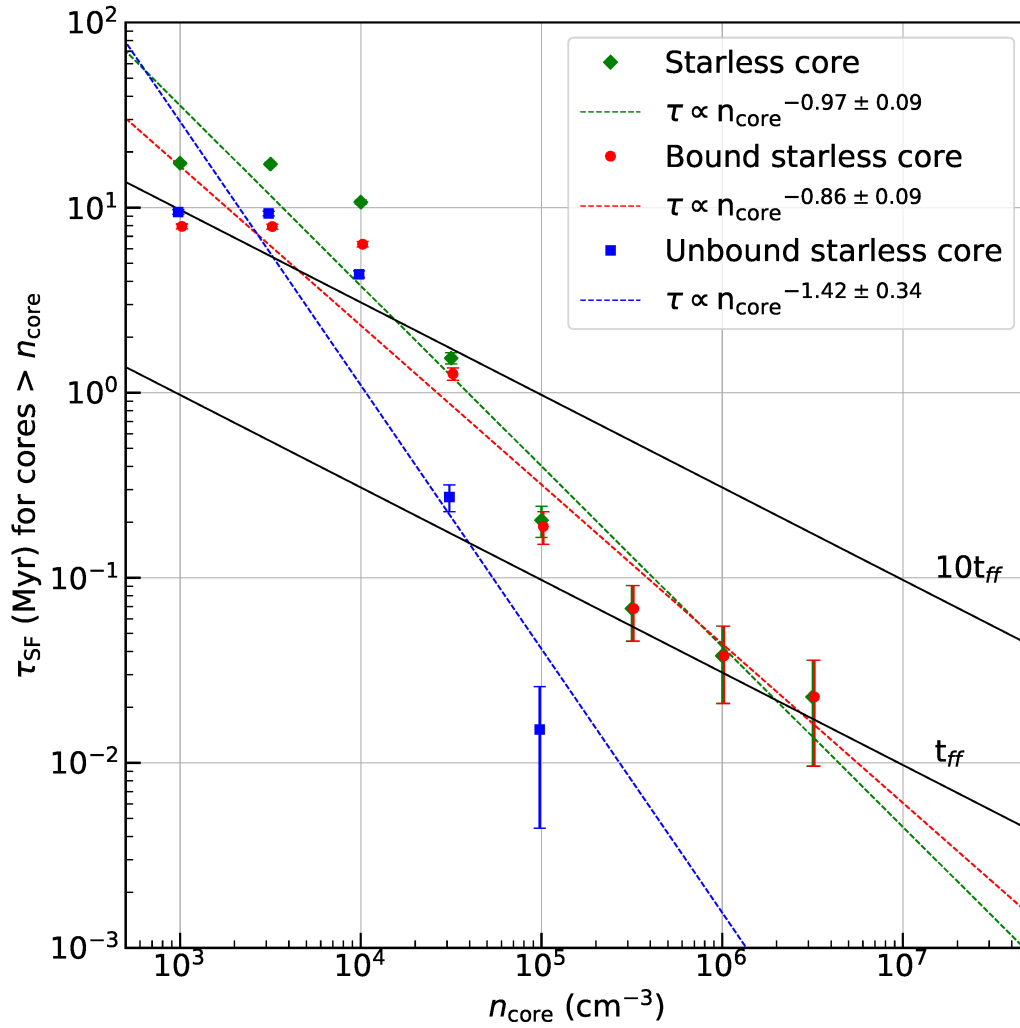


Figure 3.20: Same figure as Figure 3.19 but for Orion A.

3.3.3 Core Physical Quantities Along the Declination Axis

We investigate the core physical properties along the declination axis, focusing on four properties: the central velocity (Figure 3.21), the velocity width (Figure 3.22), the core mass (Figure 3.23), and core density (Figure 3.24). Since the dense filamentary ridge from north to south, we can see the core properties along the main filament as well in this analysis. In the figures, the core declination is represented as the offset from $-5^{\circ}30'$ in the unit of arc minute.

The gradient of central velocity from the northern region to the southern region is seen in the declination – core central velocity relation of Figure 3.21; the core central velocity in the northern region is $\sim 10 \text{ km s}^{-1}$ in panel (a) and it in the southern region is $\sim 5 \text{ km s}^{-1}$ in panel (d). The declination – core velocity FWHM relation is shown in Figure 3.22. The bound starless cores with large velocity FWHM of $\sim 1 \text{ km s}^{-1}$ concentrated at around declination of $-5^{\circ}7'$, which corresponds to OMC-1. The concentration of high-mass cores and high-density cores are seen in the declination – core mass and declination – core density relations in Figures 3.23 and 3.24. This implies significant differences in core physical properties between the OMC-1 area and the OMC-2/3 area. Besides, core properties in the OMC-2/3 area, OMC-4/5 area, L1641N area, and L1641C area seem not to have notable differences. As we discuss in Section 3.4.2, the global compression is supposed to be one of the main origins of the distinctive core properties in OMC-1.

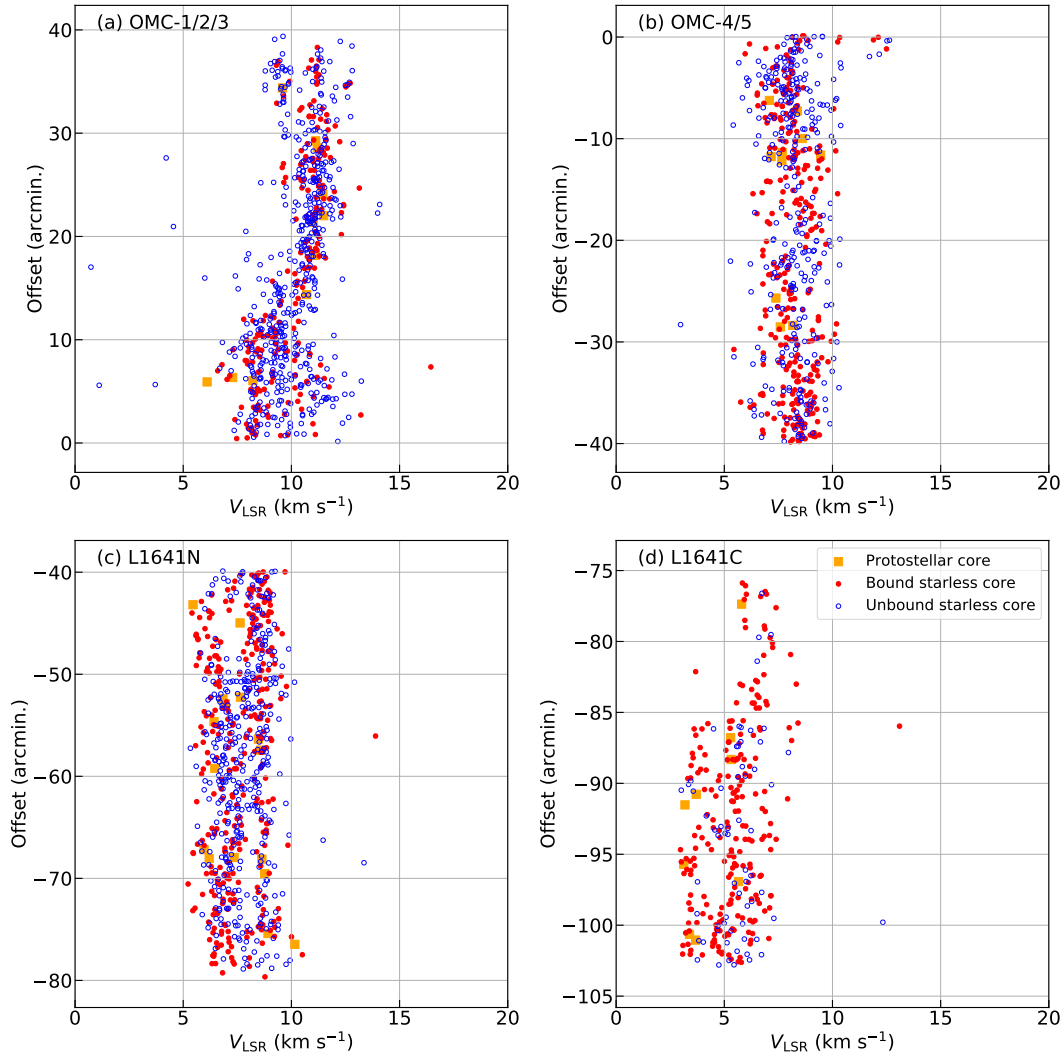


Figure 3.21: The declination – core central velocity relation in the four subregions in Orion A. The definition of the four panels is the same area as Figure 3.6. The vertical axes are the offset from $-5^{\circ}30'$ in the unit of arc minute. The red-filled circles, blue open circles, and orange squares correspond to bound starless, unbound, and protostellar cores, respectively.

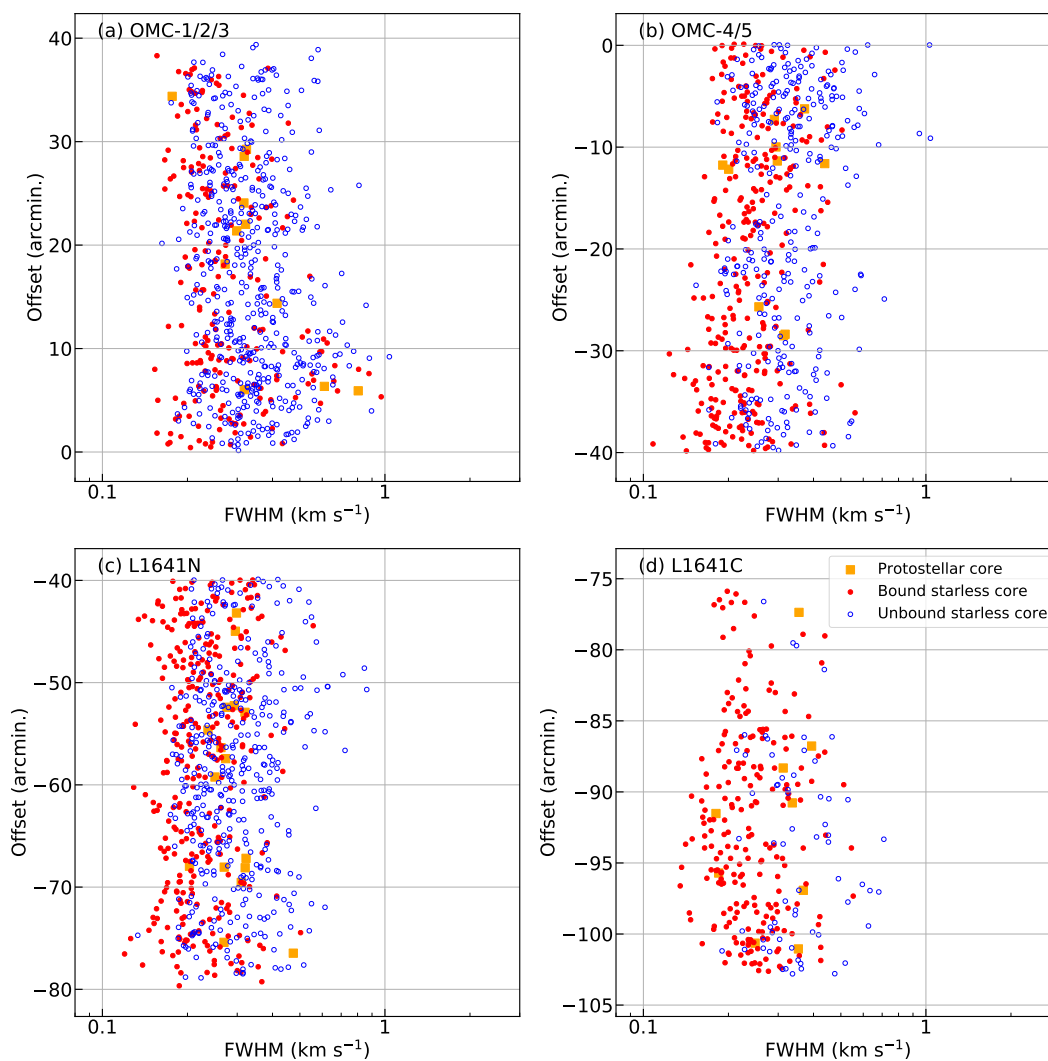


Figure 3.22: The declination – core velocity FWHM relation in the four subregions in Orion A. The details are same as Figure 3.21.

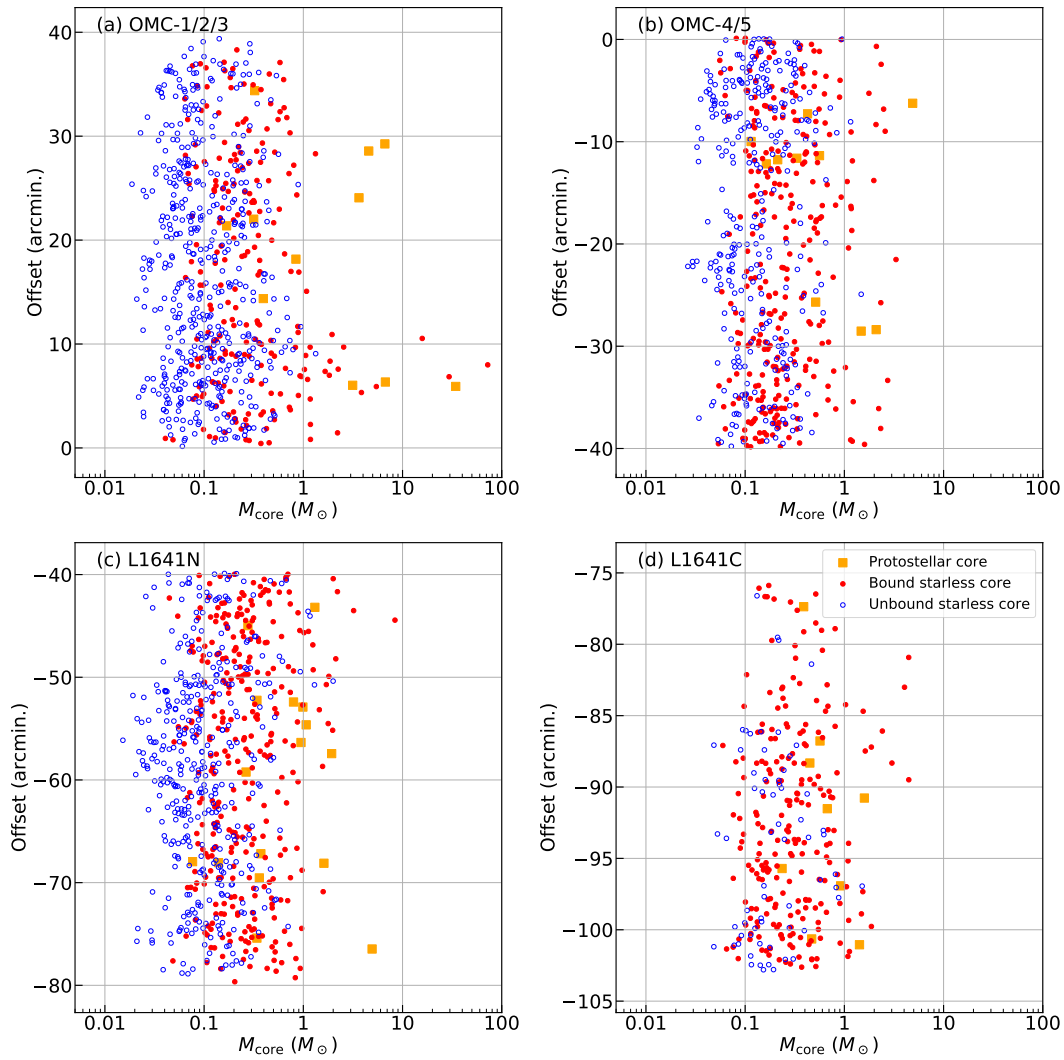


Figure 3.23: The declination – core mass relation in the four subregions in Orion A. The details are same as Figure 3.21.

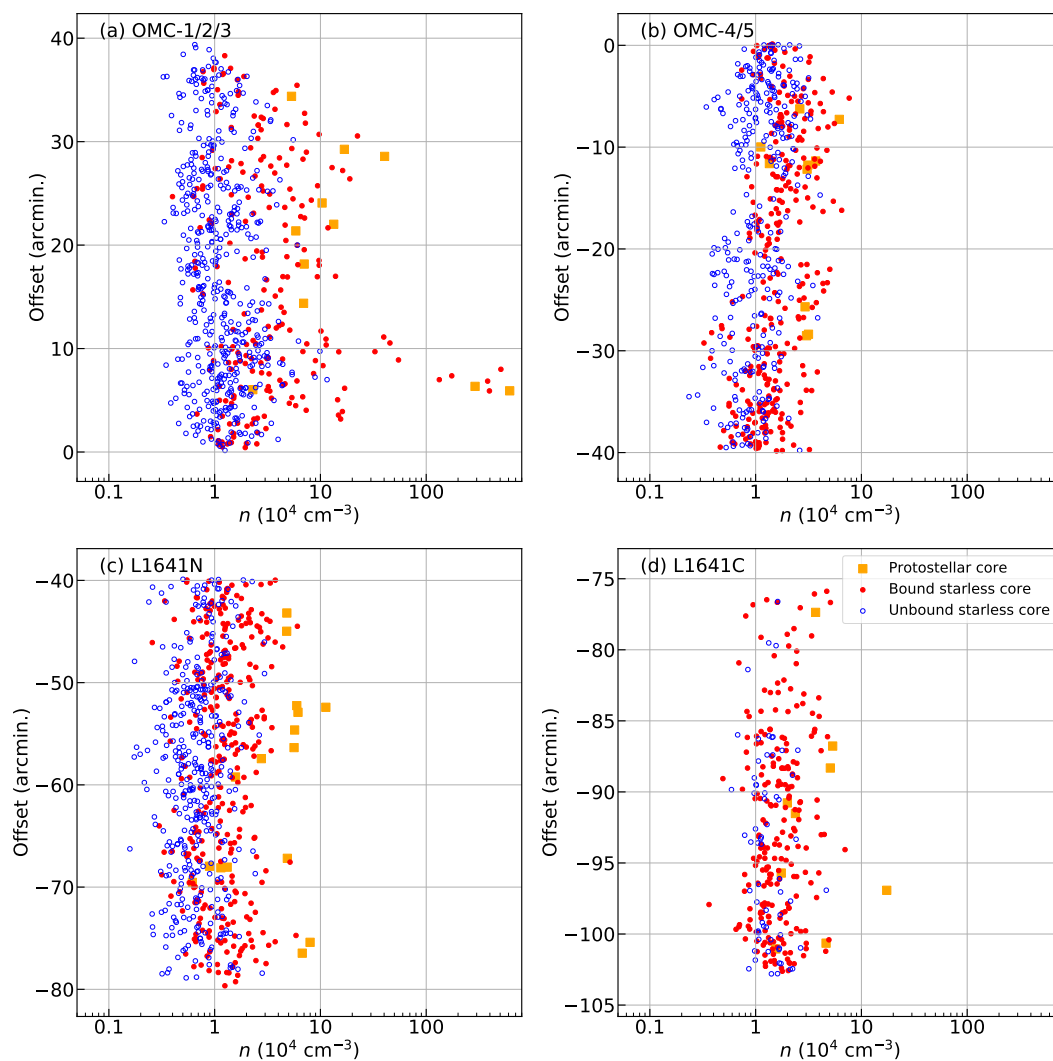


Figure 3.24: The declination – core density relation in the four subregions in Orion A. The details are same as Figure 3.21.

3.4 CMFs in Orion A

One interpretation of the shallow slope of CMF reported by [Motte, Nony, et al. \(2018\)](#) is a time evolution of the slope. However, our analysis of core lifetime does not show the apparent dependence of the core free-fall time on the core mass except for several cores located mainly in the OMC-1/2/3 area (see Section 3.3.2). Thus, we assume that the core lifetimes do not depend on the core masses, and the CMF's shape does not evolve with time. We only consider the move parallel to the core mass axis with time. In the main text, we constructed CMFs with uniform sized bins. Then, based on the analysis of PPV data from numerical simulation in Section 2.6, we constructed CMFs with variably sized bins and show them in Appendix B.3.

In order to discuss the turnover mass of CMF, we estimated the completeness of core identification, and we describe the procedure in this section. We note that this method is the same as [Takemura, Nakamura, Kong, et al. \(2021\)](#) and [Takemura, Nakamura, Ishii, et al. \(2021\)](#).

- (1) Created a three-dimensional artificial gaussian core in a PPV space for each mass bin of CMF and fixed the mass to the central mass of each mass bin in a log scale.
- (2) Calculate dispersion along the position and velocity axes as a size of an artificial gaussian core from a core size - mass relation and a velocity width - mass relation. Core size is derived as $\sqrt{\sigma_{\text{major}}\sigma_{\text{minor}}}$, where the major axis of the projection onto the plane of sky derived from the intensity weighted the

second moment in the direction of most prolonged elongation and that in the direction perpendicular to the major axis which is included in the output of Dendrogram.

- (3) Converted the core mass to $C^{18}O$ ($J=1-0$) LTE flux based on the assumptions of optically thin emission and LTE condition. The excitation temperature and abundance ratio of $C^{18}O$ to H_2 are set to $T_{\text{ex}} = 20$ K and $X_{C^{18}O}$ (Takemura, Nakamura, Ishii, et al. 2021).
- (4) Insert one artificial gaussian core to the trunks of observed PPV data avoiding overlap with the true cores.
- (5) Apply Dendrogram to the data with the same input parameter in Section 3.2.1 and check whether the inserted core is identified as an individual leaf.
- (6) Repeat the (4) and (5) procedures 1000 times for each mass bin and compute the detection probability of the inserted core.
- (7) Define the completeness limit as the lowest-mass bin with a detection probability larger than 90%.

In addition to the completeness limit, we estimated the mass detection limit based on the observational noise level and the Dendrogram's input parameter. The mass detection limit is defined as the smallest mass, which satisfies our selection threshold of core identification in Section 3.2.1. The total $C^{18}O$ ($J=1-0$) flux of the core is calculated as $4\sigma \times 1 \text{ pixel} + 3\sigma \times (60-1) \text{ pixels}$. In the CMFs of our analysis, we only show the completeness limit since the mass detection limit is $\sim 0.016 M_{\odot}$, which is much smaller than the completeness limit.

Table 3.8 shows the CMF's properties in Orion A and its subregions, and we

discuss their properties in Sections 3.4.1 and 3.4.2. The turnover mass is a central mass of the turnover mass bin in a log scale of each CMF. From the discussion of unbound cores in Section 3.3.2, we focus on the CMF with bound starless cores there.

Table 3.8: The Summary of CMF Properties in Orion A and its Subregions

Region	Category	Turnover Mass (M_{\odot})	High-mass Slope Power-law index \pm Error	Highest Mass (M_{\odot})
Orion A	Identified Core	0.07	-2.20 ± 0.06	72.21
	Starless Core	0.07	-2.25 ± 0.10	72.21
	Bound Starless Core	0.10	-2.18 ± 0.11	72.21
(a) OMC-1/2/3 area	Identified Core	0.04	-1.89 ± 0.06	72.21
	Starless Core	0.04	-1.93 ± 0.10	72.21
	Bound Starless Core	0.10	-1.77 ± 0.11	72.21
(b) OMC-4/5 area	Identified Core	0.07	-2.35 ± 0.11	4.88
	Starless Core	0.07	-2.20 ± 0.07	3.31
	Bound Starless Core	0.10	-2.03 ± 0.08	3.31
(c) L1641N area	Identified Core	0.07	-2.48 ± 0.14	8.39
	Starless Core	0.07	-2.44 ± 0.15	8.39
	Bound Starless Core	0.10	-2.41 ± 0.17	8.39
(d) L1641C area	Identified Core	0.15	-2.44 ± 0.26	4.46
	Starless Core	0.15	-2.41 ± 0.25	4.46
	Bound Starless Core	0.15	-2.34 ± 0.24	4.46

3.4.1 CMFs in Entire Cloud

The CMFs of identified cores, starless cores, and bound starless cores in Orion A are shown in Figure 3.25 (a). Figure 3.25 (b) consists of CMF for bound starless cores in Orion A and IMF in the ONC region (Takemura, Nakamura, Kong, et al. 2021). We note that the definition of the mass bin is slightly different from IMF shown in (Takemura, Nakamura, Kong, et al. 2021), and then, the turnover mass and power-law indices are also slightly changed. The turnover masses of CMFs for starless cores and bound starless cores in Orion A are $\sim 0.07 M_{\odot}$ and $\sim 0.10 M_{\odot}$. Then, their slopes are -2.25 ± 0.10 and -2.18 ± 0.11 . We derived a best-fit

single power-law function between two mass bins higher than the turnover and the high-mass end of each CMF.

The ONC IMF has a turnover at $\sim 0.20 M_{\odot}$ which is near to the turnover of CMF for bound cores in Orion A as well as the ONC CMF (Takemura, Nakamura, Kong, et al. 2021). The slopes of Orion A CMF and ONC IMF, which have a slope of -2.44 ± 0.18 are also not distinguishable when we take into account the uncertainties. Therefore, mass accretion from the surrounding material is expected to explain the relationship between observed CMF–IMF.

3.4.2 CMFs in Subregions in Orion A

Figure 3.26 shows the CMFs in four subregions in Orion A. Their properties are summarised in Table 3.8. All CMFs for bound cores have a similar turnover massed at $\sim 0.1\text{--}0.2 M_{\odot}$, but we see differences on the slopes above the turnovers. While the CMFs for bound cores have a Salpeter-like slope in L1641N/V 380 Ori area and L1641C area, the CMFs' slopes in the OMC-1/2/3 area and OMC-4/5 area are shallower than a Salpeter-like slope. Significantly, the CMF's slope in OMC-1/2/3 area of -1.77 ± 0.11 is remarkably shallower than IMF. Another feature of OMC-1/2/3 CMF is that it extends to a higher mass of $\geq 10 M_{\odot}$. In L1641N/V 380 Ori area, there is only one high-mass core of $\sim 10 M_{\odot}$ that is the most massive core in the area. For the other two subregions, the maximum core mass is as small as $\sim 5 M_{\odot}$. Therefore, this suggests that cutoff mass at the high-mass end of CMF depends on the cloud environment, and this will take over to IMF if the one-to-one correspondence between stellar mass and core mass exits as suggested in (Hsu et al.

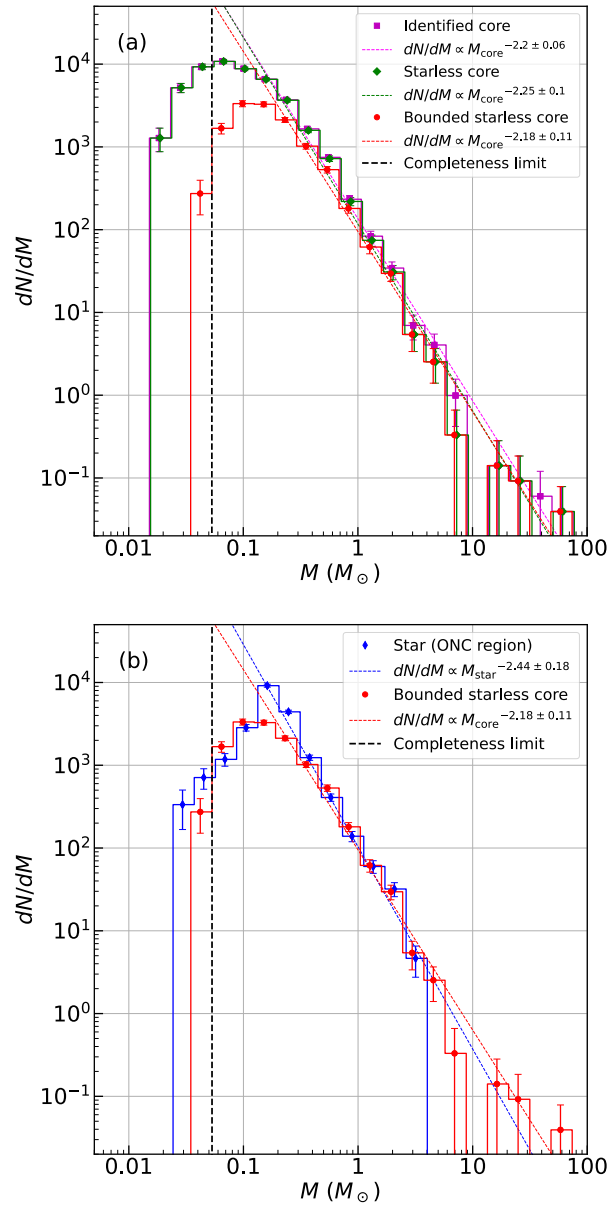


Figure 3.25: (a) The observed CMFs for identified cores (magenta), starless cores (green), and bound starless cores (red) in Orion A. The error bars show the statistical uncertainty calculated as the square root of the number of cores in each mass bin, $\sqrt{N_{\text{core}}}$. The dotted colored lines show the best-fit power-law functions of each CMF between two mass bins above the turnover and the high-mass end. The vertical dashed line is a completeness limit. (b) The CMF for bound starless cores in Orion A and IMF in the ONC region (blue). The configuration of panels is changed from the paper.

2013).

So far, we have discussed the CMF property when CMF's shape does not evolve with time. Then, investigate the time evolution of CMF here since several massive cores in the OMC-1/2/3 area have shorter free-fall times compared to the other cores. The high-mass end of OMC-1/2/3 CMF of $\geq 10 M_{\odot}$ may be affected by the time evolution. On the other hand, a CMF with other lower-mass cores is thought to be less affected by the effect. When CMF evolves with time, the high-mass part of CMF is expected to get steeper as star formation proceeds because of the different timescale of star formation between low- and high-mass cores. The time evolution that steepens a CMF is not ruled out, but such evolution appears to contradict the recent proposal of CMF evolution (Motte, Nony, et al. 2018). In addition, the expected steep slope is not observed in this study either and our results support the later evolution of a CMF.

However, specifying the most crucial process that made Orion A is not easy. For example, a cloud-cloud collision process can create a filamentary ridge as a northern part of Orion A through an off-center collision of two clouds (Wu et al. 2017; Lim et al. 2021; Yasuo Fukui, Habe, et al. 2021). The gravitational contraction along the main ridge toward OMC-1 is pointed out by Hacar et al. (2017). What is interesting is that L1641N/V380 Ori area contains several intermediate-mass cores, and the properties of these intermediate-mass cores look similar to other lower-mass cores, even though intermediate-mass cores extend the CMF to slightly larger masses. Nakamura, Miura, et al. (2012) discussed the possibility of a cloud-cloud collision of this area, L1641N/V380 Ori area. In the northern part, OMC-1/2/3 area,

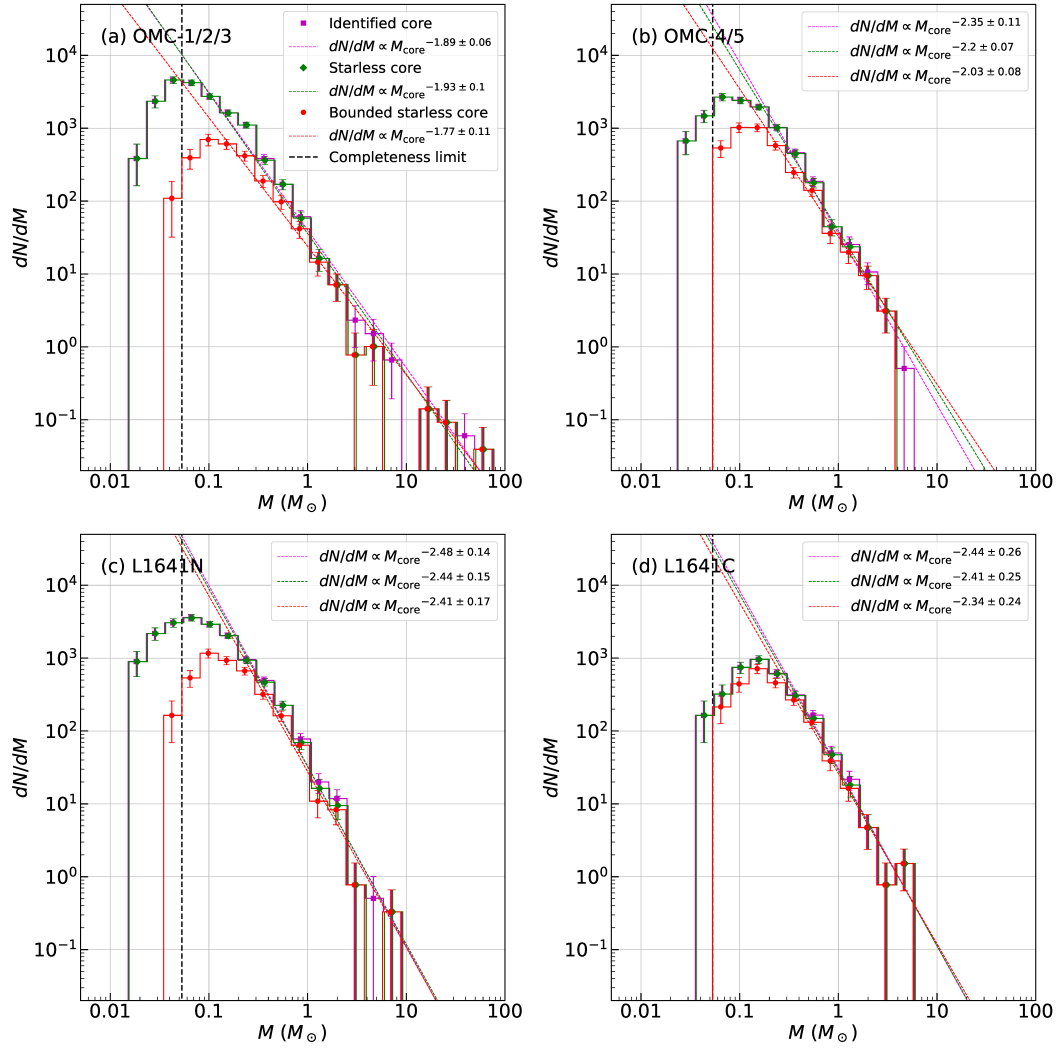


Figure 3.26: The CMFs of subregions in Orion A and each panel correspond to each subregion. The details are same as Figure 3.25 (a).

compression with supernovae and star formation triggered by that is suggested (Bally 2010; Kounkel 2021). In addition, it is shown that the global colliding flows can also create similar filamentary structures by Ntormousi et al. (2011) and Gómez and Vázquez-Semadeni (2014). Moreover, Hartmann and Burkert (2007) also showed that the global gravitational collapse of a sheet-like cloud creates colliding flows that form the Orion A-like structure.

3.5 Core Growth with Mass Accretion from Surrounding Material

As seen in Section 3.3.1, protostellar cores tend to have larger masses than the starless cores, and this probably indicates that the starless cores grow with mass accretion of the surrounding material. We investigate the accretion process by estimating the mass accretion rate in two different ways, as follows.

- (1) The accretion rate required to double the core mass within the typical core lifetime of 10 times of a core free-fall time, $\dot{M}_{\text{required}}$.
- (2) The Bondi-Hoyle-Lyttleton accretion rate from a typical clump, \dot{M}_{Bondi} .

In case (1), the mass ratio of a star and a final core mass corresponding to SFE in a core-collapse star formation scenario is 0.5. The accretion rate is calculated as

$$\begin{aligned} \dot{M}_{\text{required}} &= \frac{M_{\text{core}}}{10t_{\text{ff}}} \\ &\sim 6.5 \times 10^{-7} \left(\frac{M_{\text{core}}}{1 M_{\odot}} \right) \times \left(\frac{n_{\text{core}}}{4 \times 10^4 \text{ cm}^{-3}} \right)^{1/2} M_{\odot} \text{ yr}^{-1}. \end{aligned} \quad (3.8)$$

This accretion rate is proportional to core mass, and the core growth with this accretion rate shifts a CMF to the right without changing its shape. The accretion rate of Bondi accretion is computed as

$$\begin{aligned} \dot{M}_{\text{Bondi}} &= \frac{\pi \rho G^2 M^2}{\sigma^3} \\ &\sim 4.1 \times 10^{-9} \left(\frac{n_{\text{clump}}}{10^3 \text{ cm}^{-3}} \right) \times \left(\frac{M_{\text{core}}}{1 M_{\odot}} \right)^2 \left(\frac{\sigma_{\text{clump}}}{1 \text{ km s}^{-1}} \right)^{-3} M_{\odot} \text{ yr}^{-1}, \end{aligned} \quad (3.9)$$

where we set a density and a velocity dispersion of a typical clump to 10^3 cm^{-3} and 1 km s^{-1} (e.g. [Krumholz and Christopher F. McKee 2008](#); [Kong, Arce, Feddersen, et al. 2018](#)). Comparing the Equations 3.8 and 3.9, Bondi accretion from a typical clump is too small to grow the cores within a reasonable timescale. A special situation like the gravitational contraction of gravitationally unstable clumps can achieve a high accretion rate through Bondi accretion. Such a situation is expected in competitive accretion or global gravitational collapse models ([Ian A. Bonnell and Matthew R. Bate 2006](#); [Vázquez-Semadeni et al. 2019](#)) and mass converging flow along dense filaments in the inertial-inflow model ([Padoan, Pan, et al. 2020](#); [Pelkonen et al. 2021](#)). The dense clumps or filaments are needed for the high mass accretion rate, but it is not achieved in most of the observed areas in Orion A except for the OMC-1 area.

Another concern of core growth with Bondi accretion is that the mass accretion rate is proportional to M_{core}^2 , which changes the slope of CMF as cores grow. In order to check whether a CMF's slope changes when the mass accretion rate is proportional to M_{core}^2 , we used identified bound starless cores in Orion A. We

assumed that mass accretion continues until $1 M_{\odot}$ core obtains another $1 M_{\odot}$ from the surrounding cloud. Here we assumed that there is enough amount of material to grow all cores around cores. The resultant CMF is shown in Figure 3.27, and the power-law index of CMF evolves from -2.18 ± 0.11 to -1.62 ± 0.08 by the mass accretion. Even if we fit the CMF below $100 M_{\odot}$, the evolved CMF has a slope of -2.02 ± 0.05 . Then, the result means that CMF's slope changes with Bondi accretion as core growth proceeds. The analytical study from the filament to cores by S.-i. Inutsuka (2001) (see Section 1.7.3) suggests that even if the mass accretion along a filament is taken into account, a CMF always has Salpeter's IMF-like slope except for the first one free-fall time. Then, the Bondi accretion contradicts the suggestion.

In any case, a high mass accretion rate is expected when a large amount of material surrounds the core. Since J. C. Tan et al. (2014) provides the mass accretion rate in the clump-fed model as a function of column density (see Equation 1.3), we construct CMFs by setting the threshold of column density at positions of cores in Appendix B.4.

The larger masses of protostellar cores than starless cores can be explained by merging among dense cores. If this is a dominant core growth process, the feature of frequent core merging should be observed, but we do not have clear evidence of it. In addition, whether the shape preserves during the core evolution is unclear, and various CMFs are expected to observe so far, but we do not have such results either.

We expect that the future observations of various star-forming regions in differ-

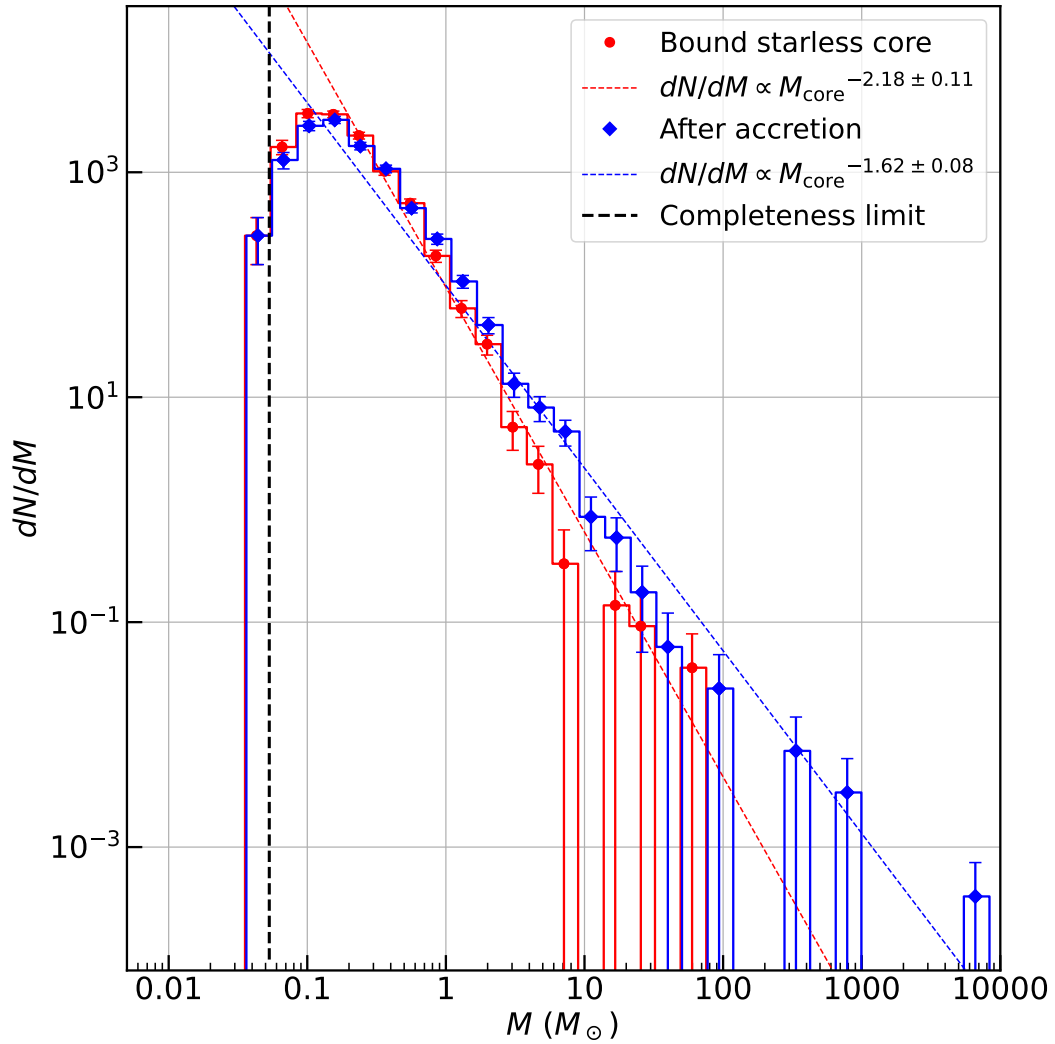


Figure 3.27: The CMF of bound starless cores in Orion A (red) and predicted CMF with Bondi accretion (blue). The details are same as Figure 3.25 (a).

ent star formation stages have a clue to reveal the properties of core growth.

3.6 Summary of This Chapter

We conducted a dense cores survey in Orion A using the CARMA+NRO45-m combined C¹⁸O ($J=1-0$) data. Then, we provide the complete core catalog in [Takemura, Nakamura, Arce, et al. \(2023\)](#). We accomplished the [Remaining task 2] in Section 1.10 by providing the catalog. We note that this study is one of the widest-field (1×3 degree²) unbiased dense core surveys in Orion A with a high spatial resolution ($8'' \sim 3000$ AU). We list the principal results and discussions of this Chapter as follows.

1. We identified 2341 cores by applying astrodendro to the observed C¹⁸O ($J=1-0$) PPV data and several additional selection criteria as Section 3.2.1. Then, we grouped the identified cores into two categories of starless and protostellar cores with the VISION protostar catalog, and each category contains 2295 cores and 46 cores, respectively.
2. The protostellar cores tend to have larger masses, higher density, and a smaller virial ratio compared to starless cores. The differences probably indicate that the prestellar cores grow by mass accretion from the surrounding material. Although we classified more than half of starless cores as unbound cores, we cannot distinguish whether unbound cores evolve into bound cores and form stars with mass accretion or disperse based on this survey.
3. The core physical properties of velocity width, mass, and density in the OMC-

1/2/3 area, especially those in the OMC-1 area, have different distributions from those in the other areas in Orion A. Their distributions in OMC-1/2/3 have shallow tails at large velocity, high-density, and high-mass ends. The bound cores with large velocity FWHM ($\geq 5 \text{ km s}^{-1}$) and massive cores ($\geq 10 M_{\odot}$) only exist in OMC-1/2/3 area.

4. CMF properties in Orion A resemble CMF and IMF in the ONC region. The turnover masses of CMFs in four subregions do not have apparent differences either. However, the slope at the high-mass end of CMF in the OMC-1/2/3 area is obviously shallower than the other areas.
5. The free-fall times other than the several massive cores in OMC-1 are approximately the same. Then, most bound cores seem to evolve to stars in the same timescale of a few times the free-fall time. This intimate that cores consist of the current CMF evolves into IMF simultaneously. The mapping from the current CMF to future IMF may be similar to that of past CMF to the current IMF.
6. The Bondi-Hoyle-Lyttleton accretion from a typical clump to a core is much smaller than that required to double the core mass within the core lifetime. Then, more effective mass accretion processes are expected to grow core masses during a reasonable timescale. Since the cores locate along the filamentary structures of clouds and their column densities are higher than typical clumps, mass accretion along the filament is a predominant candidate of a mass accretion process (see also Appendix B.3).

4. Conclusions and Future Prospects

In this thesis, we presented two studies aimed to reveal the core growth by mass accretion from observations of CMFs: a dense core survey with three-dimensional MHD simulation data (Chapter 2) and a dense core survey in Orion A with CARMA+NRO45-m combined C¹⁸O ($J=1-0$) data (Chapter 3). The main result of each study is summarized in Sections 2.7 and 3.6. Then, we suggest prospects based on the results of this thesis as follows. Section 4.1 is related to Chapter 2 and Sections 4.2 and 4.3 are inspired by Chapter 3.

4.1 Observation of True CMFs

As discussed in Chapter 2, the observation method affects both CMFs observed with continuum and molecular lines. When we construct CMFs with continuum observation, the effects of the overlap of cores along the line of sight and background column density should be compensated. The correction with the detection probability is thought to be an effective way to ease the overlap effect. The actual core mass will be calculated by subtracting the column density around the core or

convoluting with some function like gaussian during core identification. For PPV CMFs, we presented that they have steeper slopes at the high-mass ends because of the line broadening. However, as we showed in Chapter 3, the effect is not so severe in the actual observed data since the observed line width - mass relation in Orion A is shallower than PPV data from the numerical simulation. In addition, the effect of overlapping and ambient column density is also less severe than in PP data. Therefore, we suppose that observation with optically thin molecular lines tracing high-density regions is the best way to construct true CMFs. We note that the FoV should be wide as possible to cover not only the center of the cloud but also its fringe. Also, relatively extended cores that are thought to be newly born or pressure-confined cores are needed to cover. Some of such cores may be eliminated in observations with interferometers depending on the observation setup and cloud morphology. Then, single-dish observations like LST (Large Submillimeter Telescope) in the future have the advantage of detecting them.

4.2 Filaments and Their Hubs

As we presented in Section 1.6 and Chapter 3, we suggested the mass accretion process from ambient material to dense cores and core growth with it. We note that the mass accretion process is not taken into account in the core collapse scenario of star formation (See Section 1.2). Future observational and theoretical studies to reveal the mass accretion rate and the mass reservoir are expected. When we estimate the mass accretion rate, although the simple Bondi accretion from

a typical clump is inefficient for growing cores, the mass accretion along the filament suppose to achieve a high-mass accretion rate enough to do so. Especially, cores in the intersections of filaments called hubs such as OMC-1 are expected to grow very efficiently, and the systems may play an essential role in high-mass star formation, as mentioned in many previous observations. The comparison of physical properties among cores in hubs, in filaments, and outside the filament is a promising way to explore the core growth focusing on the function of filaments. Besides, statistical observations of velocity structure along not only the massive filament or hub but also less massive filament are desired to investigate the mass accretion process and the mass accretion rate. Here, the massive filament of NGC 6334 filament in Taurus has already been observed by [Shimajiri, Ph. André, et al. \(2019\)](#). This kind of observation has become possible thanks to the high-spatial and velocity resolutions and sensitivity of ALMA (and ngVLA in the future).

4.3 Gravitationally Unbound Cores

In Chapter 3, we showed that more than half of starless cores are gravitationally unbound cores. This is consistent with the argument of [Kirk et al. \(2017\)](#), which says that most cores are gravitationally unbound and confined by external pressure. Since mass accretion is expected, there is a possibility that unbound cores evolve into bound cores and begin star formation. This possibility leads to the question of whether all prestellar core is born as the gravitationally bound core. The mass accretion calculated in Section 4.2 will give a clue to answer this question. If

star formation in unbound cores is predicted, mapping from unbound core mass function to bound core mass function and IMF will be a new target of future observations.

Bibliography

- Ali, Babar and Alberto Noriega-Crespo (Sept. 2004). “A Mid-Infrared Survey of L1641N with ISOCAM”. In: *ApJ* 613.1, pp. 374–380. DOI: [10.1086/422902](https://doi.org/10.1086/422902). arXiv: [astro-ph/0402120](https://arxiv.org/abs/astro-ph/0402120) [astro-ph].
- Alves, J., M. Lombardi, and C. J. Lada (Jan. 2007). “The mass function of dense molecular cores and the origin of the IMF”. In: *A&A* 462.1, pp. L17–L21. DOI: [10.1051/0004-6361:20066389](https://doi.org/10.1051/0004-6361:20066389). arXiv: [astro-ph/0612126](https://arxiv.org/abs/astro-ph/0612126) [astro-ph].
- Alves de Oliveira, C. et al. (Mar. 2012). “Spectroscopy of new brown dwarf members of ρ Ophiuchi and an updated initial mass function”. In: *A&A* 539, A151, A151. DOI: [10.1051/0004-6361/201118230](https://doi.org/10.1051/0004-6361/201118230). arXiv: [1201.1912](https://arxiv.org/abs/1201.1912) [astro-ph.GA].
- Andersen, M. et al. (Oct. 2011). “The low-mass initial mass function in the Orion nebula cluster based on HST/NICMOS III imaging”. In: *A&A* 534, A10, A10. DOI: [10.1051/0004-6361/201117062](https://doi.org/10.1051/0004-6361/201117062). arXiv: [1108.5581](https://arxiv.org/abs/1108.5581) [astro-ph.SR].
- André, Ph., A. Belloche, et al. (Sept. 2007). “The initial conditions of star formation in the Ophiuchus main cloud: Kinematics of the protocluster condensations”. In: *A&A* 472.2, pp. 519–535. DOI: [10.1051/0004-6361:20077422](https://doi.org/10.1051/0004-6361:20077422). arXiv: [0706.1535](https://arxiv.org/abs/0706.1535) [astro-ph].
- André, Ph., A. Men’shchikov, et al. (July 2010). “From filamentary clouds to prestellar cores to the stellar IMF: Initial highlights from the Herschel Gould Belt Survey”. In: *A&A* 518, L102, p. L102. DOI: [10.1051/0004-6361/201014666](https://doi.org/10.1051/0004-6361/201014666). arXiv: [1005.2618](https://arxiv.org/abs/1005.2618) [astro-ph.GA].
- Bally, John (Aug. 2010). “Astrophysics: Waves on Orion’s shores”. In: *Nature* 466.7309, pp. 928–929. DOI: [10.1038/466928a](https://doi.org/10.1038/466928a).
- Bally, John et al. (Jan. 1987). “Filamentary Structure in the Orion Molecular Cloud”. In: *ApJL* 312, p. L45. DOI: [10.1086/184817](https://doi.org/10.1086/184817).
- Bastian, N., K. R. Covey, and M. R. Meyer (Sept. 2010). “A Universal Stellar Initial Mass Function? A Critical Look at Variations”. In: *ARA&A* 48, pp. 339–

389. DOI: [10.1146/annurev-astro-082708-101642](https://doi.org/10.1146/annurev-astro-082708-101642). arXiv: [1001.2965](https://arxiv.org/abs/1001.2965) [astro-ph.GA].
- Beichman, C. A. et al. (Aug. 1986). “Candidate Solar-Type Protostars in Nearby Molecular Cloud Cores”. In: *ApJ* 307, p. 337. DOI: [10.1086/164421](https://doi.org/10.1086/164421).
- Beuther, H. and P. Schilke (Feb. 2004). “Fragmentation in Massive Star Formation”. In: *Science* 303.5661, pp. 1167–1169. DOI: [10.1126/science.1094014](https://doi.org/10.1126/science.1094014). arXiv: [astro-ph/0402501](https://arxiv.org/abs/astro-ph/0402501) [astro-ph].
- Bodenheimer, P. H. (2011). *Principles of Star Formation*. DOI: [10.1007/978-3-642-15063-0](https://doi.org/10.1007/978-3-642-15063-0).
- Bohlin, R. C., B. D. Savage, and J. F. Drake (Aug. 1978). “A survey of interstellar H I from Lambda absorption measurements. II.” In: *ApJ* 224, pp. 132–142. DOI: [10.1086/156357](https://doi.org/10.1086/156357).
- Bonatto, C., Jr. Santos J. F. C., and E. Bica (Jan. 2006). “Mass functions and structure of the young open cluster NGC 6611”. In: *A&A* 445.2, pp. 567–577. DOI: [10.1051/0004-6361:20052793](https://doi.org/10.1051/0004-6361:20052793). arXiv: [astro-ph/0509805](https://arxiv.org/abs/astro-ph/0509805) [astro-ph].
- Bonnell, I. A. et al. (Feb. 2011). “The efficiency of star formation in clustered and distributed regions”. In: *MNRAS* 410.4, pp. 2339–2346. DOI: [10.1111/j.1365-2966.2010.17603.x](https://doi.org/10.1111/j.1365-2966.2010.17603.x). arXiv: [1009.1152](https://arxiv.org/abs/1009.1152) [astro-ph.GA].
- Bonnell, Ian A. and Matthew R. Bate (July 2006). “Star formation through gravitational collapse and competitive accretion”. In: *MNRAS* 370.1, pp. 488–494. DOI: [10.1111/j.1365-2966.2006.10495.x](https://doi.org/10.1111/j.1365-2966.2006.10495.x). arXiv: [astro-ph/0604615](https://arxiv.org/abs/astro-ph/0604615) [astro-ph].
- Bonnell, Ian A., Stephen G. Vine, and Matthew R. Bate (Apr. 2004). “Massive star formation: nurture, not nature”. In: *MNRAS* 349.2, pp. 735–741. DOI: [10.1111/j.1365-2966.2004.07543.x](https://doi.org/10.1111/j.1365-2966.2004.07543.x). arXiv: [astro-ph/0401059](https://arxiv.org/abs/astro-ph/0401059) [astro-ph].
- Bontemps, S., P. André, et al. (June 2001). “ISOCAM observations of the rho Ophiuchi cloud: Luminosity and mass functions of the pre-main sequence embedded cluster”. In: *A&A* 372, pp. 173–194. DOI: [10.1051/0004-6361:20010474](https://doi.org/10.1051/0004-6361:20010474). arXiv: [astro-ph/0103373](https://arxiv.org/abs/astro-ph/0103373) [astro-ph].
- Bontemps, S., Ph. André, et al. (July 2010). “The Herschel first look at protostars in the Aquila rift”. In: *A&A* 518, L85, p. L85. DOI: [10.1051/0004-6361/201014661](https://doi.org/10.1051/0004-6361/201014661). arXiv: [1005.2634](https://arxiv.org/abs/1005.2634) [astro-ph.GA].
- Briceño, C. et al. (Nov. 2002). “The Initial Mass Function in the Taurus Star-forming Region”. In: *ApJ* 580.1, pp. 317–335. DOI: [10.1086/343127](https://doi.org/10.1086/343127).

- Brunt, Christopher M. and Mark H. Heyer (Feb. 2002). “Interstellar Turbulence. I. Retrieval of Velocity Field Statistics”. In: *ApJ* 566.1, pp. 276–288. DOI: [10.1086/338031](https://doi.org/10.1086/338031).
- Burgess, A. S. M. et al. (Dec. 2009). “Young T-dwarf candidates in IC 348”. In: *A&A* 508.2, pp. 823–831. DOI: [10.1051/0004-6361/200912444](https://doi.org/10.1051/0004-6361/200912444). arXiv: [0909.0917](https://arxiv.org/abs/0909.0917) [[astro-ph.SR](#)].
- Chabrier, G. (July 2003). “Galactic Stellar and Substellar Initial Mass Function”. In: *PASP* 115.809, pp. 763–795. DOI: [10.1086/376392](https://doi.org/10.1086/376392). arXiv: [astro-ph/0304382](https://arxiv.org/abs/astro-ph/0304382) [[astro-ph](#)].
- Chabrier, Gilles (2005). “The Initial Mass Function: From Salpeter 1955 to 2005”. In: *The Initial Mass Function 50 years later. Edited by E. Corbelli and F. Palla, INAF Osservatorio Astrofisico di Arcetri, Firenze, Italy; H. Zinnecker, Astrophysikalisches Potsdam, Germany. Astrophysics and Space Science Library Volume 327. Published by Springer, Dordrecht, 2005, p.41.* Ed. by E. Corbelli, F. Palla, and H. Zinnecker. Vol. 327. Astrophysics and Space Science Library, p. 41. DOI: [10.1007/978-1-4020-3407-7_5](https://doi.org/10.1007/978-1-4020-3407-7_5).
- Chen, H. et al. (Apr. 1993). “Infrared and Optical Imaging of IRAS Sources with CO Outflow: A Snapshot of Early Star Formation”. In: *ApJ* 407, p. 639. DOI: [10.1086/172546](https://doi.org/10.1086/172546).
- Cheng, Yu et al. (Feb. 2018). “The Core Mass Function in the Massive Protocluster G286.21+0.17 Revealed by ALMA”. In: *ApJ* 853.2, 160, p. 160. DOI: [10.3847/1538-4357/aaa3f1](https://doi.org/10.3847/1538-4357/aaa3f1). arXiv: [1706.06584](https://arxiv.org/abs/1706.06584) [[astro-ph.GA](#)].
- Christie, Duncan, Benjamin Wu, and Jonathan C. Tan (Oct. 2017). “GMC Collisions as Triggers of Star Formation. IV. The Role of Ambipolar Diffusion”. In: *ApJ* 848.1, 50, p. 50. DOI: [10.3847/1538-4357/aa8a99](https://doi.org/10.3847/1538-4357/aa8a99). arXiv: [1706.07032](https://arxiv.org/abs/1706.07032) [[astro-ph.GA](#)].
- Cameron, F., G. H. Rieke, and M. J. Rieke (Dec. 1996). “Properties of Low-Mass Objects in NGC 2024”. In: *ApJ* 473, p. 294. DOI: [10.1086/178144](https://doi.org/10.1086/178144).
- Da Rio, N., M. Robberto, L. A. Hillenbrand, et al. (Mar. 2012). “The Initial Mass Function of the Orion Nebula Cluster across the H-burning Limit”. In: *ApJ* 748.1, 14, p. 14. DOI: [10.1088/0004-637X/748/1/14](https://doi.org/10.1088/0004-637X/748/1/14). arXiv: [1112.2711](https://arxiv.org/abs/1112.2711) [[astro-ph.GA](#)].
- Da Rio, N., M. Robberto, D. R. Soderblom, et al. (Oct. 2010). “A Multi-color Optical Survey of the Orion Nebula Cluster. II. The H-R Diagram”. In: *ApJ* 722.2, pp. 1092–1114. DOI: [10.1088/0004-637X/722/2/1092](https://doi.org/10.1088/0004-637X/722/2/1092). arXiv: [1008.1265](https://arxiv.org/abs/1008.1265) [[astro-ph.GA](#)].
- Das, Indrani, Shantanu Basu, and Philippe André (May 2021). “Variation of the core lifetime and fragmentation scale in molecular clouds as an indication

- of ambipolar diffusion”. In: *A&A* 649, L13, p. L13. DOI: [10.1051/0004-6361/202140404](https://doi.org/10.1051/0004-6361/202140404). arXiv: [2104.10179](https://arxiv.org/abs/2104.10179) [[astro-ph.GA](#)].
- De Marchi, G., F. Paresce, and S. Portegies Zwart (July 2010). “On the Temporal Evolution of the Stellar Mass Function in Galactic Clusters”. In: *ApJ* 718.1, pp. 105–111. DOI: [10.1088/0004-637X/718/1/105](https://doi.org/10.1088/0004-637X/718/1/105). arXiv: [1005.4593](https://arxiv.org/abs/1005.4593) [[astro-ph.GA](#)].
- di Francesco, J. et al. (Jan. 2007). “An Observational Perspective of Low-Mass Dense Cores I: Internal Physical and Chemical Properties”. In: *Protostars and Planets V*. Ed. by Bo Reipurth, David Jewitt, and Klaus Keil, p. 17. arXiv: [astro-ph/0602379](https://arxiv.org/abs/astro-ph/0602379) [[astro-ph](#)].
- Dib, S. (Oct. 2014). “Testing the universality of the IMF with Bayesian statistics: young clusters”. In: *MNRAS* 444.2, pp. 1957–1981. DOI: [10.1093/mnras/stu1521](https://doi.org/10.1093/mnras/stu1521). arXiv: [1405.3287](https://arxiv.org/abs/1405.3287) [[astro-ph.GA](#)].
- Duchêne, Gaspard and Adam Kraus (Aug. 2013). “Stellar Multiplicity”. In: *ARA&A* 51.1, pp. 269–310. DOI: [10.1146/annurev-astro-081710-102602](https://doi.org/10.1146/annurev-astro-081710-102602). arXiv: [1303.3028](https://arxiv.org/abs/1303.3028) [[astro-ph.SR](#)].
- Erickson, K. L. et al. (Oct. 2011). “The Initial Mass Function and Disk Frequency of the ρ Ophiuchi Cloud: An Extinction-limited Sample”. In: *AJ* 142.4, 140, p. 140. DOI: [10.1088/0004-6256/142/4/140](https://doi.org/10.1088/0004-6256/142/4/140). arXiv: [1109.0561](https://arxiv.org/abs/1109.0561) [[astro-ph.SR](#)].
- Evans Neal J., II et al. (Apr. 2009). “The Spitzer c2d Legacy Results: Star-Formation Rates and Efficiencies; Evolution and Lifetimes”. In: *ApJS* 181.2, pp. 321–350. DOI: [10.1088/0067-0049/181/2/321](https://doi.org/10.1088/0067-0049/181/2/321). arXiv: [0811.1059](https://arxiv.org/abs/0811.1059) [[astro-ph](#)].
- Feddersen, Jesse R. et al. (June 2020). “The CARMA-NRO Orion Survey: Protostellar Outflows, Energetics, and Filamentary Alignment”. In: *ApJ* 896.1, 11, p. 11. DOI: [10.3847/1538-4357/ab86a9](https://doi.org/10.3847/1538-4357/ab86a9). arXiv: [2004.03504](https://arxiv.org/abs/2004.03504) [[astro-ph.GA](#)].
- Flaccomio, E. et al. (May 1999). “BVRI photometry of the star-forming region NGC 2264: the initial mass function and star-forming rate”. In: *A&A* 345, pp. 521–530.
- Fukui, Y. et al. (Dec. 1986). “Discovery of Seven Bipolar Outflows by an Unbiased Survey”. In: *ApJL* 311, p. L85. DOI: [10.1086/184803](https://doi.org/10.1086/184803).
- Fukui, Yasuo, Asao Habe, et al. (Jan. 2021). “Cloud-cloud collisions and triggered star formation”. In: *PASJ* 73, S1–S34. DOI: [10.1093/pasj/psaa103](https://doi.org/10.1093/pasj/psaa103). arXiv: [2009.05077](https://arxiv.org/abs/2009.05077) [[astro-ph.GA](#)].
- Fukui, Yasuo, Kazufumi Torii, et al. (June 2018). “A New Look at the Molecular Gas in M42 and M43: Possible Evidence for Cloud-Cloud Collision that Triggered Formation of the OB Stars in the Orion Nebula Cluster”. In: *ApJ*

- 859.2, 166, p. 166. DOI: [10.3847/1538-4357/aac217](https://doi.org/10.3847/1538-4357/aac217). arXiv: [1701.04669](https://arxiv.org/abs/1701.04669) [astro-ph.GA].
- Furlan, E. et al. (May 2016). “The Herschel Orion Protostar Survey: Spectral Energy Distributions and Fits Using a Grid of Protostellar Models”. In: *ApJS* 224.1, 5, p. 5. DOI: [10.3847/0067-0049/224/1/5](https://doi.org/10.3847/0067-0049/224/1/5). arXiv: [1602.07314](https://arxiv.org/abs/1602.07314) [astro-ph.SR].
- Genzel, Reinhard and Juergen Stutzki (Jan. 1989). “The Orion molecular cloud and star-forming region.” In: *ARA&A* 27, pp. 41–85. DOI: [10.1146/annurev.aa.27.090189.000353](https://doi.org/10.1146/annurev.aa.27.090189.000353).
- Goldsmith, Paul F. (1987). “Molecular Clouds: An Overview”. In: *Interstellar Processes, Proceedings of a symposium, held at Grand Teton National Park, Wyo., July, 1986, Dordrecht: Reidel, 1987, edited by David J. Hollenbach, and Harley A. Thronson. Astrophysics and Space Science Library, Vol. 134, p.51*. Ed. by D. J. Hollenbach and Jr. Thronson H. A. Vol. 134, p. 51. DOI: [10.1007/978-94-009-3861-8_3](https://doi.org/10.1007/978-94-009-3861-8_3).
- Gómez, Gilberto C. and Enrique Vázquez-Semadeni (Aug. 2014). “Filaments in Simulations of Molecular Cloud Formation”. In: *ApJ* 791.2, 124, p. 124. DOI: [10.1088/0004-637X/791/2/124](https://doi.org/10.1088/0004-637X/791/2/124). arXiv: [1308.6298](https://arxiv.org/abs/1308.6298) [astro-ph.GA].
- Großschedl, Josefa E. et al. (Nov. 2018). “3D shape of Orion A from Gaia DR2”. In: *A&A* 619, A106, A106. DOI: [10.1051/0004-6361/201833901](https://doi.org/10.1051/0004-6361/201833901). arXiv: [1808.05952](https://arxiv.org/abs/1808.05952) [astro-ph.GA].
- Guzmán, Andrés E. et al. (Dec. 2015). “Far-infrared Dust Temperatures and Column Densities of the MALT90 Molecular Clump Sample”. In: *ApJ* 815.2, 130, p. 130. DOI: [10.1088/0004-637X/815/2/130](https://doi.org/10.1088/0004-637X/815/2/130). arXiv: [1511.00762](https://arxiv.org/abs/1511.00762) [astro-ph.SR].
- Hacar, A. et al. (June 2017). “Gravitational collapse of the OMC-1 region”. In: *A&A* 602, L2, p. L2. DOI: [10.1051/0004-6361/201730732](https://doi.org/10.1051/0004-6361/201730732). arXiv: [1703.03464](https://arxiv.org/abs/1703.03464) [astro-ph.GA].
- Haisch K. E., Jr., E. A. Lada, and C. J. Lada (Sept. 2000). “A Near-Infrared L-Band Survey of the Young Embedded Cluster NGC 2024”. In: *AJ* 120.3, pp. 1396–1409. DOI: [10.1086/301521](https://doi.org/10.1086/301521). arXiv: [astro-ph/0006219](https://arxiv.org/abs/astro-ph/0006219) [astro-ph].
- Hartmann, Lee and Andreas Burkert (Jan. 2007). “On the Structure of the Orion A Cloud and the Formation of the Orion Nebula Cluster”. In: *ApJ* 654.2, pp. 988–997. DOI: [10.1086/509321](https://doi.org/10.1086/509321). arXiv: [astro-ph/0609679](https://arxiv.org/abs/astro-ph/0609679) [astro-ph].
- Hennebelle, Patrick (Mar. 2018). “The FRIGG project: From intermediate galactic scales to self-gravitating cores”. In: *A&A* 611, A24, A24. DOI: [10.1051/0004-6361/201731071](https://doi.org/10.1051/0004-6361/201731071). arXiv: [1709.07619](https://arxiv.org/abs/1709.07619) [astro-ph.GA].

- Heyer, Mark H. and Christopher M. Brunt (Nov. 2004). “The Universality of Turbulence in Galactic Molecular Clouds”. In: *ApJL* 615.1, pp. L45–L48. DOI: [10.1086/425978](https://doi.org/10.1086/425978). arXiv: [astro-ph/0409420](https://arxiv.org/abs/astro-ph/0409420) [astro-ph].
- Hillenbrand, L. A. and J. M. Carpenter (Sept. 2000). “Constraints on the Stellar/Substellar Mass Function in the Inner Orion Nebula Cluster”. In: *ApJ* 540.1, pp. 236–254. DOI: [10.1086/309309](https://doi.org/10.1086/309309). arXiv: [astro-ph/0003293](https://arxiv.org/abs/astro-ph/0003293) [astro-ph].
- Hillenbrand, L. A. (May 1997). “On the Stellar Population and Star-Forming History of the Orion Nebula Cluster”. In: *AJ* 113, pp. 1733–1768. DOI: [10.1086/118389](https://doi.org/10.1086/118389).
- Holman, K. et al. (July 2013). “Mapping the core mass function on to the stellar initial mass function: multiplicity matters”. In: *MNRAS* 432.4, pp. 3534–3543. DOI: [10.1093/mnras/stt705](https://doi.org/10.1093/mnras/stt705). arXiv: [1304.7666](https://arxiv.org/abs/1304.7666) [astro-ph.SR].
- Hsu, Wen-Hsin et al. (Feb. 2013). “Evidence for Environmental Dependence of the Upper Stellar Initial Mass Function in Orion A”. In: *ApJ* 764.2, 114, p. 114. DOI: [10.1088/0004-637X/764/2/114](https://doi.org/10.1088/0004-637X/764/2/114). arXiv: [1212.1171](https://arxiv.org/abs/1212.1171) [astro-ph.SR].
- Hwang, Jihye et al. (June 2021). “The JCMT BISTRO Survey: The Distribution of Magnetic Field Strengths toward the OMC-1 Region”. In: *ApJ* 913.2, 85, p. 85. DOI: [10.3847/1538-4357/abf3c4](https://doi.org/10.3847/1538-4357/abf3c4). arXiv: [2103.16144](https://arxiv.org/abs/2103.16144) [astro-ph.GA].
- Ikeda, N. and Y. Kitamura (Nov. 2009). “A C¹⁸O Study of the Origin of the Power-Law Nature in the Initial Mass Function”. In: *ApJL* 705.1, pp. L95–L98. DOI: [10.1088/0004-637X/705/1/L95](https://doi.org/10.1088/0004-637X/705/1/L95). arXiv: [0910.2757](https://arxiv.org/abs/0910.2757) [astro-ph.SR].
- Ikeda, N., K. Sunada, and Y. Kitamura (Aug. 2007). “A Survey of Dense Cores in the Orion A Cloud”. In: *ApJ* 665.2, pp. 1194–1219. DOI: [10.1086/519484](https://doi.org/10.1086/519484).
- Inutsuka, Shu-ichiro (Oct. 2001). “The Mass Function of Molecular Cloud Cores”. In: *ApJL* 559.2, pp. L149–L152. DOI: [10.1086/323786](https://doi.org/10.1086/323786).
- Jessop, N. E. and D. Ward-Thompson (Jan. 2000). “A far-infrared survey of molecular cloud cores”. In: *MNRAS* 311.1, pp. 63–74. DOI: [10.1046/j.1365-8711.2000.03011.x](https://doi.org/10.1046/j.1365-8711.2000.03011.x). arXiv: [astro-ph/9908230](https://arxiv.org/abs/astro-ph/9908230) [astro-ph].
- Johnstone, D., M. Fich, et al. (Sept. 2001). “Large Area Mapping at 850 Microns. III. Analysis of the Clump Distribution in the Orion B Molecular Cloud”. In: *ApJ* 559.1, pp. 307–317. DOI: [10.1086/322323](https://doi.org/10.1086/322323).
- Johnstone, D., C. D. Wilson, et al. (Dec. 2000). “Large-Area Mapping at 850 Microns. II. Analysis of the Clump Distribution in the ρ Ophiuchi Molecular Cloud”. In: *ApJ* 545.1, pp. 327–339. DOI: [10.1086/317790](https://doi.org/10.1086/317790).
- Kirk, H. et al. (Sept. 2017). “The Green Bank Ammonia Survey: Dense Cores under Pressure in Orion A”. In: *ApJ* 846.2, 144, p. 144. DOI: [10.3847/1538-4357/aa8631](https://doi.org/10.3847/1538-4357/aa8631). arXiv: [1708.05426](https://arxiv.org/abs/1708.05426) [astro-ph.GA].

- Kong, Shuo (Mar. 2019). “The Core Mass Function in the Infrared Dark Cloud G28.37+0.07”. In: *ApJ* 873.1, 31, p. 31. DOI: [10.3847/1538-4357/aaffd5](https://doi.org/10.3847/1538-4357/aaffd5).
- Kong, Shuo, Héctor G. Arce, Jesse R. Feddersen, et al. (June 2018). “The CARMA-NRO Orion Survey”. In: *ApJS* 236.2, 25, p. 25. DOI: [10.3847/1538-4365/aabafc](https://doi.org/10.3847/1538-4365/aabafc). arXiv: [1803.11522](https://arxiv.org/abs/1803.11522) [astro-ph.GA].
- Kong, Shuo, Héctor G. Arce, Maria José Maureira, et al. (Mar. 2019). “Widespread Molecular Outflows in the Infrared Dark Cloud G28.37+0.07: Indications of Orthogonal Outflow-filament Alignment”. In: *ApJ* 874.1, 104, p. 104. DOI: [10.3847/1538-4357/ab07b9](https://doi.org/10.3847/1538-4357/ab07b9). arXiv: [1903.05273](https://arxiv.org/abs/1903.05273) [astro-ph.GA].
- Kong, Shuo, Héctor G. Arce, Yancy Shirley, et al. (May 2021). “Evidence of Core Growth in the Dragon Infrared Dark Cloud: A Path for Massive Star Formation”. In: *ApJ* 912.2, 156, p. 156. DOI: [10.3847/1538-4357/abefe7](https://doi.org/10.3847/1538-4357/abefe7). arXiv: [2103.08697](https://arxiv.org/abs/2103.08697) [astro-ph.GA].
- Könyves, V., Ph. André, A. Men’shchikov, P. Palmeirim, et al. (Dec. 2015). “A census of dense cores in the Aquila cloud complex: SPIRE/PACS observations from the Herschel Gould Belt survey”. In: *A&A* 584, A91, A91. DOI: [10.1051/0004-6361/201525861](https://doi.org/10.1051/0004-6361/201525861). arXiv: [1507.05926](https://arxiv.org/abs/1507.05926) [astro-ph.GA].
- Könyves, V., Ph. André, A. Men’shchikov, N. Schneider, et al. (July 2010). “The Aquila prestellar core population revealed by Herschel”. In: *A&A* 518, L106, p. L106. DOI: [10.1051/0004-6361/201014689](https://doi.org/10.1051/0004-6361/201014689). arXiv: [1005.2981](https://arxiv.org/abs/1005.2981) [astro-ph.SR].
- Kounkel, M. (Jan. 2021). “Supernovae in the Orion: the missing link in the star forming history of the region”. In: *American Astronomical Society Meeting Abstracts*. Vol. 53. American Astronomical Society Meeting Abstracts, 114.02, p. 114.02.
- Kramer, C. et al. (Jan. 1998). “Clump mass spectra of molecular clouds”. In: *A&A* 329, pp. 249–264.
- Kroupa, P. (Apr. 2001). “On the variation of the initial mass function”. In: *MNRAS* 322.2, pp. 231–246. DOI: [10.1046/j.1365-8711.2001.04022.x](https://doi.org/10.1046/j.1365-8711.2001.04022.x). arXiv: [astro-ph/0009005](https://arxiv.org/abs/astro-ph/0009005) [astro-ph].
- (Jan. 2002). “The Initial Mass Function of Stars: Evidence for Uniformity in Variable Systems”. In: *Science* 295.5552, pp. 82–91. DOI: [10.1126/science.1067524](https://doi.org/10.1126/science.1067524). arXiv: [astro-ph/0201098](https://arxiv.org/abs/astro-ph/0201098) [astro-ph].
- Krumholz, Mark R. and Christopher F. McKee (Feb. 2008). “A minimum column density of 1gcm^{-2} for massive star formation”. In: *Nature* 451.7182, pp. 1082–1084. DOI: [10.1038/nature06620](https://doi.org/10.1038/nature06620). arXiv: [0801.0442](https://arxiv.org/abs/0801.0442) [astro-ph].

- Lada, E. A. and C. J. Lada (Apr. 1995). “Near-Infrared Images of IC 348 and the Luminosity Functions of Young Embedded Star Clusters”. In: *AJ* 109, p. 1682. DOI: [10.1086/117396](https://doi.org/10.1086/117396).
- Lee, Chang Won and Philip C. Myers (July 1999). “A Catalog of Optically Selected Cores”. In: *ApJS* 123.1, pp. 233–250. DOI: [10.1086/313234](https://doi.org/10.1086/313234). arXiv: [astro-ph/9901175](https://arxiv.org/abs/astro-ph/9901175) [[astro-ph](#)].
- Levine, J. L. et al. (Aug. 2006). “Low-Mass Stars and Brown Dwarfs in NGC 2024: Constraints on the Substellar Mass Function”. In: *ApJ* 646.2, pp. 1215–1229. DOI: [10.1086/504964](https://doi.org/10.1086/504964). arXiv: [astro-ph/0604315](https://arxiv.org/abs/astro-ph/0604315) [[astro-ph](#)].
- Lim, Wanggi et al. (Jan. 2021). “Star cluster formation in Orion A”. In: *PASJ* 73, S239–S255. DOI: [10.1093/pasj/psaa035](https://doi.org/10.1093/pasj/psaa035). arXiv: [2004.03668](https://arxiv.org/abs/2004.03668) [[astro-ph.SR](#)].
- Liu, Mengyao et al. (Aug. 2018). “The Core Mass Function across Galactic Environments. II. Infrared Dark Cloud Clumps”. In: *ApJ* 862.2, 105, p. 105. DOI: [10.3847/1538-4357/aacb7c](https://doi.org/10.3847/1538-4357/aacb7c). arXiv: [1806.02213](https://arxiv.org/abs/1806.02213) [[astro-ph.GA](#)].
- Lombardi, M. et al. (June 2014). “Herschel-Planck dust optical-depth and column-density maps. I. Method description and results for Orion”. In: *A&A* 566, A45, A45. DOI: [10.1051/0004-6361/201323293](https://doi.org/10.1051/0004-6361/201323293). arXiv: [1404.0032](https://arxiv.org/abs/1404.0032) [[astro-ph.SR](#)].
- Lucy, L. B. (June 1974). “An iterative technique for the rectification of observed distributions”. In: *AJ* 79, p. 745. DOI: [10.1086/111605](https://doi.org/10.1086/111605).
- Luhman, K. L. (Dec. 2000). “The Initial Mass Function of Low-Mass Stars and Brown Dwarfs in Taurus”. In: *ApJ* 544.2, pp. 1044–1055. DOI: [10.1086/317232](https://doi.org/10.1086/317232).
- (Dec. 2004). “New Brown Dwarfs and an Updated Initial Mass Function in Taurus”. In: *ApJ* 617.2, pp. 1216–1232. DOI: [10.1086/425647](https://doi.org/10.1086/425647). arXiv: [astro-ph/0411447](https://arxiv.org/abs/astro-ph/0411447) [[astro-ph](#)].
- (Nov. 2007). “The Stellar Population of the Chamaeleon I Star-forming Region”. In: *ApJS* 173.1, pp. 104–136. DOI: [10.1086/520114](https://doi.org/10.1086/520114). arXiv: [0710.3037](https://arxiv.org/abs/0710.3037) [[astro-ph](#)].
- Luhman, K. L., César Briceño, et al. (June 2003). “New Low-Mass Members of the Taurus Star-forming Region”. In: *ApJ* 590.1, pp. 348–356. DOI: [10.1086/374983](https://doi.org/10.1086/374983). arXiv: [astro-ph/0304414](https://arxiv.org/abs/astro-ph/0304414) [[astro-ph](#)].
- Luhman, K. L., E. E. Mamajek, et al. (Sept. 2009). “An Infrared/X-Ray Survey for New Members of the Taurus Star-Forming Region”. In: *ApJ* 703.1, pp. 399–419. DOI: [10.1088/0004-637X/703/1/399](https://doi.org/10.1088/0004-637X/703/1/399). arXiv: [0911.5451](https://arxiv.org/abs/0911.5451) [[astro-ph.GA](#)].
- Luhman, K. L., Dawn E. Peterson, and S. T. Megeath (Dec. 2004). “Spectroscopic Confirmation of the Least Massive Known Brown Dwarf in Chamaeleon”. In:

- ApJ 617.1, pp. 565–568. DOI: [10.1086/425228](https://doi.org/10.1086/425228). arXiv: [astro-ph/0411445](https://arxiv.org/abs/astro-ph/0411445) [astro-ph].
- Luhman, K. L. and G. H. Rieke (Nov. 1999). “Low-Mass Star Formation and the Initial Mass Function in the ρ Ophiuchi Cloud Core”. In: ApJ 525.1, pp. 440–465. DOI: [10.1086/307891](https://doi.org/10.1086/307891). arXiv: [astro-ph/9905286](https://arxiv.org/abs/astro-ph/9905286) [astro-ph].
- Luhman, K. L., John R. Stauffer, et al. (Aug. 2003). “A Census of the Young Cluster IC 348”. In: ApJ 593.2, pp. 1093–1115. DOI: [10.1086/376594](https://doi.org/10.1086/376594). arXiv: [astro-ph/0304409](https://arxiv.org/abs/astro-ph/0304409) [astro-ph].
- Lyo, A. R. et al. (May 2006). “A deep photometric survey of the η Chamaeleontis cluster down to the brown dwarf - planet boundary”. In: MNRAS 368.3, pp. 1451–1455. DOI: [10.1111/j.1365-2966.2006.10232.x](https://doi.org/10.1111/j.1365-2966.2006.10232.x). arXiv: [astro-ph/0604054](https://arxiv.org/abs/astro-ph/0604054) [astro-ph].
- Machida, M. N., S. Inutsuka, and T. Matsumoto (July 2009). “First Direct Simulation of Brown Dwarf Formation in a Compact Cloud Core”. In: ApJL 699.2, pp. L157–L160. DOI: [10.1088/0004-637X/699/2/L157](https://doi.org/10.1088/0004-637X/699/2/L157). arXiv: [0907.3255](https://arxiv.org/abs/0907.3255) [astro-ph.SR].
- Machida, M. N. and T. Matsumoto (Mar. 2012). “Impact of protostellar outflow on star formation: effects of the initial cloud mass”. In: MNRAS 421.1, pp. 588–607. DOI: [10.1111/j.1365-2966.2011.20336.x](https://doi.org/10.1111/j.1365-2966.2011.20336.x). arXiv: [1108.3564](https://arxiv.org/abs/1108.3564) [astro-ph.SR].
- Maíz Apellániz, J. and L. Úbeda (Aug. 2005). “Numerical Biases on Initial Mass Function Determinations Created by Binning”. In: ApJ 629.2, pp. 873–880. DOI: [10.1086/431458](https://doi.org/10.1086/431458). arXiv: [astro-ph/0505012](https://arxiv.org/abs/astro-ph/0505012) [astro-ph].
- Mamajek, E. E., W. A. Lawson, and E. D. Feigelson (Nov. 2000). “The η Chamaeleontis Cluster: Origin in the Sco-Cen OB Association”. In: ApJ 544.1, pp. 356–374. DOI: [10.1086/317181](https://doi.org/10.1086/317181). arXiv: [astro-ph/0005583](https://arxiv.org/abs/astro-ph/0005583) [astro-ph].
- Maruta, Hajime et al. (May 2010). “Physical Properties of Dense Cores in the ρ Ophiuchi Main Cloud and a Significant Role of External Pressures in Clustered Star Formation”. In: ApJ 714.1, pp. 680–698. DOI: [10.1088/0004-637X/714/1/680](https://doi.org/10.1088/0004-637X/714/1/680). arXiv: [0907.2558](https://arxiv.org/abs/0907.2558) [astro-ph.SR].
- Mathis, J. S. (Jan. 1990). “Interstellar dust and extinction.” In: ARA&A 28, pp. 37–70. DOI: [10.1146/annurev.aa.28.090190.000345](https://doi.org/10.1146/annurev.aa.28.090190.000345).
- Matzner, C. D. and C. F. McKee (Dec. 2000). “Efficiencies of Low-Mass Star and Star Cluster Formation”. In: ApJ 545.1, pp. 364–378. DOI: [10.1086/317785](https://doi.org/10.1086/317785). arXiv: [astro-ph/0007383](https://arxiv.org/abs/astro-ph/0007383) [astro-ph].
- Meingast, Stefan et al. (Mar. 2016). “VISION - Vienna survey in Orion. I. VISTA Orion A Survey”. In: A&A 587, A153, A153. DOI: [10.1051/0004-6361/201527160](https://doi.org/10.1051/0004-6361/201527160). arXiv: [1601.01687](https://arxiv.org/abs/1601.01687) [astro-ph.GA].

- Men'shchikov, A. et al. (July 2010). "Filamentary structures and compact objects in the Aquila and Polaris clouds observed by Herschel". In: *A&A* 518, L103, p. L103. DOI: [10.1051/0004-6361/201014668](https://doi.org/10.1051/0004-6361/201014668). arXiv: [1005.3115](https://arxiv.org/abs/1005.3115) [astro-ph.GA].
- Menten, K. M. et al. (Nov. 2007). "The distance to the Orion Nebula". In: *A&A* 474.2, pp. 515–520. DOI: [10.1051/0004-6361:20078247](https://doi.org/10.1051/0004-6361:20078247). arXiv: [0709.0485](https://arxiv.org/abs/0709.0485) [astro-ph].
- Miller, G. E. and J. M. Scalo (Nov. 1979). "The Initial Mass Function and Stellar Birthrate in the Solar Neighborhood". In: *ApJS* 41, p. 513. DOI: [10.1086/190629](https://doi.org/10.1086/190629).
- Miville-Deschênes, M. -A., F. Levrier, and E. Falgarone (Aug. 2003). "On the Use of Fractional Brownian Motion Simulations to Determine the Three-dimensional Statistical Properties of Interstellar Gas". In: *ApJ* 593.2, pp. 831–847. DOI: [10.1086/376603](https://doi.org/10.1086/376603). arXiv: [astro-ph/0304539](https://arxiv.org/abs/astro-ph/0304539) [astro-ph].
- Motte, F., P. Andre, and R. Neri (Aug. 1998). "The initial conditions of star formation in the rho Ophiuchi main cloud: wide-field millimeter continuum mapping". In: *A&A* 336, pp. 150–172.
- Motte, F., P. André, et al. (June 2001). "A SCUBA survey of the NGC 2068/2071 protoclusters". In: *A&A* 372, pp. L41–L44. DOI: [10.1051/0004-6361:20010543](https://doi.org/10.1051/0004-6361:20010543). arXiv: [astro-ph/0105019](https://arxiv.org/abs/astro-ph/0105019) [astro-ph].
- Motte, F., S. Bontemps, and F. Louvet (Sept. 2018). "High-Mass Star and Massive Cluster Formation in the Milky Way". In: *ARA&A* 56, pp. 41–82. DOI: [10.1146/annurev-astro-091916-055235](https://doi.org/10.1146/annurev-astro-091916-055235). arXiv: [1706.00118](https://arxiv.org/abs/1706.00118) [astro-ph.GA].
- Motte, F., T. Nony, et al. (Apr. 2018). "The unexpectedly large proportion of high-mass star-forming cores in a Galactic mini-starburst". In: *Nature Astronomy* 2, pp. 478–482. DOI: [10.1038/s41550-018-0452-x](https://doi.org/10.1038/s41550-018-0452-x). arXiv: [1804.02392](https://arxiv.org/abs/1804.02392) [astro-ph.GA].
- Muench, A. A., E. A. Lada, and C. J. Lada (Apr. 2000). "Modeling the Near-Infrared Luminosity Functions of Young Stellar Clusters". In: *ApJ* 533.1, pp. 358–371. DOI: [10.1086/308638](https://doi.org/10.1086/308638). arXiv: [astro-ph/9912384](https://arxiv.org/abs/astro-ph/9912384) [astro-ph].
- Muench, A. A., E. A. Lada, C. J. Lada, and J. Alves (July 2002). "The Luminosity and Mass Function of the Trapezium Cluster: From B Stars to the Deuterium-burning Limit". In: *ApJ* 573.1, pp. 366–393. DOI: [10.1086/340554](https://doi.org/10.1086/340554). arXiv: [astro-ph/0203122](https://arxiv.org/abs/astro-ph/0203122) [astro-ph].
- Muench, A. A. et al. (Apr. 2003). "A Study of the Luminosity and Mass Functions of the Young IC 348 Cluster Using FLAMINGOS Wide-Field Near-Infrared Images". In: *AJ* 125.4, pp. 2029–2049. DOI: [10.1086/373925](https://doi.org/10.1086/373925). arXiv: [astro-ph/0301276](https://arxiv.org/abs/astro-ph/0301276) [astro-ph].

- Mužić, K. et al. (May 2011). “Substellar Objects in Nearby Young Clusters (SONYC). III. Chamaeleon-I”. In: *ApJ* 732.2, 86, p. 86. DOI: [10.1088/0004-637X/732/2/86](https://doi.org/10.1088/0004-637X/732/2/86). arXiv: [1103.0978](https://arxiv.org/abs/1103.0978) [[astro-ph.GA](#)].
- Najita, J. R., G. P. Tiede, and J. S. Carr (Oct. 2000). “From Stars to Superplanets: The Low-Mass Initial Mass Function in the Young Cluster IC 348”. In: *ApJ* 541.2, pp. 977–1003. DOI: [10.1086/309477](https://doi.org/10.1086/309477). arXiv: [astro-ph/0005290](https://arxiv.org/abs/astro-ph/0005290) [[astro-ph](#)].
- Nakamura, Fumitaka, Shun Ishii, et al. (Sept. 2019). “Nobeyama 45-m mapping observations toward nearby molecular clouds, Orion A, Aquila Rift, and M17: Project overview”. In: *arXiv e-prints*, arXiv:1909.05980, arXiv:1909.05980. arXiv: [1909.05980](https://arxiv.org/abs/1909.05980) [[astro-ph.GA](#)].
- Nakamura, Fumitaka, Tomoya Miura, et al. (Feb. 2012). “Evidence for Cloud-Cloud Collision and Parsec-scale Stellar Feedback within the L1641-N Region”. In: *ApJ* 746.1, 25, p. 25. DOI: [10.1088/0004-637X/746/1/25](https://doi.org/10.1088/0004-637X/746/1/25). arXiv: [1110.6225](https://arxiv.org/abs/1110.6225) [[astro-ph.SR](#)].
- Nakano, T., T. Hasegawa, and C. Norman (Sept. 1995). “The Mass of a Star Formed in a Cloud Core: Theory and Its Application to the Orion A Cloud”. In: *ApJ* 450, p. 183. DOI: [10.1086/176130](https://doi.org/10.1086/176130).
- Nakano, T., R. Nishi, and T. Umebayashi (July 2002). “Mechanism of Magnetic Flux Loss in Molecular Clouds”. In: *ApJ* 573.1, pp. 199–214. DOI: [10.1086/340587](https://doi.org/10.1086/340587). arXiv: [astro-ph/0203223](https://arxiv.org/abs/astro-ph/0203223) [[astro-ph](#)].
- Ntormousi, Evangelia et al. (Apr. 2011). “Formation of Cold Filamentary Structure from Wind-blown Superbubbles”. In: *ApJ* 731.1, 13, p. 13. DOI: [10.1088/0004-637X/731/1/13](https://doi.org/10.1088/0004-637X/731/1/13). arXiv: [1011.5751](https://arxiv.org/abs/1011.5751) [[astro-ph.GA](#)].
- Nutter, D. and D. Ward-Thompson (Feb. 2007). “A SCUBA survey of Orion - the low-mass end of the core mass function”. In: *MNRAS* 374.4, pp. 1413–1420. DOI: [10.1111/j.1365-2966.2006.11246.x](https://doi.org/10.1111/j.1365-2966.2006.11246.x). arXiv: [astro-ph/0611164](https://arxiv.org/abs/astro-ph/0611164) [[astro-ph](#)].
- Offner, S. S. R. et al. (Jan. 2014). “The Origin and Universality of the Stellar Initial Mass Function”. In: *Protostars and Planets VI*. Ed. by Henrik Beuther et al., p. 53. DOI: [10.2458/azu_uapress_9780816531240-ch003](https://doi.org/10.2458/azu_uapress_9780816531240-ch003). arXiv: [1312.5326](https://arxiv.org/abs/1312.5326) [[astro-ph.SR](#)].
- Oliveira, J. M., R. D. Jeffries, and J. Th. van Loon (Jan. 2009). “The low-mass initial mass function in the young cluster NGC6611”. In: *MNRAS* 392.3, pp. 1034–1050. DOI: [10.1111/j.1365-2966.2008.14140.x](https://doi.org/10.1111/j.1365-2966.2008.14140.x). arXiv: [0810.4444](https://arxiv.org/abs/0810.4444) [[astro-ph](#)].
- Onishi, Toshikazu et al. (Aug. 2002). “A Complete Search for Dense Cloud Cores in Taurus”. In: *ApJ* 575.2, pp. 950–973. DOI: [10.1086/341347](https://doi.org/10.1086/341347).

- Ossenkopf, V. and Th. Henning (Nov. 1994). “Dust opacities for protostellar cores.” In: *A&A* 291, pp. 943–959.
- Pabst, C. et al. (Jan. 2019). “Disruption of the Orion molecular core 1 by wind from the massive star θ^1 Orionis C”. In: *Nature* 565.7741, pp. 618–621. DOI: [10.1038/s41586-018-0844-1](https://doi.org/10.1038/s41586-018-0844-1). arXiv: [1901.04221](https://arxiv.org/abs/1901.04221) [astro-ph.GA].
- Padoan, Paolo and Åke Nordlund (Sept. 2002). “The Stellar Initial Mass Function from Turbulent Fragmentation”. In: *ApJ* 576.2, pp. 870–879. DOI: [10.1086/341790](https://doi.org/10.1086/341790). arXiv: [astro-ph/0011465](https://arxiv.org/abs/astro-ph/0011465) [astro-ph].
- Padoan, Paolo, Åke Nordlund, et al. (June 2007). “Two Regimes of Turbulent Fragmentation and the Stellar Initial Mass Function from Primordial to Present-Day Star Formation”. In: *ApJ* 661.2, pp. 972–981. DOI: [10.1086/516623](https://doi.org/10.1086/516623). arXiv: [astro-ph/0701795](https://arxiv.org/abs/astro-ph/0701795) [astro-ph].
- Padoan, Paolo, Liubin Pan, et al. (Sept. 2020). “The Origin of Massive Stars: The Inertial-inflow Model”. In: *ApJ* 900.1, 82, p. 82. DOI: [10.3847/1538-4357/abaa47](https://doi.org/10.3847/1538-4357/abaa47). arXiv: [1911.04465](https://arxiv.org/abs/1911.04465) [astro-ph.GA].
- Palla, F. and S. W. Stahler (Nov. 1999). “Star Formation in the Orion Nebula Cluster”. In: *ApJ* 525.2, pp. 772–783. DOI: [10.1086/307928](https://doi.org/10.1086/307928).
- Park, B. G. et al. (Aug. 2000). “The Pre-Main-Sequence Stars and Initial Mass Function of NGC 2264”. In: *AJ* 120.2, pp. 894–908. DOI: [10.1086/301459](https://doi.org/10.1086/301459).
- Parravano, A., C. F. McKee, and D. J. Hollenbach (Jan. 2011). “An Initial Mass Function for Individual Stars in Galactic Disks. I. Constraining the Shape of the Initial Mass Function”. In: *ApJ* 726.1, 27, p. 27. DOI: [10.1088/0004-637X/726/1/27](https://doi.org/10.1088/0004-637X/726/1/27). arXiv: [1010.2452](https://arxiv.org/abs/1010.2452) [astro-ph.GA].
- Pelkonen, V. -M. et al. (June 2021). “From the CMF to the IMF: beyond the core-collapse model”. In: *MNRAS* 504.1, pp. 1219–1236. DOI: [10.1093/mnras/stab844](https://doi.org/10.1093/mnras/stab844). arXiv: [2008.02192](https://arxiv.org/abs/2008.02192) [astro-ph.SR].
- Pineda, Jaime E., Erik W. Rosolowsky, and Alyssa A. Goodman (July 2009). “The Perils of Clumpfind: The Mass Spectrum of Substructures in Molecular Clouds”. In: *ApJL* 699.2, pp. L134–L138. DOI: [10.1088/0004-637X/699/2/L134](https://doi.org/10.1088/0004-637X/699/2/L134). arXiv: [0906.0331](https://arxiv.org/abs/0906.0331) [astro-ph.GA].
- Preibisch, T., T. Stanke, and H. Zinnecker (Oct. 2003). “Constraints on the IMF and the brown dwarf population of the young cluster IC 348”. In: *A&A* 409, pp. 147–158. DOI: [10.1051/0004-6361:20030973](https://doi.org/10.1051/0004-6361:20030973).
- Price, D. J., T. S. Tricco, and M. R. Bate (June 2012). “Collimated jets from the first core”. In: *MNRAS* 423.1, pp. L45–L49. DOI: [10.1111/j.1745-3933.2012.01254.x](https://doi.org/10.1111/j.1745-3933.2012.01254.x). arXiv: [1203.2933](https://arxiv.org/abs/1203.2933) [astro-ph.SR].

- Pudritz, R. E. et al. (Jan. 2007). “Disk Winds, Jets, and Outflows: Theoretical and Computational Foundations”. In: *Protostars and Planets V*. Ed. by Bo Reipurth, David Jewitt, and Klaus Keil, p. 277. arXiv: [astro-ph/0603592](https://arxiv.org/abs/astro-ph/0603592) [[astro-ph](#)].
- Rana, N. C. (Oct. 1987). “Mass function of stars in the solar neighbourhood”. In: *A&A* 184.1-2, pp. 104–118.
- Richardson, William Hadley (Jan. 1972). “Bayesian-Based Iterative Method of Image Restoration”. In: *Journal of the Optical Society of America (1917-1983)* 62.1, p. 55.
- Rieke, G. H., N. M. Ashok, and R. P. Boyle (Apr. 1989). “The Initial Mass Function in the Rho Ophiuchi Cluster”. In: *ApJL* 339, p. L71. DOI: [10.1086/185422](https://doi.org/10.1086/185422).
- Rosolowsky, E. W. et al. (June 2008). “Structural Analysis of Molecular Clouds: Dendrograms”. In: *ApJ* 679.2, pp. 1338–1351. DOI: [10.1086/587685](https://doi.org/10.1086/587685). arXiv: [0802.2944](https://arxiv.org/abs/0802.2944) [[astro-ph](#)].
- Roy, A. et al. (Dec. 2015). “Possible link between the power spectrum of interstellar filaments and the origin of the prestellar core mass function”. In: *A&A* 584, A111, A111. DOI: [10.1051/0004-6361/201526431](https://doi.org/10.1051/0004-6361/201526431). arXiv: [1509.01819](https://arxiv.org/abs/1509.01819) [[astro-ph.GA](#)].
- Sadaghiani, M. et al. (Mar. 2020). “Physical properties of the star-forming clusters in NGC 6334. A study of the continuum dust emission with ALMA”. In: *A&A* 635, A2, A2. DOI: [10.1051/0004-6361/201935699](https://doi.org/10.1051/0004-6361/201935699). arXiv: [1911.06579](https://arxiv.org/abs/1911.06579) [[astro-ph.SR](#)].
- Sagar, R. and U. C. Joshi (Nov. 1979). “A study of the young open cluster NGC 6611”. In: *Ap&SS* 66.1, pp. 3–12. DOI: [10.1007/BF00648356](https://doi.org/10.1007/BF00648356).
- Salpeter, E. E. (Jan. 1955). “The Luminosity Function and Stellar Evolution.” In: *ApJ* 121, p. 161. DOI: [10.1086/145971](https://doi.org/10.1086/145971).
- Sánchez-Monge, Á. et al. (July 2017). “The physical and chemical structure of Sagittarius B2. II. Continuum millimeter emission of Sgr B2(M) and Sgr B2(N) with ALMA”. In: *A&A* 604, A6, A6. DOI: [10.1051/0004-6361/201730426](https://doi.org/10.1051/0004-6361/201730426). arXiv: [1704.01805](https://arxiv.org/abs/1704.01805) [[astro-ph.GA](#)].
- Sanhueza, Patricio et al. (Dec. 2019). “The ALMA Survey of 70 μm Dark High-mass Clumps in Early Stages (ASHES). I. Pilot Survey: Clump Fragmentation”. In: *ApJ* 886.2, 102, p. 102. DOI: [10.3847/1538-4357/ab45e9](https://doi.org/10.3847/1538-4357/ab45e9). arXiv: [1909.07985](https://arxiv.org/abs/1909.07985) [[astro-ph.GA](#)].
- Scalo, John (1998). “The IMF Revisited: A Case for Variations”. In: *The Stellar Initial Mass Function (38th Herstmonceux Conference) edited by Gary Gilmore and Debbie Howell. ASP Conference Series, Vol. 142, 1998, p.201*. Ed. by G. Gilmore and D. Howell. Vol. 142. Astronomical Society of the Pacific Conference Series, p. 201.

- Scelsi, L., A. Maggio, et al. (June 2007). “New pre-main sequence candidates in the Taurus-Auriga star forming region”. In: *A&A* 468.2, pp. 405–412. DOI: [10.1051/0004-6361:20065544](https://doi.org/10.1051/0004-6361:20065544).
- Scelsi, L., G. Sacco, et al. (Nov. 2008). “Optical spectroscopy of X-ray sources in the Taurus molecular cloud: discovery of ten new pre-main sequence stars”. In: *A&A* 490.2, pp. 601–612. DOI: [10.1051/0004-6361:200810178](https://doi.org/10.1051/0004-6361:200810178). arXiv: [0809.2171](https://arxiv.org/abs/0809.2171) [[astro-ph](#)].
- Shimajiri, Y., Ph. André, et al. (Dec. 2019). “Probing fragmentation and velocity sub-structure in the massive NGC 6334 filament with ALMA”. In: *A&A* 632, A83, A83. DOI: [10.1051/0004-6361/201935689](https://doi.org/10.1051/0004-6361/201935689). arXiv: [1910.02622](https://arxiv.org/abs/1910.02622) [[astro-ph.GA](#)].
- Shimajiri, Y., R. Kawabe, et al. (Nov. 2011). “Star Formation in the Orion A Molecular Cloud”. In: *EAS Publications Series*. Ed. by M. Röllig et al. Vol. 52. EAS Publications Series, pp. 307–308. DOI: [10.1051/eas/1152060](https://doi.org/10.1051/eas/1152060).
- Slesnick, C. L., L. A. Hillenbrand, and J. M. Carpenter (Aug. 2004). “The Spectroscopically Determined Substellar Mass Function of the Orion Nebula Cluster”. In: *ApJ* 610.2, pp. 1045–1063. DOI: [10.1086/421898](https://doi.org/10.1086/421898). arXiv: [astro-ph/0404292](https://arxiv.org/abs/astro-ph/0404292) [[astro-ph](#)].
- Smith, Britton D. et al. (Apr. 2017). “GRACKLE: a chemistry and cooling library for astrophysics”. In: *MNRAS* 466.2, pp. 2217–2234. DOI: [10.1093/mnras/stw3291](https://doi.org/10.1093/mnras/stw3291). arXiv: [1610.09591](https://arxiv.org/abs/1610.09591) [[astro-ph.CO](#)].
- Song, I., B. Zuckerman, and M. S. Bessell (Jan. 2004). “Probing the Low-Mass Stellar End of the η Chamaeleontis Cluster”. In: *ApJ* 600.2, pp. 1016–1019. DOI: [10.1086/380086](https://doi.org/10.1086/380086). arXiv: [astro-ph/0309678](https://arxiv.org/abs/astro-ph/0309678) [[astro-ph](#)].
- Spitzer, L. and T. T. Army (Nov. 1978). “Physical Processes in the Interstellar Medium”. In: *American Journal of Physics* 46.11, pp. 1201–1201. DOI: [10.1119/1.11466](https://doi.org/10.1119/1.11466).
- Stanke, T. et al. (Feb. 2006). “An unbiased search for the signatures of protostars in the ρ Ophiuchi molecular cloud . II. Millimetre continuum observations”. In: *A&A* 447.2, pp. 609–622. DOI: [10.1051/0004-6361:20041331](https://doi.org/10.1051/0004-6361:20041331). arXiv: [astro-ph/0511093](https://arxiv.org/abs/astro-ph/0511093) [[astro-ph](#)].
- Stutz, A. M. and J. Kainulainen (May 2015). “Evolution of column density distributions within Orion A \star ”. In: *A&A* 577, L6, p. L6. DOI: [10.1051/0004-6361/201526243](https://doi.org/10.1051/0004-6361/201526243). arXiv: [1504.05188](https://arxiv.org/abs/1504.05188) [[astro-ph.GA](#)].
- Stutzki, J. and R. Guesten (June 1990). “High Spatial Resolution Isotopic CO and CS Observations of M17 SW: The Clumpy Structure of the Molecular Cloud Core”. In: *ApJ* 356, p. 513. DOI: [10.1086/168859](https://doi.org/10.1086/168859).

- Sung, H. and M. S. Bessell (Dec. 2010). “The Initial Mass Function and Young Brown Dwarf Candidates in NGC 2264. IV. The Initial Mass Function and Star Formation History”. In: *AJ* 140.6, pp. 2070–2085. DOI: [10.1088/0004-6256/140/6/2070](https://doi.org/10.1088/0004-6256/140/6/2070). arXiv: [1010.0747 \[astro-ph.SR\]](https://arxiv.org/abs/1010.0747).
- Sung, H., M. S. Bessell, et al. (Feb. 2008). “The Initial Mass Function and Young Brown Dwarf Candidates in NGC 2264. III. Photometric Data”. In: *AJ* 135.2, pp. 441–466. DOI: [10.1088/0004-6256/135/2/441](https://doi.org/10.1088/0004-6256/135/2/441).
- Swift, Jonathan J. and Jonathan P. Williams (May 2008). “On the Evolution of the Dense Core Mass Function”. In: *ApJ* 679.1, pp. 552–556. DOI: [10.1086/587506](https://doi.org/10.1086/587506). arXiv: [0802.2099 \[astro-ph\]](https://arxiv.org/abs/0802.2099).
- Takemura, Hideaki, Fumitaka Nakamura, Héctor G. Arce, et al. (Feb. 2023). “CARMA-NRO Orion Survey: Unbiased Survey of Dense Cores and Core Mass Functions in Orion A”. In: *ApJS* 264.2, 35, p. 35. DOI: [10.3847/1538-4365/aca4d4](https://doi.org/10.3847/1538-4365/aca4d4). arXiv: [2211.10215 \[astro-ph.GA\]](https://arxiv.org/abs/2211.10215).
- Takemura, Hideaki, Fumitaka Nakamura, Shun Ishii, et al. (June 2021). “The C¹⁸O core mass function toward Orion A: Single-dish observations”. In: *PASJ* 73.3, pp. 487–503. DOI: [10.1093/pasj/psab014](https://doi.org/10.1093/pasj/psab014). arXiv: [2103.08526 \[astro-ph.GA\]](https://arxiv.org/abs/2103.08526).
- Takemura, Hideaki, Fumitaka Nakamura, Shuo Kong, et al. (Mar. 2021). “The Core Mass Function in the Orion Nebula Cluster Region: What Determines the Final Stellar Masses?” In: *ApJL* 910.1, L6, p. L6. DOI: [10.3847/2041-8213/abe7dd](https://doi.org/10.3847/2041-8213/abe7dd). arXiv: [2103.08527 \[astro-ph.GA\]](https://arxiv.org/abs/2103.08527).
- Tan, J. C. et al. (Jan. 2014). “Massive Star Formation”. In: *Protostars and Planets VI*. Ed. by Henrik Beuther et al., p. 149. DOI: [10.2458/azu_uapress_9780816531240-ch007](https://doi.org/10.2458/azu_uapress_9780816531240-ch007). arXiv: [1402.0919 \[astro-ph.GA\]](https://arxiv.org/abs/1402.0919).
- Tanabe, Yoshihiro et al. (Dec. 2019). “Nobeyama 45 m mapping observations toward Orion A. I. Molecular Outflows”. In: *PASJ* 71, S8, S8. DOI: [10.1093/pasj/psz100](https://doi.org/10.1093/pasj/psz100). arXiv: [1910.07495 \[astro-ph.SR\]](https://arxiv.org/abs/1910.07495).
- Tatematsu, Ken’ichi et al. (Apr. 2016). “Angular momentum of the N₂H⁺ cores in the Orion A cloud”. In: *PASJ* 68.2, 24, p. 24. DOI: [10.1093/pasj/psw002](https://doi.org/10.1093/pasj/psw002). arXiv: [1601.00362 \[astro-ph.GA\]](https://arxiv.org/abs/1601.00362).
- Testi, L. and A. I. Sargent (Nov. 1998). “Star Formation in Clusters: A Survey of Compact Millimeter-Wave Sources in the Serpens Core”. In: *ApJL* 508.1, pp. L91–L94. DOI: [10.1086/311724](https://doi.org/10.1086/311724). arXiv: [astro-ph/9809323 \[astro-ph\]](https://arxiv.org/abs/astro-ph/9809323).
- Tokuda, Kazuki et al. (Aug. 2020). “FRAGMENTATION AND EVOLUTION OF DENSE CORES JUDGED BY ALMA (FREJA). I. OVERVIEW: INNER ~1000 AU STRUCTURES

- of Prestellar/Protostellar Cores in Taurus”. In: *ApJ* 899.1, 10, p. 10. DOI: [10.3847/1538-4357/ab9ca7](https://doi.org/10.3847/1538-4357/ab9ca7). arXiv: [2006.06361](https://arxiv.org/abs/2006.06361) [[astro-ph.GA](#)].
- Vázquez-Semadeni, Enrique et al. (Dec. 2019). “Global hierarchical collapse in molecular clouds. Towards a comprehensive scenario”. In: *MNRAS* 490.3, pp. 3061–3097. DOI: [10.1093/mnras/stz2736](https://doi.org/10.1093/mnras/stz2736). arXiv: [1903.11247](https://arxiv.org/abs/1903.11247) [[astro-ph.GA](#)].
- Walker, M. F. (Mar. 1961). “Studies of Extremely Young Clusters.IV. NGC 6611.” In: *ApJ* 133, p. 438. DOI: [10.1086/147047](https://doi.org/10.1086/147047).
- Wang, >Ke (June 2018). “Temperature, Turbulence, and Kinematics of the Giant Filamentary Infrared Dark Cloud G28.34+0.06 at ~ 0.1 pc Resolution”. In: *Research Notes of the American Astronomical Society* 2.2, 52, p. 52. DOI: [10.3847/2515-5172/aacb29](https://doi.org/10.3847/2515-5172/aacb29).
- Wang, Peng et al. (Jan. 2010). “Outflow Feedback Regulated Massive Star Formation in Parsec-Scale Cluster-Forming Clumps”. In: *ApJ* 709.1, pp. 27–41. DOI: [10.1088/0004-637X/709/1/27](https://doi.org/10.1088/0004-637X/709/1/27). arXiv: [0908.4129](https://arxiv.org/abs/0908.4129) [[astro-ph.SR](#)].
- Williams, D. M. et al. (Nov. 1995). “The Low-Mass IMF in the rho Ophiuchi Cluster”. In: *ApJ* 454, p. 144. DOI: [10.1086/176473](https://doi.org/10.1086/176473).
- Williams, J. P., E. J. de Geus, and L. Blitz (June 1994). “Determining Structure in Molecular Clouds”. In: *ApJ* 428, p. 693. DOI: [10.1086/174279](https://doi.org/10.1086/174279).
- Wu, Benjamin et al. (Feb. 2017). “GMC Collisions as Triggers of Star Formation. II. 3D Turbulent, Magnetized Simulations”. In: *ApJ* 835.2, 137, p. 137. DOI: [10.3847/1538-4357/835/2/137](https://doi.org/10.3847/1538-4357/835/2/137). arXiv: [1606.01320](https://arxiv.org/abs/1606.01320) [[astro-ph.GA](#)].
- Zhang, Qizhou et al. (May 2015). “Fragmentation of Molecular Clumps and Formation of a Protocluster”. In: *ApJ* 804.2, 141, p. 141. DOI: [10.1088/0004-637X/804/2/141](https://doi.org/10.1088/0004-637X/804/2/141). arXiv: [1503.03017](https://arxiv.org/abs/1503.03017) [[astro-ph.SR](#)].

A. Appendix of Chapter 2

A.1 Analysis of PP Data

A.1.1 Dense Core Survey and Construction of CMFs with PP data in yz and zx planes

In this appendix, we show the results of analyses of PP data in yz and zx planes. We summarize the results of dense core surveys with PP data projected onto the yz plane and zx plane in Tables A.1 and A.2. These cores are identified as Figures A.1 and A.2, and their CMFs are constructed as Figures A.3 and A.4. The properties of CMFs are summarized in Tables A.5 and A.6. The relationship among PP CMF without subtraction, PP CMF with subtraction, PPP CMF, and PPP CMF overlap affected similarly to the xy column density map case of Section 2.5. The collision of two clouds occurred in the xy plane, but we have not found any significant differences among the projection to derive the column density map. Therefore, the discussion in Section 2.5 does not depend on the direction of projection.

Table A.1: The Results of Dense Core Survey with PP Data (yz Plane)

Case No.	Number of Identified Cores
1	609
2 (fiducial)	673
3	757
4	789
5	804
6	808

Table A.2: The Results of Dense Core Survey with PP Data (zx Plane)

Case No.	Number of Identified Cores
1	623
2 (fiducial)	691
3	766
4	796
5	811
6	814

Table A.3: The Summary of Core Properties Identified with PP Data (yz plane) Using Fiducial Parameter

Core property	minimum	maximum	mean \pm std.
$2R_{\text{core}}$ (pc)	0.12	0.88	0.2 ± 0.09
M_{core} (M_{\odot})	3.08	921.7	53.03 ± 86.38
$M_{\text{core,sub}}$ (M_{\odot})	0.13	856.43	25.17 ± 68.71
$N_{\text{core,mean}}$ (g cm^{-2})	0.05	10.37	0.37 ± 0.64
$N_{\text{core,peak}}$ (g cm^{-2})	0.05	157.68	1.53 ± 6.97

Table A.4: The Summary of Core Properties Identified with PP Data (zx Plane) Using Fiducial Parameter

Core property	minimum	maximum	mean \pm std.
$2R_{\text{core}}$ (pc)	0.12	1.11	0.2 ± 0.11
M_{core} (M_{\odot})	3.27	843.14	50.31 ± 86.39
$M_{\text{core,sub}}$ (M_{\odot})	0.12	803.24	23.52 ± 66.39
$N_{\text{core,mean}}$ (g cm^{-2})	0.05	12.02	0.36 ± 0.7
$N_{\text{core,peak}}$ (g cm^{-2})	0.05	154.3	1.49 ± 6.84

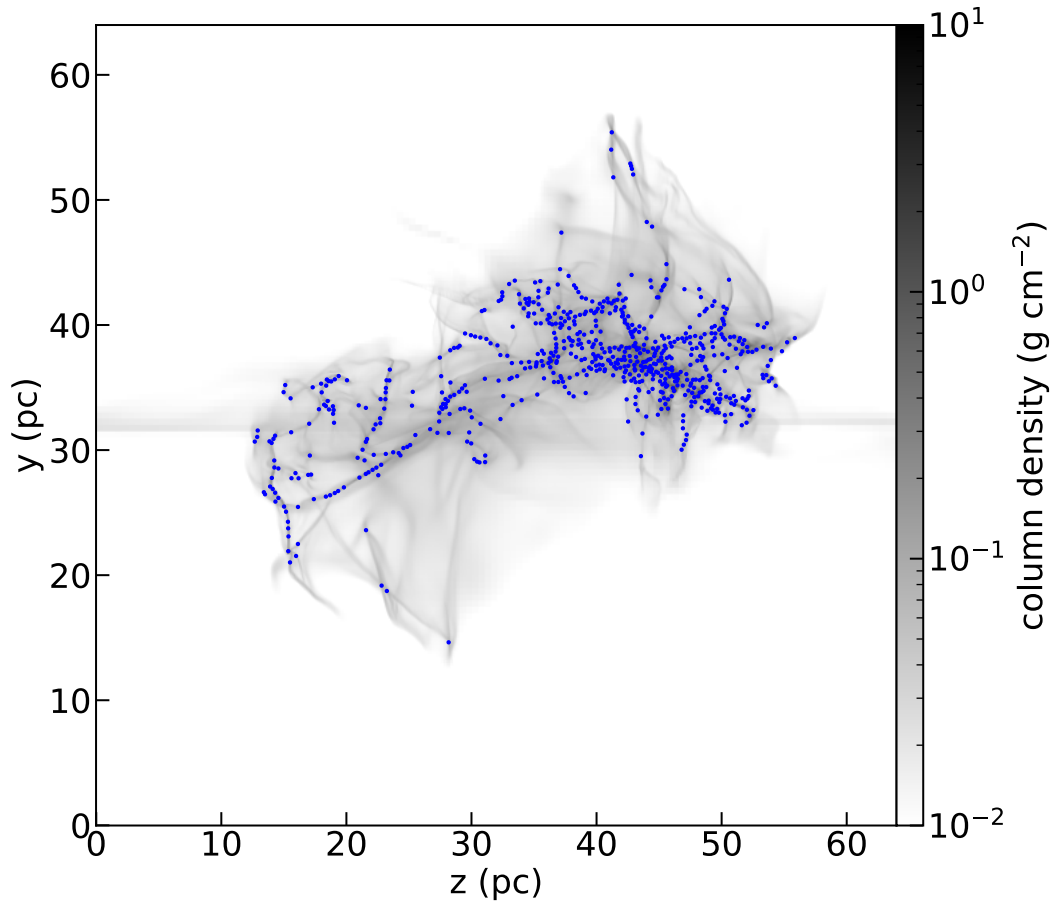


Figure A.1: The identified cores with yz PP data are potted onto the column density map in yz plane.

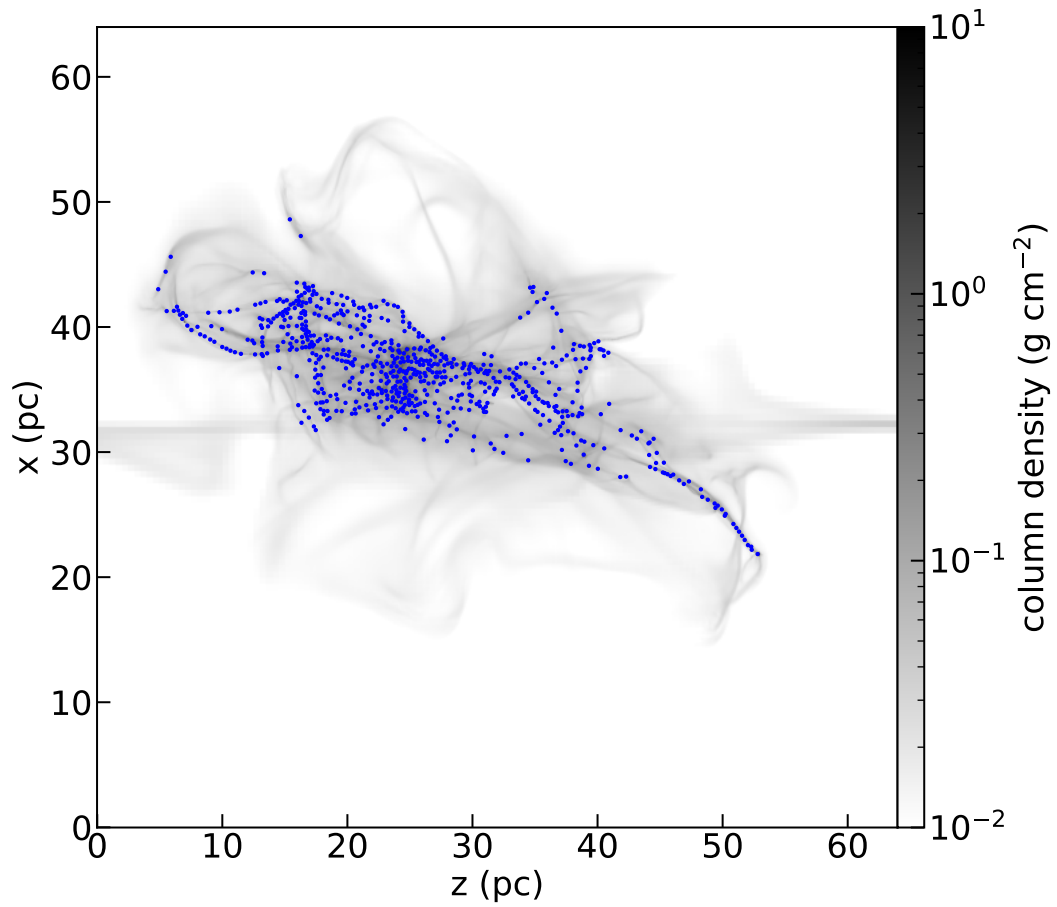


Figure A.2: The identified cores with zx PP data are potted onto the column density map in zx plane.

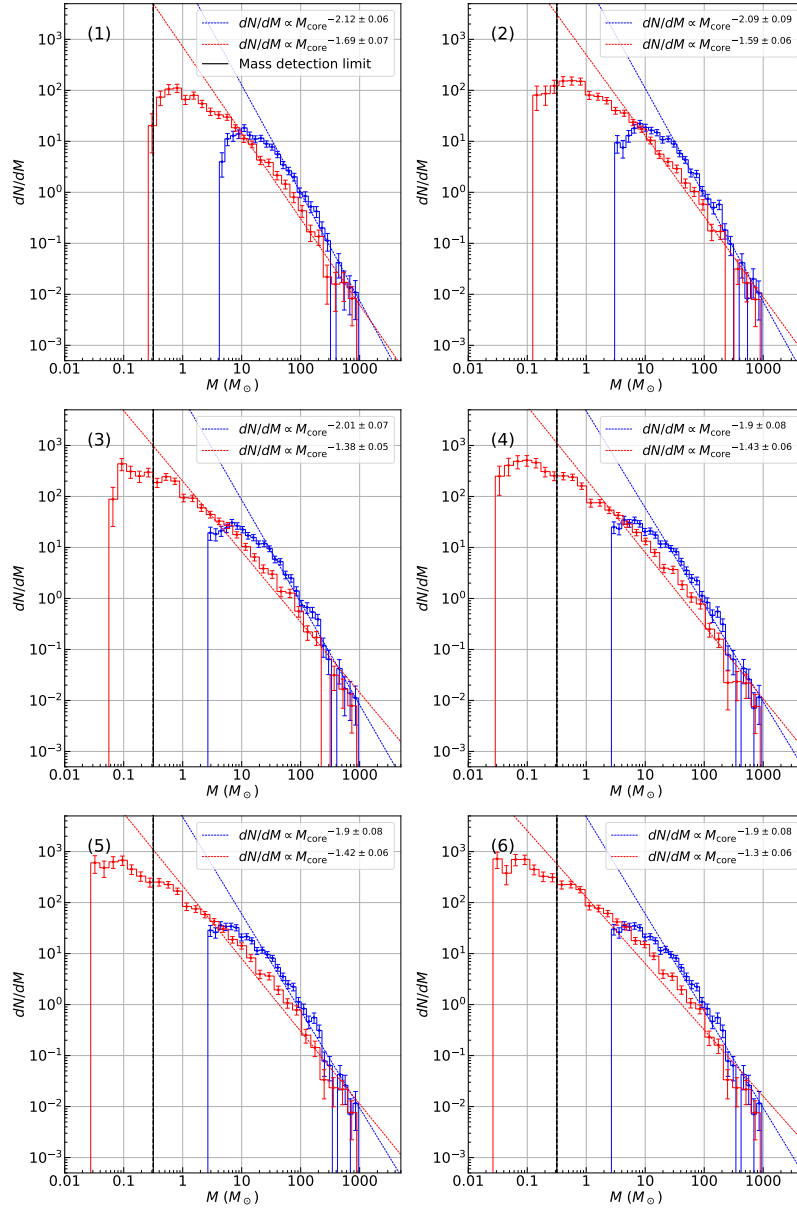


Figure A.3: The PP CMFs for all parameter cases in yz plane. The details are the same as Figure 2.2.

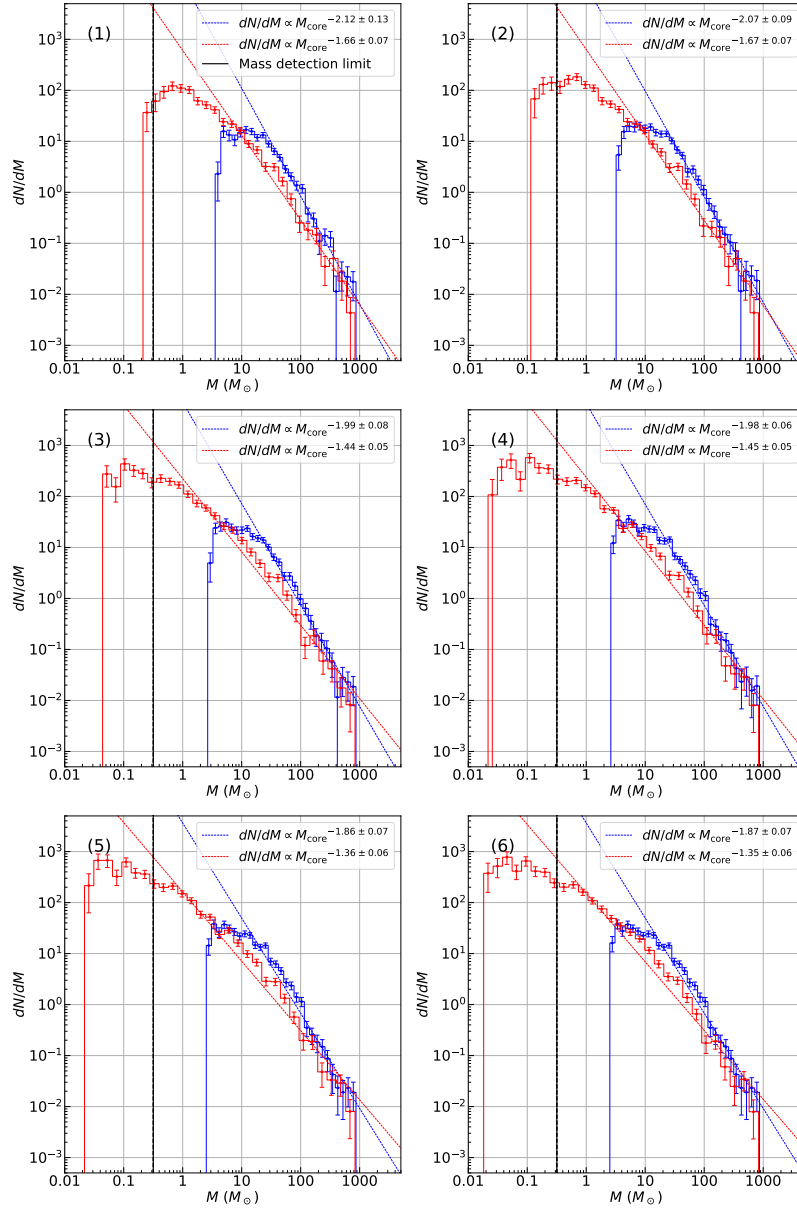


Figure A.4: The PP CMFs for all parameter cases in z_x plane. The details are the same as Figure 2.2.

Table A.5: The CMF Properties with PP Pata in yz Plane

Case No.	Category	Turnover Mass M_{\odot}	$\alpha \pm \sigma_{\alpha}$
1	w/o subtraction	11.04	-2.12 ± 0.06
	w/ subtraction	0.8	-1.69 ± 0.07
2 (fiducial)	w/o subtraction	8.14	-2.09 ± 0.09
	w/ subtraction	0.57	-1.59 ± 0.06
3	w/o subtraction	6.83	-2.01 ± 0.07
	w/ subtraction	0.09	-1.38 ± 0.05
4	w/o subtraction	4.41	-1.9 ± 0.08
	w/ subtraction	0.1	-1.43 ± 0.06
5	w/o subtraction	4.41	-1.9 ± 0.08
	w/ subtraction	0.1	-1.42 ± 0.06
6	w/o subtraction	4.41	-1.9 ± 0.08
	w/ subtraction	0.03	-1.3 ± 0.06

Table A.6: The CMF Properties with PP Data in zx Plane

Case No.	Category	Turnover Mass M_{\odot}	$\alpha \pm \sigma_{\alpha}$
1	w/o subtraction	11.84	-2.12 ± 0.13
	w/ subtraction	0.67	-1.66 ± 0.07
2 (fiducial)	w/o subtraction	8.12	-2.07 ± 0.09
	w/ subtraction	0.69	-1.67 ± 0.07
3	w/o subtraction	5.44	-1.99 ± 0.08
	w/ subtraction	0.1	-1.44 ± 0.05
4	w/o subtraction	5.24	-1.98 ± 0.06
	w/ subtraction	0.11	-1.45 ± 0.05
5	w/o subtraction	3.38	-1.86 ± 0.07
	w/ subtraction	0.05	-1.36 ± 0.06
6	w/o subtraction	3.38	-1.87 ± 0.07
	w/ subtraction	0.05	-1.35 ± 0.06

A.2 Analysis of PPV Data

A.2.1 Dense Core Survey and Construction of CMFs with PPV Data in yzv and zxv Spaces

In this appendix, we show the results of analyses of PPV data in yzv and zxv spaces. We summarize the results of dense core surveys with PPV data in yzv space and zxv space in Tables A.7 and A.8. Then, Figures A.5 and A.6 show the PPV CMFs in yzv space and zxv space and these properties are in Tables A.9 and A.10. Even though two clouds collide in the xy plane, the core properties and CMF properties do not have many differences with the selection of velocity axes. PPV CMFs resemble a PPP CMF, as mentioned in Section 2.6, and the discussion there does not depend on the direction, at least in our simulation data. We note that the velocity range along the y axis is larger than that along the x and z axes.

Table A.7: The Results of Dense Core Survey with PPV Data (yzv Space)

Case No.	Number of Identified Cores
1	1129
2 (fiducial)	1134
3	1136
4	1136
5	1136
6	1136

Table A.8: The Results of Dense Core Survey with PPV Data (zxv Space)

Case No.	Number of Identified Cores
1	971
2 (fiducial)	978
3	979
4	979
5	979
6	979

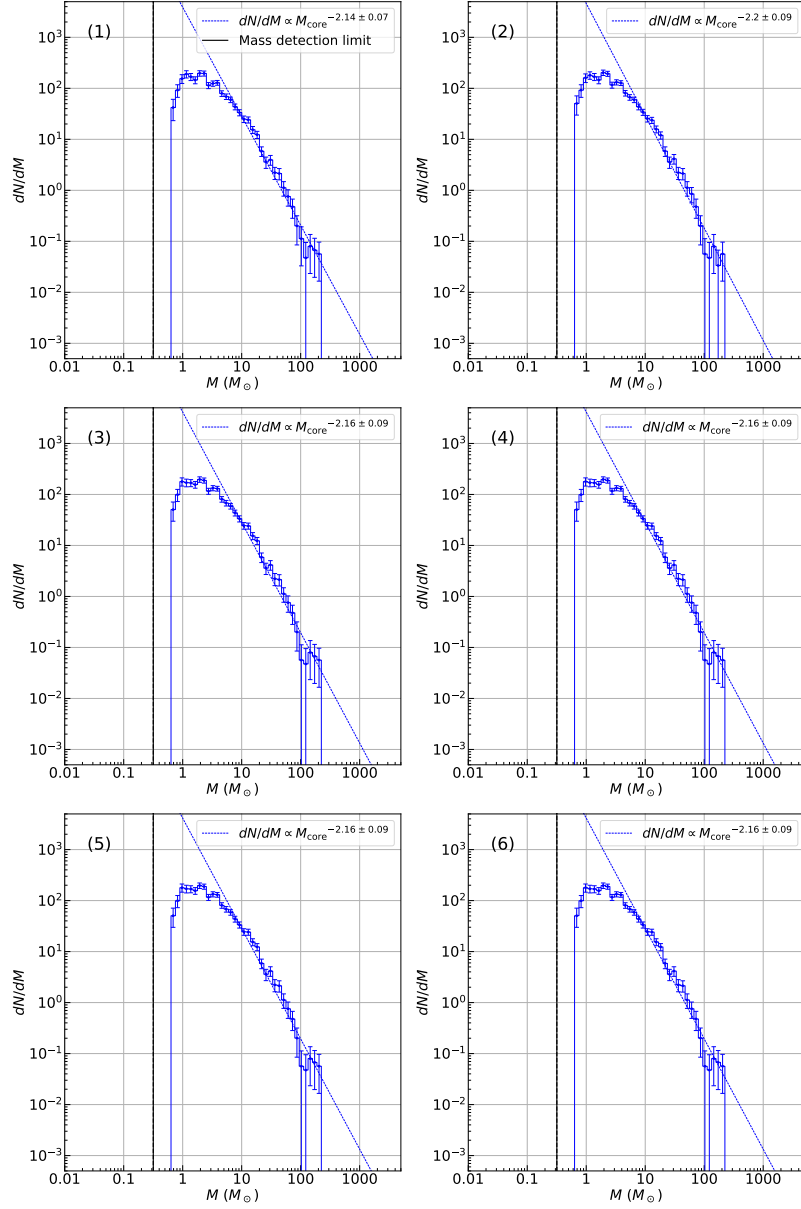


Figure A.5: The PPV CMFs for all parameter cases in yzv space. The details are the same as Figure 2.2.

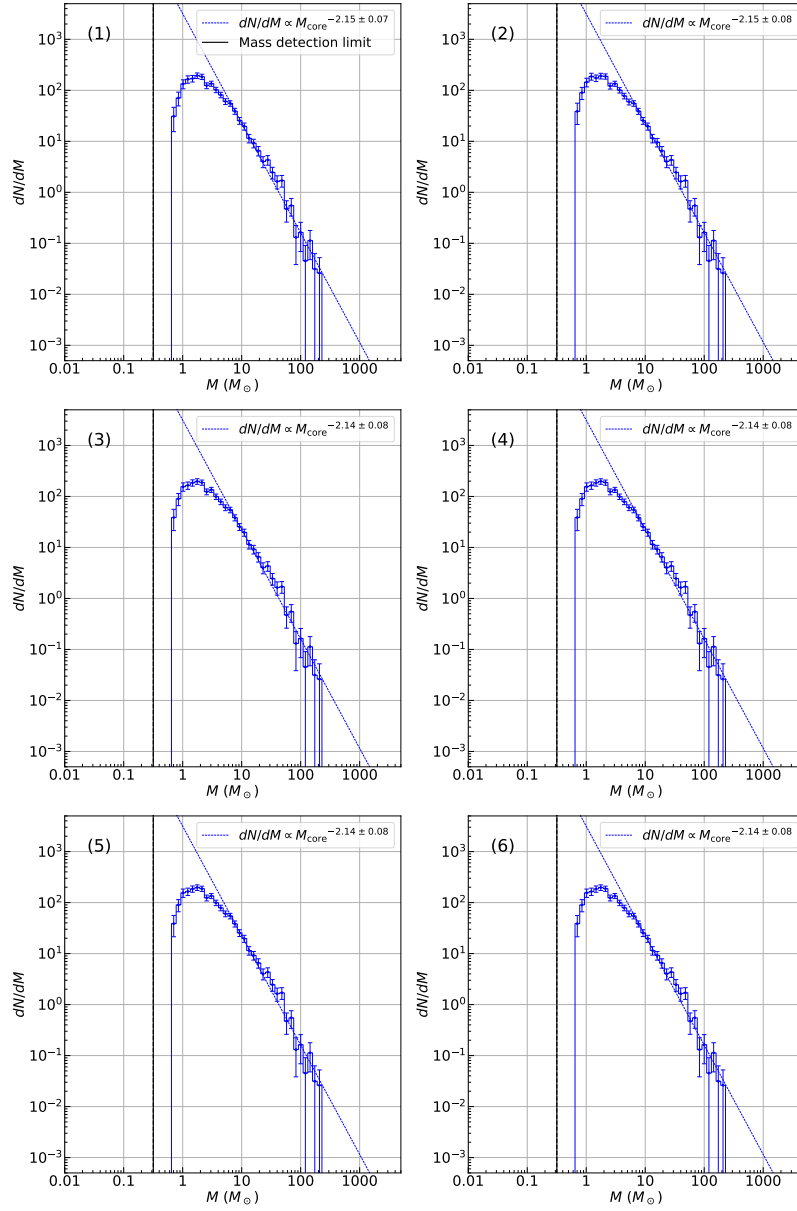


Figure A.6: The PPV CMFs for all parameter cases in zxv space. The details are the same as Figure 2.2.

Table A.9: The CMF Properties with PPV Data in yzv Space

Case No.	Turnover Mass M_{\odot}	$\alpha \pm \sigma_{\alpha}$
1	1.94	-2.14 ± 0.07
2 (fiducial)	1.94	-2.2 ± 0.09
3	1.94	-2.16 ± 0.09
4	1.94	-2.16 ± 0.09
5	1.94	-2.16 ± 0.09
6	1.94	-2.16 ± 0.09

Table A.10: The CMF Properties with PPV Data in zxv Space

Case No.	Turnover Mass M_{\odot}	$\alpha \pm \sigma_{\alpha}$
1	1.76	-2.15 ± 0.07
2 (fiducial)	1.76	-2.15 ± 0.08
3	1.76	-2.14 ± 0.08
4	1.76	-2.14 ± 0.08
5	1.76	-2.14 ± 0.08
6	1.76	-2.14 ± 0.08

B. Appendix of Chapter 3

B.1 Virial Analysis

In Section 3.2.2 of the main text, we defined the cores with $\alpha_{\text{vir}} < 2$ and $\alpha_{\text{vir}} \geq 2$ as gravitationally bound and unbound cores. However, the definition seems not to be always appropriate for classification because we calculate virial ratio assuming a spherically symmetric core with no magnetic field. Then, we investigate the influence on our main conclusion when we change the adopted threshold of the virial ratio by adopting $\alpha_{\text{vir}} < 1$ as a condition of bound cores and discuss the core properties in this appendix. The smaller threshold reduces the number of bound cores, as shown in Table B.1 as expected. This will affect the estimation of a core lifetime and CMF properties.

Table B.1: The Summary of Number of Starless Cores with $\alpha \leq 1$

Region	Condition of bound core	
	$\alpha_{\text{vir}} < 2$	$\alpha_{\text{vir}} < 1$
Orion A	1045	408
(a) OMC-1/2/3 area	212	75
(b) OMC-4/5 area	291	102
(c) L1641N area	321	126
(d) L1641C area	221	105

First, we show the core lifetime – core density relations for four subregions in Figure B.1 following Figure 3.19 in Section 3.3.2 the main text. The lifetimes of less dense bound cores with $\leq 10^5 \text{ cm}^{-3}$ become shorter. On the other hand, the lifetimes of the denser cores with $> 10^5 \text{ cm}^{-3}$ are not affected by the adopted threshold. Also, the trend that most of the core lifetimes are between 5 and 30 free-fall times is not changed. Therefore, we conclude that the impact of a different definition of bound cores is small on discussing a core lifetime unless a much

smaller virial ratio is set as a condition of bound cores.

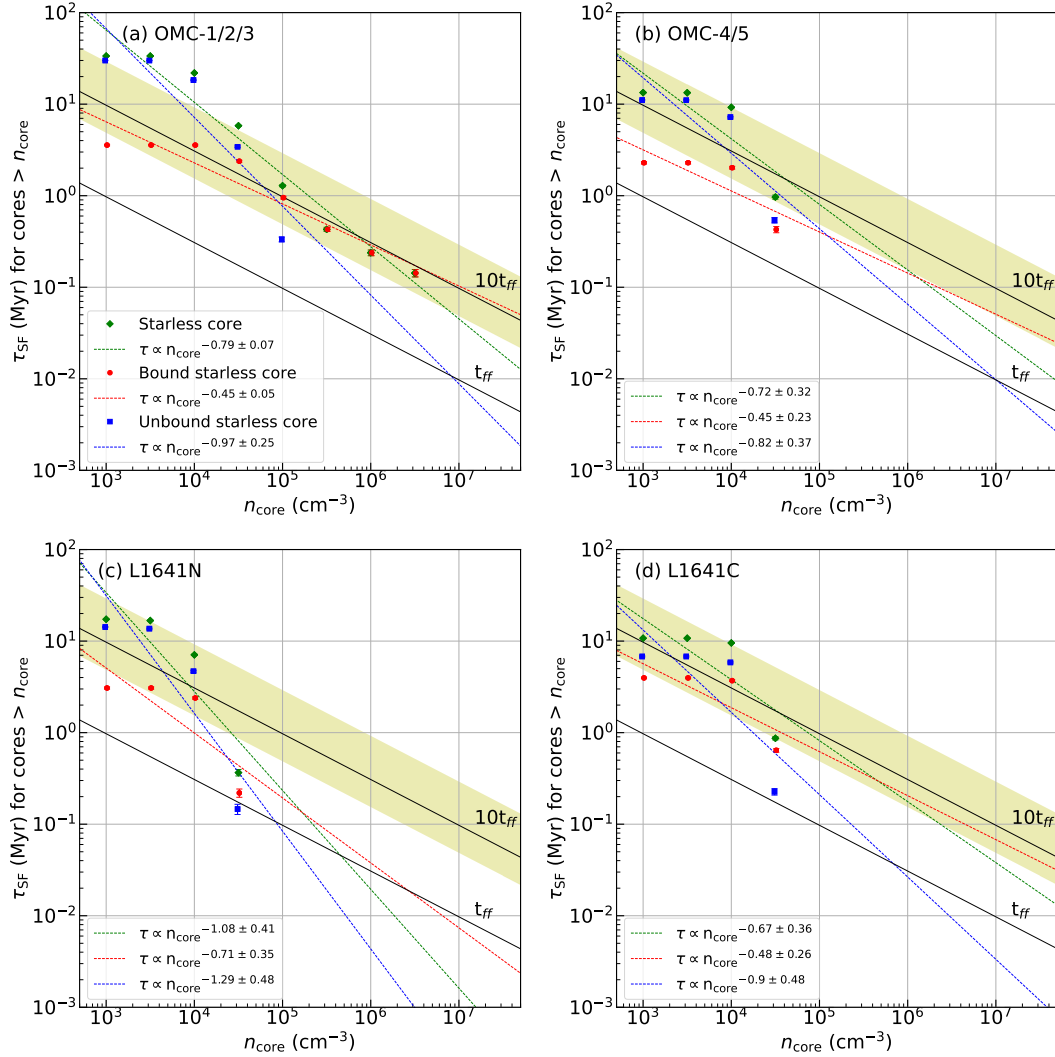


Figure B.1: The same as Figure 3.19 but $\alpha_{\text{vir}} < 1$ is a condition of a bound core.

Second, we show the CMFs of four regions in Figure B.2 following Figure 3.26 in Section 3.4.2 in the main text. The CMF parameters are summarized in Table B.2. Since we just changed the condition of bound cores, the CMF properties of starless cores are the same as the main text. From the virial ratio – mass relation in Figure 3.16, lower-mass cores tend to have smaller virial ratios. Then, a part of the low-mass cores that are classified as bound cores in the main text is reclassified as

unbound cores in this appendix. Contrary, higher-mass bound cores are reclassified as bound cores again. The effect makes the bound core MF slopes shallower and the turnover masses larger by one or two mass bins. Because the slopes of all CMF in all subregions are shallower, the comparison among subregions is unaffected. Even if the turnover mass shifts by one or two mass bins, it becomes $\sim 0.2 M_{\odot}$ that resembles the turnover mass of IMF in the ONC region (See Figure 3.25 (b)). Therefore, we summarise that there is no severe impact on the discussion of mass accretion based on CMF properties. However, the description of mapping from CMF to IMF may be affected; CMFs can be shallower when we use a small virial ratio to define bound cores.

Table B.2: The Summary of CMF Parameters in Orion A and Subregions in Figure B.2

Region	Category	Turnover Mass (M_{\odot})	High-mass Slope Power-law index \pm Error	Highest Mass (M_{\odot})
Orion A	Identified Core	0.15	-2.44 ± 0.26	72.21
	Starless Core	0.15	-2.41 ± 0.25	72.21
	Bound Starless Core	0.15	-2.34 ± 0.24	72.21
(a) OMC-1/2/3 area	Identified Core	0.04	-1.89 ± 0.06	72.21
	Starless Core	0.04	-1.93 ± 0.10	72.21
	Bound Starless Core	0.24	-1.55 ± 0.13	72.21
(b) OMC-4/5 area	Identified Core	0.07	-2.35 ± 0.11	4.88
	Starless Core	0.07	-2.20 ± 0.07	3.31
	Bound Starless Core	0.15	-1.80 ± 0.13	3.31
(c) L1641N area	Identified Core	0.07	-2.48 ± 0.14	8.39
	Starless Core	0.07	-2.44 ± 0.15	8.39
	Bound Starless Core	0.15	-2.24 ± 0.27	8.39
(d) L1641C area	Identified Core	0.15	-2.44 ± 0.26	4.46
	Starless Core	0.15	-2.41 ± 0.25	4.46
	Bound Starless Core	0.15	-2.09 ± 0.24	4.46

B.2 Two-Sample KS Test of Core Properties in Subregions of Orion A

In this appendix, we show the results of the KS test of each core physical property among each core category in Tables B.3, B.4, B.5, and B.6 for OMC-1/2/3 area, OMC-4/5 area, L1641N/V380 Ori area, and L1641C area, respectively. We performed the KS test for three pairs in each region: starless cores and protostellar cores, bound starless cores and unbound starless cores, and bound starless cores and protostellar cores. Since the number of protostellar cores in each subregion is small, the results of the KS test using protostellar core samples probably contain

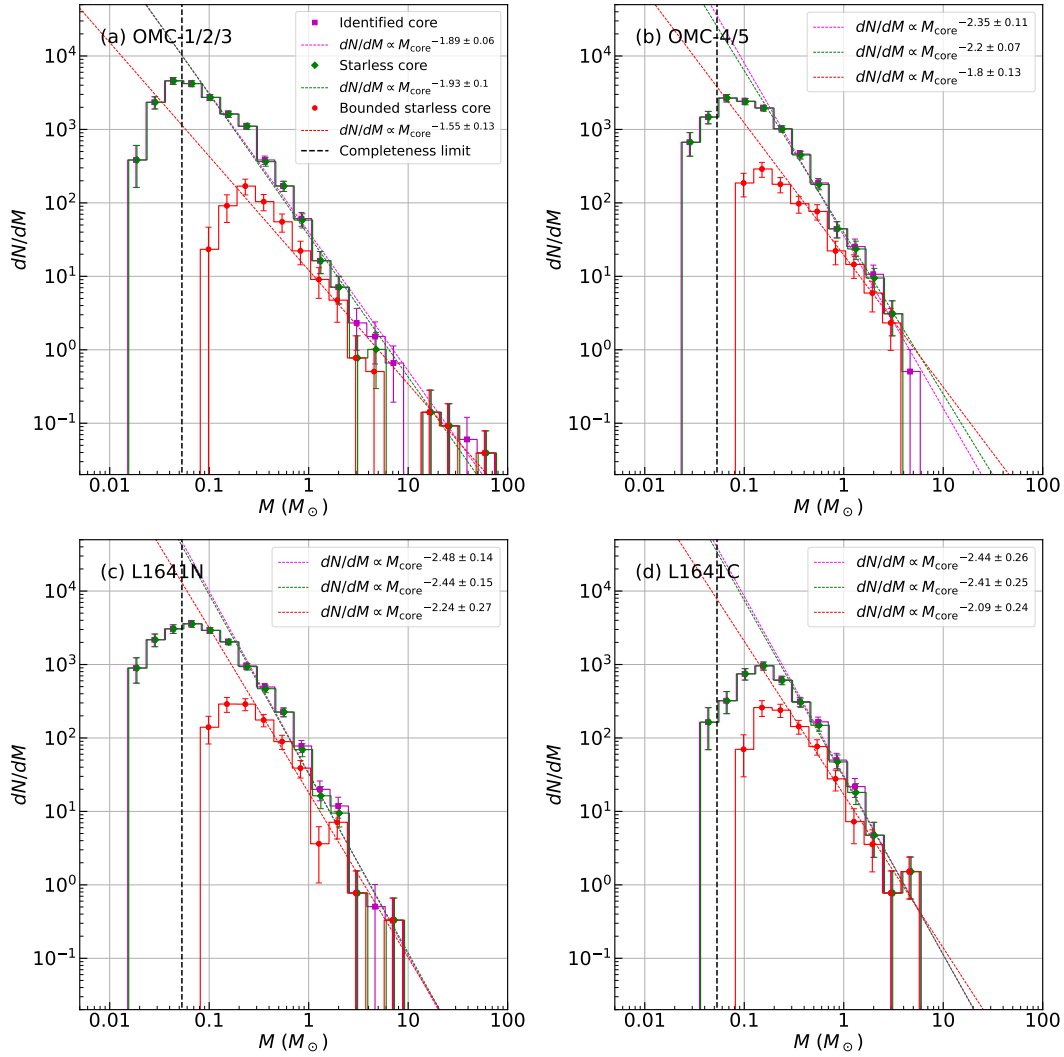


Figure B.2: The same as Figure 3.26 but $\alpha_{\text{vir}} < 1$ is a condition of a bound core.

large uncertainties. The p-values between bound and unbound cores for velocity width in FWHM, mass, and number density are much smaller than 0.05 in all subregions. Thus, the results suggest they have statistically different distributions, as discussed in Section 3.3.

Table B.3: The Results of KS Test of Core Properties in OMC-1/2/3 Area

Core Property	Category	p-value
Diameter (pc)	Starless Core & Protostellar Core	6.43×10^{-1}
	Bound Starless Core & Unbound Starless Core	9.12×10^{-1}
	Bound Starless Core & Protostellar Core	7.39×10^{-1}
Aspect Ratio	Starless Core & Protostellar Core	6.95×10^{-1}
	Bound Starless Core & Unbound Starless Core	1.30×10^{-2}
	Bound Starless Core & Protostellar Core	9.42×10^{-1}
FWHM (km s^{-1})	Starless Core & Protostellar Core	2.35×10^{-1}
	Bound Starless Core & Unbound Starless Core	1.13×10^{-14}
	Bound Starless Core & Protostellar Core	4.69×10^{-3}
Mass (M_{\odot})	Starless Core & Protostellar Core	2.32×10^{-6}
	Bound Starless Core & Unbound Starless Core	6.81×10^{-25}
	Bound Starless Core & Protostellar Core	3.59×10^{-3}
Number Density (10^4 cm^{-3})	Starless Core & Protostellar Core	1.75×10^{-8}
	Bound Starless Core & Unbound Starless Core	7.05×10^{-31}
	Bound Starless Core & Protostellar Core	6.04×10^{-5}
Virial Ratio	Starless Core & Protostellar Core	6.04×10^{-5}
	Bound Starless Core & Unbound Starless Core	-
	Bound Starless Core & Protostellar Core	2.22×10^{-5}

Besides, we also conducted the KS test among physical properties of bound and unbound cores in different subregions for reference. Tables B.7, B.8, B.9, B.10, B.11, and B.12 represent the results for diameter, aspect ratio, velocity FWHM, mass, density, and virial ratio, respectively.

B.3 CMF with Variable Sized Bin

In the main text, we constructed CMFs with uniform sized bins. Then, this appendix shows the CMFs of four subregions with variably sized bins. Figure B.3 and Table B.13 present the CMFs and their properties in the four subregions. According to the analysis of numerical simulation data in Section 2.6, PPV CMF with variably

Table B.4: The Results of KS Test of Core Properties in OMC-4/5 Area

Core Property	Category	p-value
Diameter (pc)	Starless Core & Protostellar Core	7.53×10^{-1}
	Bound Starless Core & Unbound Starless Core	5.85×10^{-3}
	Bound Starless Core & Protostellar Core	9.01×10^{-1}
Aspect Ratio	Starless Core & Protostellar Core	4.76×10^{-1}
	Bound Starless Core & Unbound Starless Core	7.27×10^{-1}
	Bound Starless Core & Protostellar Core	3.83×10^{-1}
FWHM (km s^{-1})	Starless Core & Protostellar Core	2.91×10^{-1}
	Bound Starless Core & Unbound Starless Core	0
	Bound Starless Core & Protostellar Core	8.68×10^{-3}
Mass (M_{\odot})	Starless Core & Protostellar Core	1.16×10^{-2}
	Bound Starless Core & Unbound Starless Core	6.76×10^{-14}
	Bound Starless Core & Protostellar Core	9.16×10^{-2}
Number Density (10^4 cm^{-3})	Starless Core & Protostellar Core	3.91×10^{-5}
	Bound Starless Core & Unbound Starless Core	2.84×10^{-14}
	Bound Starless Core & Protostellar Core	6.26×10^{-4}
Virial Ratio	Starless Core & Protostellar Core	6.26×10^{-4}
	Bound Starless Core & Unbound Starless Core	-
	Bound Starless Core & Protostellar Core	3.85×10^{-3}

Table B.5: The Results of KS Test of Core Properties in L1641N Area

Core Property	Category	p-value
Diameter (pc)	Starless Core & Protostellar Core	8.72×10^{-1}
	Bound Starless Core & Unbound Starless Core	1.83×10^{-5}
	Bound Starless Core & Protostellar Core	3.58×10^{-1}
Aspect Ratio	Starless Core & Protostellar Core	7.71×10^{-1}
	Bound Starless Core & Unbound Starless Core	1.11×10^{-1}
	Bound Starless Core & Protostellar Core	4.85×10^{-1}
FWHM (km s^{-1})	Starless Core & Protostellar Core	1.75×10^{-2}
	Bound Starless Core & Unbound Starless Core	9.99×10^{-16}
	Bound Starless Core & Protostellar Core	7.57×10^{-5}
Mass (M_{\odot})	Starless Core & Protostellar Core	4.73×10^{-6}
	Bound Starless Core & Unbound Starless Core	9.99×10^{-16}
	Bound Starless Core & Protostellar Core	3.75×10^{-3}
Number Density (10^4 cm^{-3})	Starless Core & Protostellar Core	5.86×10^{-7}
	Bound Starless Core & Unbound Starless Core	9.99×10^{-16}
	Bound Starless Core & Protostellar Core	4.73×10^{-6}
Virial Ratio	Starless Core & Protostellar Core	4.73×10^{-6}
	Bound Starless Core & Unbound Starless Core	-
	Bound Starless Core & Protostellar Core	7.41×10^{-3}

Table B.6: The Results of KS Test of Core Properties in L1641C Area

Core Property	Category	p-value
Diameter (pc)	Starless Core & Protostellar Core	5.98×10^{-1}
	Bound Starless Core & Unbound Starless Core	1.26×10^{-1}
	Bound Starless Core & Protostellar Core	5.57×10^{-1}
Aspect Ratio	Starless Core & Protostellar Core	5.53×10^{-1}
	Bound Starless Core & Unbound Starless Core	8.73×10^{-1}
	Bound Starless Core & Protostellar Core	5.60×10^{-1}
FWHM (km s^{-1})	Starless Core & Protostellar Core	8.59×10^{-2}
	Bound Starless Core & Unbound Starless Core	2.78×10^{-15}
	Bound Starless Core & Protostellar Core	1.50×10^{-2}
Mass (M_{\odot})	Starless Core & Protostellar Core	2.03×10^{-3}
	Bound Starless Core & Unbound Starless Core	3.26×10^{-4}
	Bound Starless Core & Protostellar Core	5.15×10^{-3}
Number Density (10^4 cm^{-3})	Starless Core & Protostellar Core	1.05×10^{-2}
	Bound Starless Core & Unbound Starless Core	1.18×10^{-4}
	Bound Starless Core & Protostellar Core	2.05×10^{-2}
Virial Ratio	Starless Core & Protostellar Core	2.05×10^{-2}
	Bound Starless Core & Unbound Starless Core	-
	Bound Starless Core & Protostellar Core	9.60×10^{-2}

Table B.7: The Results of KS Test of Core Diameter Among Four Subregions

		OMC-1/2/3	OMC-4/5	L1641N	L1641C
OMC-1/2/3	Bound Starless Core	-	3.75×10^{-10}	6.66×10^{-16}	2.34×10^{-11}
	Unbound Starless Core	-	1.67×10^{-5}	2.26×10^{-9}	1.37×10^{-4}
OMC-4/5	Bound Starless Core	-	-	3.17×10^{-5}	1.20×10^{-1}
	Unbound Starless Core	-	-	9.72×10^{-2}	2.93×10^{-1}
L1641N	Bound Starless Core	-	-	-	4.02×10^{-2}
	Unbound Starless Core	-	-	-	7.80×10^{-1}

Table B.8: The Results of KS Test of Core Aspect Ratio Among Four Subregions

		OMC-1/2/3	OMC-4/5	L1641N	L1641C
OMC-1/2/3	Bound Starless Core	-	2.22×10^{-1}	1.84×10^{-1}	4.74×10^{-2}
	Unbound Starless Core	-	4.53×10^{-1}	5.89×10^{-1}	3.65×10^{-1}
OMC-4/5	Bound Starless Core	-	-	7.34×10^{-1}	8.49×10^{-1}
	Unbound Starless Core	-	-	8.76×10^{-1}	8.20×10^{-1}
L1641N	Bound Starless Core	-	-	-	3.39×10^{-1}
	Unbound Starless Core	-	-	-	6.40×10^{-1}

Table B.9: The Results of KS Test of Core Velocity Width Among Four Subregions

		OMC-1/2/3	OMC-4/5	L1641N	L1641C
OMC-1/2/3	Bound Starless Core	-	3.22×10^{-3}	4.46×10^{-8}	1.69×10^{-2}
	Unbound Starless Core	-	3.75×10^{-1}	1.13×10^{-6}	2.63×10^{-1}
OMC-4/5	Bound Starless Core	-	-	1.50×10^{-2}	8.26×10^{-1}
	Unbound Starless Core	-	-	5.21×10^{-4}	1.15×10^{-1}
L1641N	Bound Starless Core	-	-	-	1.17×10^{-2}
	Unbound Starless Core	-	-	-	7.38×10^{-5}

Table B.10: The Results of KS test of Core Mass Among Four Subregions

		OMC-1/2/3	OMC-4/5	L1641N	L1641C
OMC-1/2/3	Bound Starless Core	-	3.87×10^{-1}	7.25×10^{-1}	1.67×10^{-1}
	Unbound Starless Core	-	2.99×10^{-4}	2.83×10^{-1}	2.61×10^{-8}
OMC-4/5	Bound Starless Core	-	-	5.91×10^{-1}	6.04×10^{-3}
	Unbound Starless Core	-	-	1.07×10^{-4}	1.88×10^{-3}
L1641N	Bound Starless Core	-	-	-	4.39×10^{-2}
	Unbound Starless Core	-	-	-	1.73×10^{-8}

Table B.11: The Results of KS Test of Core Density Among Four Subregions

		OMC-1/2/3	OMC-4/5	L1641N	L1641C
OMC-1/2/3	Bound Starless Core	-	9.55×10^{-13}	6.66×10^{-16}	4.26×10^{-14}
	Unbound Starless Core	-	4.12×10^{-1}	3.12×10^{-26}	8.19×10^{-6}
OMC-4/5	Bound Starless Core	-	-	1.49×10^{-7}	1.14×10^{-1}
	Unbound Starless Core	-	-	2.00×10^{-15}	1.17×10^{-5}
L1641N	Bound Starless Core	-	-	-	1.25×10^{-9}
	Unbound Starless Core	-	-	-	2.06×10^{-24}

Table B.12: The Results of KS Test of Virial Ratio Among Four Subregions

		OMC-1/2/3	OMC-4/5	L1641N	L1641C
OMC-1/2/3	Bound Starless Core	-	9.78×10^{-1}	3.45×10^{-1}	8.44×10^{-3}
	Unbound Starless Core	-	2.83×10^{-6}	2.19×10^{-2}	4.24×10^{-9}
OMC-4/5	Bound Starless Core	-	-	6.96×10^{-1}	4.16×10^{-3}
	Unbound Starless Core	-	-	2.38×10^{-2}	2.58×10^{-3}
L1641N	Bound Starless Core	-	-	-	2.84×10^{-2}
	Unbound Starless Core	-	-	-	5.20×10^{-6}

sized bins is shallower above its turnover than the true CMF. Then, each CMF in Figure B.3 seems to be shallower than the true CMF in each subregion as well. At least CMFs with variably sized bins in this appendix are shallower than CMFs with uniform sized bins in the main text (see Figure 3.26). For turnovers, they resemble the CMFs with uniform sized bins. As we discussed in Section 3.3.2, the observed CMFs are considered to be not much different from the true CMFs. Therefore, the mapping from observed CMF to IMF should be studied with CMFs with uniform sized bins.

However, CMF with variably sized bins helps investigate and compare typical core properties among subregions since the CMF is biased around the turnover in which the cores and mass bins are concentrated. The power-law indices at the high-mass ends can be divided into two groups: the OMC-1/2/3 and OMC-4/5 areas and the L1641N and L1641C areas. The former has shallower slopes than the latter group. We see outstanding filamentary structure in OMC-1/2/3 and OMC-4/5 areas, but no such structure exists in L1641N and L1641C areas. Then, the difference in the slope of CMF is thought to be caused by the presence or absence of filaments.

B.4 CMFs with Column Density Threshold

In this appendix, we construct CMFs in Orion A by setting the thresholds of minimum column density at positions of cores N_{H_2} : $5 \times 10^{21} \text{ cm}^{-2}$ and 10^{22} cm^{-2} . Figure B.4 is the PDF of a column density at a core position in a cumulative form. Then, the CMFs with each column density thresholds and their properties are shown in Figure B.5 and Table B.14, respectively. The slopes above the turnovers of CMFs become shallow when we set a column density threshold. Also, the slopes are shallower with a higher column density threshold. The fraction of subregions

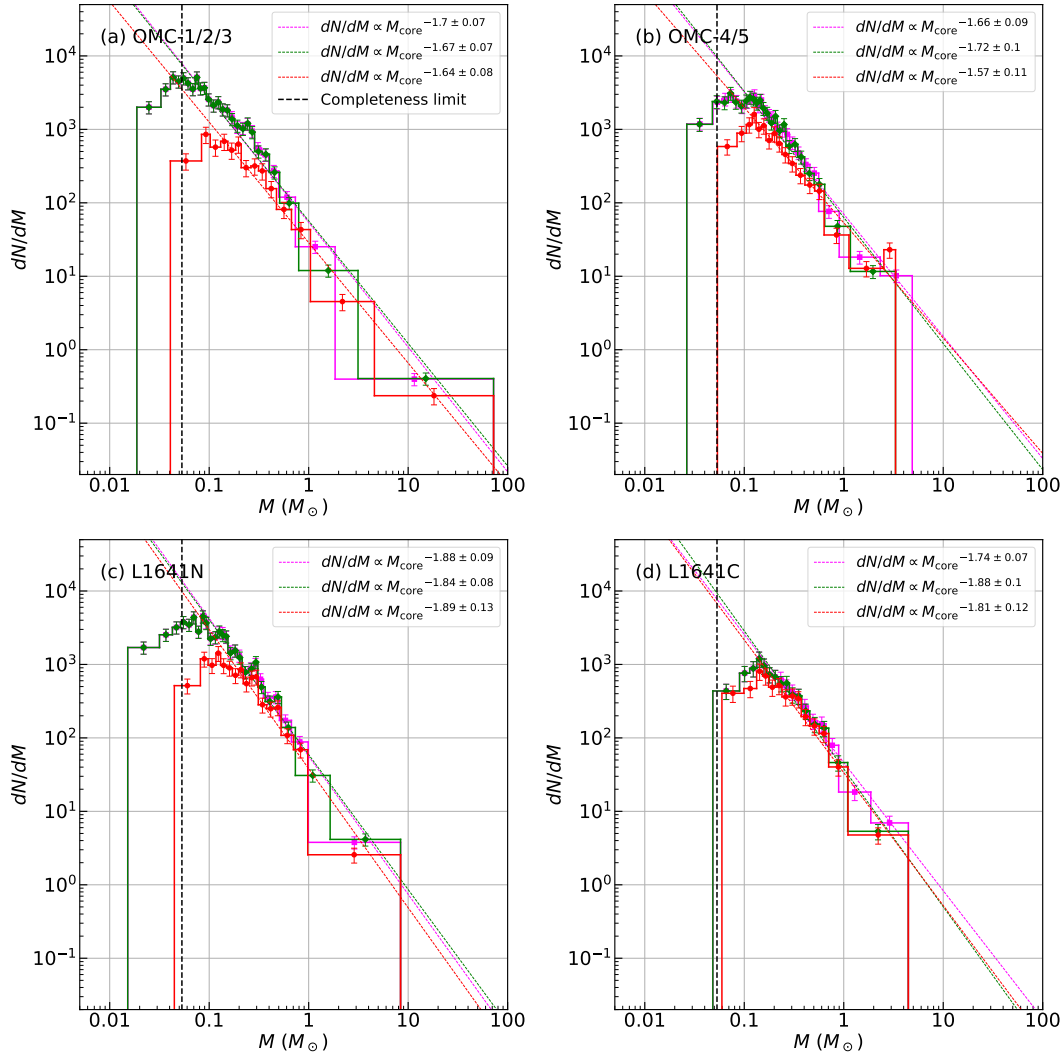


Figure B.3: The CMFs of subregions in Orion A with variable sized bin. Others are the same as Figure 3.26.

Table B.13: The Summary of CMF Properties in Subregions of Orion A with Variable Sized Bin

Region	Category	Turnover Mass (M_{\odot})	High-mass Slope Power-low index \pm Error
(a) OMC-1/2/3 area	Identified Core	0.04	-1.70 ± 0.07
	Starless Core	0.04	-1.67 ± 0.07
	Bound Starless Core	0.09	-1.64 ± 0.08
(b) OMC-4/5 area	Identified Core	0.07	-1.66 ± 0.09
	Starless Core	0.07	-1.72 ± 0.10
	Bound Starless Core	0.13	-1.57 ± 0.11
(c) L1641N	Identified Core	0.09	-1.88 ± 0.09
	Starless Core	0.09	-1.84 ± 0.08
	Bound Starless Core	0.12	-1.89 ± 0.13
(d) L1641C	Identified Core	0.14	-1.74 ± 0.07
	Starless Core	0.14	-1.88 ± 0.10
	Bound Starless Core	0.14	-1.81 ± 0.12

to which the cores composing the CMFs belong is shown in Figure B.6. The fractions with a threshold of $5 \times 10^{21} \text{ cm}^{-2}$ resemble that without a threshold. On the other hand, the fraction of OMC-1/2/3 and OMC-4/5 regions becomes higher with a threshold of 10^{22} cm^{-2} , and prominent filamentary structures are seen in the regions. Therefore, filaments are supposed to play an important role in core growth if CMF becomes shallower with mass accretion.

Table B.14: The Summary of CMF Parameters in Orion A with Column Density Thresholds

Column Density (cm^{-2})	Category	Turnover Mass (M_{\odot})	High-mass Slope Power-low index \pm Error	Highest Mass (M_{\odot})
(a) $>5 \times 10^{21}$	Identified Core	0.07	-2.13 ± 0.06	72.21
	Starless Core	0.07	-2.18 ± 0.10	72.21
	Bound Starless Core	0.10	-2.13 ± 0.10	72.21
(b) $>10^{22}$	Identified Core	0.10	-2.01 ± 0.06	72.21
	Starless Core	0.10	-2.05 ± 0.10	72.21
	Bound Starless Core	0.15	-2.00 ± 0.11	72.21

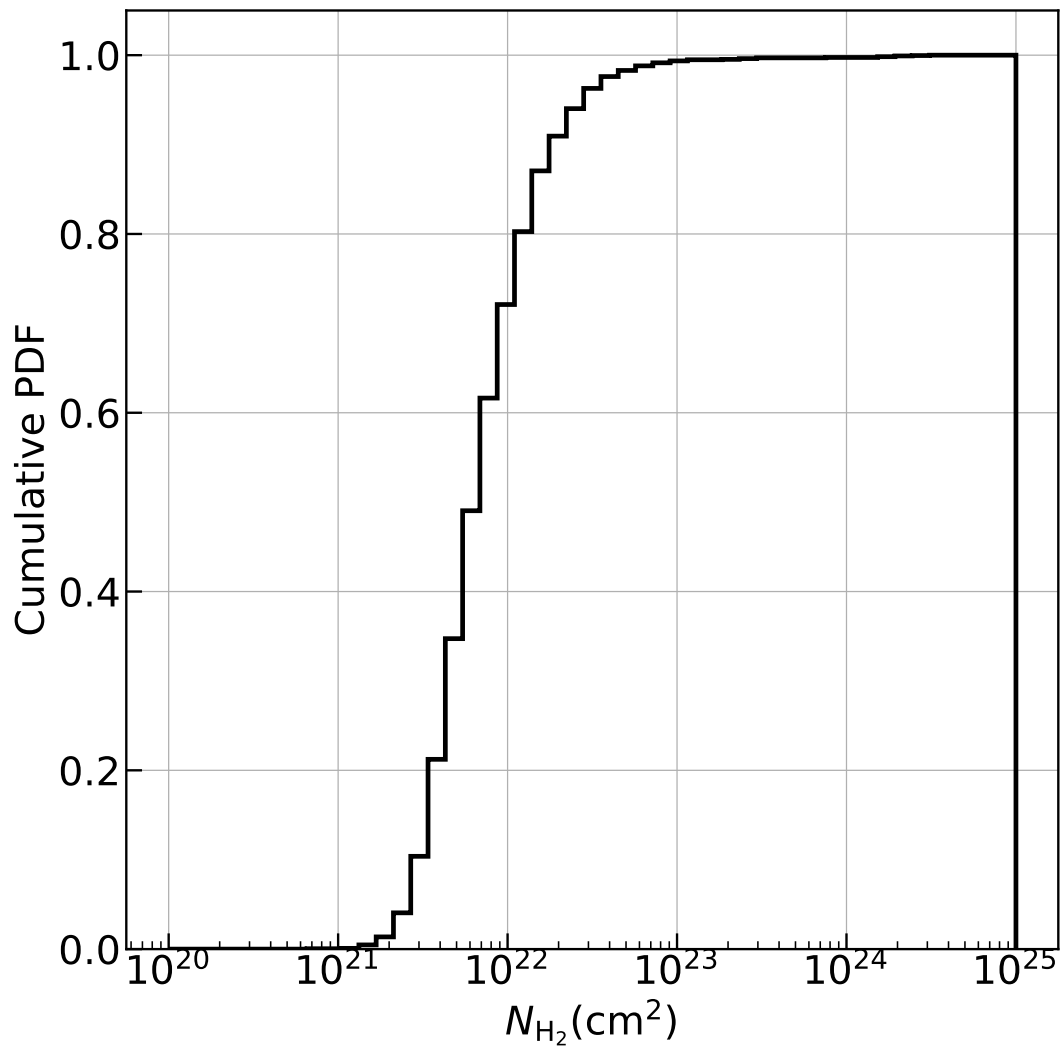


Figure B.4: The cumulative PDF of mean column density at a core position.

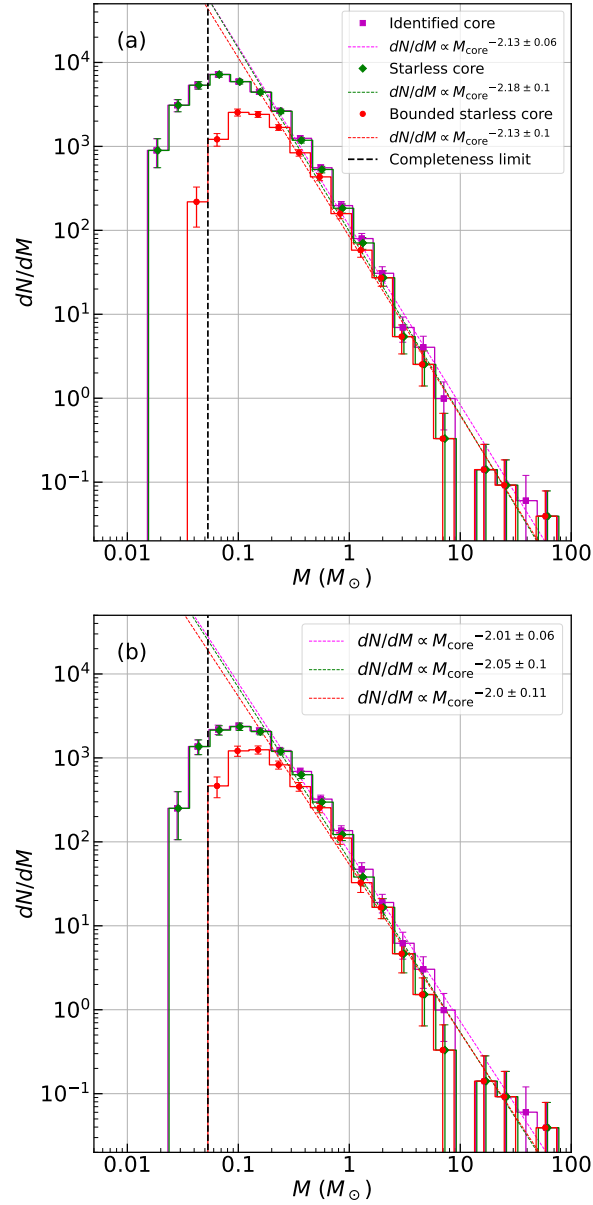


Figure B.5: The CMF in Orion A with column density thresholds of (a) $5 \times 10^{21} \text{ cm}^{-2}$ and (b) 10^{22} cm^{-2} . The details are same as Figure 3.25 (a).

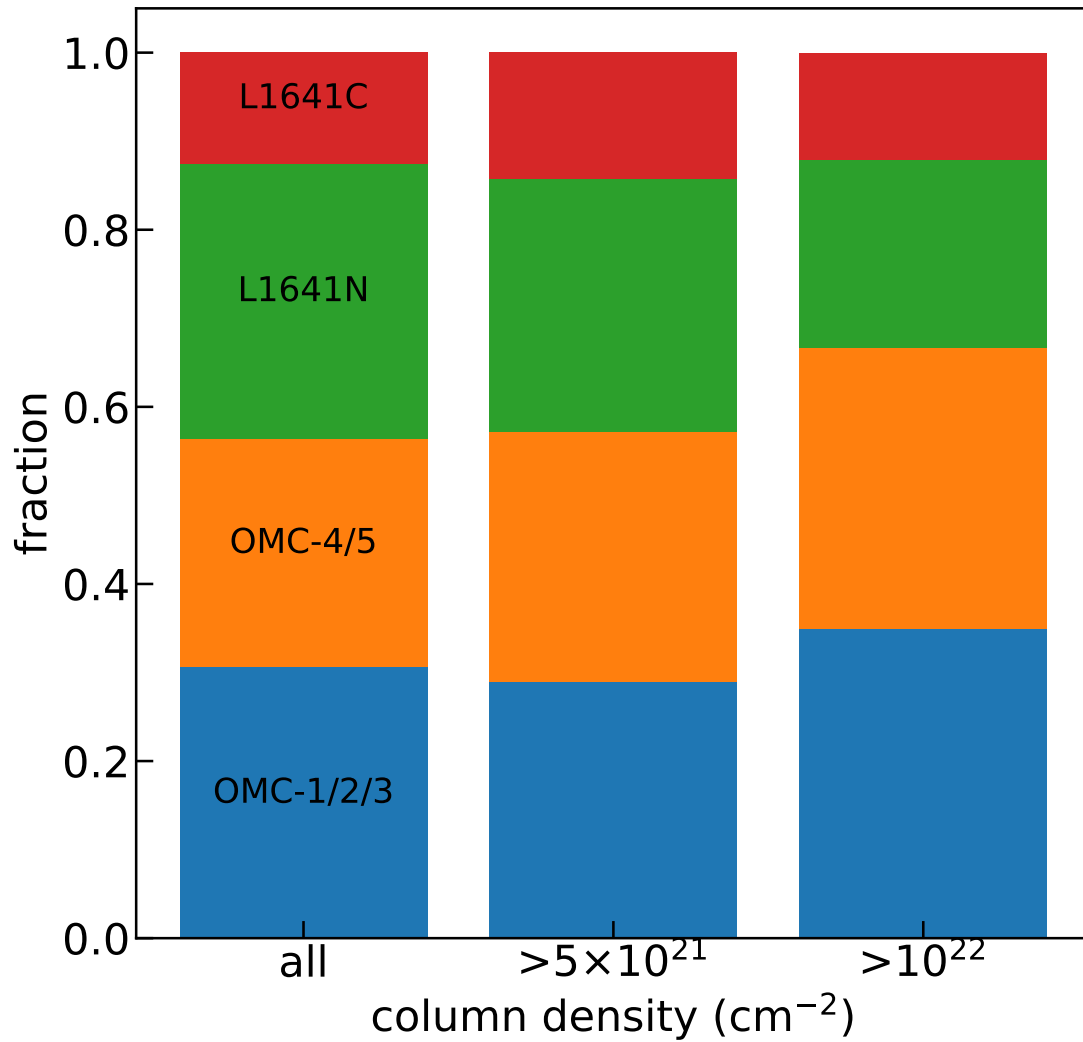


Figure B.6: The fraction of subregions of cores compose each CMF with column density threshold: OMC-1/2/3 (blue), OMC-4/5 (orange), L1641N (green), and L1641C (red), respectively.